Kamchai Choosrithong

A Contribution to Deep Excavation Analysis with the Finite Element Method

DOCTORAL THESIS

to achieve the university degree of

Doktor der technischen Wissenschaften

submitted to

Graz University of Technology

Supervisor

Ao.Univ.-Prof. Dipl.-Ing. Dr.techn. Helmut F. Schweiger, MSc.

Institute of Soil Mechanics, Foundation Engineering and Computational Geotechnics
Graz University of Technology, Austria

Prof. Noppadol Phien-Wej, MSc., Ph.D

Department of Civil Engineering and Infrastructure
Field of Study Geotechnical and Earth Resources Engineering
Asian Institute of Technology, Thailand

Graz, January 2020

Affidavit

I declare that I have authored this thesis independently, that I have not used other than the declared sources/resources, and that I have explicitly indicated all material which has been quoted either literally or by content from the sources used. The text document uploaded to TUGRAZonline is identical to the present doctoral thesis.

…………………	…………………………………………
Date	Signature

Acknowledgements

This dissertation would not have been possible without the continuous support and advice of Ao.Univ.-Prof. Dipl.-Ing. Dr.techn. Helmut F. Schweiger. I thank you Helmut for giving me the opportunity to work under his supervision and for providing the resources and the academic environment essential for performing the work summarised in this thesis. I am very grateful to his valuable guidance, discussions and encouragement throughout the study period. Appreciation by words is not sufficient to him who not only encouraged to apply, but also made the study successful complete.

Thanks are due to Univ.-Prof. Dipl.-Ing. Dr.techn. Roman Marte, Head of the Institute of Soil Mechanics, Foundation Engineering and Computational Geotechnics for making the research facilities available to me. I would also like to thank you Roman for all professional discussions and personal advice

I am grateful to Prof. Noppadol Phien-Wej of Asian Institute of Technology, Thailand for reviewing this thesis.

I thank all colleagues at the Institute of Soil Mechanics, Foundation Engineering and Computational Geotechnics for a very pleasant working environment and the many fruitful discussions, research related or otherwise. In particular, I would like to thank Carla Fabris, Mirva Gega, Patrick Pichler, Christopher Krammer, Laurin Hauser, Franz Tschuchnigg, Matthias Rebhan and Simon Oberhollenzer.

I would like to thank my family and Thai friends for all their support throughout this period of study.

The Ernst Mach Grant, ASEA-UNINET scholarship financed by the Bundesministerium für Bildung, Wissenschaft und Forschung (BMBWF) is gratefully acknowledged.

Graz, January 2020 Kamchai Choosrithong

Kurzfassung

Ein Beitrag zur Berechnung von Tiefen Baugruben mit der Finite-Elemente-Methode

Die Ausführung von Ingenieurbauwerken und die Dimensionierung tiefer Baugruben sind bei ungünstigen Baugrundverhältnissen im Allgemeinen mit erheblichen Schwierigkeiten verbunden. Dies ist insbesondere bei der Errichtung geotechnischer Strukturen in weichen Böden der Fall, da diese sensitiv auf Verformungen reagieren und geringe Festigkeit besitzen. Numerische Methoden stellen ein wertvolles Hilfsmittel dar, um das mechanische Verhalten tiefer Baugruben zu beurteilen, und tragen neben hochentwickelten Verfahrenstechniken zu einer sicheren und wirtschaftlichen Bauweise bei. Auf Grund der komplexen Randbedingungen wird neben anderen numerischen Methoden vor allem die Finite-Elemente-Methode unter Anwendung hochwertiger Stoffgesetze eingesetzt.

In dieser Arbeit werden numerische Analysen von tiefen Baugruben mit der Finite-Elemente-Methode vorgestellt. Zu Beginn wird eine Übersicht über das mechanische Verhalten geotechnischer Strukturen gegeben, wobei der Schwerpunkt auf Faktoren, die die Stabilität beeinflussen, gelegt wird. Anschließend werden wichtige Aspekte der Anwendung der Finiten-Elemente-Methode für Baugruben diskutiert, wobei besonderes Augenmerk auf die numerische Modellierung, die Stoffmodelle und die Baugrund-Bauwerks-Interaktion gelegt wird. Explizite Beachtung findet der Einfluss der Stützkonstruktion auf das Verhalten von Baugruben, insbesondere wenn Versagen einzelner Konstruktionselemente maßgebend sind, wie zum Beispiel eine ungenügende Einbindung der Verbauwand oder das Versagen einzelner Aussteifungselemente. Der Einfluss des Stoffmodells mit dem der Baugrund bzw. die Stützelemente beschrieben werden, wird ebenfalls untersucht.

Abschließend werden Fallbeispiele vorgestellt. Die Berechnungsergebnisse werden durch einen Vergleich mit in-situ Messungen von Wandverschiebungen, Baugrundverformungen und Öberflächensetzungen beurteilt. Die Vergleiche zeigen, dass eine erfolgreiche numerische Berechnung die Berücksichtigung von Anisotropie und Nichtlinearität im Bereich kleiner Verzerrungen für den Boden sowie des nichtlinearen Verhaltens der Stützkonstruktion erfordern kann. Die Berechnungsergebnisse zeigen, dass mit hochwertigen Berechnungs- und Stoffmodellen zuverlässige Prognosen erstellt werden können. Die Bedeutung einer sorgfältigen Bestimmung der Kennwerte für Baugrund und Strukturelemente wird hervorgehoben.

Abstract

A Contribution to Deep Excavation Analysis with the Finite Element Method

Deep excavation design and the execution of civil engineering structures in difficult ground conditions are usually associated with substantial difficulties. This is especially important for the construction of underground structures in soft soil, since these types of soil are sensitive to deformation and possess low strength. For safe and economic construction, in addition to highly developed construction technologies, numerical methods represent a suitable tool for assessing the performance of deep excavations. Due to the complexity of boundary conditions, the finite element method, amongst other numerical techniques, is widely used whereas advanced constitutive models have to be employed.

In this thesis, analyses of deep excavations by means of the finite element method are presented. It begins with an overview of the behaviour of underground structures by focusing on the factors influencing excavation stability. Subsequently, the finite element method for deep excavations is reviewed, placing emphasis on numerical modelling and constitutive models within soil-structure interaction. Explicit focus is put on the influence of structural support systems on the behaviour of underground structures, in particular when failures dominate the overall performance of deep excavations, e.g. due to insufficient embedment depth of the retaining wall or failure of individual struts. The influence of constitutive models describing the mechanical behaviour of soil and structural support elements is investigated.

Finally, an analysis of case histories on deep excavations is presented. Model predictions are evaluated through comparisons with extensive field data, including wall deflections, soil deformations and surface settlement. Comparison with field observations shows that successful numerical prediction may require consideration of anisotropy at the small strain range and the small-strain nonlinearity of the soil, together with the non-linear behaviour of structural support systems. The results demonstrate that reliable predictions can be achieved by advanced constitutive models and advanced methods of analysis. The study also emphasises the need for a careful determination of input parameters for the soil layers and the structural support system.

Table of contents

List of symbols and abbreviations

The symbols used in this thesis are listed in alphabetic order. Additional explanation is provided in the text at first appearance.

Small letters

a	[-]	increase of ε_{cp} with increase of p' in concrete model
c'	[kPa]	effective cohesion
$f_{c,1}/f_{c,28}$	[-]	time dependency of strength
$f_{c,28}$	[kPa]	uniaxial compressive strength
f_{c0n}	[-]	normalised initially mobilised strength (compression)
f_{cfn}	[-]	normalised failure mobilised strength (compression)
f_{cun}	[-]	normalised residual mobilised strength (compression)
ft	[kPa]	uniaxial tensile strength
$f_{t,smeared}$	[kN/m^2]	tensile strength for smeared section
f_{tun}	[-]	normalised residual tensile strength
h	[m]	the average spacing between support
k_x, k_z	[m/s]	saturated hydraulic permeability in horizontal direction
k_y	[m/s]	saturated hydraulic permeability in vertical direction
m	[-]	power of stress dependency stiffness
n_{GP}	[-]	number of stress points per element
p'	[kN/m^2]	mean effective stress
p'_0	[kN/m^2]	initial mean effective stress
q	[kN/m^2]	deaviatoric stress
s_u	[kN/m^2]	undrained shear strength
t_{hydr}	[days]	time for full hydration (usually 28 days)
t_{50}^{cr}	[days]	time for 50% for creep strains
u_c	[kN/m^2]	final steady-state excess pore pressure
u_i	[kN/m^2]	initial excess pore pressure

Capital letters

A_{el}	[-]	size of the finite element
A_{mat}	[-]	shear hardening parameter of the multilaminate model
C_S	[%]	cement-soil content
$\boldsymbol{D}$	[-]	linear elastastic stiffness
E'	[-]	drained stiffness
EA	[kN[	axial stiffness
E'_h	[kN/m^2]	elastic modulus in horizontal direction
E'_{h0}	[kN/m^2]	small strain elastic modulus in horizontal direction
$E'_{h0,ref}$	[kN/m^2]	small strain elastic modulus in horizontal direction at reference pressure
EI	[kNm^2]	flexural rigidity
E_{50}	[kN/m^2]	secant modulus at 50% of deviatoric stress at failure
$E_{50,ref}$	[kN/m^2]	secant modulus at 50% of deviatoric stress at reference stress
E_{oed}	[kN/m^2]	actual stiffness for primary oedometer loading
$E_{oed,ref}$	[kN/m^2]	reference stiffness for primary oedometer loading
E_{ur}	[kN/m^2]	unloading/reloading modulus at actural stress
$E_{ur,ref}$	[kN/m^2]	unloading/reloading modulus at reference stress
E'_v	[kN/m^2]	elastic modulus in vertical direction
E'_{v0}	[kN/m^2]	small strain elastic modulus in vertical direction
$E'_{h0,ref}$	[kN/m^2]	small strain elastic modulus in vertical direction at reference pressure
E_1/E_{28}	[-]	time dependency of elastic stiffness
E_u	[kN/m^2]	undrained stiffness
G_c	[kN/m]	compressive fracture energy
G_s	[kN/m^2]	secant shear modulus
G_t	[kN/m]	tensile fracture energy
G_0	[kN/m^2]	initial isotropic shear modulus at small strains
$G_{0,ref}$	[kN/m^2]	initial isotropic shear modulus at small strains at reference pressure
$G_{ur,ref}$	[kN/m^2]	un- and reloading shear modulus at reference pressure
H	[m]	excavation depth

H_c	[-]	normalised compression softening parameter
H_t	[-]	normalised tension softening parameter
K	[-]	hardening parameter
K_0	[-]	lateral earth pressure coefficient at rest
K_{0nc}	[-]	lateral earth pressure coefficient at rest for normally consolidated conditions
L_{eq}	[m]	the characteristic length of the finite element
M_{net}	[kNm]	net bendimg moment for reinforced concrete section
M_p	[kNm]	maximum bending moment
N	[-]	stability number
N_p	[kN]	maximum compressive capacity
OCR	[-]	over-consolidation ratio
S	[-]	effective system stiffness
R_f	[-]	failure ratio
W_C	[%]	water-cement ratio
$W_{smeared}$	[m^3]	section modulus for smeared section

Small Greek letters

γ	[kN/m^3]	unit weight of soil
$\gamma_{0.7}$	[-]	shear strain at which G_{max} is reduced to 70%
γ_{sat}	[kN/m^3]	bulk unit weight of soil below ground water table
γ_{unsat}	[kN/m^3]	bulk unit weight of soil above ground water table
γ_w	[kN/m^3]	unit weight of water
ε	[-]	total strains
ε^{e} ,ε^{p} ,ε^{cr}	[-]	elastic strains, plastic strains and creep strains
ε^{shr} ,$\varepsilon^{shr}_{\infty}$	[-]	shrinkage and final shrinkage strains
ε^{p}_{3}	[-]	minor plastic train
ε^{p}_{cp}	[-]	minor plastic strain at peak in uniaxial compression
ε_{deg}	[-]	local degradation strain
ε_{deg1}, ε_{deg2}	[-]	local degradation strain defining onset of stiffness degradation and transition to large strains
ν', ν'_{ur}	[-]	drained Poisson’s ratio at large strain

ν'_{hh}	[-]	Poisson’s ratio within isotropic plane
ν'_{hh0}	[-]	initial Poisson’s ratio within isotropic plane
ν'_{vh}, ν'_{vh}	[-]	cross-anisotropic Poisson’s ratio
$\nu'_{vh,iso}$	[-]	cross-anisotropic Poisson’s ratio at isotropic stress
ν'_{vh0}, ν'_{vh0}	[-]	initial cross-anisotropic Poisson’s ratio
ν_{ur}	[-]	unloading effective Poisson’s ratio
σ	[kN/m^2]	stress / total stress
$\sigma'_1,\sigma'_2,\sigma'_3$	[kN/m^2]	major, intermediate and minor principle effective stiffness
σ'_h	[kN/m^2]	horizontal effective stiffness
σ'_{h0}	[kN/m^2]	initial horizontal effective stiffness
σ'_{nc}	[kN/m^2]	effective preconsolidation pressure
σ_t	[kN/m^2]	tensile strength
σ_{ref}	[kN/m^2]	reference stress
σ'_v	[kN/m^2]	vertical effective stiffness
σ'_{v0}	[kN/m^2]	initial vertical effective stiffness
τ, τ_{mob}, τ_{rel}	[kN/m^2]	shear stress, mobilised shear stress and relative shear stress
φ'	[°]	effective friction angle
φ'_i	[°]	initial mobilised friction angle
φ'_{cs}	[°]	effective friction angle at critical state
φ'_m	[°]	mobilised friction angle
φ'^{*}_m	[°]	mobilised friction angle at minimum mobilised dilatancy
φ_{max}	[°]	maximum friction angle at peak strength
φ^{cr}	[-]	ratio between creep and elastic strains
ψ'	[°]	dilatancy angle
ψ_m	[°]	mobilised dilatancy angle
$\psi_{m,min}$	[°]	minimum of mobilised dilatancy angle

Abbreviations

EC 7	Eurocode 7
FE	finite element

FEM	finite element method
GHS	Generalised hardening soil model
HS	Hardening soil model
HSS	Hardening soil small model
MIP	mixed-in-place
MLS	Multilaminate model

1 Introduction

1.1 Motivation

Deep excavation design and the execution of civil engineering structures in difficult ground conditions are usually associated with substantial difficulties. This is especially important with the construction of underground structures in soft soils, since the types of soil are sensitive to deformation and possess low shear strength. The expected displacement under working load conditions may be relatively large, and this potentially leads to damages to structural support systems, to existing structures and eventually poses a risk to human life during the executions, as well as throughout the lifespan of the projects concerned.

In many cases, overall failure, i.e. ultimate limit state, occurs when there is an inadequate safety margin established against the collapse of any significant element of a soil-structural system. Within the worst combinations of loading and material properties, imperfections in the construction quality of the supporting system, i.e. wall-embedment depth and insufficient bearing capacity of the connections, are considered as major contributing factors to the ultimate failure (e.g. Puller 2003, COI 2005, Chen et al. 2015). In optimum design an adequate safety margin with respect to the design code is generally required to cover for the uncertainties inherent in geotechnical engineering in order to avoid such situations and, hence, triggering mechanisms must be understood. As standard practices do not usually cover details concerning possible failure initiation during excavation, at least the near-failure behaviour of structural support systems, i.e. supported deep excavation, must be understood in detail in order to reduce the potential risks for overall failure of the structure.

Due to the complexity of boundary value problems, numerical methods represent suitable tools for assessing stress and deformation in the design of deep excavation activities and other geotechnical structures. The mechanical behaviour of geomaterials as well as structural components is significantly complex when the behaviour prior to a failure is of particular interest. In order to achieve this goal, the choice of an appropriate constitutive model for describing the stress-strain behaviour of the ground and structural components is essential.

In this thesis the behaviour of structural systems supporting deep excavation has been studied by means of the finite element method in order to gain insight into the mechanisms within soil-structure interaction from selected case histories. The influence of constitutive models describing the mechanical behaviour of soil and structural support elements are also investigated.

It is common practice for numerical analysis to be conducted adopting simple two-dimensional analyses involving either plane strain or axisymmetric conditions, but the information provided can sometimes be misleading. When dealing with deep excavations, such a simplification is very often not justified. Therefore, a full three-dimensional is required. Moreover, comparisons with field observations show that successful prediction requires the consideration of the small-strain nonlinearity of soil and the non-linear behaviour of structural support systems. Consequently, advanced constitutive models for soils are essential, and the input parameters should be calibrated against the extensive laboratory testing. Meeting all these requirements poses many challenges to engineers and researchers in practice.

This research is expected to have practical implications on the design and construction of deep excavation projects. The main focus of this study concerns the evaluation of the capability of finite element analysis in elaborating various aspects of performance of underground structures and providing increased confidence in terms of prediction purposes and practical approaches to projects. The findings and lessons learnt from numerical analyses represent the inspiration and motivation underpinning the research.

1.2 Scope and outline of the thesis

A brief introduction of the behaviour of underground structures is given at the beginning of the thesis, where the main focus is related to structural support system stiffness and its influence on construction activities. Additionally, the general approach concerning stability is discussed. The factors governing overall failure are highlighted to clarify the relationship between research and practice.

An introduction to deep excavation analysis by means of the finite element method is considered in chapter 3. It is noted that the relevant literature refers to numerical studies of deep excavations. The basic assumptions of two- and three- dimensional modelling are included. The requirements and roles within the constitutive model describing the mechanical behaviour of soil and cement-treated soils are emphasized. Special issues regarding the modelling of structural components and wall installation are also discussed.

A series of parametric studies are conducted by means of the finite element method for a 30-m deep excavation project in marine clay supported by a diaphragm wall and multiple layers of struts. Imperfections in underground structures, namely the insufficient embedment depth of the wall into the stiff soil layer and the failure of individual struts, are investigated in Chapter 4.

Chapter 5 presents an analysis of mixed-in-place (MIP) columns acting as retaining structure supporting excavation in a slope. An advanced constitutive model is applied to capture the behaviour of cement-treated soil where the progressive development of cracks dominates overall performance. It is shown that design of such structures compatible with Eurocode 7 requirements is perfectly feasible adopting finite element methods.

In chapter 6 a study is made of the factors involved in the potential failure of shaft excavation projects using the finite element method. This preliminary study will attempt to identify some of the causes of cracks initiation and the effects of geometrical imperfections within secant pile shaft excavations by means of FE-investigations. Suggestions for further study are also discussed.

In chapter 7 numerical analyses of case histories on deep excavations is presented. The importance of the constitutive model in analysing deep excavations is indicated by comparing results from excavations in Bangkok and Chicago subsoil conditions. Details concerning the predicted undrained shear strength, small strain non-linearity, stress dependent stiffness and influence of anisotropic small strain stiffness are emphasised. Additionally, a numerical investigation of the time-dependent behaviour of support systems is undertaken revealing that the results of predicted ground movements prove to be significant.

Conclusions and recommendations for further research projects are given in chapter 8, while references are provided in chapter 9.

2 Deep excavations – an overview

In this chapter an overview of the behaviour of supported deep excavation is presented. Assessment of ground deformation is of practical importance; thus a very stiff support system (i.e. a diaphragm wall supported by layers of struts) has to be considered in such a way that the embedment is placed on competent ground layers to limit ground movement. Structural forces are also kept within a limited state and do not allow large deflections. However, unusually large deflections during excavation are discussed, where the behaviour of excavation depends on particular geological conditions. Emphasis is placed on the stability of excavations and a detailed assessment of structural performance as reported in practical guidelines and published literature.

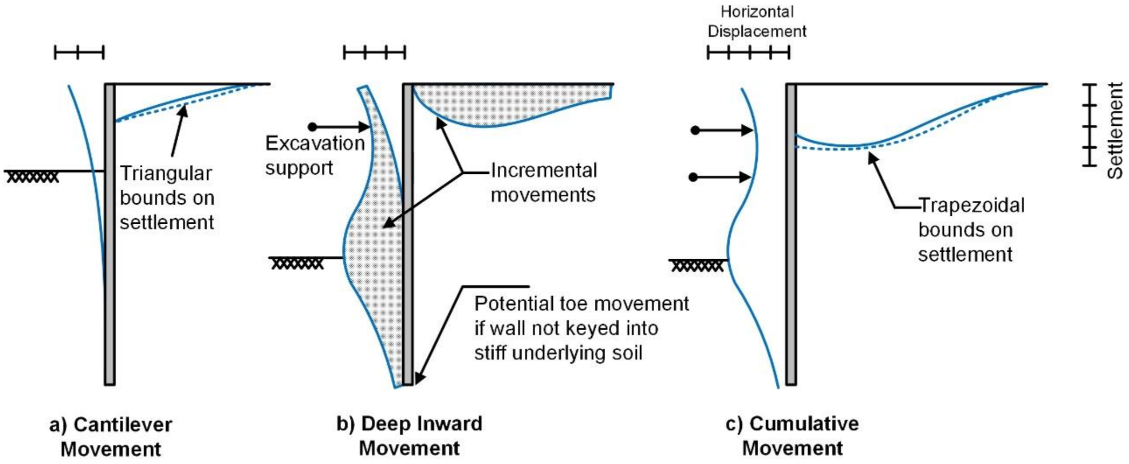

Fig. 1: Typical profiles of movement for braced and tieback walls (after Clough & O’Rourke 1990)

2.1 Behaviour of deep excavations

Lateral wall deformations and ground surface settlements reflect the performance of excavation support systems. As presented by Clough & O’Rourke (1990), the deformation pattern depends significantly on the particular excavation stages; cantilever movement occurs at early stages when the first level of lateral support has yet to be installed, while bulging wall movements happen as the project proceeds to deeper levels depending on the presence and number of struts employed, as indicated in Fig. 1. Cumulative wall and ground surface displacement are shown in Fig. 1c.

Ground surface settlements can be represented as a trapezoidal profile in cases with deep excavation in soft to medium clay wherein deep inward movements are predominant in lateral wall deformation. If cantilever movements dominate, as can occur in excavation in sand and stiff to very hard clay, settlements tend to follow triangular, spandrel, and concave settlement profiles (Ou et al. 1993, Hsieh & Ou, 1998).

In a number of related empirical studies the effects of excavation and installation have been investigated in terms of deep excavation projects around the world using a simplified approach (Peck 1969, Clough & O'Rourke 1990, Long 2001, Moorman, 2004). On the other hand, the analytical approach, called the Mobilized Strength Method (MSD) based on the use of plastic deformation mechanisms, has been used in several studies (Bolton et al. 2009, Osman & Bolton 2006, Lam & Bolton 2011). However, this method is considered conservative in the sense that maximum soil deformation behind the wall is equal to the wall deflection observed.

2.1.1 On the system stiffness

Ground movements are most influenced by the support system stiffness when levels of average, acceptable standard workmanship are achieved during the construction and installation of support systems. The stiffness of a lateral support system is a complex function of wall flexural rigidity, structural stiffness of the support elements, and the horizontal and vertical spacing of the supports.

The complex soil-structure interaction of an excavation support system and excavation-induced ground movement can be represented in three-dimensional analyses (Ou et al. 2000, Lin et al. 2003, Zdravkovic et al. 2005, Finno et al. 2007). Due to its complexity, a direct quantitative approach is often not possible and, therefore, design methods for these types of systems have to rely on the back-analysis or inverse-modelling of the performance of actual excavation support systems (Finno & Roboski 2005, Blackburn & Finno 2007, Bryson & Zapata-Medina 2012).

Clough et al. (1989) presented the state of practice for analyzing and selecting support systems. The design chart allows for the estimation of maximum lateral wall movements as a function of effective system stiffness and the factor of safety against base stability found in the literature (Fig. 2). The effective system stiffness parameter is given by:

$$S = EI/(\gamma_w h^4) \tag{1}$$

where EI is the flexible rigidity per unit width of the wall in which E is the modulus of elasticity of the wall element and I is the moment of inertia per length of wall, γ_w the unit weight of water, and h the average support spacing. However, it should be noted that the stiffness of the support itself (i.e. struts) is not taken into consideration in Equation 1.

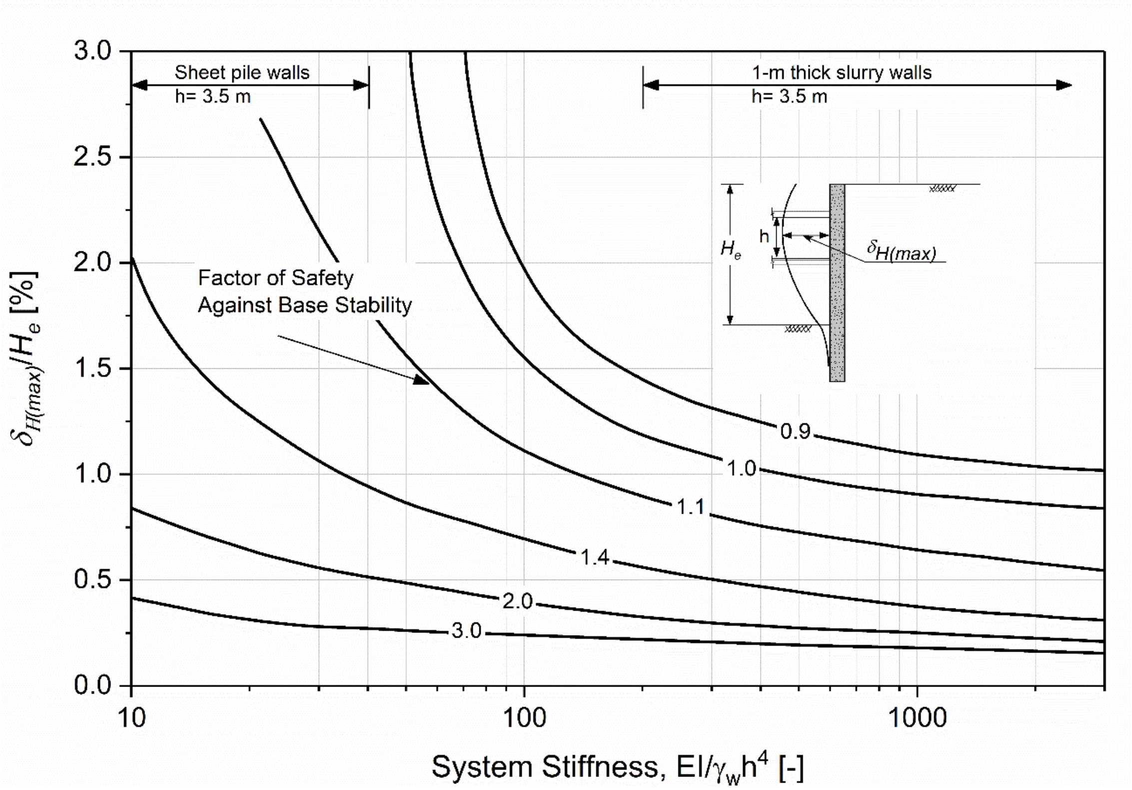

Fig. 2: Influence of system stiffness on lateral wall deflections for excavation in clay (after Clough & O’Rourke 1990)

Clough & O’Rourke (1990) based on Fig. 2, concluded that for stiff clay, where basal stability is typically not an issue, wall stiffness and support spacing have a small influence on ground movements. This is because in most circumstances these soils are stiff enough to minimize the need for stiff support systems. The variations in soil stiffnesses and coefficients of lateral earth pressure have a more profound effect on wall behaviour compared to system stiffness. For soft to medium clay, the resulting deformations are most affected by support system stiffness and, thus, this represents the key design parameter used to control ground movements.

Furthermore, the observation that the stiffness of retaining walls and support systems have less effect on movement than expected, may lead to the conclusion that the increasing stiffness of current retaining systems may have reached such a high level that it hardly influences relatively deformations to any significant degree. In this context, attention is drawn to the numerical study of deep excavations in clay by Potts & Day (1990), where it was shown that the maximum bending moment of retaining walls could be reduced by 80% using a flexible wall (sheet pile), instead of a very stiff wall (diaphragm wall), resulting in only a slight increase in movement. A number of comparisons and correlations of wall stiffness and lateral wall deformation are given in Long (2001) and Moorman (2004).

2.1.2 Influence of lateral support systems

The effect of support stiffness on deformation mechanisms was investigated by means of numerical and centrifuge modelling by Jen (1998) and Lam (2010), respectively. A reduction in strut stiffness increases the incidence of wall deflections occurring above excavation level, with maximum wall deflection occurring closer to excavated levels, whereas the lateral deflection below excavation levels is not influenced by the stiffness of strutting systems. As the struts become more compressible (lower axial stiffness), the maximum wall movement increases with negligible change in the extent of settlement trough, and the reduction of strut stiffness also causes the soil to develop a shallower failure mechanism.

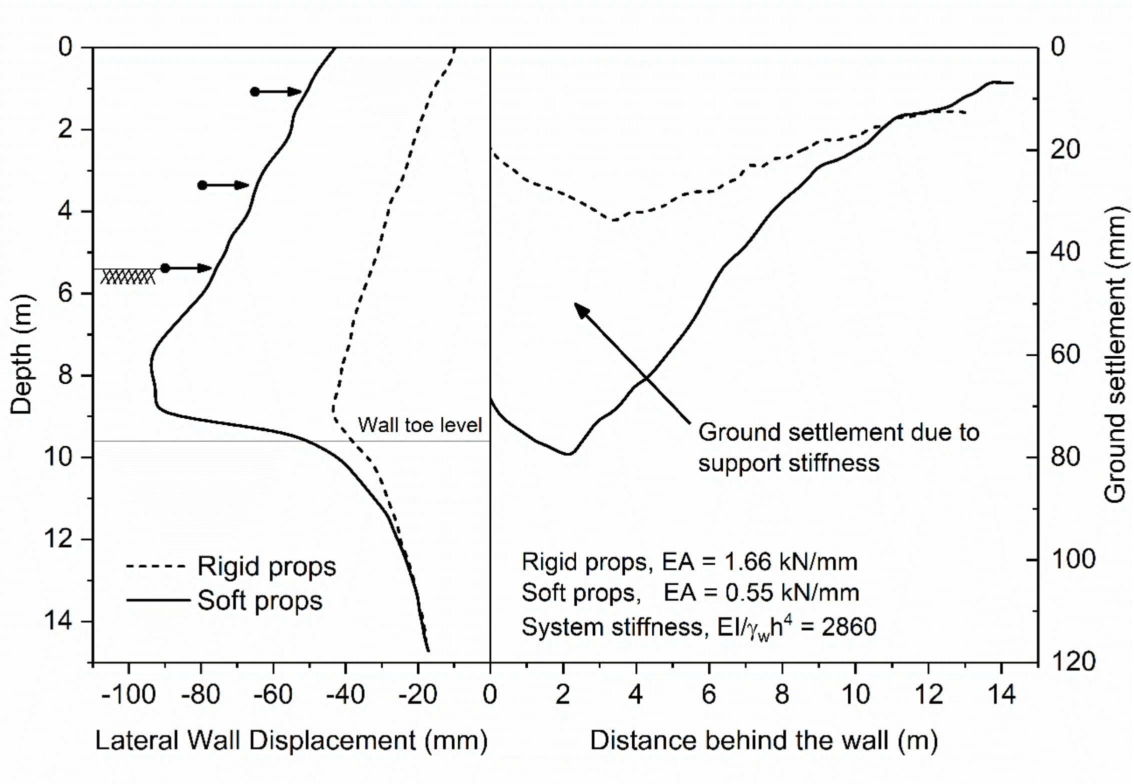

Fig. 3: Influence of support stiffness on ground deformations (after Lam et al., 2014)

The effect of strutting stiffness on excavation behaviour using a stiff wall is shown in Fig. 3. Since the soft response of the strutting system used allows rigid body lateral displacement of the wall, soil on the active side is sheared at an angle of 45°. A spandrel type settlement profile occurs with a width equal to the depth of the wall. Fig. 4 shows that the soil strain initiated on the retained side may have induced the strain-dependent degradation of the soil stiffness, triggering considerable deformation as the excavation goes deeper (Lam 2010, Lam et al. 2014).

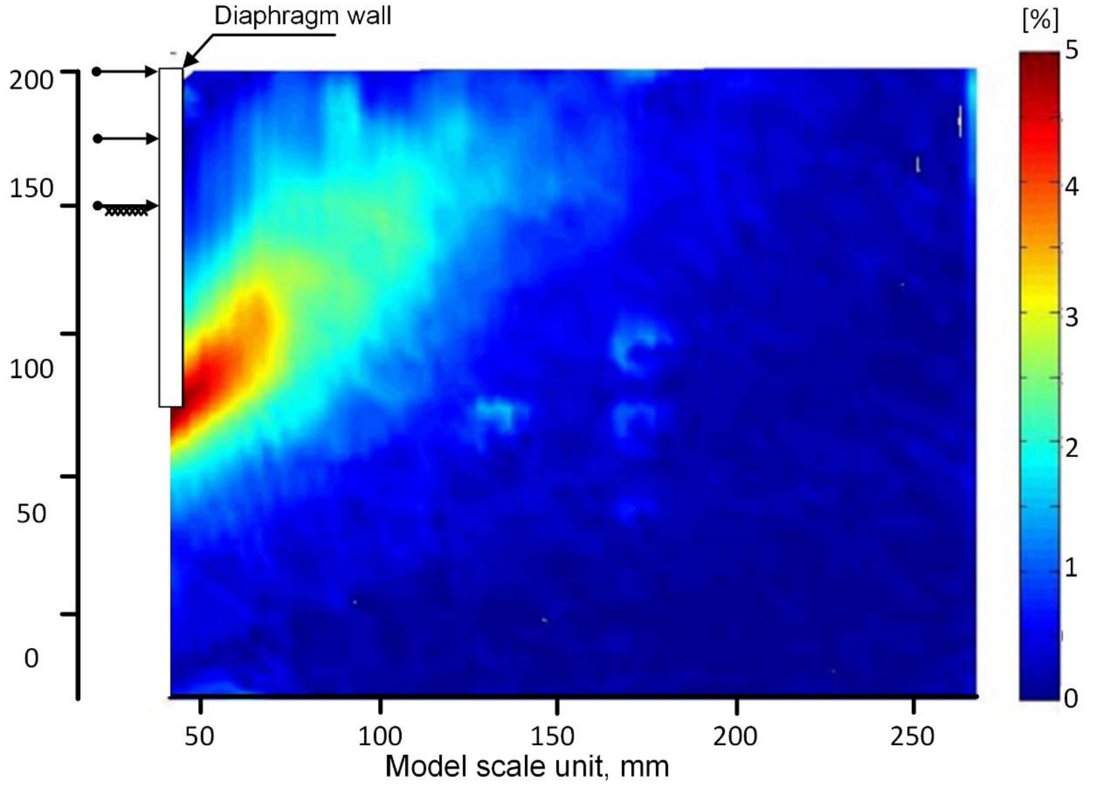

Fig. 4: Engineering strain plots of softer behaviour of strut systems (after Lam 2010)

- **Time dependency of supports**

The influence of time-dependent and thermal effects has not been considered explicitly in the analysis of deep excavations, but have been used as justification of the discrepancies recorded between computations and observed performances of excavation projects. Hight & Higgins (1994) stated that the performance of support systems (i.e. effective strength and stiffness of system) can be significantly reduced by thermal effects, creep, and/or shrinkage. This has an influence on predicted displacements, and as a consequence on bending moments. Kung (2009) looked at that the contribution of the thermal shrinkage of floor slabs to the observed lateral wall deflections. A similar observation has been reported by Haghayeghi & Mirzakashani (1994). Conceptually, concrete slabs tied to the perimeter wall experience a volumetric reduction due to drying shrinkage and creep thus inducing additional ground movement.

However, it is difficult to quantify these effects as well as the temperature-related movements during the construction stages, and only the sources above reported such phenomena in the literature. The thermal-induced strains in support cause addition axial loads and bending moments as reported by several studies (Boone & Crawford 2000, Hashash et al. 2003, Blackburn & Finno 2007).

The time-dependent properties related to shrinkage, creep and ageing of the concrete used in floor slabs and ring beams for basement and excavation shaft excavation have been studied extensively by Arboleda-Monsalve & Finno (2015) and Arboleda-Monsalve et al. (2018). They concluded that ground movements are attributed to rapid construction sequences, time-dependent variables and the temperature affecting structural support systems.

It is apparent that the strength and stiffness of support systems can have a significant influence on the observed and predicted behaviour of walls. Care must be taken not to over-estimate the effectiveness of such supports. However, in some instances, struts are pre-stressed in order to minimise the problems associated with bending effects, thereby maximising the effectiveness of the support.

2.1.3 Effect of wall toe fixity conditions

Wall kick-out behaviour is generally observed when adequate wall penetration into a stiff bearing layer or toe wall fixity cannot be achieved. The competent soil layer affects wall deflection below the excavation level, particularly at the wall toe level.

Bolton & Powrie (1987) investigated the potential collapse of unsupported retaining walls in clay soil by means of a centrifuge model. It was found that hydraulic action (i.e. water filling in an opened crack on retained side) has an influence for shorter wall embedment depth.

Hashash & Whittle (1996) demonstrated that wall deflections are clearly influenced by embedment depth which is reflected in maximum bending moments. Their results also showed that a failure mechanism in the soil is less clear when the wall is considered as elastic material. Similarly, Karlsrud & Andresen (2005) showed that reduced wall embedment depth is dominated by cantilever movement and eventually leads to an increase in bending moments occurring at the upper strut level due to unbalanced earth pressure below excavation levels.

2.1.4 Effects of wall installation

Wall installation effects, caused by excavation and the use of stabilizing fluids or fluid concrete (Gunn & Clayton 1992), can create changes in earth pressure and ground movement, even with an in situ mixed-in-place secant pile wall (Lüftenegger et al. 2013, Marte et al. 2017). Richards et al. (2006), for instance, investigated changes in the stress state of bored pile walls in overconsolidated clay conditions and found a reduction of earth pressure ratio K_0 from 1 to 0.8, with no subsequent further change after 10 months. For overconsolidated soils, the installation process can significantly relieve lateral stress and reduce the earth pressure applied to the retained side of a wall. This will, therefore, reduce the induced forces on support and bending moments (Gunn & Clayton 1992, Powrie, et al. 1998, Richards et al. 2006). Moreover, the vibrating and extracting effects of sheet piles in case of temporary support vibration may contribute to ground movements (Fujita 1994). Finno et al. (1989) reported that the induced pore pressure induced by sheet pile installation and strut preloading plays a significant role in the development of shear zones of the retained side.

The observations of Burland & Hancock (1977) in their research revealed that settlement behind a pile wall due to installation was found to constitute approximately 50% of the total deformations for excavations in London clay. However, more than 60% of the total settlement is due to the installation of diaphragm walls in soft soil (e.g. Poh & Wong 1998). Muramatsu & Abe (1996) reported that the measured horizontal and vertical movements (approximately half of the total deformations) around very stiff circular shafts are an inherent consequence of the construction process. Nevertheless, it is rather challenging to quantify the change in lateral stress caused by installation as this depends on the in-situ state, structural geometry and particular construction details. Symons & Carder (1993) suggested reducing the total stress of approximately 10% to bored piles in OC clay and of 20% to the installation of diaphragm walls. Similarly, CIRIA C580 (Gaba et al. 2003) recommends reducing the lateral earth pressure K_0 from 1.0 to 0.8 and using $K_0 = 1 - sin\varphi'$ for OC and NC soils, respectively.

2.2 Excavation stability in soft soils

Stability requirements often influence the design of lateral support systems. If the factor of safety is below an acceptable level, expensive ground improvements may be necessary to stabilize the soil below the final excavated level. In current practice, safety factors are still determined employing simple limit equilibrium analysis in many cases. However, because displacement-based finite-element analysis is routinely applied to assess displacements and stresses of working load conditions, this technique is increasingly being used to calculate ultimate limit states and, consequently, factors of safety, usually utilizing so-called strength reduction techniques. Results comparable to those obtained with limit equilibrium methods have been reported in the literature (e.g. Ukritchon et al. 2003).

Failure of deep excavations may not result in a complete collapse, rather it manifests itself in large movements. Deep-seated rotational type and basal heave are among the possible modes of failure, as shown in Fig. 5. The safety and robustness of structural support systems have to be ensured in the design of an underground structure and, thus, the overloading of a single support element should not lead to a collapse of the system. As far as deep excavations are concerned, overall failure is more likely to occur as a result of inadequate strutting or passive soil failure due to inadequate penetration depth, rather than any flexural failure of the wall itself (Puller 2003).

At the point of failure, soil pressures acting on the wall will not only depend on soil properties, but also the influence of the wall on the soil. Relative vertical movement between the soil and the wall control the mobilisation of wall friction. The bending flexibility of the wall and the mode of deformation can result in pressure redistribution (arching) within the soil mass. These effects have to be considered in order to fully understand likely failure mechanisms.

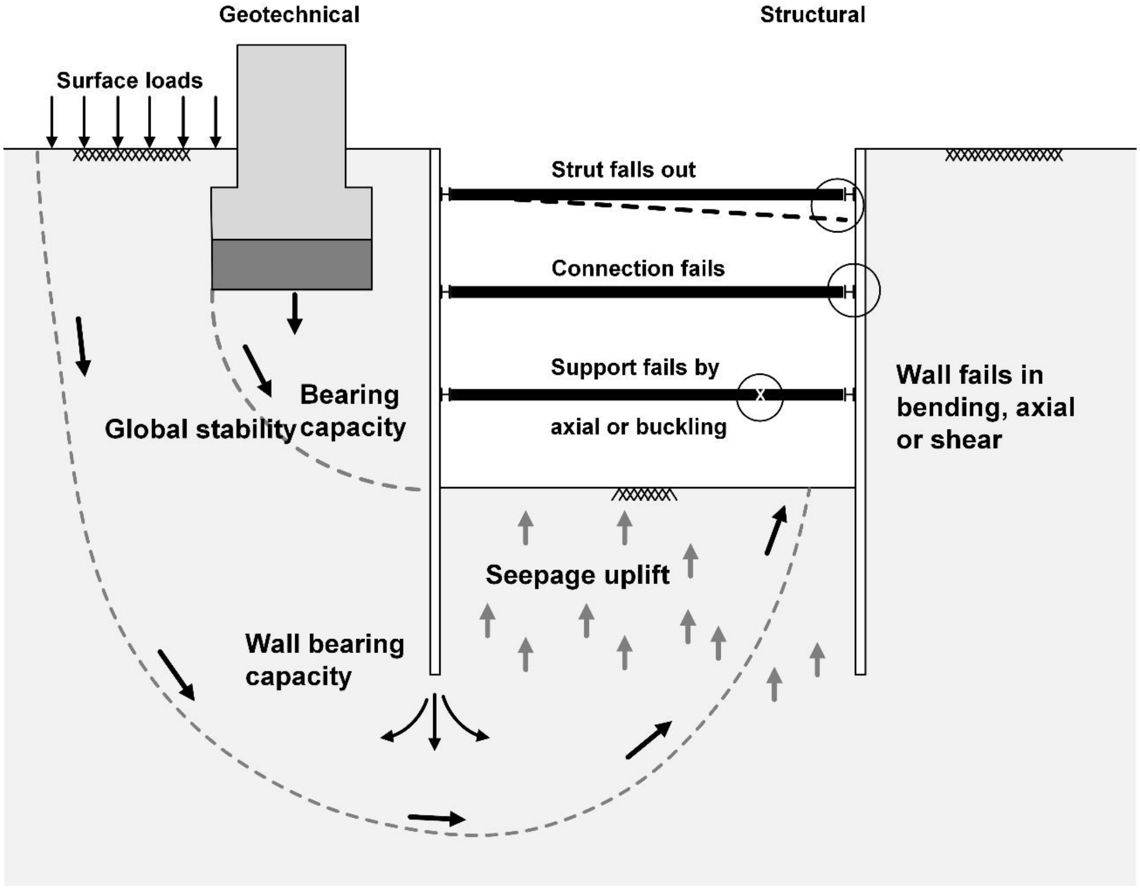

Fig. 5: Modes of failure with excavation support systems (after Marr & Hawkes 2010)

Fig. 5 shows various failure modes for braced excavations. Similar failure modes (i.e. fall out, connection fail and buckling) occur for most types of lateral supports, including struts, rakers, tiebacks and soil nails. In general, in the design of a retaining structure, the following points should be considered:

- Moment equilibrium of the system (overturn)
- Horizontal force equilibrium (sliding)
- Vertical equilibrium (bearing capacity)
- Overstress of any part of the structure (bending, shear or hinge mechanisms)

- General stability of soil around the structure (slope failure, overall stability, basal stability)

The stability of the structure has to be secured both in the short-term and the long-term whereas the latter will usually reveal the worst conditions (Clayton et al. 1993).

2.2.1 Basal stability

Based on the reported observations, the base instability associated with hydraulic uplift, accompanied by excessive basal heave, leads to the inward movement of the wall and, hence, ground surface settlement behind the wall.

In cases of excavations in soft clay underlain with a subaquifer, an excavation may lose stability due to hydraulic uplift as reported in several studies, e.g. Milligan & Lo (1970) or Moore & Longworth (1979). Hong & Ng (2013) investigated the initiation of basal heave failure mechanisms due to hydraulic uplift by means of centrifuge testing and FE-analysis. The uplift pressure required to initiate the upward movement of soil inside an excavation area is about 1.2 times that of the overburden pressure within which the wall embedment depth does not penetrate the stiff bearing layer. The basal resistance consists of the overburden pressure inside the excavation and the downward shear stress developed along the soil-wall interface. Similar observations were found in the case histories reported by Milligan & Lo (1970).

The failure mechanism can be described using conventional limit equilibrium analysis as outlined by Terzaghi (1943) and Bjerrum & Eide (1956), which is analogous to a foundation bearing capacity failure (but with a negative load), as shown in Fig. 6. For excavations in homogeneous clay, the stability of the excavation can be most conveniently expressed in terms of the stability number, N

$$N = \gamma H / s_u \tag{2}$$

where γ and s_u represent the average total unit weight and undrained shear strength in the retained soil. Equation 2 implies that a larger stability factor N corresponds to higher potential of base instability, leading to overall failure. Extensions of this approach consider modifications of the bearing capacity factors N_c, the location of the vertical shear surface in the retained soil, the inclusion of shear tractions along this plane, effects on anisotropic shear strength in clay (Clough & Hansen 1981, Kempfert & Stadel 1997, Hsieh et al. 2008), the effects of embedment (Terzaghi 1943, Eide et al. 1972, Weißenbach 1997) and the potential yielding of walls (O’Rourke 1993).

Even though these modifications take into account the increased basal stability associated with wall embedment depth, none of the existing solutions considers the failure of the wall. The modified Terzaghi method corresponds to the case of a rigid wall, while O'Rourke's method relies on the assumed deflection mode shape. In reality, the failure of a braced excavation can occur due to shear distortion in the soil mass and/or bending of the structural support element.

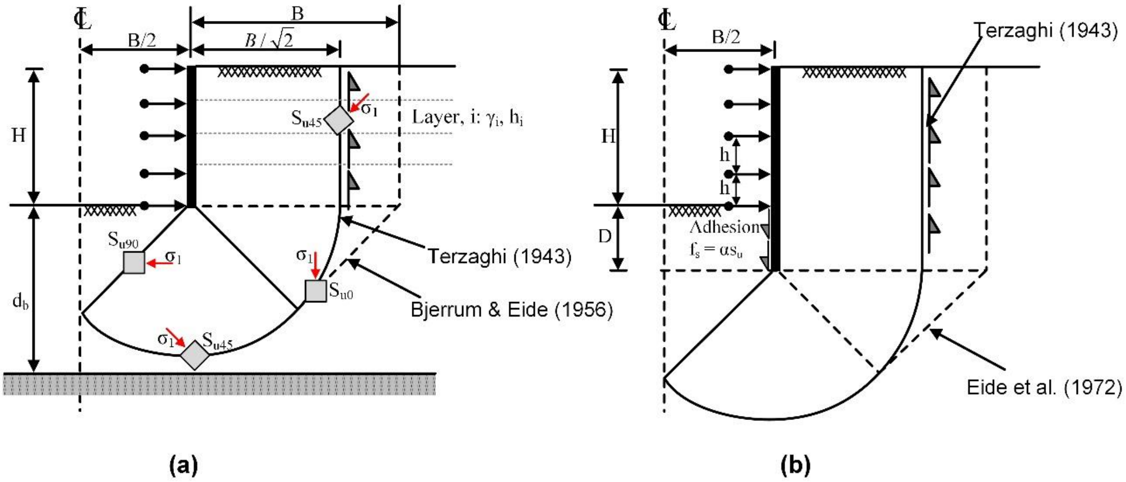

Fig. 6: Basal stability mechanisms: (a) without all embedment depth; and (b) with wall embedment depth (after Ukritchon et al. 2003)

2.2.2 Influence of wall embedded depth

Wall embedded depth plays a significant role in both the design and practice of projects. Whittle & Davies (2006) stated that the effects of wall embedment depth reflected the assumption of drainage conditions within the soil underneath the excavations. For low permeability soils, the assumption of free-draining material with pore pressures (below the base of the excavation) controlled by the excavated level can only be achieved in practice if the diaphragm walls form a hydraulic cut-off (i.e. extend into the competent layers) and relief wells are installed to reduce uplift pressures in subaquifer layers. The assumption of free-draining conditions is concluded to be highly unrealistic, implying no reduction in pore pressure below the base of excavation, and therefore this would lead to premature basal failure through hydraulic uplift.

Hashash & Whittle (1996) have shown by numerical means that the wall length affects the stability of the excavation, it nevertheless has an insignificant effect on the maximum predicted settlement and heave as excavation approaches failure. Moreover, based on a series of parametric studies, structural failure (i.e. ultimate bending moment has been reached) is likely to occur prior to the development of failure mechanism in the soil, in particular in the case where the ratio of excavation depth to wall length is smaller than 56%.

Ukritchon, et al. (2003) pointed out the importance of wall length associated with basal instability using the numerical limit analysis of upper and lower bound solutions. It was demonstrated that the failure mechanisms of embedded walls are dominated by the plastic bending moment capacity, undrained shear strength of clay and ratio of embedment to excavated depth. However, for very rigid walls (i.e. diaphragm walls), basal failure is initiated by an upward movement of a rigid body of soil mass inside the excavated area with plastic straining below the wall toe level.

The method of evaluating basal stability by quantifying the effect of wall embedment depth has been discussed by Do et al. (2013). The so-called intersection method (the inflection point of the plot between a nodal displacement and the strength reduction ratio) shows a complementary agreement with field observations of developed failure mechanisms.

In practice, however, this is due to the stratigraphy of subsoil conditions potentially affecting the installation of wall levels directly. The imperfection, namely the insufficient embedment depth, can occur when a wall is installed to specified design elevation, rather than in response to embedment requirements. This condition may lead to a misleading design assumption also with hydraulic cut-off and requires a detailed analysis (e.g. Puller 2003, Whittle & Davies 2006; Bahrami, et al., 2018).

2.2.3 Failure of lateral support systems

Osterberg (1989) introduced the concept of redundancy in geotechnical applications considering the chance of reducing failure throughout the construction period (i.e. preliminary investigation, soil boring, laboratory testing, design analysis and construction).

In general, the designs of retaining structures (wall and support elements) are carried out individually. Therefore, the system may not be robust enough and lack redundancy. It is equally important to ensure the safety of the entire structure, in addition to single support elements in order to avoid catastrophic failure. If a single support fails, the neighbouring elements can take over the redistributed load as well as the functional system of the failed element.

An example of a braced excavation case history carried out in Chicago clay conditions by Finno (2018) showed that due to a very robust system, a fail-safe condition is satisfied during excavation. However, it is argued that the conservative design based on apparent earth pressure generally leads to a redundant system because the ground movement associated with excavation is not explicitly considered.

The ductility of support systems is a significant factor in terms of improving redundancy and preventing collapse (Husain & Tsopelas 2004). It is evident that brittle failure (i.e. a large sudden reduction of bearing capacity) of a strut-waler connection initiates the progressive failure of very deep excavation projects in soft soil conditions (COI 2005). Moreover, the localized failure of a retaining structure can take place in cases neglecting the contribution of brittle behaviour in cement-treated soils as retaining structures (e.g. Lee 2014, Choosrithong et al. 2019).

Low et al. 2012, Pong et al. 2012 and Goh et al. 2018 following the technical reference (TR26 2010) have investigated the consequences of failed single support elements on the redistribution of imposed load on the remaining support system. The load of a failed strut will transfer to adjacent struts in a three-dimensional aspect and therefore cause the others to fail if there is inadequate bearing capacity.

3 Deep excavations by means of FEM

3.1 Introduction

Numerical methods, and in particular the finite element method, are widely used for analyzing deep excavation problems. A comprehensive framework has been developed that considers all complex soil-structure interactions ranging from the design of excavation support systems to the prediction of ground movements and the effect of construction activities, such as wall installation, dewatering, and ground improvement. However, this requires a sound knowledge of soil mechanics and the behaviour of constitutive models, as well as the numerical method used combined with practical experience. The usefulness and accuracy of the numerical analysis in predicting wall and ground movements is mainly affected by the constitutive models of the soil and the availability of procedures to model complex construction processes (e.g. Clough & Duncan 1971, Potts & Fourie 1986, Hashash & Whittle 1996, Zdravkovic et al. 2005).

Finite element calculations always contain uncertainties related to soil properties, support system details and construction procedures. It is necessary to simulate numerically all aspects of construction activities, i.e. by modelling cycles of excavation and support installation, as well as the removal of supports or pre-tensioning of tied-back ground anchors, that affect stress conditions around the cut in order to obtain accurate predictions (Finno 2009).

It is essential to use a realistic constitutive model that can predict the highly non-linear soil responses due to the high soil-interaction in deep excavations where different zones of soil experience widely different stress paths. The undrained shear strength of the soil, which governs the stability of braced excavation in soft soil in the short term undrained conditions, has to be predicted accurately by the constitutive model when analyses are performed in terms of effective stresses. Moreover, it is equally important to incorporate advanced constitutive models to capture the essential features of the mechanical behaviour of structural support systems.

The first part of this chapter provides a general literature review concerning the numerical analysis of deep excavations. Some essential aspects of two- and three-dimensional modelling are highlighted. The role of constitutive modelling, which is important in describing the mechanical behaviour of soil and structural support systems, is also presented.

3.2 Two - and three - dimensional modelling

There are many geotechnical problems that can be solved in either plane strain or axisymmetric conditions but depending on the complexity of geometry, soil layering or loading conditions, full three-dimensional analysis may be required in particular for deep excavation and tunnelling problems.

Zdravkovic et al. (2005) summarized that two-dimensional plane strain analysis is commonly applied in current design practise in order to assess ground and wall movements in the centre along the longer side of a generally rectangular shape, whereas an axisymmetric analysis should be adopted for the shorter side and in the corner of an excavation site (Fig. 7a). A number of previous publications carried out 3D modelling with special attention to the corner effect by comparing the results from 2D analyses (e.g. Ou et al. 1996, Ou et al. 2000). These analyses have employed elastic perfectly plastic material to represent soil behaviour and isotropic behaviour of structural support element (i.e. the same stiffness in all directions), although it has been argued that the anisotropic stiffness of retaining walls has an influence on wall deflections and out-of-plane stress redistribution, as a consequence of joints between panels and non-continuous reinforcement (Potts, 2003, Zdravkovic et al. 2005).

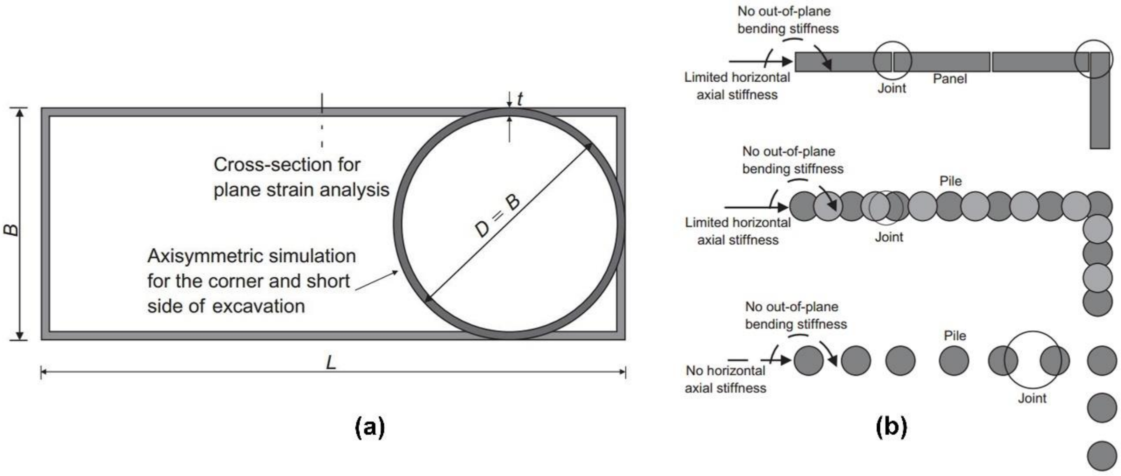

Fig. 7: (a) Schematic representation for 2D analyses; (b) different wall types (after Zdravkovic et al. 2005)

Fig. 7b shows that the out-of-plane bending moment cannot be reproduced in cases including secant or contiguous pile walls. Moreover, as a consequence of joints between panels or individual elements, the axial stiffness in the horizontal direction of the wall is much lower than the stiffness of plain concrete. The assumption of isotropic stiffness (i.e. the same stiffness in all directions) introduces a significant limitation to analyses. For instance, in cases of a circular excavation, an axisymmetric analysis with isotropic wall stiffness delivers very small ground and wall movements (Cabarkapa et al. 2003, Schwamb 2014). This assumption is unrealistic because the behaviour of the wall will be dominated by the compression of the joints between panels or piles. Therefore, three-dimensional modelling is required to achieve realistic predictions with respect to ground and wall movements and structural forces. Zdravkovic et al. (2005) suggested that it is necessary to reduce out-of-plane wall stiffness to account for the three-dimensional aspects.

In certain special cases, for example when variations of wall curvature and embedment depth (Lee et al. 2011, Choosrithong & Schweiger 2018, Choosrithong & Schweiger 2019), progressive failure of lateral support systems (Cheng et al. 2017; Cheng et al. 2017, Choosrithong et al. 2019) and spatial earth pressure redistribution and complex excavation processes (Moormann & Klein 2013, Whittle et al. 2015, Fuentes et al. 2018) are of particular interest, full 3D modelling is required.

3.3 Role of advanced constitutive models

3.3.1 A general requirement for constitutive models

The constitutive model should be able to represent the most important aspects of soil behaviour. Such behaviour is dominated by the type of soft soil, stress and strain history (preconsolidation), and the deposition process (i.e. bonding and structure). For example, many soils exhibit anisotropic behaviour of strength and stiffness, dense sands and overconsolidated clay show a pronounced post peak behaviour.

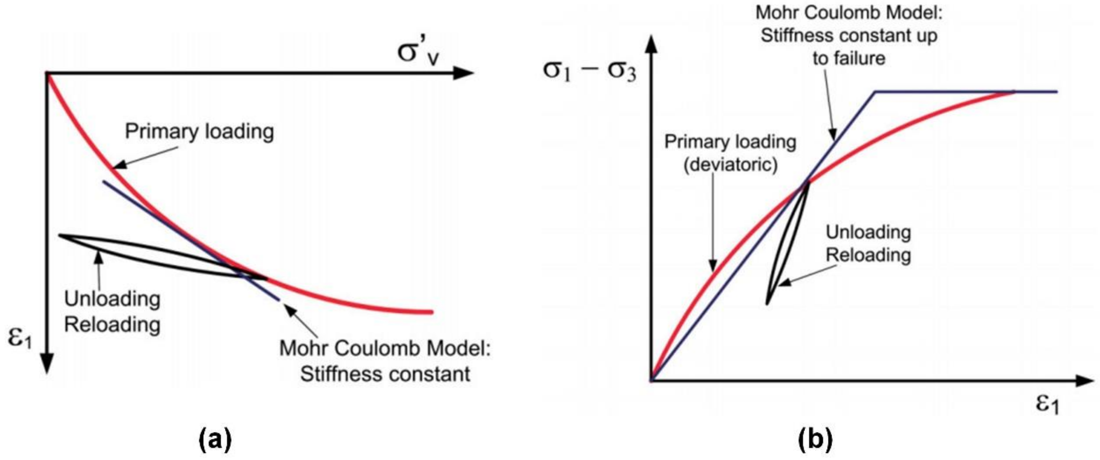

Fig. 8: Schematic diagram for typical results of laboratory test: (a) one-dimensional compression test; (b) triaxial compression test

Therefore, it is essential to clearly identify the purpose of a numerical analysis and define the results required. This is obviously problem-dependent and cannot be generalized. Thus, the decision concerning how sophisticated the model needs to be answered in each particular case. For example, when only a failure mechanism is of interest, a simple elastic-perfectly plastic Mohr-Coulomb model will be adequate, whereas for deformation analysis of an excavation this would be by no means appropriate. Similarly, for highly anisotropic soil the application of an isotropic constitutive model may lead to poor results. Additionally, if the bonding and structure of natural clay are neglected, realistic deformations cannot be obtained because if significant plastic straining occurs, the structure of the soil will be destroyed leading to large displacements. On the contrary, if the strain range is small, and only insignificant destructuration occurs, a model representing the behaviour of structure soil without consideration of destructuration will be sufficient.

Fig. 8 depicts schematically typical results from one-dimensional and triaxial compression tests to illustrate basic aspects of soil behaviour. It apparently shows that the assumption of a linear stress-strain relationship of an elastic-perfectly plastic model is inadequately representing the highly non-linear behaviour up to failure.

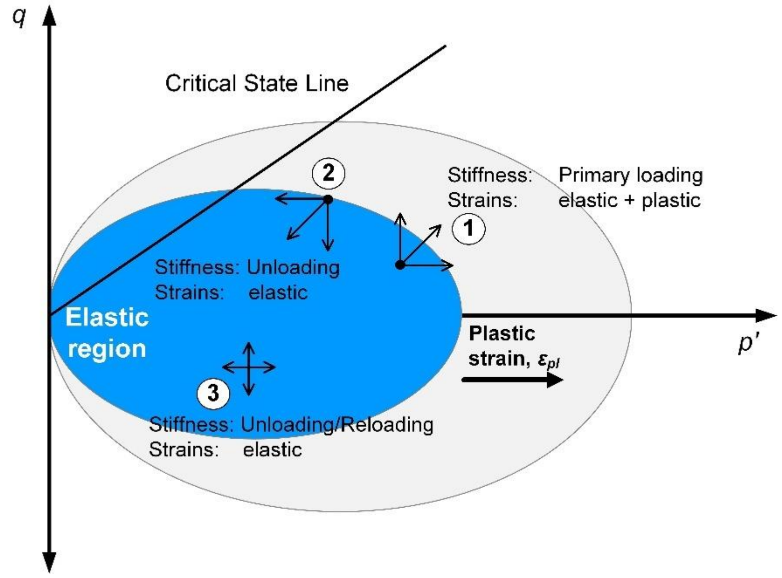

Fig. 9: Modified Cam Clay and the role of yield surface in definitions of stiffness

This section aims to summarise important aspects of constitutive models for soils related to excavation problems. The analyses of deep excavation performed with a simple constitutive model (i.e. elastic-perfectly plastic Mohr-Coulomb model) do not always predict reasonable surface settlement troughs, usually they are shallower and wider than those observed in field measurements. This leads to underestimating structural forces and bending moments in diaphragm walls (Ng & Lings 1995, Schweiger 2001).

Historically, for practical purposes, the development of the modified Cam Clay model (Fig. 9) represents the first step in describing more realistically the stress-strain behaviour of soils and has been widely used in engineering practice with typical applications in the analysis of embankments on soft soils. The model is based on critical state soil mechanics and introduces a single elliptic yield surface separating elastic from plastic behaviour and differentiates between loading and unloading/reloading stiffnesses for different stress paths. However, for excavation problems, the single surface plasticity model has a major disadvantage because plastic strains take place predominantly for compressive stress path and stress paths remain inside the yield surface for stress paths related to excavation occurred therefore elastic behaviour is predicted (Potts & Zdravkovic 2001, Schweiger 2008). In addition to the volumetric yield surface, a deviatoric yield surface was introduced in order to overcome the aforementioned problems (e.g. Vermeer 1978).

Typical stress paths related to deep excavation are shown in Fig. 10. with two hardening mechanisms, namely isotropic and deviatoric hardening mechanisms (i.e. Hardening soil model in FE-code Plaxis, Brinkgreve et al. 2017).

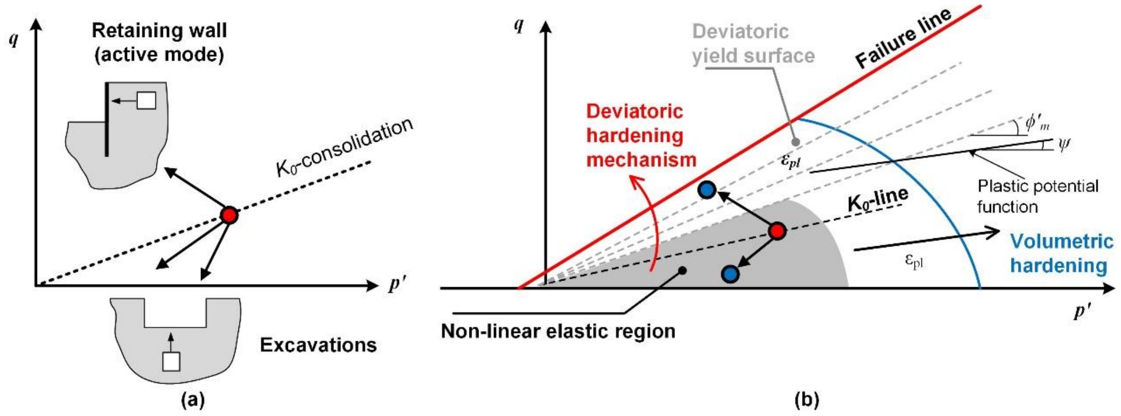

Fig. 10: (a) Typical stress paths in deep excavation and (b) stress paths in soil elements

3.3.2 Small strain stiffness

Experimental data for normally consolidated clays (e.g. Finno & Cho 2011) and reconstituted overconsolidated clays (e.g. Jardine, et al. 1984, Burland, 1990, Atkinson et al. 1990, Clayton & Heymann 2001) revealed not only that soil behaviour is non-linear elastic in the small strain range, but also the effects of previous and recent stress history on stiffness responses. The stiffness of soil cannot be assumed to be constant even in the small strain range and by neglecting this, results can be misleading (Jardine et al. 1986, Ng & Lings 1995, Addenbrooke et al. 1997, Mašín, 2009).

A realistic prediction of ground movements induced by deep excavation and tunnelling requires using models which account for pre-failure behaviour (i.e. a non-linear stress strain relationship before reaching the ultimate state) and small strain stiffness behaviour, i.e. a stiffness measured in the strain range approximately below 10^{-5} where stiffness is approximately constant, as illustrated in Fig. 11.

Potts & Zdravkovic (2001), Whittle et al. (1993), Benz (2007) and Schweiger (2008), for instance, concluded that the introduction of small strain stiffness improves predicted ground movement compared to field observations and shows a smaller influence on mesh sensitivity. It was also shown that the bending moment and force induced in the structural support system are the consequence of the predicted displacement profile. Furthermore, Whittle et al. 1993 stated that the predicted settlement trough is affected by three main factors: (1) soil-wall interfaces, which control soil movement close to a wall; (2) modelling of small strain non-linearity which affects both the magnitude and distribution of settlement; and (3) plane strain geometry, which exaggerates far field movements at lateral distances comparable to the length of a rectangular excavation.

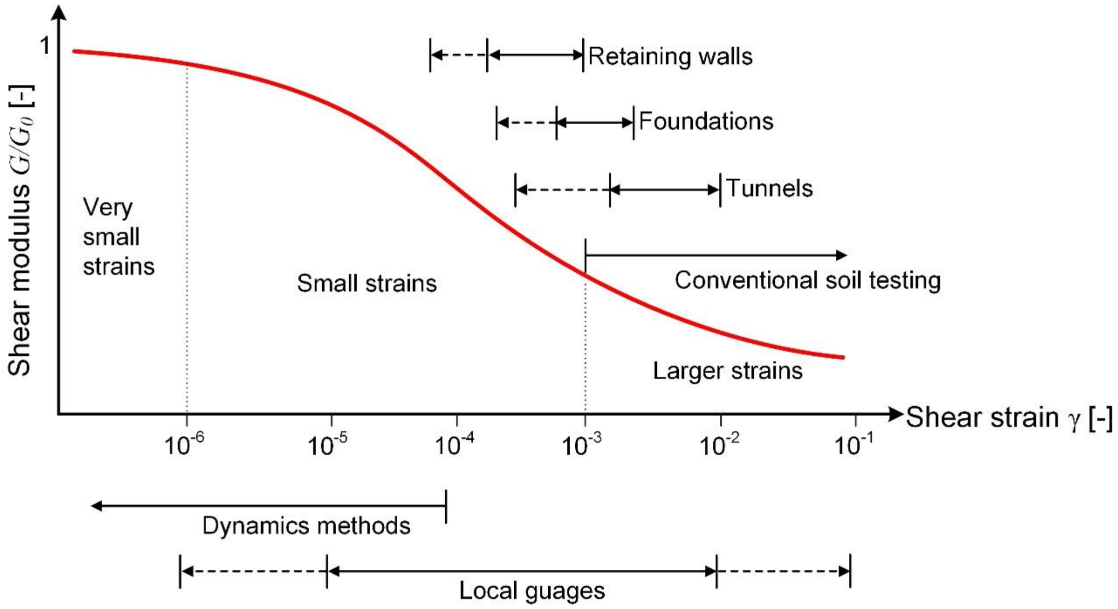

Fig. 11: Characteristic ranges of soil stiffness as function of shear strain amplitudes modified (after Atkinson & Sallfors 1991)

3.3.3 Anisotropy

The mechanical behaviour of natural soils tends to behave initially anisotropic due to the sedimentation process, the structure of particles and subsequent loading history. It is apparent that omitting anisotropy represents an oversimplification of soil behaviour. Clough & Hansen (1981) demonstrated the effects of strength and stiffness anisotropy of braced excavations in soft soils.

In most practical cases, soil is generally assumed to behave isotropically at very small strains, however natural soil behaves as very stiff and non-linear anisotropic in small strain ranges, as observed in laboratory tests (e.g. Pennington et al. 1997, Ng et al. 2004, Nishimura et al. 2005, Gasparre et al. 2007, Cho & Finno 2010; Nishimura 2014). The influence of anisotropy on the behaviour of geostructures have been thoroughly studied, i.e. the influence of both strength anisotropy (Hashash & Whittle 1996, Schweiger et al. 2009) and small strain stiffness anisotropy (Addenbrooke et al. 1997, Ng, et al. 2004, Schädlich & Schweiger 2013). Mašin & Herle (2005) compared various constitutive models and confirmed that in order to obtain realistic ground movements, a constitutive model should be able to capture anisotropic small strain non-linearity and stiffness dependency on stress path direction. Small-strain behaviour and stiffness anisotropy have been incorporated by Teng et al. (2014) to predict the ground movements induced by excavations. The results show a satisfactory agreement between predicted and monitored data and indicate discrepancies between anisotropic and isotropic models in predicting surface settlement and lateral soil movement in a range of about 10 to 43%.

3.3.4 Effective stress-based analysis

Atkinson (1993) outlined stress paths in relation to undrained behaviour in deep excavations, as shown in Fig. 12. An effective stress path corresponds to undrained loading (A' to B') and swelling or reduction in mean normal effective stress (B' to C'). The initial excess pore pressure u_i is generated immediately after the excavation which is negative (i.e. u_i is less than the final steady-state pore pressure u_c). The total stress remains approximately unchanged. Nevertheless, the pore pressure continues rising over a period of time. This demonstrates that unlike foundation or embankment problems, where the stability increases with drainage, the safety factor of a retaining structure will decrease with time.

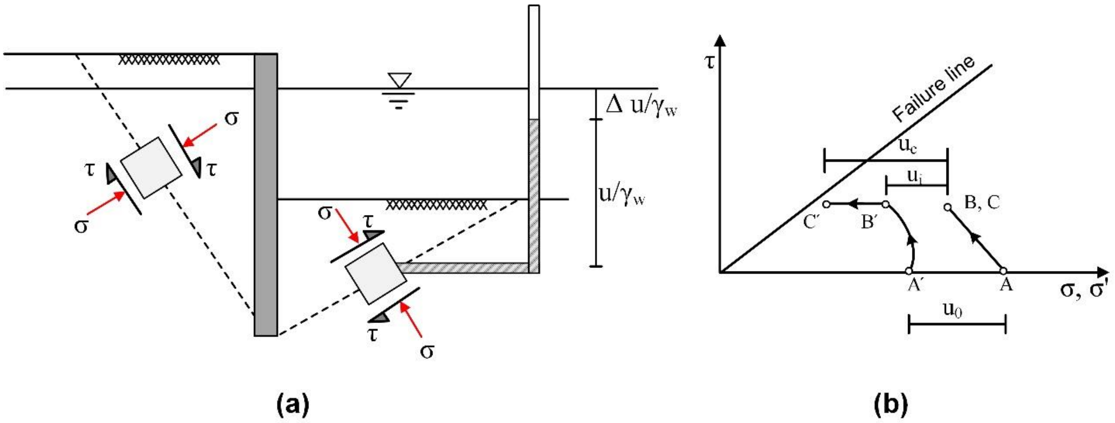

Fig. 12: Changes of stress and pore pressure within deep excavation (after Atkinson 1993)

Janbu (1997) and Freiseder (1998) presented case histories of deep excavations in clay and concluded that the assessment of stability should be carried out in terms of effective stress analysis. From their analyses, it can be seen that stresses and pore water pressures recovery corresponding with a steady state of seepage may occur after a certain period of time (Fig. 13). Therefore, the simple total stress analysis for excavations in clay will frequently lead to erroneous results in terms of the factors of safety (Janbu 1997, Lafleur et al. 1988).

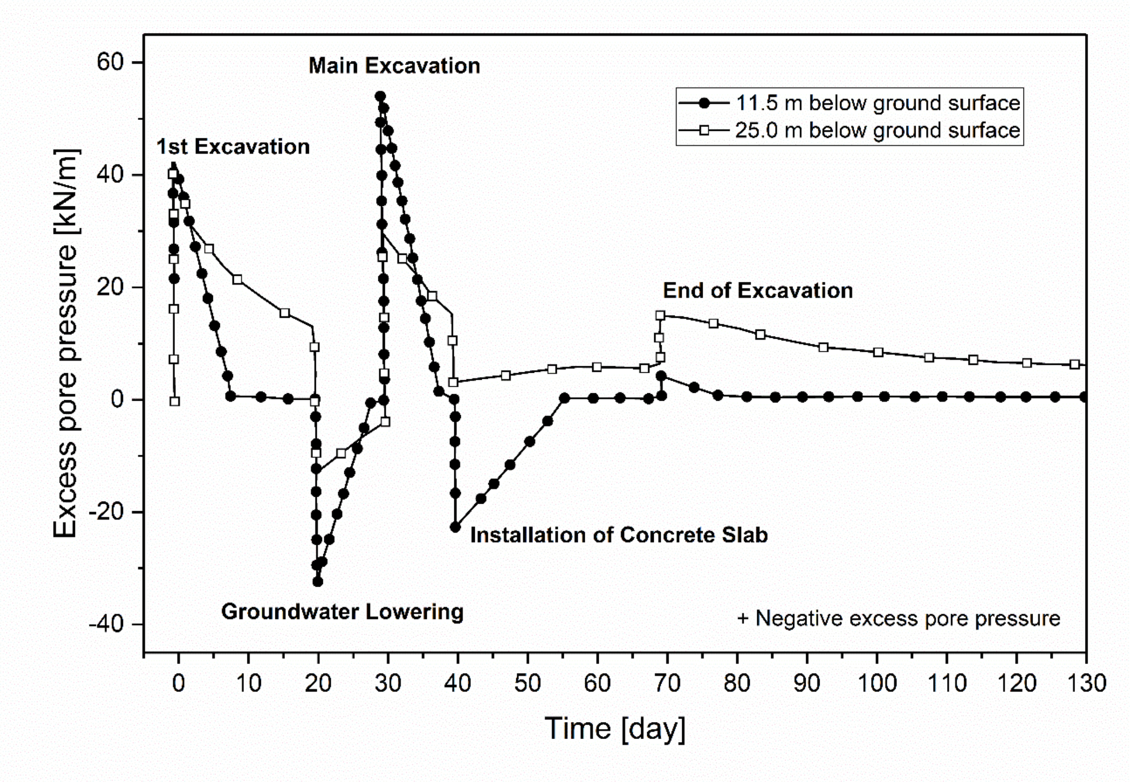

Fig. 13: Dissipation of pore pressure with time (after Freiseder 1998)

3.3.5 Modelling of undrained behaviour

Several approaches can be followed in order to perform undrained analyses by means of numerical modelling. Nevertheless, care must be taken in the analyses because the undrained behaviour of soil is a consequence of the constitutive model adopted when the analysis is performed in terms of effective stresses. The differences between these approaches can be summarised as follows:

- Approach A: analysis in terms of effective stresses and effective strength and stiffness parameters;

- Approach B: analysis in terms of effective stresses using an undrained strength parameter, but also using effective stiffness parameters;

- Approach C: analysis in terms of total stresses using undrained strength and stiffness parameters.

The total stress analysis in Approach C does not differentiate between effective stresses and pore pressures and, hence, it is not possible to take into consideration coupled consolidation. Due to its simplicity, the undrained shear strength (S_u or

C_u) and stiffness (E_u) are input parameters. Similarly, the undrained shear strength profile can be specified for soil layers in Approach B. The drawback of this approach is that the calculated excess pore pressures are in general not realistic and, hence, the consolidation analysis following loading/unloading starts with an incorrect pore pressure distribution. Therefore this approach cannot be recommended.

The consequence of an analysis in terms of effective stresses (φ' and c' in Approach A) is that the undrained shear strength is a result of the constitutive model and the effective strength and stiffness parameter adopted. Whittle & Davies (2006) showed that some elastoplastic models employing approach A may overestimate the undrained shear strength for normally and lightly overconsolidated clay (OCR < 2).

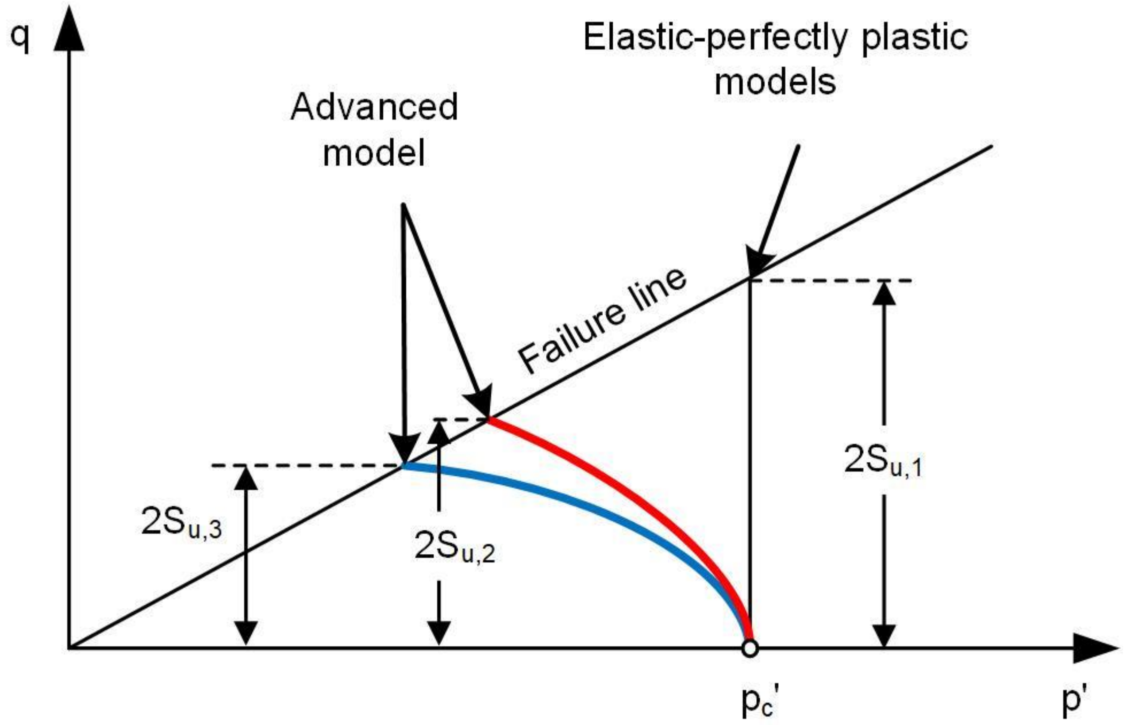

Fig. 14: Schematic diagram of effective stress path in undrained triaxial compression tests

Fig. 14 shows a schematic diagram of effective stress paths in p'- q space for undrained triaxial compression tests. Failure in undrained conditions occurs at different deviatoric stresses levels for advanced and elastic-perfectly plastic models. If employing the simple elastic-perfectly plastic Mohr-Coulomb model, the behaviour is linear elastic up to failure because the center of Mohr's circle remains unchanged in undrained loading and therefore the undrained shear strength may be overpredicted. This is crucially important because, for normally consolidated soil, mean stress p' does not remain constant.

3.3.6 Multilaminate model

In this section a brief summary of multilaminate models is given to illustrate some of the effects associated with deep excavation analysis. The multilaminate constitutive model used in this thesis is based on the developments of Wiltafsky (2003) who derived a model for application to normally to slightly overconsolidated clay, Scharinger (2007) who introduced small strain stiffness behaviour, Galavi (2007) who enhanced the model to cover inherent anisotropy, destructuration and strain softening, and Schädlich (2012) who included anisotropic soil stiffness at small strains and strain softening behaviour of stiff overconsolidated clay.

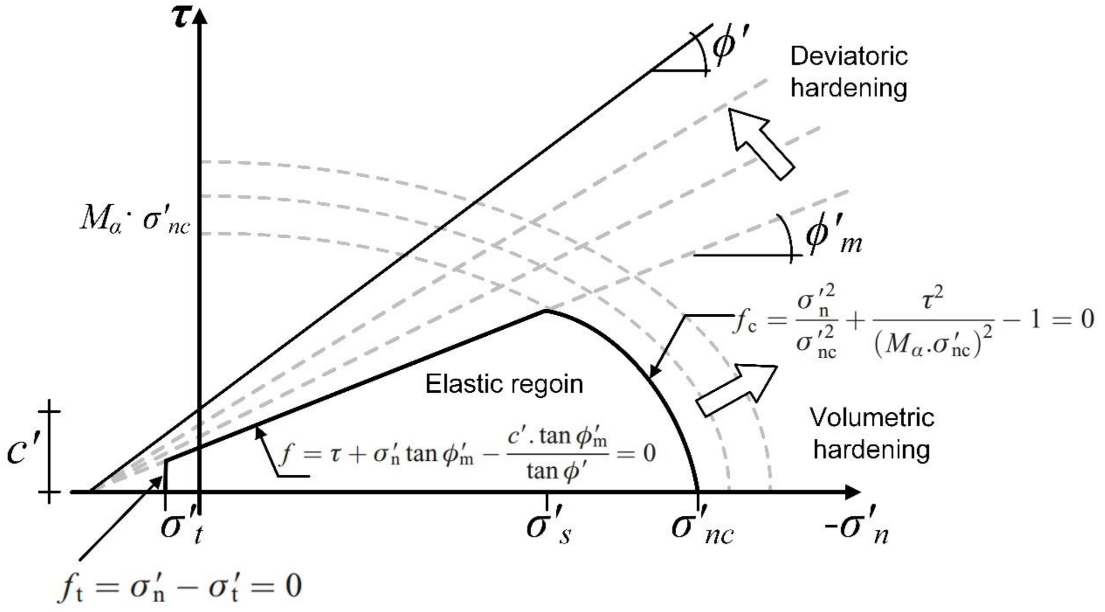

Fig. 15: Yield surface for the multilaminate constitutive model

The yield function of the multilaminate constitutive model consists of three independent functions, namely volumetric f_c, deviatoric f, and tension f_t parts of the yield surface respectively, as shown in Fig. 15. The deviatoric yield function f is an extended Mohr-Coulomb criterion, which introduces a mobilized friction angle ϕ'_m.

$$tan\phi'_m = tan\phi'_i + (tan\phi'_m - tan\phi'_i)\frac{\varepsilon^p_{\gamma cone}}{A_{mat} + \varepsilon^p_{\gamma cone}} = 0 \qquad (3)$$

where ϕ'_i, $\phi'$and ϕ'_m are initial, ultimate and modified friction angles respectively, tanϕ'_m is equal to $tan\phi'/R_f$ (failure ratio), A_{mat} is a parameter that governs the rate of deviatoric hardening, which has to be determined by calibration from triaxial compression test data. The mobilisation of friction angle is controlled by plastic shear strain $\varepsilon^{p}_{\gamma cone}$.

In the volumetric part of the yield function f_c, σ'_{nc} is the effective preconsolidation pressure stress state resulting from the loading history (Equation 4), and M_α governs the shape of f_c.

$$\sigma'_{nc} = \sigma'_{nc,i} \cdot e^{-K \cdot \varepsilon^{p}_{n,v}} \tag{4}$$

The hardening parameter K is defined as $K = (1 + e)/(\lambda - \kappa)$. λ and κ denote the compression and swelling indices, respectively. The third part of the yield surface f_t is a tension cut-off criterion. An associated flow role is assumed for f_c, and f_t and a non-associated flow for f. The plastic potential function of the deviatoric yield surface is defined by:

$$g = \tau + \sigma'_n \cdot tan\psi_m = 0 \tag{5}$$

where

$$sin\psi_m = \left(\frac{sin\phi'_m - sin\phi'_{cv}}{1 - sin\phi'_m \cdot sin\phi'_{cv}}\right) \cdot \left(\frac{sin\phi'_m}{sin\phi'}\right)^{p} \tag{6}$$

$$sin\phi'_{cv} = \frac{sin\phi' - sin\psi}{1 - sin\phi' \cdot sin\psi} \tag{7}$$

The proposed stress dilatancy formulation corresponds to the theory proposed by Rowe (1962) and modified by Søreide (2003). As already pointed out by Søreide (2003) Rowe's approach reveals a very high contractive behaviour for low mobilisation levels of the friction angle. The modified stress-dilatancy theory suggested by Søreide (2003) employs a power index p, which allows downscaling of the contractancy at lower mobilisation levels of the friction angle (Equation 6). By varying the power index from p = 1 to higher values, a significant decrease of the negative mobilised dilation angle is observed for low friction angles. The maximum contractancy is reduced and shifted to higher mobilisation levels of the friction angles, as indicated in Fig. 16b, and, thus, the effective stress paths in an undrained triaxial test seem to give a positive response (Schweiger et al. 2009). Two additional parameters used in the model controlling the shape of the curve (Scharinger 2007). The predicted undrained shear strength decreases with decreasing $\psi_{m,min}$, while ϕ'^{*}_{m} mainly influences the curvature of the effective stress path, as shown in Fig. 16a (Scharinger & Schweiger 2005).

The adopted functions for HS and HSS models are plotted for comparison, and the comparison between these models in prediction of undrained shear strength is highlighted in Section 4.3. Again, it is essential to note that the modifications of flow rule result in a difference in the predicted undrained shear strength. This demonstrates the importance of the flow rule in a general sense.

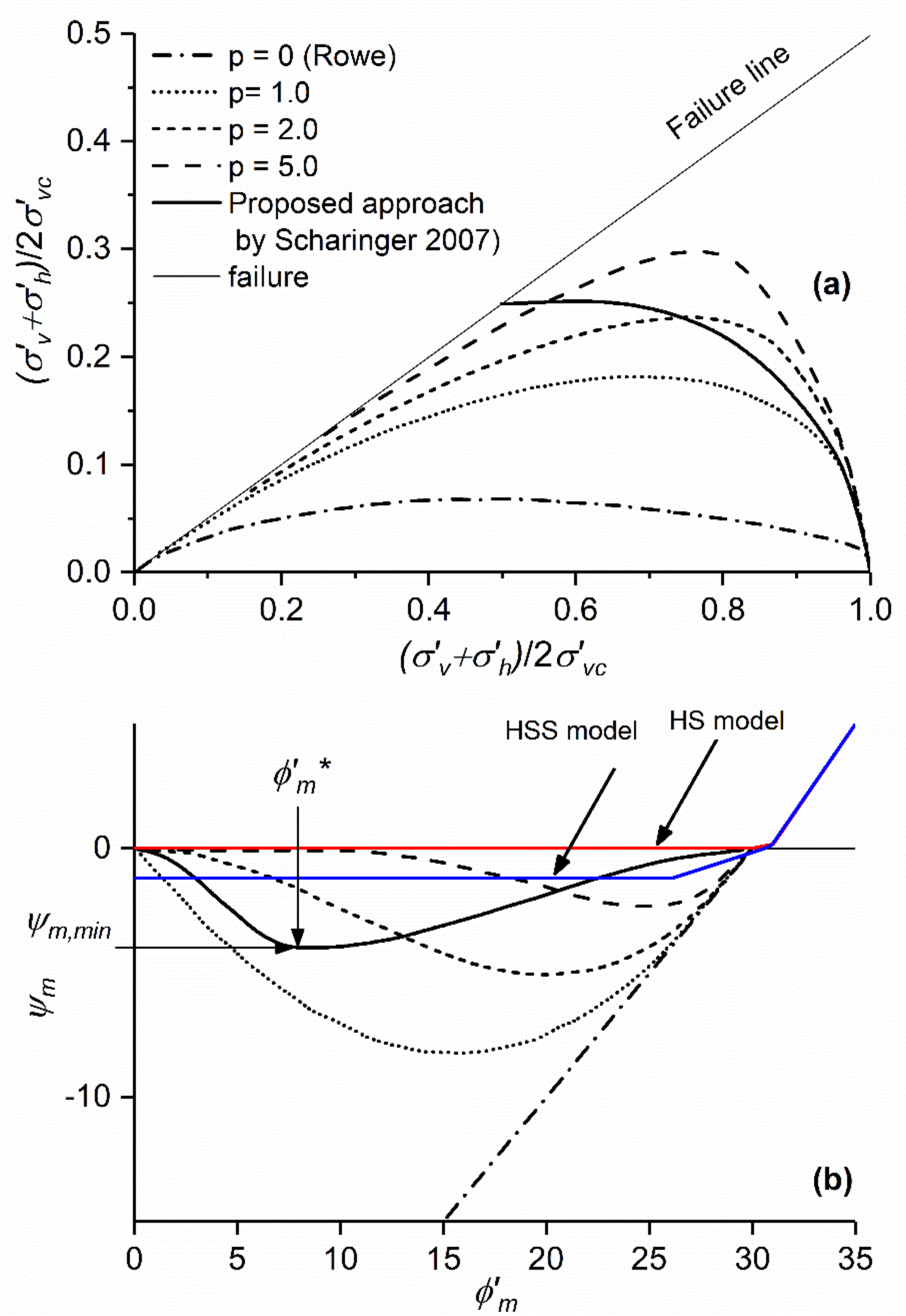

Fig. 16: Modification of stress dilatancy theory ($\phi' = 30°, \psi = 5°$) (after Schweiger et al. 2009)

3.3.7 Modelling of cement-treated soil

Cement treated soil is often used for the improvement of soft soil. Besides empirical rules, numerical analyses may be employed to assess deformation and stress state in these materials. The key consideration here is the constitutive model describing the mechanical behaviour of the improved soil. In engineering practice, simple elastic perfectly-plastic failure criteria are often applied, but these models cannot describe the mechanical behaviour of cement-treated soil when the strength is exceeded. It has been observed from experimental tests that cement-treated clay undergoes a significant loss of structure after bonding and strain-softening takes place immediately after reaching peak strength accompanied by large volumetric compression (e.g. Xiao et al. 2014). This mechanical behaviour is not reflected by the elastic-perfectly models. One characteristic that is poorly represented concerns the brittleness of the mechanical response. It is reasonable to assume that the improved soils behave as an elastoplastic material when the allowable global strain level in an excavation is generally about 0.5% of the excavation depth and this could prevent the cement-treated soil material from reaching peak strength. However, the numerical simulations of boundary value problems, e.g. cement-improved soil surrounding a circular tunnel (Tyagi et al. 2017), and in context of an excavation (Choosrithong et al. 2019), employing a Mohr-Coulomb model has significantly influenced results compared to advanced models. This is due to the fact that the Mohr-Coulomb model is unable to simulate the post-peak behaviour, which will become significant at large strain levels.

A general approach in the modelling of cement-mixed soil has been developed utilizing the concept for modelling structured soils and extending Cam Clay type models (e.g. Nova et al. 2003, Arroyo et al. 2012, Xiao et al., 2017). Assuming that the yield surface is enlarged, while keeping the shape unchanged the bonding of cemented material can be modelled by introducing a cohesion intercept of the shifted yield surface. The degradation of the structure is commonly assumed to be related to plastic volumetric and shear strains. As discussed by Arroyo et al. (2012), the application of bonded soil models to cement-improved soil has received somewhat less attention in practical applications due to the spatial variability of natural material and difficulties in calibration. Moreover, Schweiger et al. (2014) suggested that bonded soil models are not well suited to modelling concrete-like materials, such as jet grout and mixed in place columns because these materials contain high cement content up to about 50% (Lee et al. 2005) and behave like weak concrete where the modelling of tensile strength softening becomes important.

A suitable criterion should capture the limited tensile strength of these materials and it is equally important to consider post peak behaviour, i.e. modelling strain softening in tension and compression, in particular when collapse mechanisms or deformation near failure are of interest wherein structural performance is dominated by crack initiation. Schädlich & Schweiger (2014) presented a constitutive model for concrete-like materials accounting for compression and tension softening. The regularization parameters, namely characteristic length of a finite element L_{eq} , fracture energy in compression (G_c) and in tension (G_t), were introduced in order to avoid mesh dependency after reaching peak strength. The fracture energy parameters can be obtained from standard laboratories, i.e. using uniaxial compression, three-point bending and direct tensile tests. The model has been successfully applied in practical boundary value problems for modelling jet grout base slab support excavation (Schweiger et al. 2014), jet-grout columns under seismic conditions (Sedighi et al. 2017), crack initiation in grouted anchors (Fabris et al. 2018, Schweiger et al. 2019) and cement-mixed soil columns as retaining structures (Choosrithong et al. 2019).

3.4 Issues related to deep excavations

3.4.1 Modelling of structural components

The usual modelling assumption for structural support systems is that these components behave elastic perfectly plastic and that tensile stresses can be substantial. However, particularly in cases of brittle materials (unreinforced concrete and/or cement-treated soil structures), the analysis may have to account for the limits of tensile and/or compressive strengths and for softening behaviour.

von Wolffersdorff & Schweiger (2008) conducted numerical investigation on the influence of elastoplastic behaviour of support systems on the failure mechanism and factor of safety for single prop supported sheet pile walls. The safety factor for the elastic-perfectly plastic wall may be considerably less than for the case of an elastic wall. A more diffuse failure mechanism is clearly observed because the limited strength of the wall initiates plastic hinge formation.

Similarly, Do et al. (2016) carried out FE-analyses to investigate failure mechanism of deep excavation case histories in soft soil by comparing elastic and elastoplastic support systems. Their results showed that the yielding of support may initiate overall failure, whereas elastic support systems may overestimate the stability number.

Schweiger et al. (2009) investigated the behaviour of very stiff diaphragm walls considering the influence of stiffness representing uncracked sections, cracked sections, and non-linear behaviour by prescribing the relationship of allowable bending moments to diaphragm wall curvature (Eurocode 2). The predicted wall deflection based on the assumption of cracked stiffness is closer to measured data, while the non-linear model lies in between the two extreme cases.

The type of connection between wall and support can directly affect the behaviour of a structure. The different types of wall-support connections suggested by Potts & Zdravkovic (2001) are shown in Fig. 17. A simple connection is implicitly assumed in the current design, whereas most connections behave either as pin-jointed, or as full moment. Lee et al. (2011) suggested that in order to reflect the plastic-hinge properties in a wall, struts can be considered under primarily compressive force followed by strain softening or modelled with additional bending moment rotation generated by lateral deflection and buckling of the strut (P-delta effect).

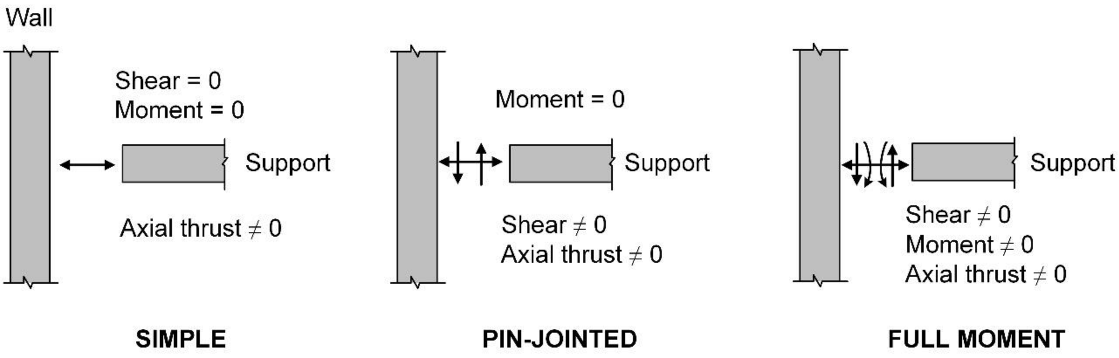

Fig. 17: Type of wall-support connection (after Potts & Zdravkovic 2001)

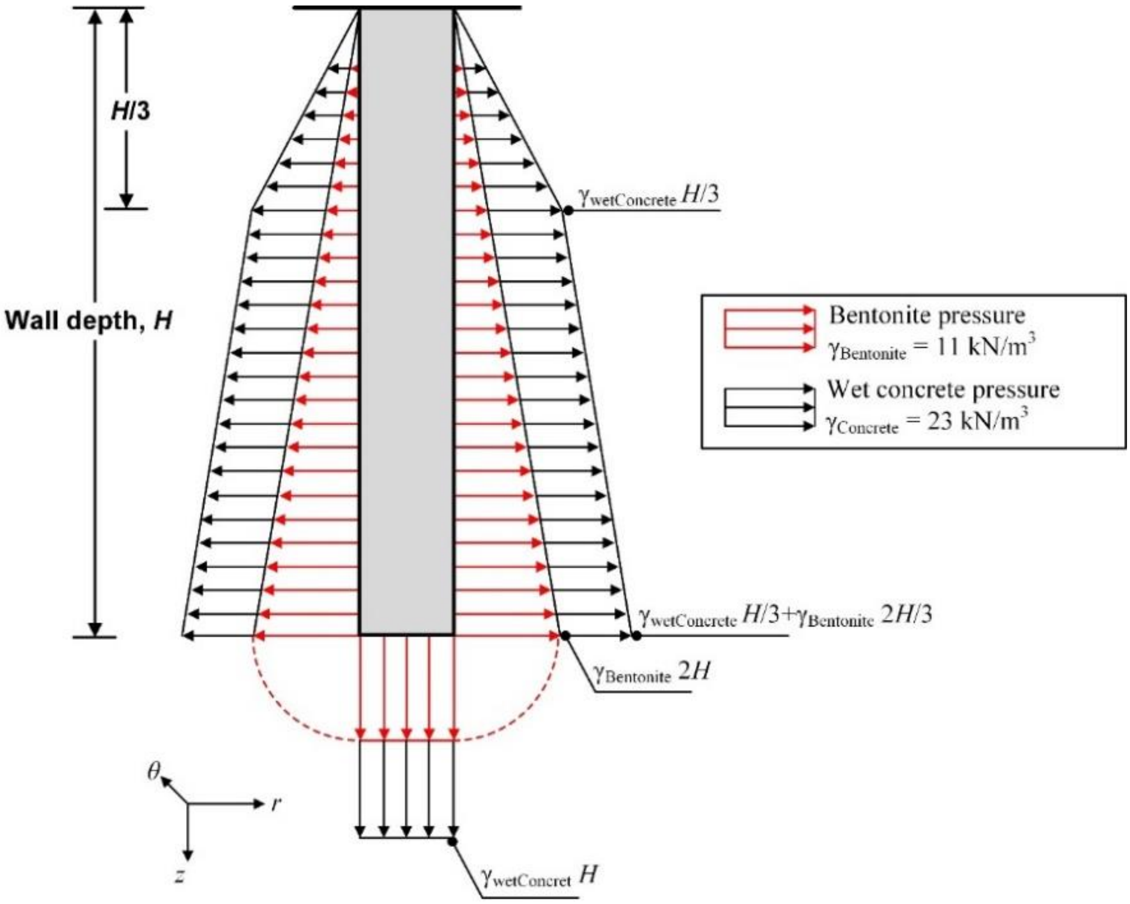

Fig. 18: Modelling of wall installation (after Gourvenec & Powrie 1999)

3.4.2 Modelling of wall installation

As mentioned earlier, the importance of bored pile and diaphragm wall installation effects on lateral stresses and the behaviour of retaining walls is commonly recognized and features in many discussions of analyses and performance. Potts et al. (2002) summarized the most common assumptions in the analysis of wall installations. There are different strategies:

- The wall is wished into place (i.e. no lateral stress reduction occurs during wall installation).
- The wall construction can be adequately represented by modelling the installation sequence under the process of placing wet concrete and the subsequent hardening of the concrete, as illustrated by Gourvenec & Powrie (1999) in Fig. 18.

De Moor (1994) investigated stress changes during wall installation. When neglecting the effect of wall installation, in particular in overconsolidated soil (i.e. London clay where $K_0 > 1$) a conservative earth pressure distribution may be the consequence. The reduction on lateral earth pressure however can be overestimated when considering installation effects under plane strain conditions. Three-dimensional aspects, such as horizontal soil arching, panel length and the installation sequence of diaphragm wall panels are also practically relevant (Ng & Yan 1999). Potts & Zdravkovic (2001) and Schwamb (2014) concluded that even if a 3D aspect of wall installation process is adopted, an advanced constitutive soil model is required to capture stress relaxation.

4 Influence of individual strut failure

4.1 Introduction

The safety and robustness of structural support systems have to be ensured in the design of an underground structure and the overloading of any single support element should not lead to the collapse of the system. As far as deep excavations are concerned, overall failure is more likely to occur as a result of inadequate strutting or passive soil failure due to inadequate penetration depth, rather than the flexural failure of the wall itself (Puller, 2003). It is therefore important that the support system is designed with a certain degree of redundancy, so that failure of any individual element does not lead to the failure of the entire structure (Frangopol & Curley 1987, Osterberg 1989, Zheng et al. 2011, Finno 2018).

To explore the initiation and failure mechanism of excavation in soft clay subjected to imperfections of structural support elements, a parametric study has been carried out by means of a three-dimensional finite element analysis. Hashash & Whittle (1996) have shown that the wall length affects the stability of the excavation but has only a minor influence on maximum wall deflections as the excavation approaches failure.

Upper and lower bound analyses have been employed to investigate the failure conditions of deep excavations and the significance of the wall embedment and bending capacity of the wall has been demonstrated, for example by Ukritchon et al. (2003). Do et al. (2013) discussed methods of evaluating safety factors against base failure by quantifying the effects of wall embedment depth. Moreover, due to corner stiffening effects, there is a substantial reduction in lateral wall deflections, (e.g. Ou et al. 1996, Lee et al. 1998, Finno et al. 2007) and the bending moment as one moves from midspan toward the corner of the excavation depending on wall types (Zdravkovic et al. 2005, Lim & Ou 2018).

Moreover, this issue has been investigated by Cheng et al. (2017) and Cheng et al. (2017) in the context of the progressive failure of cantilever contiguous pile walls. When neglecting the corner effect, it has been observed that the progressive failure is dominated by the bearing capacity of individual members. This is accompanied by stress arching behind intact wall sections, which is also considered to be an influential factor in the context of the development of progressive failure.

The effect of wall embedment depth has been addressed in 3D finite element analyses with various excavation depths by Bahrami et al. (2018) and their results indicate the expected behaviour, namely that shorter embedment depth triggers a so-called kick out behaviour. Chowdhury et al. (2013) showed that the best possible structural performance can be achieved when strut arrangements and wall embedment depth are carefully chosen. The FEM analyses by Karlsrud & Andresen (2005) demonstrated the influence of undrained shear strength in soft clay on the required penetration depth, strut loads and bending moments for a flexible sheet pile wall. Increasing the shear strength by 40% decreases the maximum strut loads and bending moment by a factor of 2 and 6, respectively.

However, a possible variation of embedment depth of diaphragm wall panels due to construction imperfections is usually neglected in practice and only the extreme case is sometimes considered for a particular cross section in a two-dimensional plane strain analysis. Similarly, considering strut failure in plane strain analyses involves per the definition failure of the entire strut level and results in over-prediction of the forces in the remaining strut layers (Pong et al. 2012). A combination of individual strut failure and insufficient embedment depth has not been studied in great detail up to now, at least not to the author’s knowledge.

In this chapter, a 30-m deep excavation project in marine clay supported by a diaphragm wall, jet grouted base slab and multiple layers of struts is analysed by means of the finite element method. The excavation problem chosen is based on a real case history (Whittle & Davies 2006, Schweiger et al. 2009, Lee et al. 2011) but has been modified for the purposes of this study. These modifications are mainly concerned with some local irregularities concerning soil layers and some minor geometrical simplifications. Nevertheless, these details influence displacements and stresses and, therefore, a comparison with in situ measurements is not considered meaningful. Emphasis is placed on investigating the initiation of the failure mechanism of the overall system due to imperfections of structural support systems, namely the insufficient embedment depth of individual panels of the diaphragm wall into a stiff soil layer and the failure of a series of individual struts.

4.2 Problem description

4.2.1 Soil condition and construction sequences

A 30 m deep excavation in marine clay is considered in this study. As mentioned above, the numerical investigations presented in this chapter are based on a real project, but some simplifications have been introduced so that no direct comparison to the design of the actual project can be made.

A typical soil profile with groundwater conditions and construction sequence is shown in Fig. 19. The support system consists of a diaphragm wall and ten layers of prestressed struts at about 3 m vertical spacing. In addition, two layers of jet grouted panels (JGP) were used to ensure increased passive resistance, while the upper JGP layer was removed after the tenth excavation level had been reached. This excavation phase was chosen for the numerical investigation of the influence of individual strut failure and reduced embedment depth on the performance of the support system because this construction phase was considered additionally critical also for the actual project due to the fact that the JGP layer is removed and does not continue to provide any lateral support because the replacement with the tenth level of struts is not yet active. Individual strut failure in upper layers has not been considered crucial because the JGP layer was still providing support for these excavation phases and, therefore, the influence of wall imperfections (shorter embedment depth) was less severe.

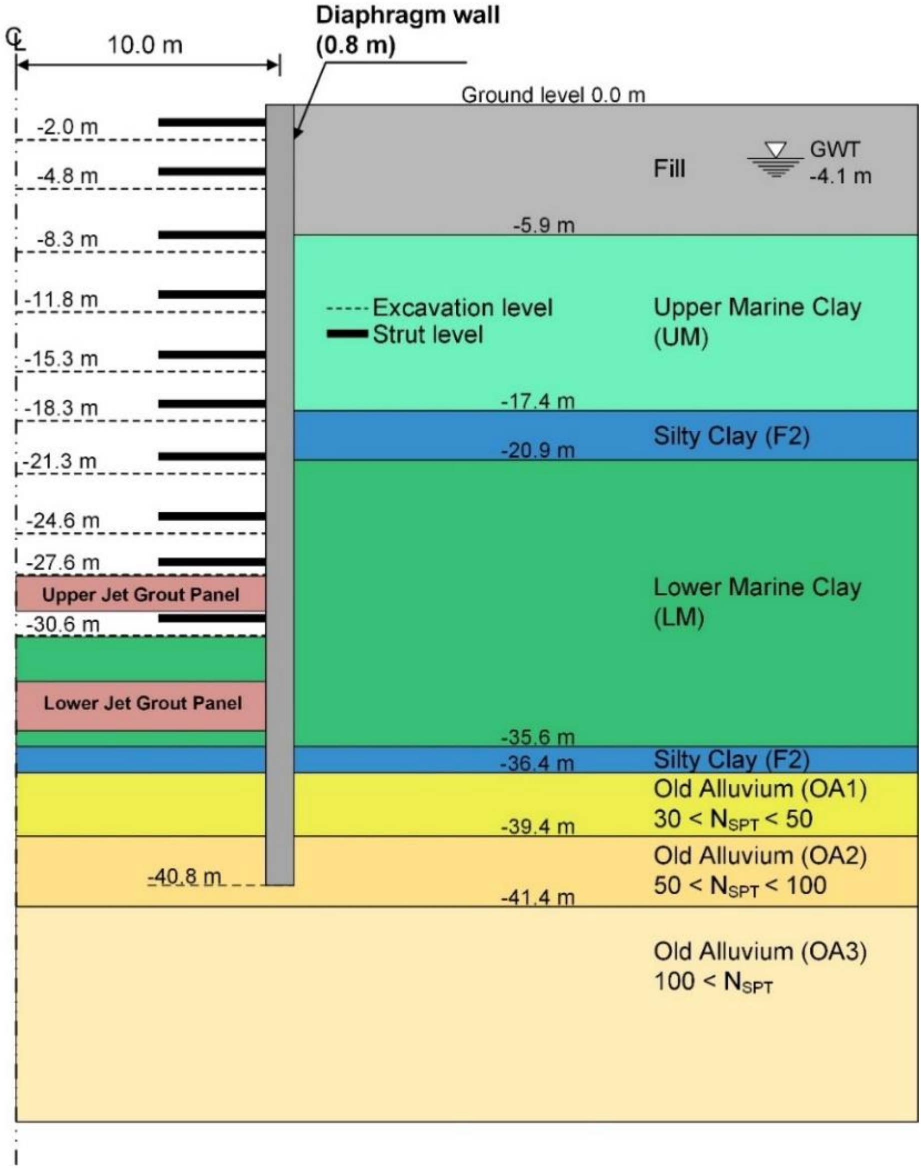

Fig. 19: Schematic sketch of soil profile and excavation sequence

4.2.2 Diaphragm wall embedment depths

To investigate the possibility of the load redistribution capacity of the lateral support system when individual struts fail, a series of three-dimensional finite element analysis assuming different wall embedment depths were carried out. A schematic three-dimensional view of the wall geometry with panels of 6.0 m width is shown in Fig. 20a, while Fig. 20b illustrates details of the investigated wall embedment variations into the stiff soil layer. A uniform embedment of the wall of 4.4 m into the stiff soil layer was taken as reference analysis.

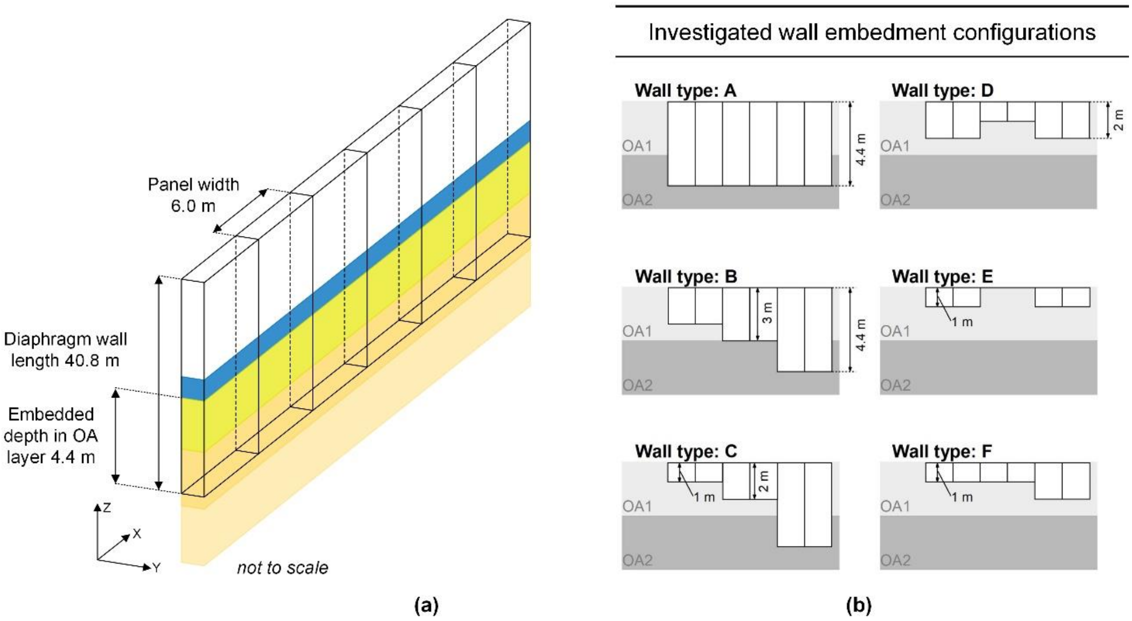

Fig. 20: (a) Schematic view of wall geometry and (b) wall configurations with different embedded levels

4.3 Soil constitutive models

The choice of the constitutive model is an important aspect in any numerical analysis, in particular when dealing with complex excavation problems as discussed in chapter 3. In this study constitutive models with double hardening plasticity and small strain stiffness behaviour are employed for the analysis (Benz, 2007, Benz et al. 2009). These are standard models implemented in the finite element code Plaxis (Brinkgreve et al. 2017) and are known as Hardening Soil model (HS), and Hardening Soil Small model (HSS).

It is the experience of the author that these models are suited for these types of problems (e.g. Schweiger et al. 2009, Choosrithong et al. 2019). In the HSS model, the stiffness-related parameters include four reference stiffnesses E_{oed}^{ref}, E_{50}^{ref}, E_{ur}^{ref}, and G_0^{ref}, which represent the stiffness moduli for primary loading in oedometric conditions, the secant modulus at 50% of the deviatoric stress at failure in a standard drained triaxial compression test, the unloading/reloading modulus, and the shear modulus at small strains, respectively. All moduli are reference values for a predefined stress level:

$$E_{oed} = E_{oed}^{ref}\left\{(c' \cdot cot\varphi' + \sigma_1')/\left(c' \cdot cot\varphi' + p_{ref}\right)\right\}^m \qquad (8)$$

$$E_{50} = E_{50}^{ref}\left\{(c' \cdot cot\varphi' + \sigma_3')/(c' \cdot cot\varphi' + p_{ref})\right\}^m \tag{9}$$

$$E_{ur} = E_{ur}^{ref}\left\{(c' \cdot cot\varphi' + \sigma_3')/(c' \cdot cot\varphi' + p_{ref})\right\}^m \tag{10}$$

$$G_0 = G_0^{ref}\left\{(c' \cdot cot\varphi' + \sigma_3')/(c' \cdot cot\varphi' + p_{ref})\right\}^m \tag{11}$$

where m is the parameter controlling the dependency of stiffness on the stress-level; σ_1' and σ_3' are major and minor principal effective stresses; p_{ref} is the reference pressure (100 kPa in this case); c is the effective cohesion and φ' is the effective angle of internal friction.

The HSS model requires nonlinear stiffness-strain degradation curves. With increasing strain, soil stiffness decreases following the hyperbolic stress-strain relationship:

$$G/G_0 = 1/(1 + 0.385 \cdot |\gamma/\gamma_{0.7}|) \tag{12}$$

where G_0 is the shear modulus at very small strains and $\gamma_{0.7}$ is the shear strain at $0.722G_0^{ref}$. The stiffness degradation curve used in this study is shown in Fig. 21 and falls within the range of data for soft soils with high plasticity clay (Teachavorasinskun et al. 2002, Jiahui, 2003, Vardanega & Bolton 2013) and Old Alluvium layers (Leung et al. 2010).

The oedometer stiffnesses, E_{oed}^{ref} of Upper (UM) and Lower Marin clay (LM) were evaluated based on the compression index, C_c. The reference secant stiffnesses, E_{50}^{ref} were taken as $1.5E_{oed}^{ref}$, while the unloading/reloading stiffnesses, E_{ur}^{ref} were assumed to $5.0E_{50}^{ref}$ based on experience and data from similar analyses (e.g. (Phien-Wej et al. 2012, Schweiger, et al., 2009). The ratio $E_{ur}^{ref}/E_{50}^{ref}$ for Old Alluvium soil ranges from 4-10 with power of stress dependency stiffness, m from 0.49-0.63. The small strain parameters, G_0^{ref} and $\gamma_{0.7}$, were also obtained from laboratory and in situ tests for both Upper and Lower marine deposits, and Old Alluvium layers.

Tab. 1 summarizes the input parameters for the HSS model and these are the same for the HS model with the exception of parameters G_0^{ref} and $\gamma_{0.7}$, which are not used in this model. The coefficient of earth pressure at rest K_0^{nc} was estimated using Jaky's expression ($K_0^{nc} = 1 - sin\varphi'$), except for UM and LM layers for which *K₀* was determined from model calibration by Corral & Whittle (2010).

A simple linear elastic-perfectly plastic Mohr-Coulomb constitutive model with zero tension cut-off (i.e. no tensile stresses are allowed in the JGP) is used to simulate the material behaviour for the JGP layers. Parameters are summarized in Tab. 1.

Tab. 1: HS and HSS model parameters

Parameter	Unit	Fill	UM	F2	LM	OA1	OA2	OA3
γ_t	[kN/m^3]	19	16	19	19	20	20	20
E_{50}^{ref}	[MN/m^2]	8.5	0.81	3.0	0.95	5.7	12.6	14.1
E_{oed}^{ref}	[MN/m^2]	8.5	0.54	2.0	0.63	5.7	12.6	14.1
E_{ur}^{ref}	[MN/m^2]	25.5	4.03	9.0	4.72	54	120	141.6
m	[-]	0.5	1.0	1.0	1.0	0.6	0.6	0.6
c'	[kN/m^2]	0.1	0.1	0.1	0.1	5	5	10
φ'	[°]	30	22	24	24	32	33	35
ψ'	[°]	0.0	0.0	0.0	0.0	0.0	0.0	0.0
ν_{ur}	[-]	0.2	0.2	0.2	0.2	0.2	0.2	0.2
K_0^{nc}	[-]	0.5	0.52	0.59	0.52	0.47	0.46	0.43
G_0^{ref}	[MN/m^2]	-	10	10	12.5	130	200	400
$\gamma_{0.7}$	[%]	-	0.05	0.05	0.05	0.02	0.02	0.02

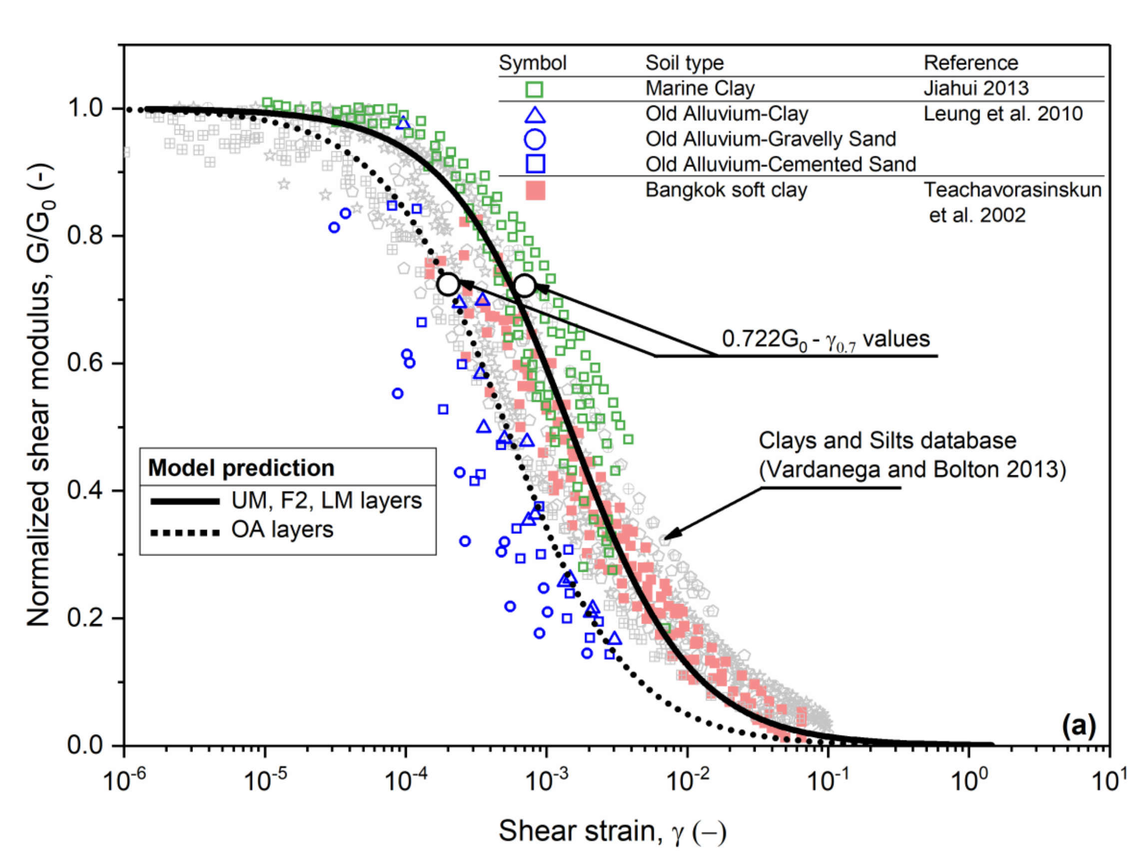

Fig. 21: Model predictions for normalised stiffness degradation curves

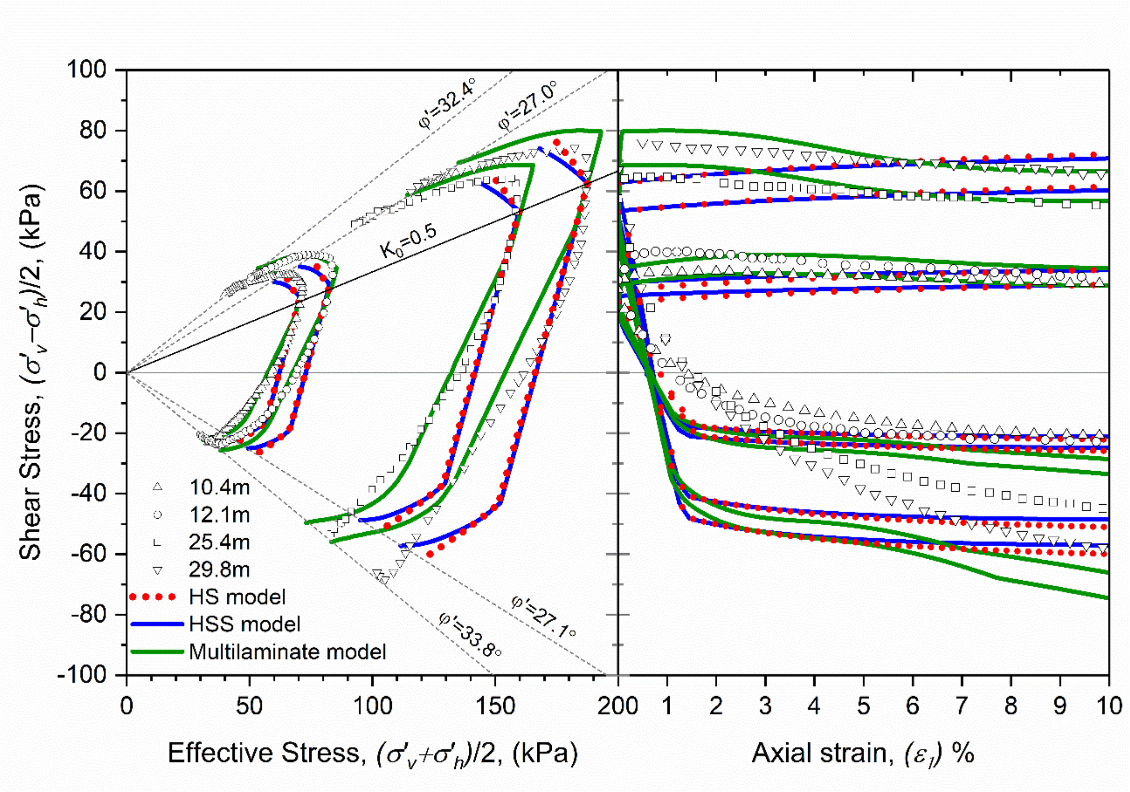

Fig. 22: Effective stress and shear stress-strain behaviour for soft marine clay (data from Corral & Whittle, 2010)

4.3.1 Undrained behaviour

In this study undrained behaviour has been assumed for the marine clay and the analysis is performed in terms of effective stresses. Therefore, the undrained shear strength does not represent an input parameter into the analysis, but is a result of the constitutive model. In order to check whether the constitutive models employed produce a realistic undrained shear strength, a comparison with experimental data, namely with results from K_0-consolidated undrained triaxial tests from Corral & Whittle (2010), has been made. Effective stress paths and stress-strain curves are shown in Fig. 22. It follows that predictions are reasonable for triaxial compression up to axial strains ε_1 of about 2% but matching in triaxial extension is less satisfactory. However, it is not the intention here to compare results with an actual case history, but rather to discuss a more general behaviour and, thus, no attempt was made to improve the predictions for triaxial extension.

It is observed that the HSS model predicts a lower undrained shear strength which is due to the fact that it uses a slightly different flow rule than the HS model (Benz, 2007, Brinkgreve et al. 2017). The importance of the flow rule, for modelling undrained behaviour in particular, has been addressed by modifying the Rowe's Stress-Dilatancy theory (Rowe, 1962), as discussed in section 3.3.6. The contractant behaviour for low mobilised friction angles in the HS model is cut-off, allowing dilatancy for high stress ratios.

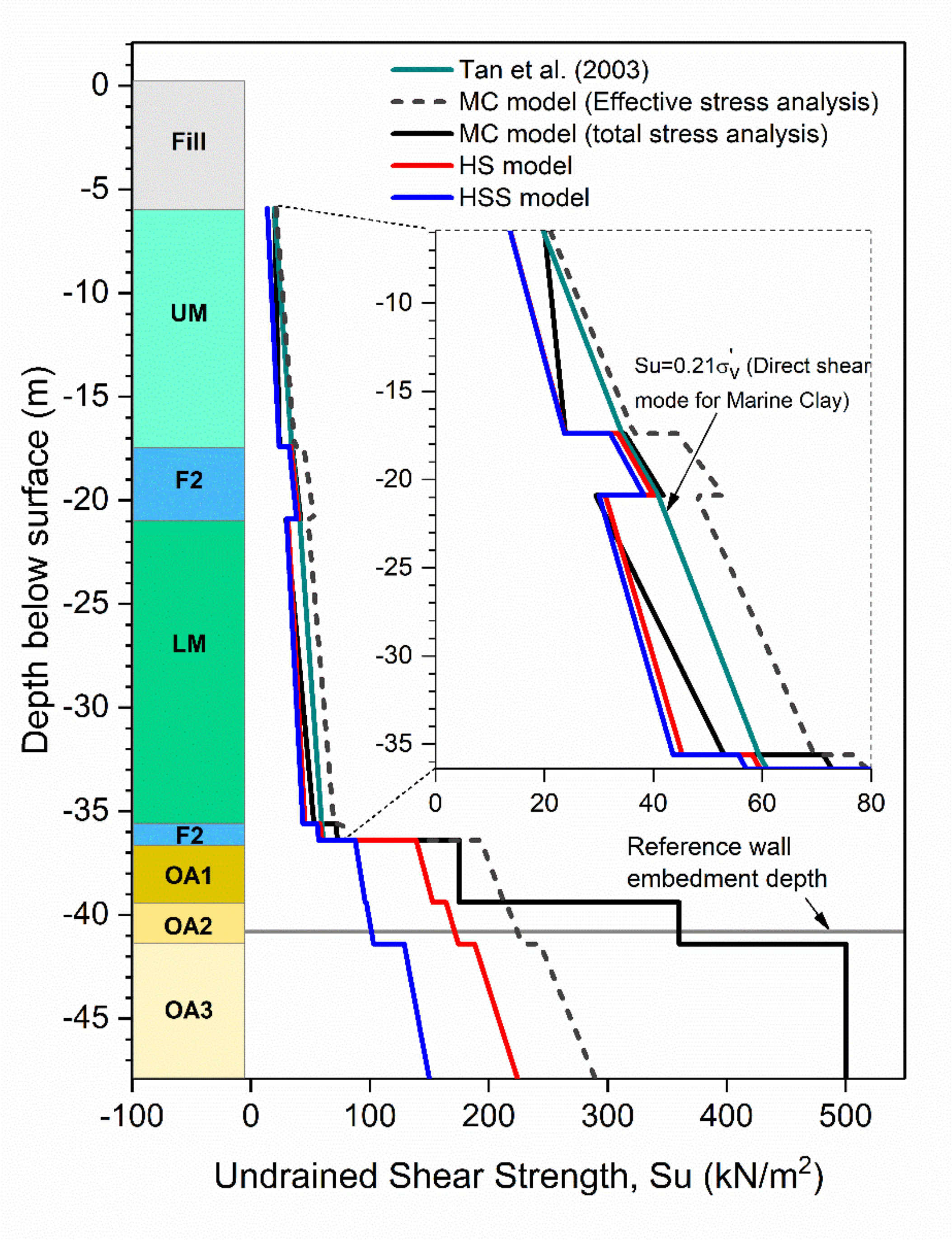

Fig. 23: Prediction of undrained shear strengths of marine clay used in analysis.

Fig. 23 summarises the undrained shear strength profile for the considered soil profile obtained by the HS and HSS model for isotropically consolidated triaxial compression. For reasons mentioned above, a slightly lower undrained shear strength is obtained with the HSS model. In addition the undrained shear strength profile which would be obtained from the Mohr-Coulomb failure criterion is also shown in Fig. 23, confirming the well-known fact that such a model would highly overpredict the undrained strength (Schweiger et al. 2009, Hsieh et al. 2017) for normally consolidated clays and, therefore the model is not used here to model the behaviour of soil layers. The profile suggested by Tan et al. (2003) is also plotted for comparison.

4.4 Finite element and geometry

The 3D finite element code Plaxis (Brinkgreve et al. 2017) has been used to model the deep excavation depicted in Fig. 19. The analysis was performed as follows:

- wall installation was considered as wished-in-place,
- excavation down to excavation level 10 was performed in steps, including groundwater lowering inside the excavation
- activating the prestressed struts.

The preloading was applied simultaneously for all struts in a layer with approximately 25-45% of the maximum capacity. Excavation level 10 was chosen as a basis from which the failure of individual struts was simulated. The load of failed struts is generally transferred vertically and horizontally to neighbouring struts. In order to simulate a consecutive failure of individual struts, the general and refined scheme of sequential failure of struts as indicated in Fig. 32a and Fig. 32b respectively, were assumed.

The potential failure of structural members was considered under primarily compressive forces assuming elastic-perfectly plastic behaviour, i.e. a maximum strut force is specified for the struts (N_P, see Tab. 3). The different strut-waler connection (i.e. splayed or non-splayed strut) was different for different struts in the original project and this property has been kept in this study. The same axial stiffness of the struts can be expected in some layers, whereas the maximum compressive capacity is different depending on the type of connection (i.e. plate or c-channel steel stiffener).

The wall was modelled by means of continuum elements in order to obtain reliable wall movements that take account of the wall thickness and resisting moment from shear stresses at the back of the wall (Zdravkovic et al. 2005). Full interface friction was assumed between the soil and the wall and with the given properties the ultimate bending capacity M_P of the wall is approximately 2500 kNm/m. The JGP layers were also assumed as wished-in-place. The waler beams are modelled with 3-noded beam elements (Fig. 25b).

The properties of structural elements are summarized in Tab. 2 and Tab. 3. The meshes used for 2D and 3D analyses are shown in Fig. 24 and Fig. 25, respectively. Lateral movements are restrained at vertical boundaries of the domain and fully fixed conditions are assumed at the bottom boundary.

Tab. 2: Input parameters for wall, waler beam and JGP layers

Parameter	Unit	Wall	Waler beam	JGP layers
		Continuum elements	Beam elements	Continuum elements
γ	[kN/m^3]	24	78.5	16
E	[MN/m^2]	30000	2100	75
c', S_u	[kN/m^2]	9300	-	150
φ'	[°]	40	-	0
ν	[°]	0.15	0.15	0.15
σ_t	[MN/m^2]	7.82	-	0

Note: γ = Unit weight, E = Young's modulus, c', S_u = Cohesion and Undrained shear strength, φ' = Friction angle, ν = Poisson's ratio, and σ_t= Tensile strength

Tab. 3: Input parameters for struts

Strut level	Installation depth	Axial stiffness, *EA*	Preload	Maximum compressive capacity, N_P
	m	kN	kN	kN
1	-1.0	3.52E+06	800	3352
2	-3.8	4.48E+06	2200	5672
3	-7.3	8.97E+06	2600	11344
4	-10.8	8.97E+06	2400	9052
5	-14.3	8.97E+06	2800	8308
6	-17.3	6.06E+06	2800	7708
7	-20.3	8.97E+06	3200	7000
8	-23.6	1.27E+07	3400	9200
9	-26.6	8.97E+06	3200	3600

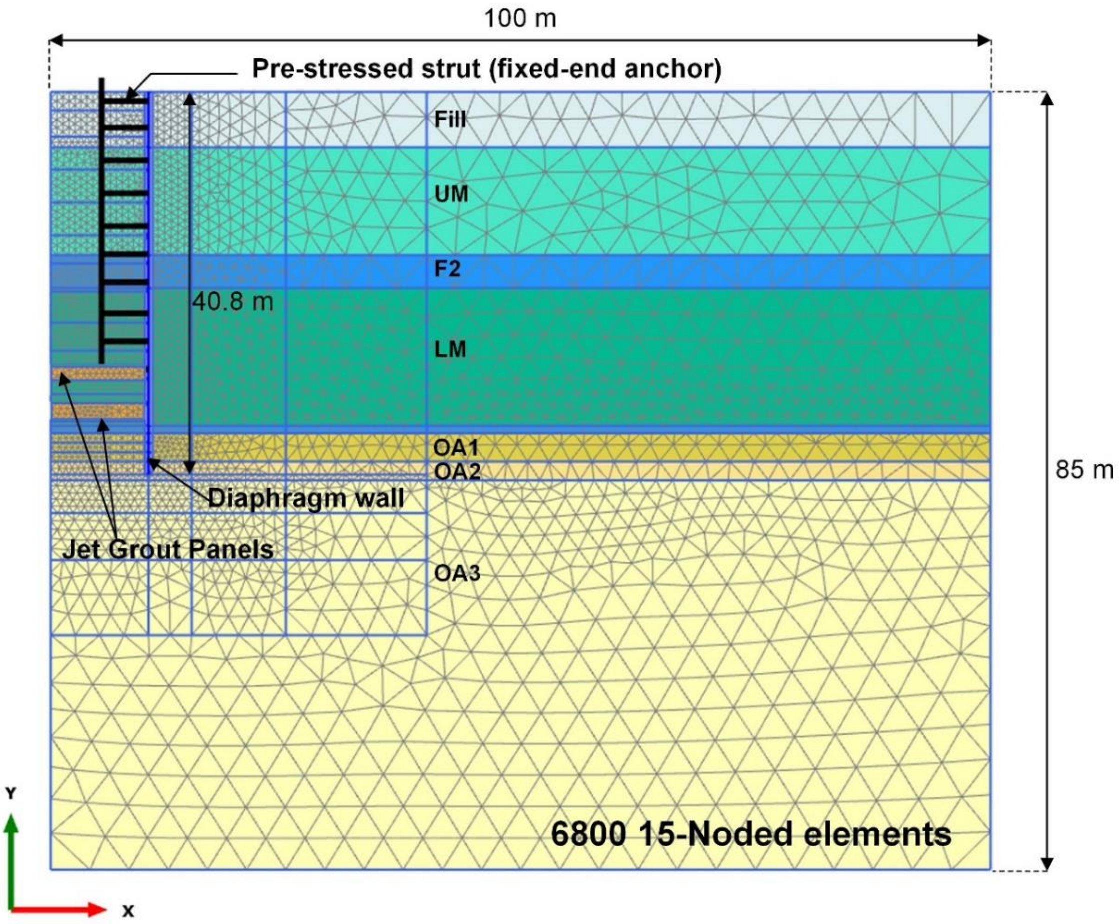

Fig. 24: Finite Element Mesh for 2D

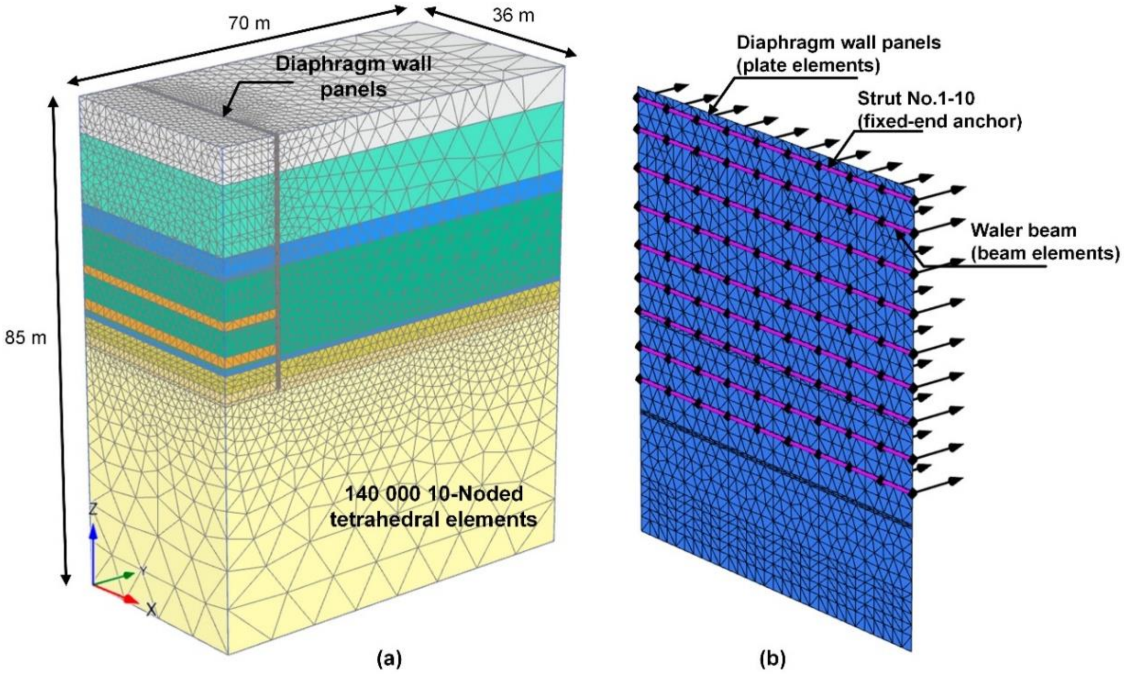

Fig. 25: (a) Finite element mesh for 3D; (b) structural modelling

4.5 Model validations

Fig. 26 and Fig. 27 compare computed lateral wall deflections for different soil models with the measurements as reported by COI (2005). As mentioned previously some modifications as compared to the actual case history have been made for the study presented here and therefore the comparison with monitored data is of qualitative nature and included here to show that the overall performance is reasonably well captured by the proposed model.

The analyses have been carried out by 2D-plane strain analysis for model validation purposes (see Fig. 24). The comparisons are for just before the failure, except for Fig. 27b where the strut is considered as having already failed (i.e. elastoplastic behaviour). Apart from cantilever movements at the early stages of excavations, the bulging mode of movement is observed around the excavation level, as expected. The computed wall deflection using the MC model with effective stress analysis is underpredicted by a factor of 5 compared to the analysis using total stresses. Additionally, a significant fixity at wall toe level is achieved in the HSS due to the effect of higher stiffness at small strain levels at OA layers.

The surface settlement trough behind the wall is depicted in Fig. 28. By accounting for small strain stiffness, a slightly narrower settlement trough is observed in the HSS model. It is interesting to note that the deepest settlement trough is observed in the analysis of MC model with total stress analysis which may result from the selected input parameters (undrained shear strengths and comparatively low stiffnesses).

Fig. 29 compares the bending moments for various models adopted for the final excavation level with the presence of nine strut layer. A difference in bending moments is observed, which resulted from the deflected shape of the wall.

Fig. 30 and Fig. 31 show the influence of JGP properties on predictions of wall deflection and bending moments for both HS and HSS soil models. It is evident that the reduced properties (strength and stiffness, see Tab. 2) of JGP lead to large deflection and significant toe rotation at final excavation (strut level nine is still in place). Similarly, the bending moments are significantly increased.

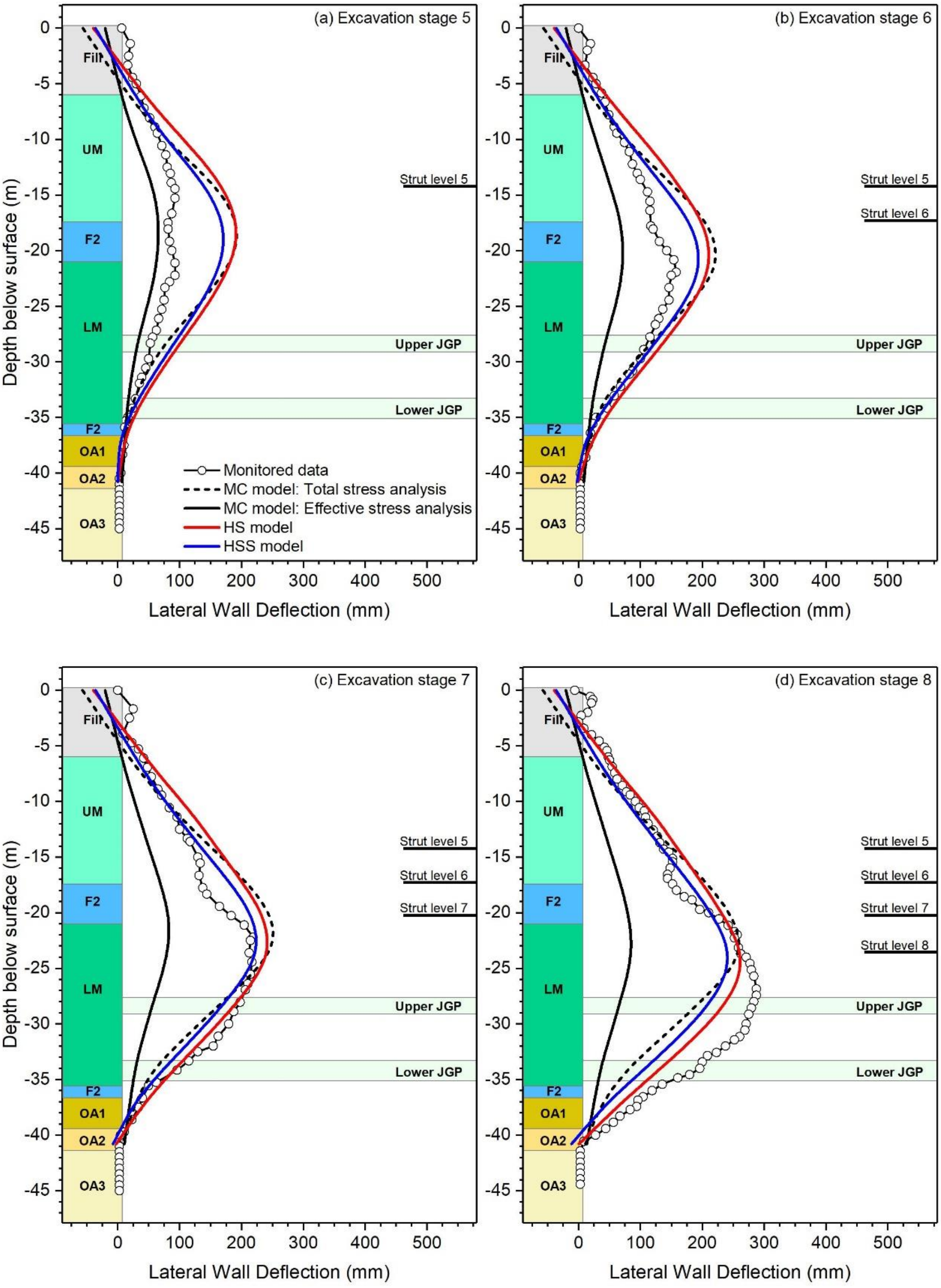

Fig. 26: Computed and measured lateral wall deflection for excavation level 5 to 8

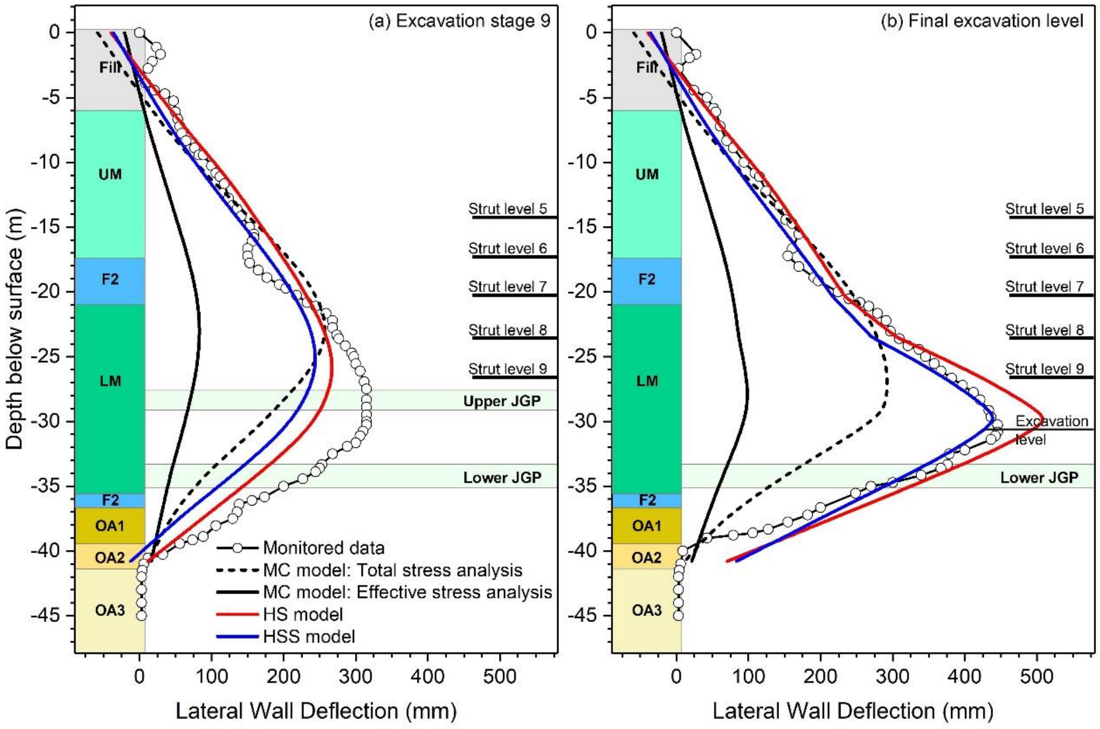

Fig. 27: Computed and measured lateral wall deflection for excavation stage 9 to final level.

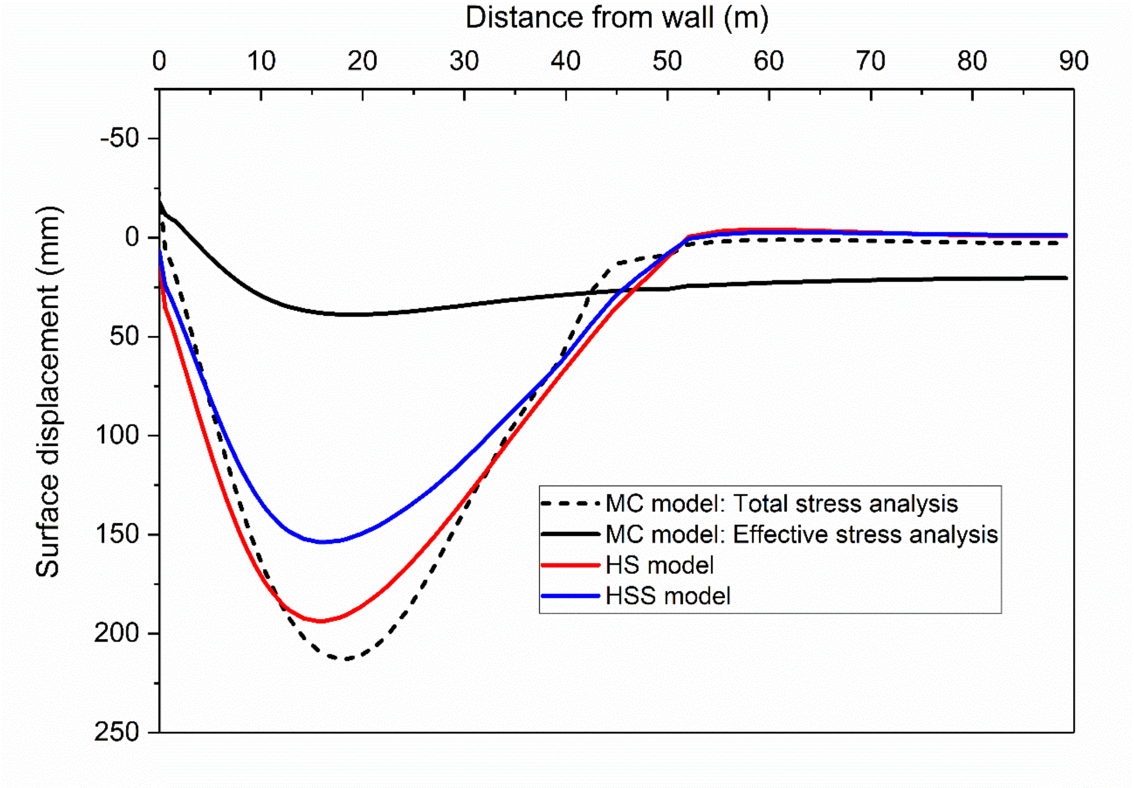

Fig. 28: Calculated vertical surface settlement

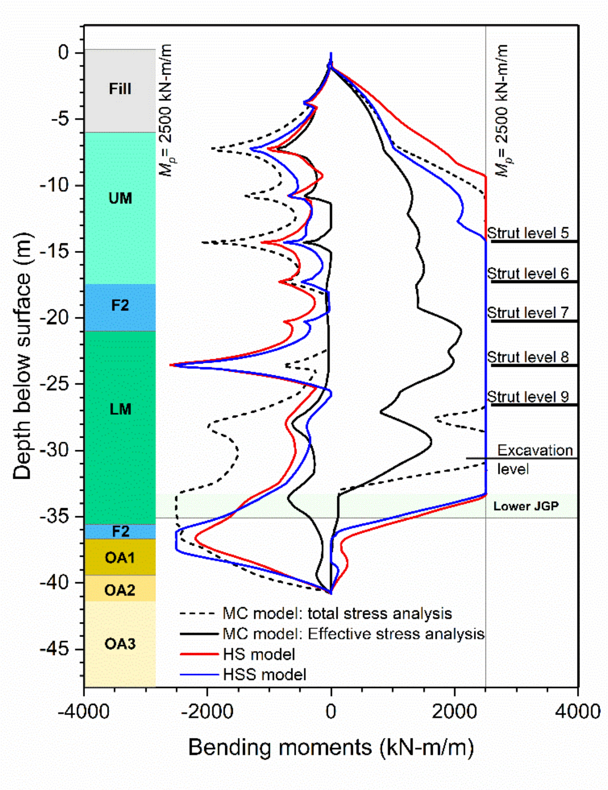

Fig. 29: Computed bending moment for different soil models

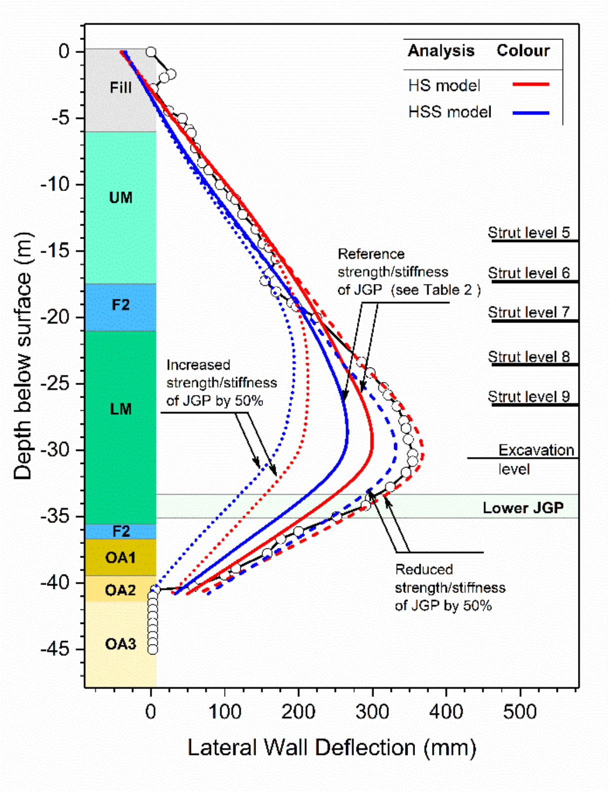

Fig. 30: Influence of JGP property on predicted lateral wall deflection

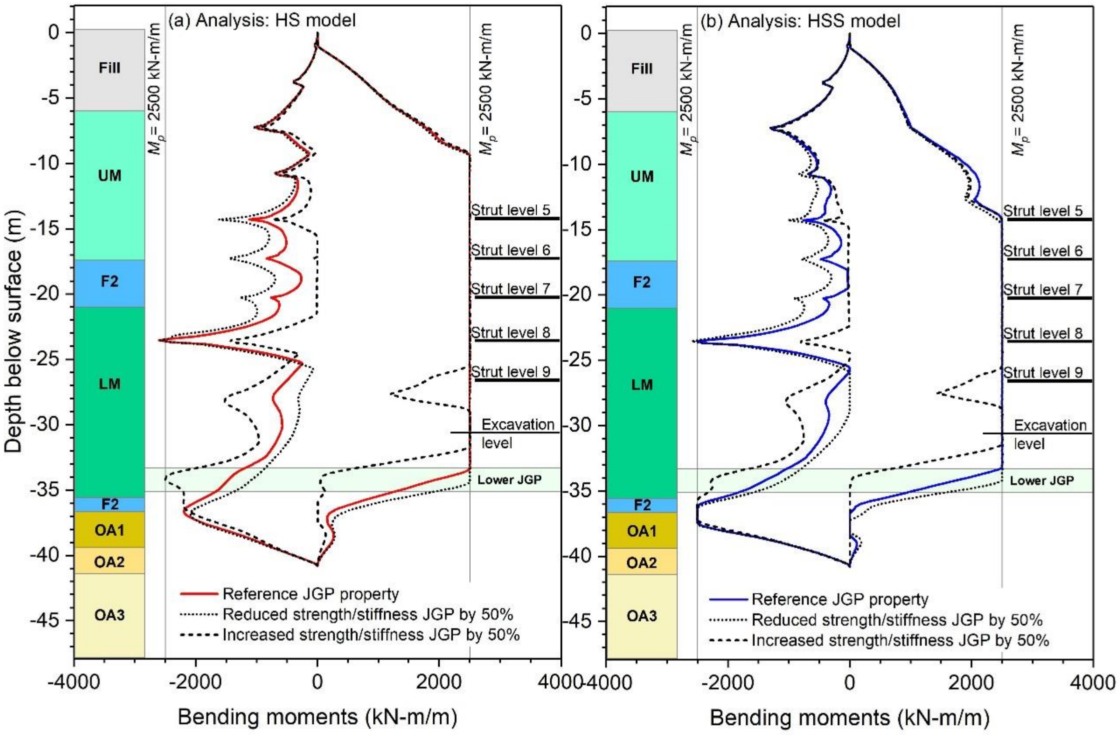

Fig. 31: Influence of JGP property on calculated bending moments

4.6 Sequential failure of individual struts

In order to simulate the failure of individual struts, the scheme of sequential failure as indicated in Fig. 32 was assumed. As mentioned previously, the starting configuration for investigating strut failure is excavation level 10 without strut level 10 being in place. The upper JGP is removed. The sequence of failed struts initiates from the first strut in the centre of the 9th strut layer and extends horizontally in level 9 as indicated by the numbering in Fig. 32a. A failure of the entire strut level is equivalent to the plane strain assumption in 2D finite element analysis. The load of a failed strut is transferred to neighbouring struts in the layer, as well as to the 8th layer and to some extent to the jet grout panel below (the lower JGP is still in place).

It should be noted that in the first series of analyses it has been assumed that neighbouring struts, being loaded due to stress redistribution, remain in place with their maximum bearing capacity, i.e. they do not influence the sequence of strut removals. In a second series of analysis a refinement of this procedure is adopted, namely that struts reaching the maximum capacity in a particular calculation phase are also removed after this phase, as depicted schematically in Fig. 32b. Scheme 32a could be considered as a ductile system behaviour, whereas scheme 32b would represent a more brittle system behaviour.

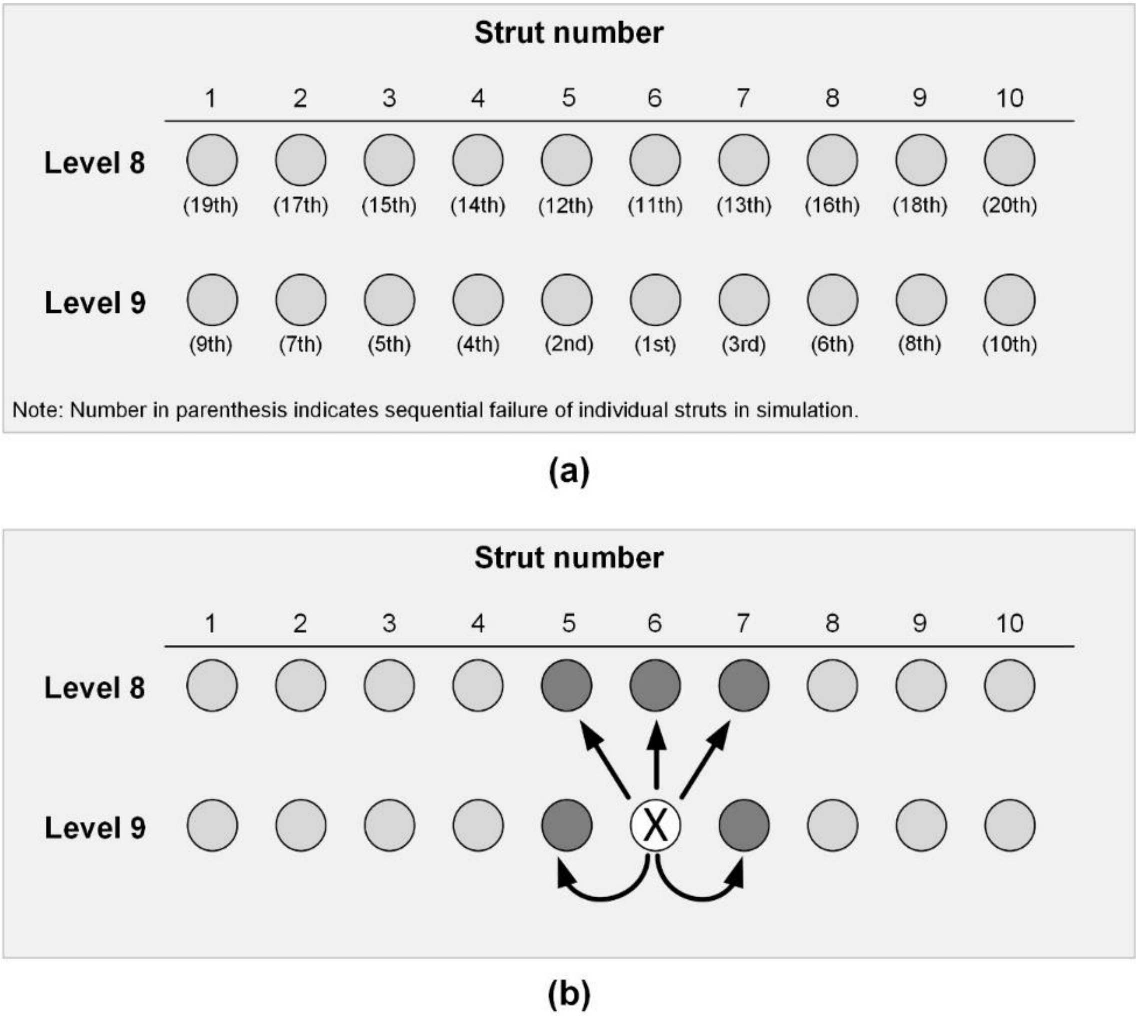

Fig. 32: Schematic diagram for simulation: (a) typical failure sequence; (b) refined failure sequence

4.6.1 Strut failure with reference embedment depth

The analysis with the reference wall embedment depth serves as a reference for the comparison, and the lateral wall deflection after excavation to level 10 and the subsequent failure of the ninth strutting level is shown in Fig. 33 for both constitutive models (HS and HSS model). The lateral wall displacement in the centre of the 3D analysis is essentially the same as that for the 2D plane strain analysis in the calculation phase “excavation level 10”, which can be expected because no stiffening effects of corners are taken into account in this study.

The differences between 2D and 3D aspects of wall deflections and bending moments (Fig. 33) after the failure of the 9th strut level can be explained by the fact that in 3D a waler beam is modelled, which influences the stress paths in the soil when the struts of the 9th level are subsequently removed and not in one step as is the case in plane strain analysis. The results in this section refer to the strut failure scheme as described in Fig. 32a.

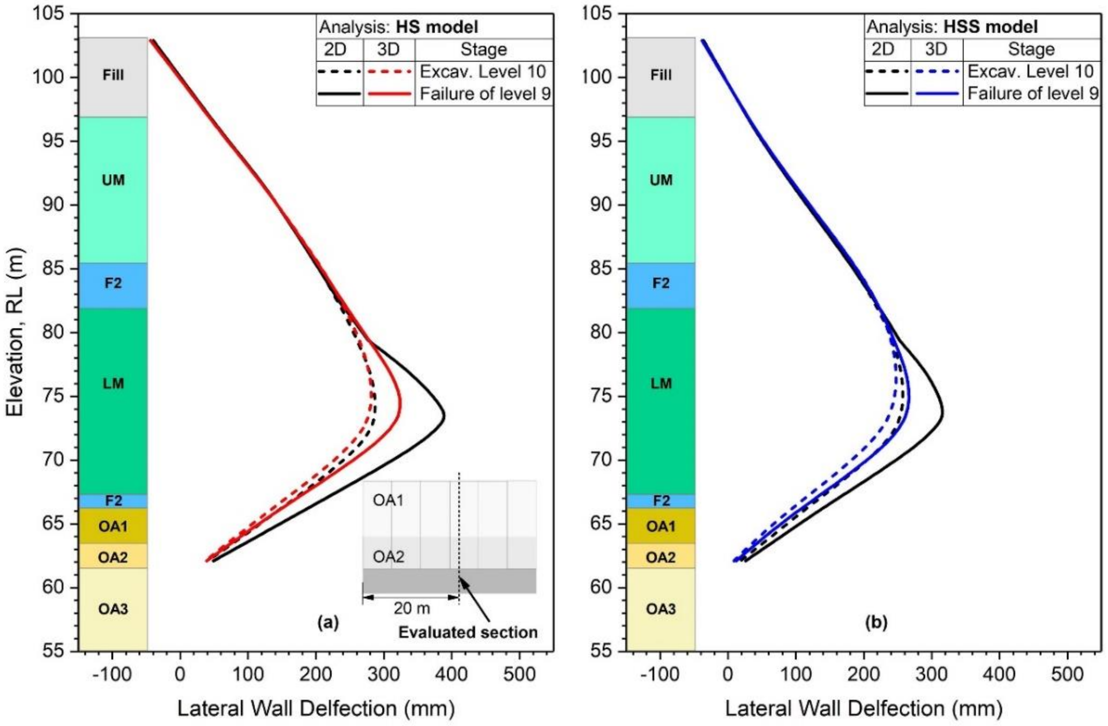

Fig. 33: Lateral wall deflection for reference embedment depth: (a) HS model; (b) HSS model

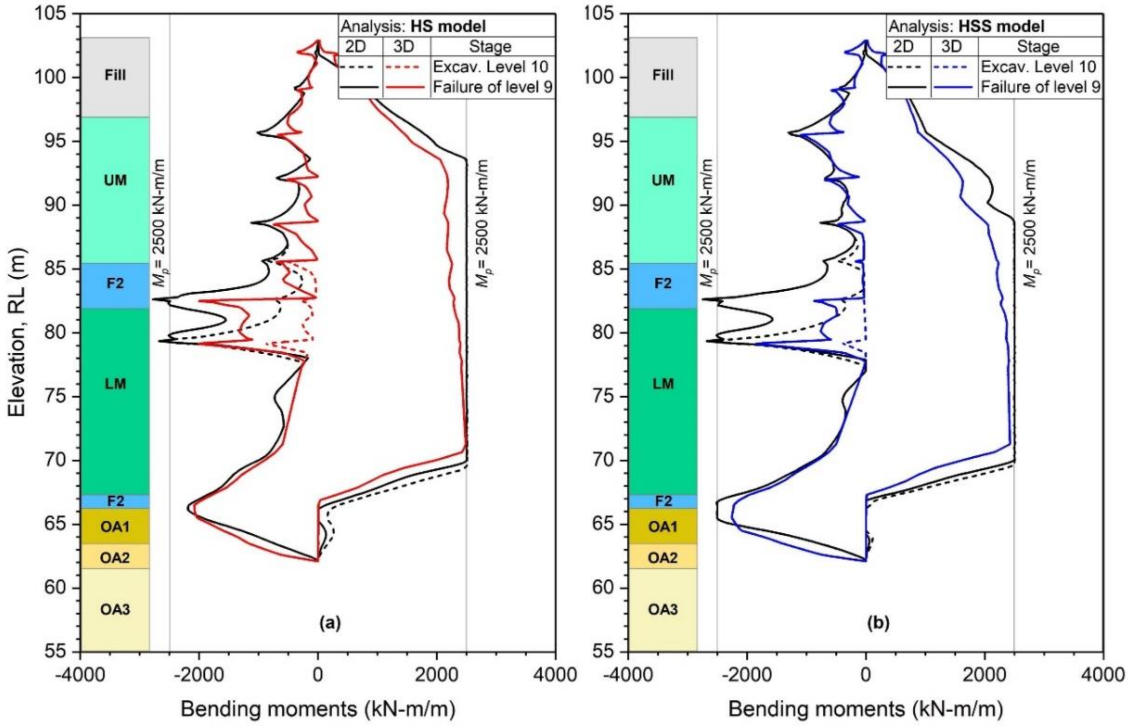

Fig. 34: Computed wall bending moments for reference embedment depth: (a) HS model; (b) HSS model

The envelopes of the calculated bending moments are shown in Fig. 34. As the moment capacity of the wall is approximately M_P = 2 500 kNm/m (based on the condition that steel is yielding and the ultimate compressive strain is reached in the compression zone) it is obvious from Fig. 34b that in this particular case the wall remains essentially elastic. It should be mentioned that the wall is modelled as isotropic material for simplicity, although it is acknowledged that diaphragm walls may exhibit anisotropic behaviour due to a non-continuous reinforcement in the longitudinal direction. It is however argued that for the purposes of this study, this aspect is not important.

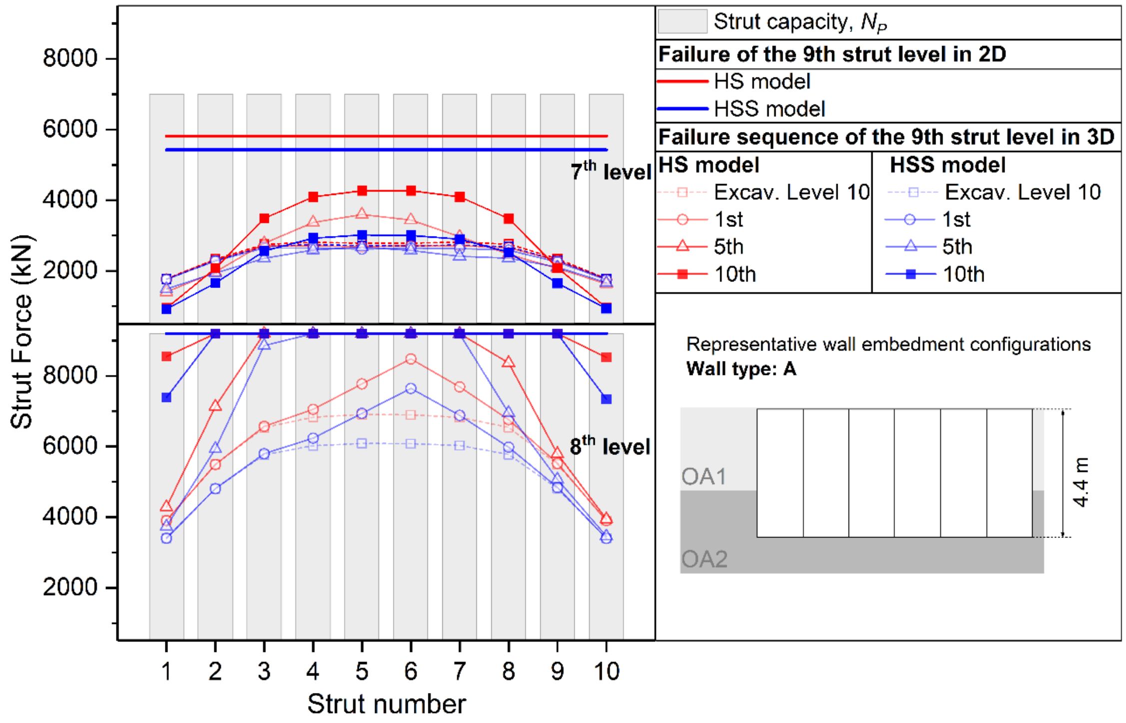

Fig. 35: Load distribution after process of sequential individual strut failure at 9th strut level

Fig. 35 compares strut forces at levels 7 and 8 with the sequential failure of individual struts at level 9. Starting from the individual strut failing at the centre, denoted as “1st”, as indicated in Fig. 32a, up to the complete failure of the 9th level (indicated as 10th). It is apparent that the load is transferred to the remaining upper struts in both vertical and diagonal directions, which eventually also approach their capacity *Np*.

The analysis employing the HS model shows a larger increase of strut forces, in particular in the 8th level, associated with larger wall movement and consequently reaches the normal force capacity *Np* earlier when compared to the HSS model after the tenth failure sequence. The HSS model behaves stiffer because the high stiffness at small strains is taken into account. For the 7th strut level the increase in strut loads is less pronounced, even though the entire strut level 9 was considered as having failed.

4.6.2 Strut failure with reduced embedment depth

Fig. 36 shows the calculated wall deflection using the HS model when removing the 10th strut of level 9 with different scenarios of panel embedment (see Fig. 20). The deflected shapes are virtually identical to the reference analysis when only a few panels are embedded less than 3 metres into the stiff layer (i.e. embedment type B and C). When more panels have shorter embedment depths, a significant increase of wall deflection at the toe is observed as expected, in particular for “wall type E”.

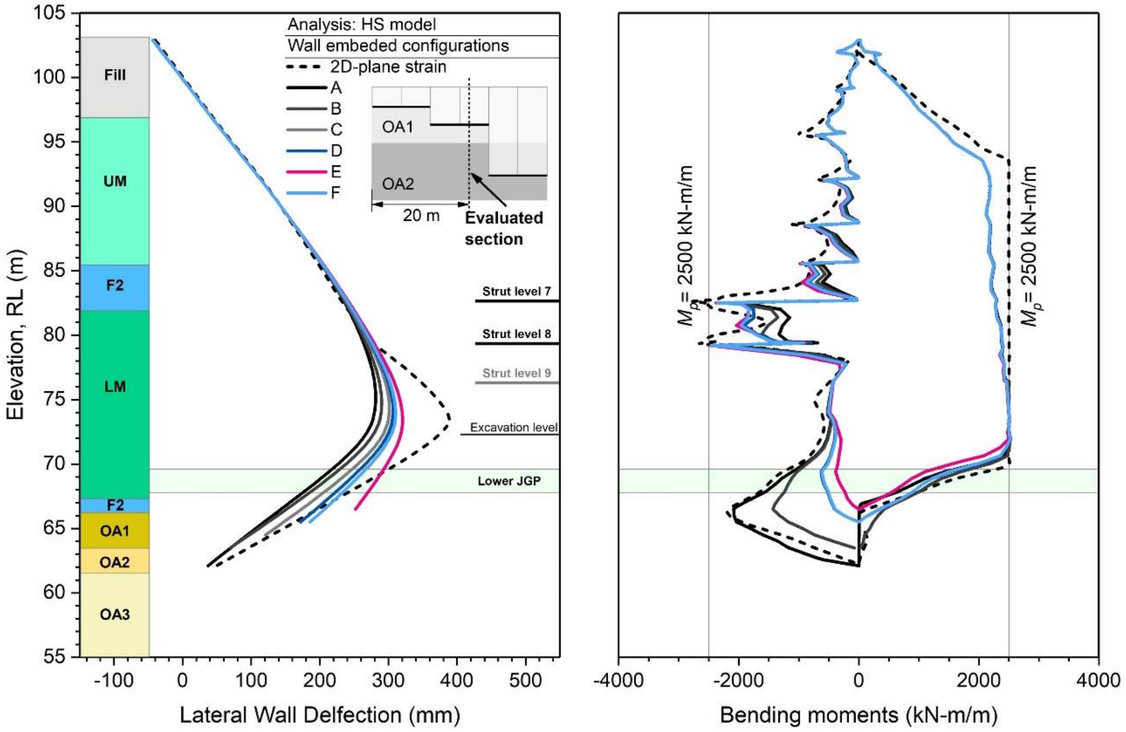

Fig. 36: Lateral wall deflections (a); computed bending moments for reduced embedment depth (b)

Fig. 37 compares wall displacements and bending moments for embedment scenario “D” (see Fig. 39) for both of the constitutive models employed. In this case the HSS model predicts failure when removing the 9th strut of strut level 9 whereas with the HS model equilibrium can still be achieved. This is a consequence of the HSS model because, in addition to small strain stiffness effects, the flow rule is also different when compared to the HS model, leading a lower undrained shear strength in the effective stress analysis of undrained conditions.

As an example for the load redistribution, Fig. 38 depicts, for different embedment scenarios, the normalized loads (as ratio to the maximum capacity *N*/*Np*) on struts at levels 8 and 7 when the first three struts of level 9 have been assumed to have failed and it is obvious that struts at level 8 rapidly reach their bearing capacity.

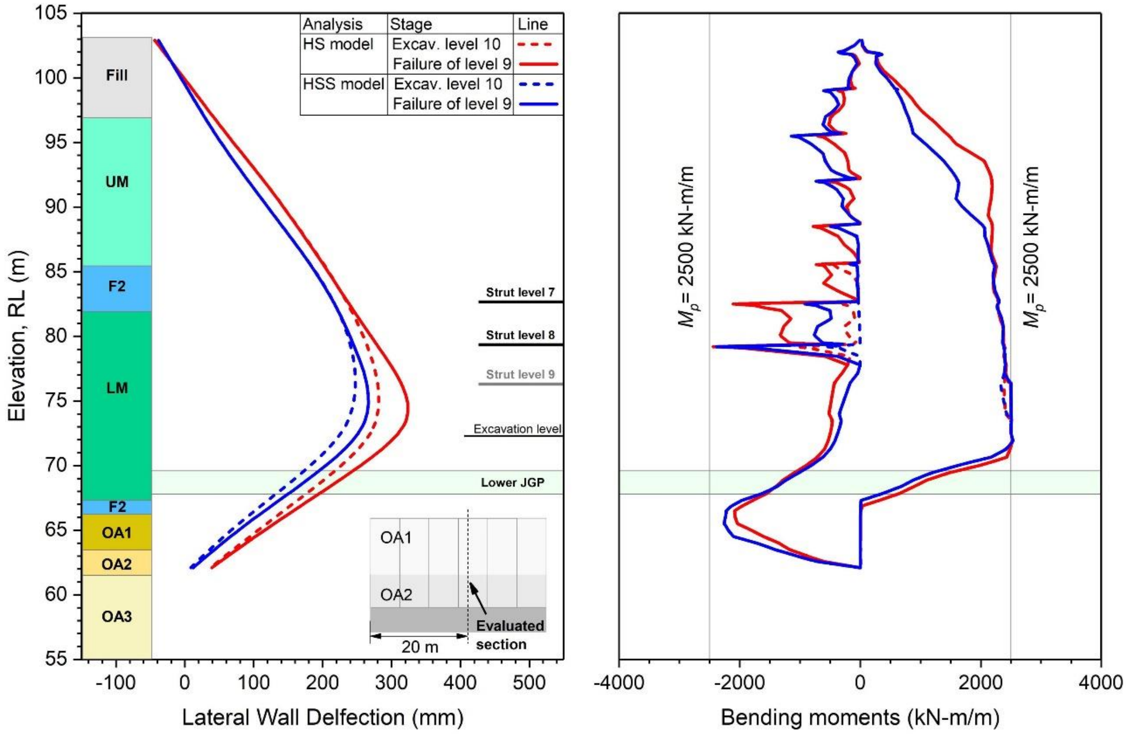

Fig. 37: Lateral wall deflections (a); computed bending moments for embedment scenario “D” (b)

4.6.3 Failure initiation

Failure in the numerical model is defined when equilibrium cannot be achieved in the numerical model, whereas stringent convergence tolerance has been adopted. Moreover, failure is indicated by the occurrence of excessive deformation, with shear stresses on the potential failure surface and by the maximum bending moment in the wall.

Fig. 39 summarises when failure occurs for different embedment scenarios highlighting again the differences with respect to the constitutive model adopted for the soil. On the vertical axis, the number of sequentially failed struts is plotted (see Fig. 32a) and on the horizontal axis, the embedment scenario is indicated. It follows that equilibrium can still be achieved with a complete failure of strut level 9 (i.e. a total of 10 struts have failed) for embedment scenarios A and B, but not for the others. This holds for the HSS model. The HS model allows for more struts to fail, but this is, as mentioned earlier, due to the fact that it predicts higher undrained shear strength than the HSS model. This emphasises the importance of choosing an appropriate constitutive model in general, but in particular in this case when the undrained shear strength of the soft soil layer is of crucial importance.

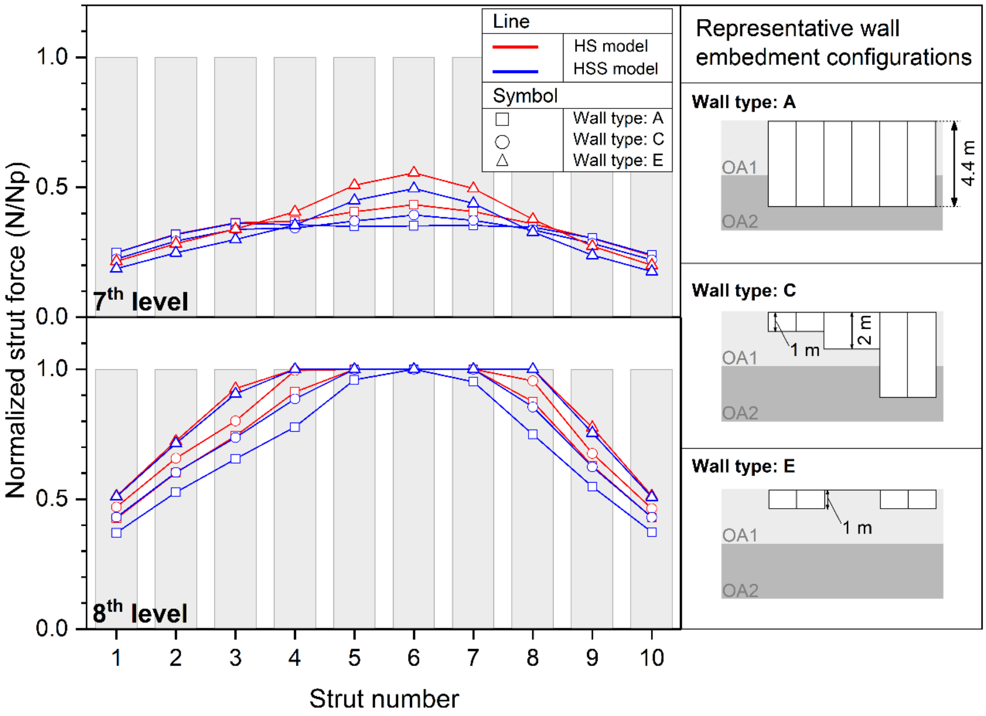

Fig. 38: Load distribution after failure of 3 struts at level 9

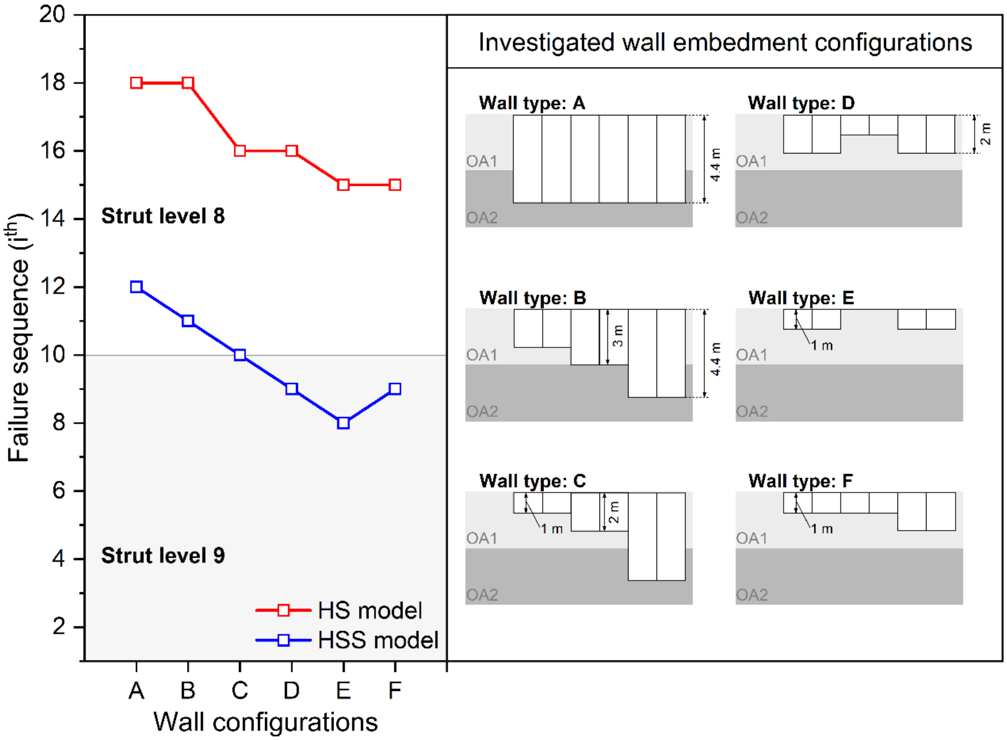

Fig. 39: Effect of wall embedment depth on different strut failure scenario

4.6.4 Influence of strut failure schemes

Fig. 40 compares wall deflections for the reference and refined failure sequences of individual struts (see Fig. 32a, 32b) at the failure point for embedment scenarios “A” and “E”. It should be noted that the maximum lateral deformations indicated in Fig. 40 are just before the analysis failed to reach equilibrium and, therefore, only one further strut is required to cause an overall collapse, as indicated in the strut failure scheme depicted in Fig. 41.

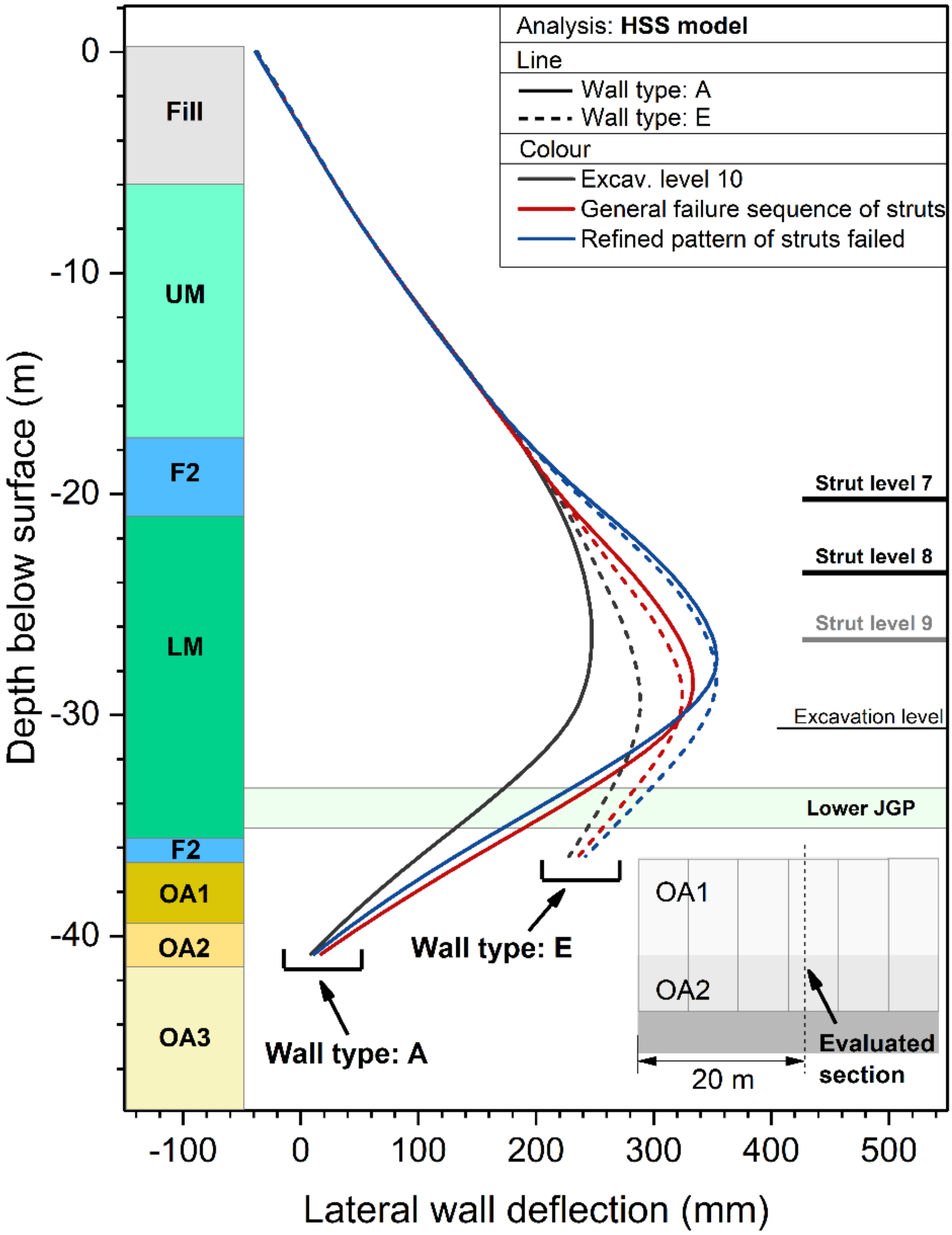

Fig. 40: Effect of strut failure scheme on lateral wall deflections

In Fig. 41 the out-of-plane bending moment (i.e. bending moment around z-axis) in the wall is plotted, normalized by the maximum bending capacity (M_2/M_p). The struts which have been assumed to have failed for each particular case are also indicated in Fig. 41. It follows that more struts have to fail in order to cause the overall failure of the system if the failure sequence according to Fig. 32a is adopted ("ductile" behaviour), as compared to the failure sequence according to Fig. 32b ("brittle" behaviour). Secondly, it is obvious that more struts have to fail for a system to collapse when the embedment depth is larger. The increase in wall bending moments is also significantly different when "brittle" strut behaviour is assumed, indicating that system failure will be a combination of exceeding both strut and wall capacity. It can be concluded that improving the ductility of the elements or connections within the system is an effective way to increase the redundancy of a system.

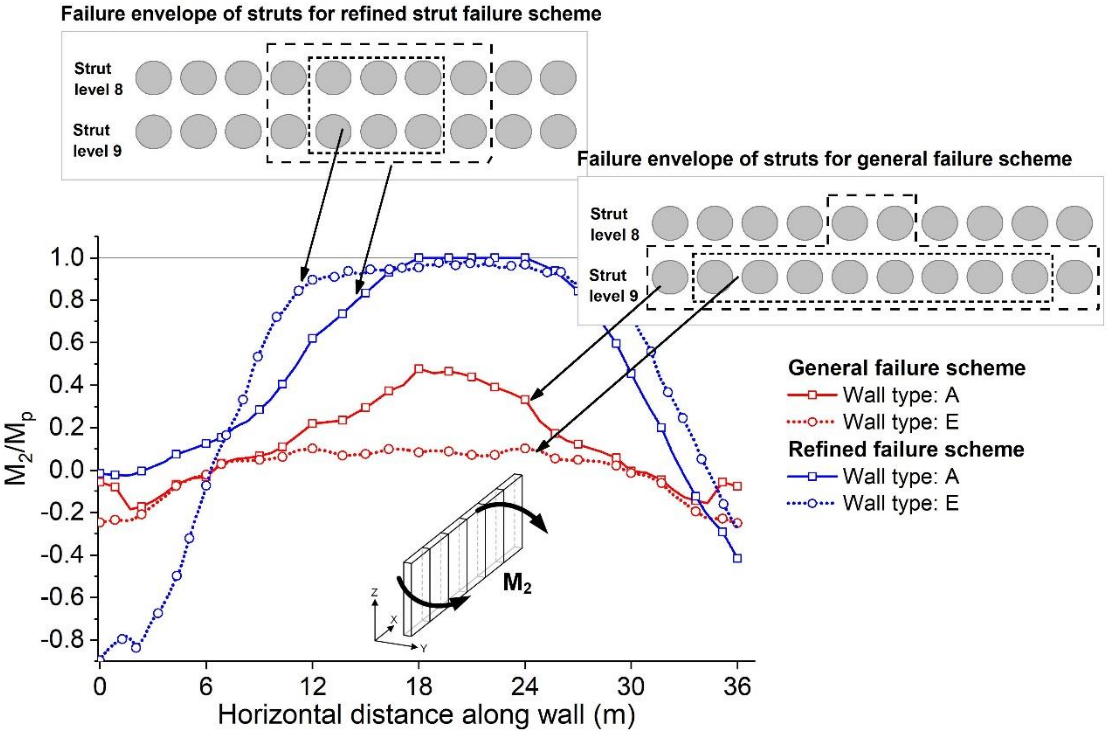

Fig. 41: Effect of strut failure scheme on out-of-plane bending moments

4.6.5 Soil failure

Fig. 42 shows contours of mobilised soil strength (a value of 1.0 is equivalent to fully mobilized strength) for embedment scenarios "A" (reference) and "D". The strength of the soil on the passive side is fully mobilized and so is the strength of the JGP layer. It is mentioned again that the failure in Fig. 42 follows the general sequential strut failure (Fig. 32a) and the corresponding number of failed struts is indicated in Fig. 39.

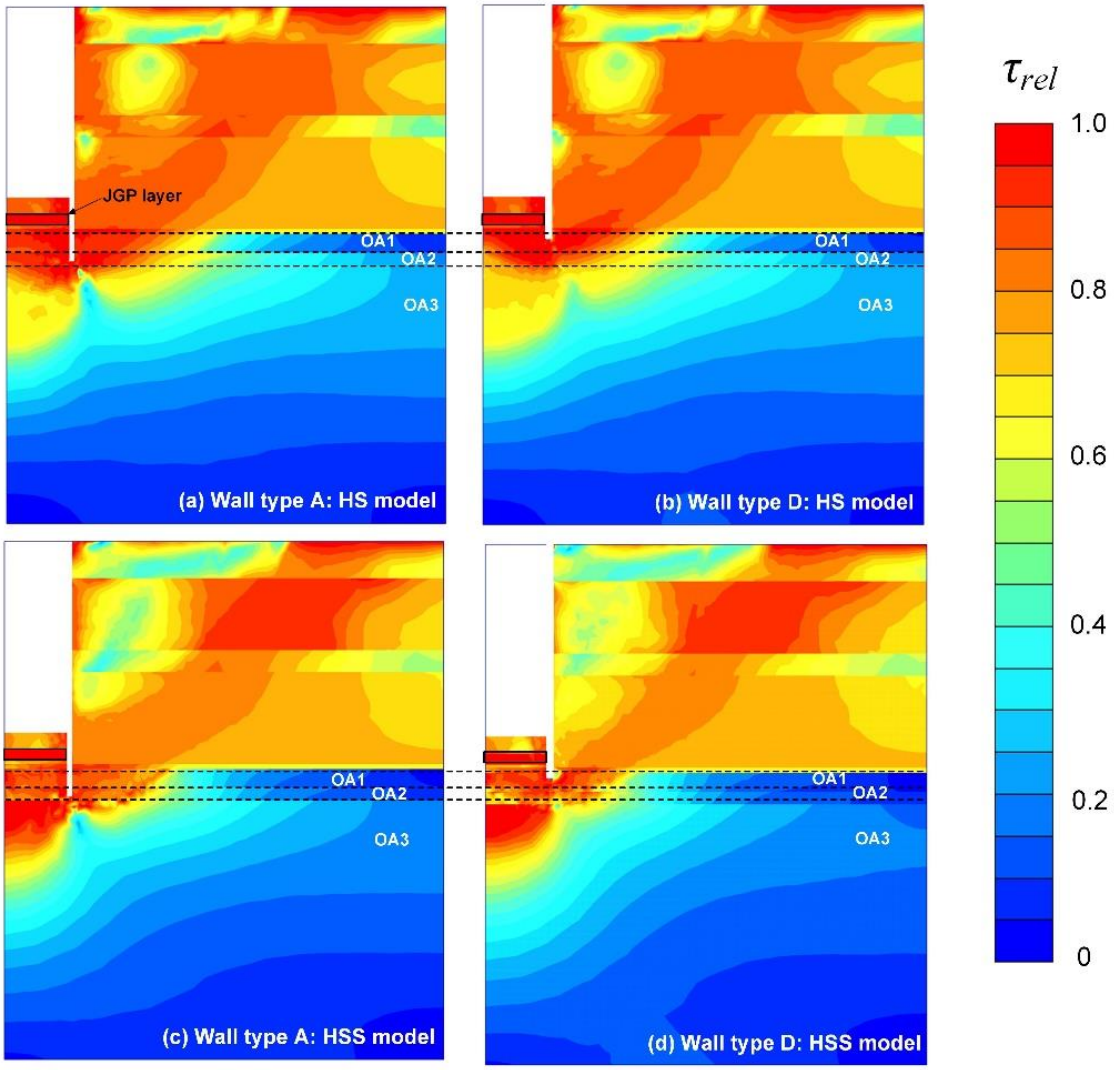

Fig. 42: Contour lines of relative shear stress prior failure

In Fig. 42, failure in soil occurs especially around the toe wall level. The relatively high shear stress concentrates around the interface between the soil and the wall on the passive side, and progresses to more competent strata (OA1 to OA3). The maximum relative shear stress ($\tau_{rel} = 1$), corresponding to the wall movement just before failure (Fig. 33 and Fig. 37) under different strut failure sequences (Fig. 39), implies that the strength of the soil and JGP layer have been fully mobilized depending on the wall lengths and soil models applied. The lower JGP layer also experiences a high relative shear stress.

The results concerning failure show consistency with the approach by Terzaghi (1943) and Eide et al. (1972) in assuming that failure occurs below the base of the wall and along the soil-wall interface. Moreover, the wall embedment not only alters the basal failure mechanism in the soil in these cases but also contributes to the stability due to potential flexural failure. The failure zone with the wall and soil is clearly seen in Fig. 43 and extends underneath the excavation level at different wall embedment depths. The failure behaviour of the wall and JGP layer is described with the Mohr-Coulomb criterion with tension cut-off in order.

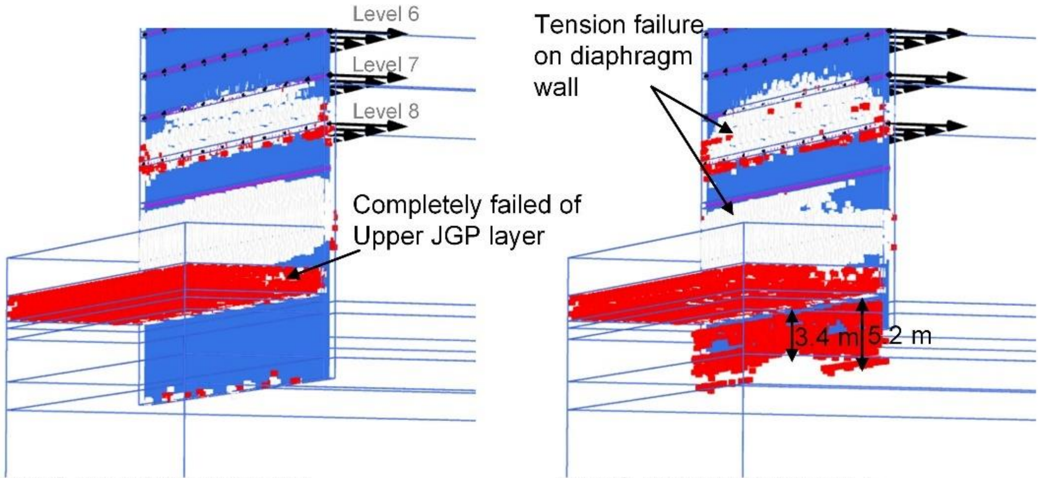

(a) HS model: Wall type: A **(b) HS model: Wall type: E**

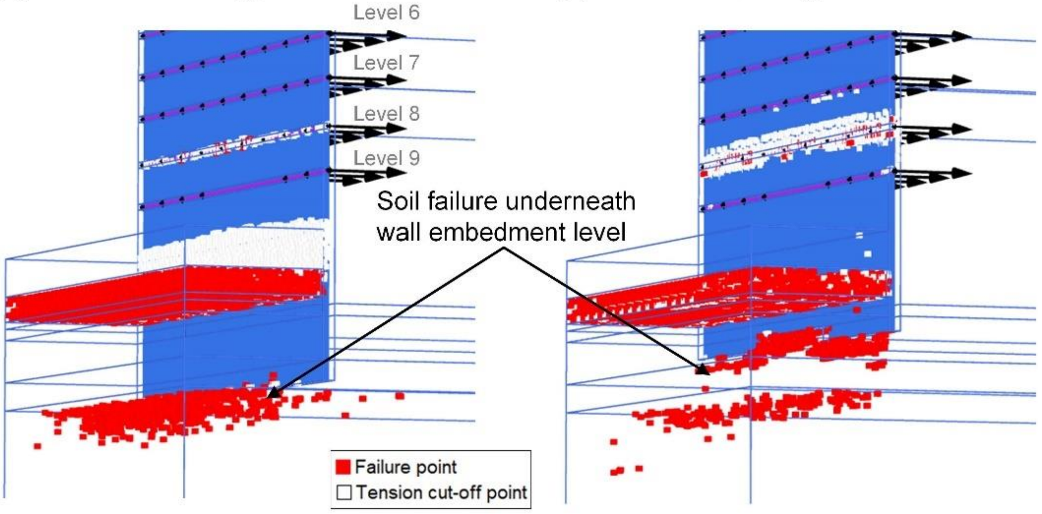

(c) HSS model: Wall type: A **(d) HSS model: Wall type: E**

Fig. 43: Plastic and tension cut-off point for soil and wall

Fig. 44 shows the effective stress paths of selected points (location indicated in Fig. 44) for wall depth scenarios A and E. Starting from in-situ stress assuming K_0 = 1, the effective stress path (i.e. the element *P1* for wall type A) moves initially vertically downwards and passive failure reaches depending on wall embedment depth scenarios. In the figure, the open symbol denotes the stress state of each soil element at the final level of excavation.

The soil at *P1* for shorter wall embedment depth (Wall type “E”), on the other hand, appears to have reached passive failure at excavation level 10 as indicated by the abrupt change of principal stresses direction. Rotation of the principal stress direction and reversal in the mean stress direction are observed in the HSS model, which occur throughout the passive side underneath the wall toe level (wall type “E”) as strut failure proceeds.

For soil element *P2* the stress state is much less pronounced in wall type “E”, while the analysis of reference wall type “A” appears to have reached passive failure when the last strut failed in both HS and HSS models (see Fig. 39). It also follows from Fig. 44 that a deep-seated failure is involved at deeper wall embedment depths after individual struts have failed (wall type “A”). As discussed previously, the HSS model requires less struts to fail in order to initiate overall failure, and the effective stress path for the HSS model reaches peak strength after the failure of strut level 9 (i.e. failure of the 12th strut, see Fig. 39).

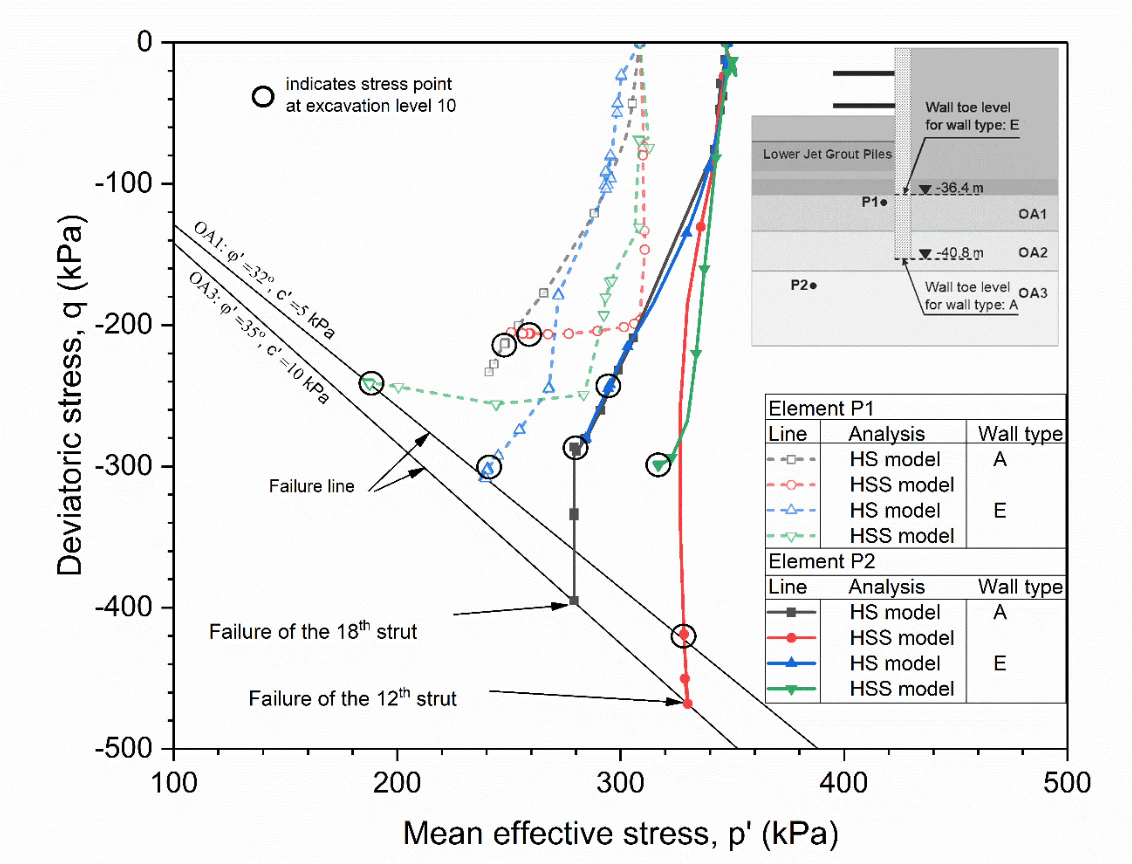

Fig. 44: Effective stress paths of selected elements for wall types A and E

4.6.6 Consequence of constitutive models adopted

In addition to HS and HSS models, the multilaminate model is employed in order to illustrate the influence of soil models on the progressive failure. The input parameters for the multilaminate model are shown in Tab. A 1. Calibrations of stress-strain curve for the multilaminate are shown in Fig. 22.

Fig. 45 compares strut forces at levels 7 and 8 with the general sequential failure of individual strut at level 9 (see Fig. 32). The analysis employing the HS and multilaminate models reveals similar load transferring mechanisms. However, it is noted that the multilaminate model predicts failure when the failure of the 9th strut of strut level 9 has been reached whereas the HSS model equilibrium can still be achieved.

Fig. 46 compares wall displacements and bending moments. The deformations are just before the analysis failed to reach equilibrium and therefore only one strut is required to cause overall collapse, as indicated in the strut failure scheme depicted in Fig. 47.

The normalized out-of-plane bending moment in the wall is shown in Fig. 47 together with the assumed failed struts for each particular case. For both general and refined failure schemes, the multilaminate model requires less struts to fail in order to initiate overall failure. Fig. 48 compares accumulated shear strains before reaching failure under the general failure scheme of struts (Fig. 32a). Strain localisation starts from underneath the wall toe and rises to the surface. The narrow zone is concentrated which is observed in the multilaminate model (Fig. 48c). Again, it is emphasised that the modification of the flow rule in the multilaminate model has a significant influence on predictions of undrained shear strength (see Fig. 22) and reflects the stress path followed prior to the failure in question (Fig. 49).

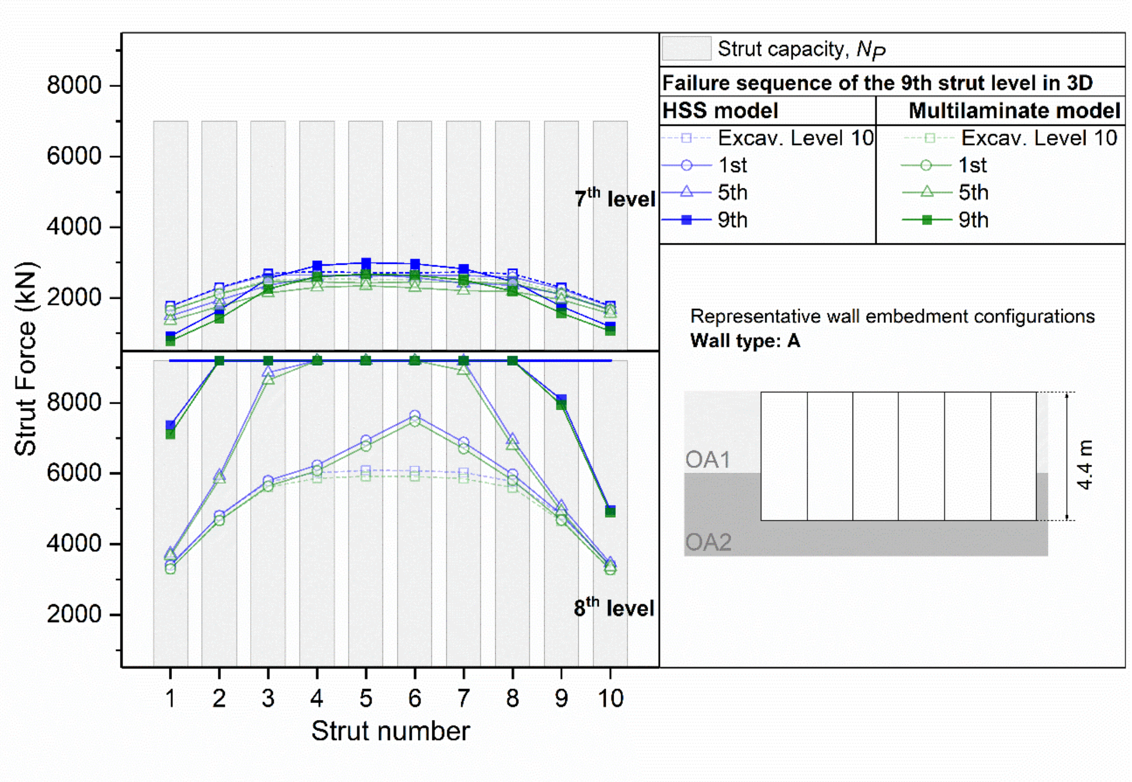

Fig. 45: Comparison of HSS and Multilaminate models for load distribution of general failure sequence of struts at 9th strut level

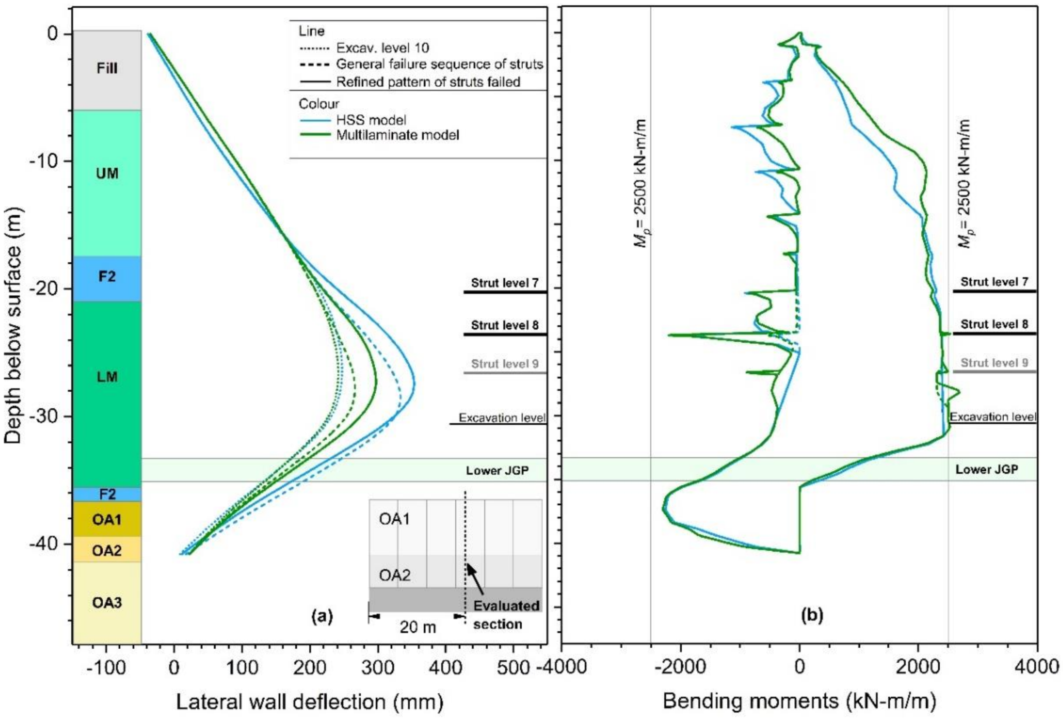

Fig. 46: Comparison of HSS and Multilaminate models: (a) effects of strut failure scheme on lateral wall deflection; (b) computed bending moments for "General failure sequence of struts"

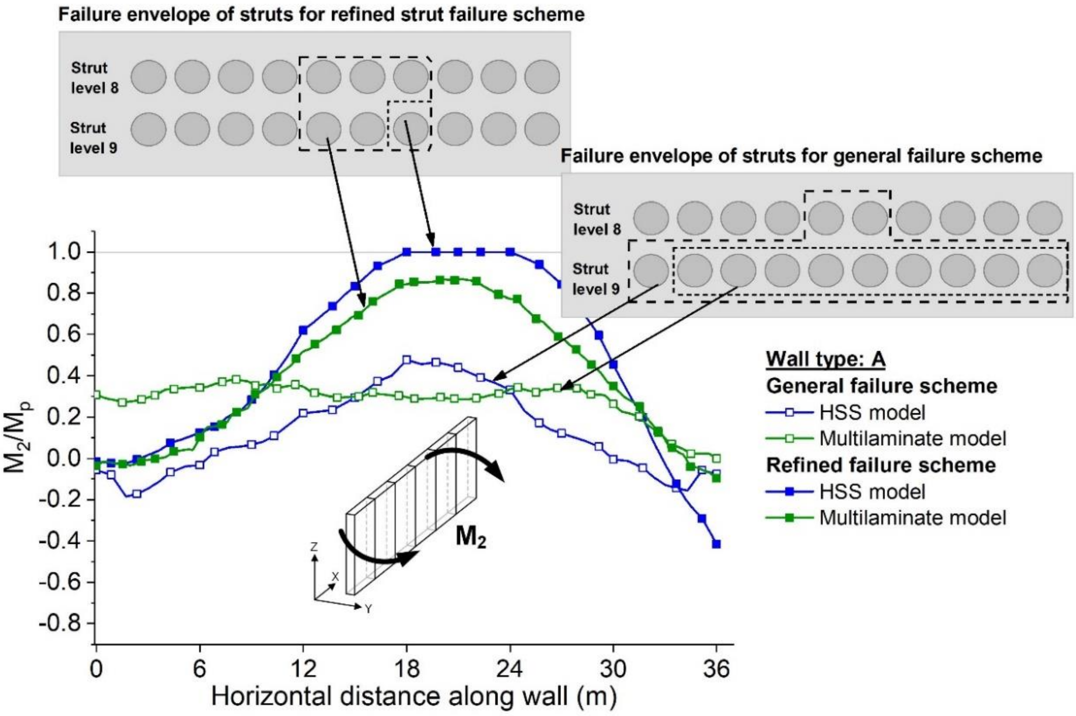

Fig. 47: Comparison of HSS and Multilaminate models for the effect of strut failure scheme on out-of-plane bending moments

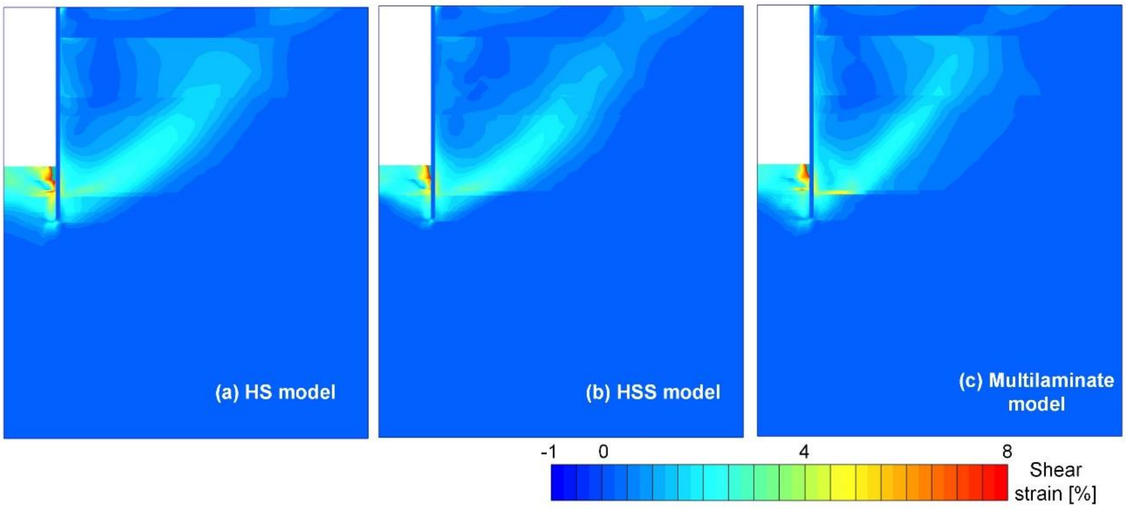

Fig. 48: Shear strains before failure for wall type “A”

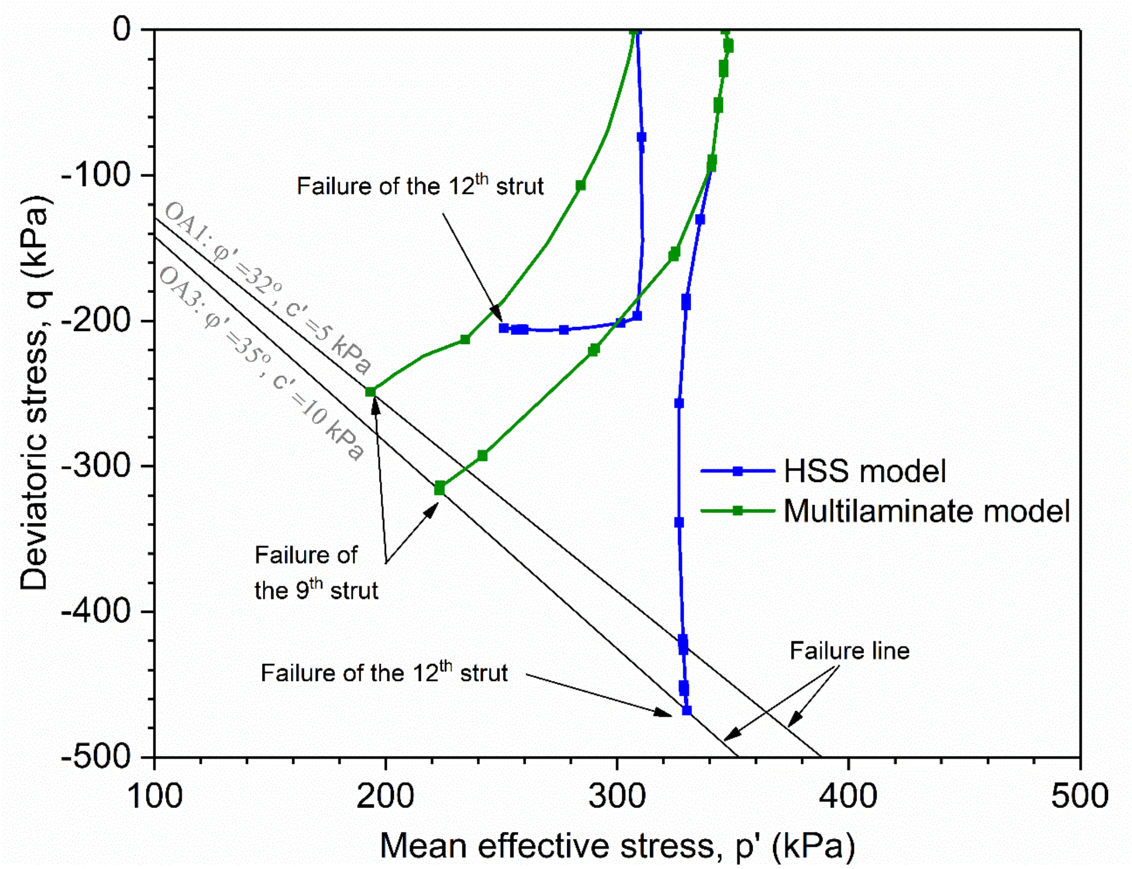

Fig. 49: Comparison of stress paths at P1 and P2

4.7 Summary and discussion

Analyses of a deep excavation in marine clay supported by a diaphragm wall and multiple layers of struts by means of the finite element method have been presented. The chapter addresses the consequences of construction imperfections, such as an insufficient embedment depth of the wall in combination with the failure of individual struts. This requires a full 3D analysis and it can be shown, for the particular example investigated in this study, that a significant stress redistribution capacity is available, and a number of struts may fail without causing the entire excavation to collapse. However, this is of course strongly dependent on the embedment depth of the wall. The importance of the constitutive model when performing an undrained analysis in terms of effective stresses has been emphasized. The main conclusions can be summarized as follows.

With the investigated wall embedment scenarios, continuous sequential failure of individual struts leads to the formation of plastic hinges in the wall near final excavation level and to an overloading of neighbouring struts, eventually causing failure. As expected, shorter wall embedment increases the load redistribution in struts, as well as reducing the number of individual struts which may fail without causing collapse of the entire system. In 2D plane strain analyses only entire layers of struts can fail and only redistribution in the vertical direction is possible. This is of course not realistic. This may lead to a more conservative design. Pre-failure deformations are less influenced by embedment length

Two different scenarios to account for strut failure in the analyses have been considered. In the reference case individual struts have been removed one by one based on a predefined sequence, even if neighbouring struts have reached their limiting capacity simulating a “ductile” behaviour. In the second case, neighbouring struts which have reached their capacity are removed from the system immediately, simulating a “brittle” behaviour. It clearly follows that these modelling assumptions lead to different results, the latter being more critical.

5 Excavation supported by Mixed-in-Place columns

5.1 Introduction

The use of mixed-in-place (MIP) columns for supporting excavations is an attractive alternative to more common retaining structures using sheet piles, diaphragms or bored pile walls, even when it comes to difficult ground conditions (e.g. Briaud et al. 2000, Poh & Wong 1998, Shao et al. 2005, Wang et al. 2018, Ignat et al. 2016, Poh & Wong 2001). For simplicity, the elastic-perfectly plastic Mohr-Coulomb failure criterion is often used in practice (see e.g. O'Rourke & McGinn 2006, Ignat et al. 2016, Wang et al. 2018, Liu et al. 2018), although more advanced models describing the mechanical behaviour of cement-treated soils have been presented in the literature (e.g. Arroyo et al. 2012, Schütz et al. 2011). A shortcoming of the standard elastoplastic model lies in the fact that they are unable to reproduce strain-softening behaviour of cement mixed soils, which occurs after the material has reached peak strength. However, in excavation work, the shear strain is generally less than about 0.1% (Atkinson & Sallfors 1991, see Fig. 11) and this could limit the soil-cement material from reaching the peak strength value.

In this chapter the results from a numerical study based on a case history are presented. The special feature of the project concerned is that ground anchors were not allowed to be installed as an additional support measure within the neighbouring ground. Thus, an arch including panels and buttresses was constructed by in-situ deep mixing in order to cope with the lateral earth pressure exerted by the soil in sloping ground conditions, as illustrated in Fig. 50. The project description has been presented in detail by Lüftenegger et al. (2013), Marte et al. (2017) and Marte et al. (2019). In general, although a reinforcement steel bar was placed in the centre of some of the columns in order to achieve ductile behaviour, the structural system remains rather brittle (see Fig. 50b). It is, therefore, necessary to take into account the brittle behaviour by also considering post peak behaviour, i.e. modelling of strain softening in tension and compression, in particular when the structural performance is dominated by crack initiation.

In recent years, much effort has gone into studying the post-peak behaviour of cement-treated soil, such as jet grouting, cement-treated soil and mixed-in-place columns considering tension softening. For example Larsson et al. (2012) and Lee (2014) studied the mechanical behaviour of cement-treated soil in experiments and full-scale excavations by means of numerical analysis. These results showed that their model captures the stress-strain relationship including the post peak behaviour. It was shown that qualitatively realistic crack patterns were predicted depending on the assumed value for the fracture energy in tension (G_t).

In this study a constitutive model for concrete-like material, originally developed by Schädlich & Schweiger (2014) for modelling the time-dependent behaviour of shotcrete for tunnelling applications, was employed for the mixed-in-place columns. The model is implemented in the finite element code Plaxis (Brinkgreve, et al. 2017) which is used for all analyses presented in this chapter. The most important features of this model relevant for the application and validation discussed in this chapter are presented in subsequent sections. The model has been successfully applied to tunnelling problems, for modelling the behaviour of jet grout slabs in the context of deep excavations (Schweiger et al. 2014, Schweiger et al. 2015, Schweiger et al. 2017), to investigate the possible crack zones in jet-grout columns when subjected to earthquake loading (Sedighi, et al. 2017) and to numerical simulation of anchor load tests where the development of cracks in the grouted body was of interest (Fabris et al. 2018). Hence, three-dimensional FE analyses are performed to investigate the behaviour of an excavation situated in a slope, supported by MIP-columns. The influence of geometrical factors (i.e. the length and number of columns) is investigated, as well as the influence of certain material parameters. Emphasis is placed on the development of crack patterns in the columns during excavation. Before discussing the results in more detail, the geometric layout of the problem, including ground conditions, is provided together with a short description of the constitutive model employed for modelling the MIP-columns.

5.2 Project description and FE-model

A detailed description of the project for this numerical study is given by Lüftenegger et al. (2013) and Marte et al. (2017). Nevertheless, the structural layout was simplified and only a representative section of the structure is analysed for the purpose of a systematic parametric study. Hence, there is no comparison between in-situ measurements and numerical simulations, and actually a comprehensive monitoring has not been performed for this project. The mixed-in-place columns form an arch of 6-m span resting on supporting wall panels oriented in the direction of the slope. The inclination of the slope is 20° for all layers. The geological conditions consist of three layers of soft (upper), medium stiff (middle), and stiff to very stiff sandy silt (lower).

A very fine mesh is required in order to obtain a reliable stress distribution and to capture the development of cracks in the columns with progressing excavation. The geometric layout, the finite element mesh (using 10-noded tetrahedrons), the simplified soil profile and the structural layout with details of the MIP structure are shown in Fig. 51 and Fig. 52, respectively. The analysis was performed as follows: starting from the in-situ slope geometry wall installation was considered as wished-in-place, and excavation down to 7 m was performed in 1 m steps.

The Hardening Soil model with small strain stiffness as implemented in the finite element code Plaxis (Brinkgreve et al. 2017) was employed to model the behaviour of the soil layers with parameters as tabulated in Tab. 4. The parameters have been determined based on the soil investigation performed for the actual project and have been taken from Lüftenegger et al. (2013). These are not discussed further in this chapter because the emphasis is on the behaviour of the MIP-columns. It is noted that the unsaturated unit weights are on the high side, but they are for a relatively high water content. Moreover, the groundwater table is in reality just below the excavation level and has not been considered in this study because the key aspect is the slope and there is no continuous water table present. The values have been taken from the report of the original project. Thus, all analyses were performed in drained conditions.

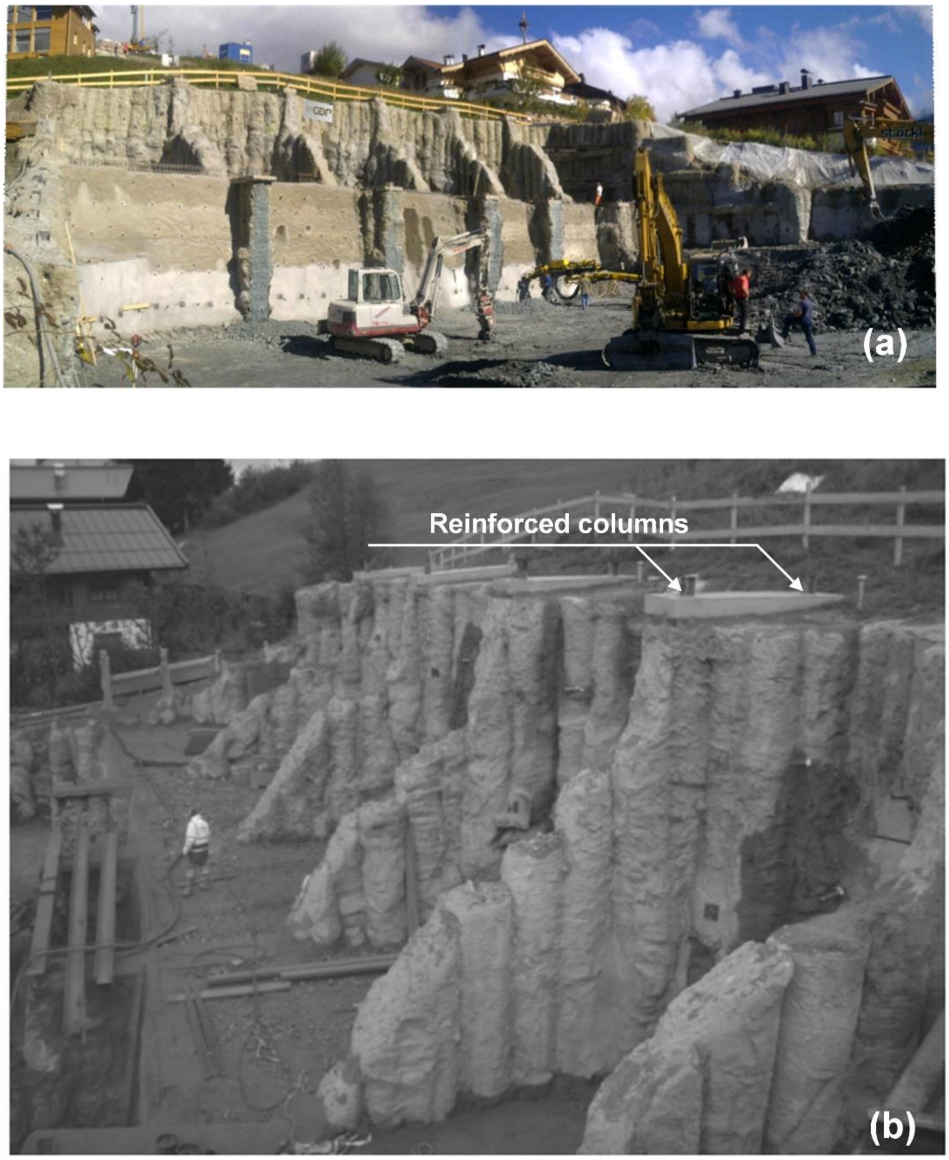

Fig. 50: Structural support system of case history (after Marte et al. 2017)

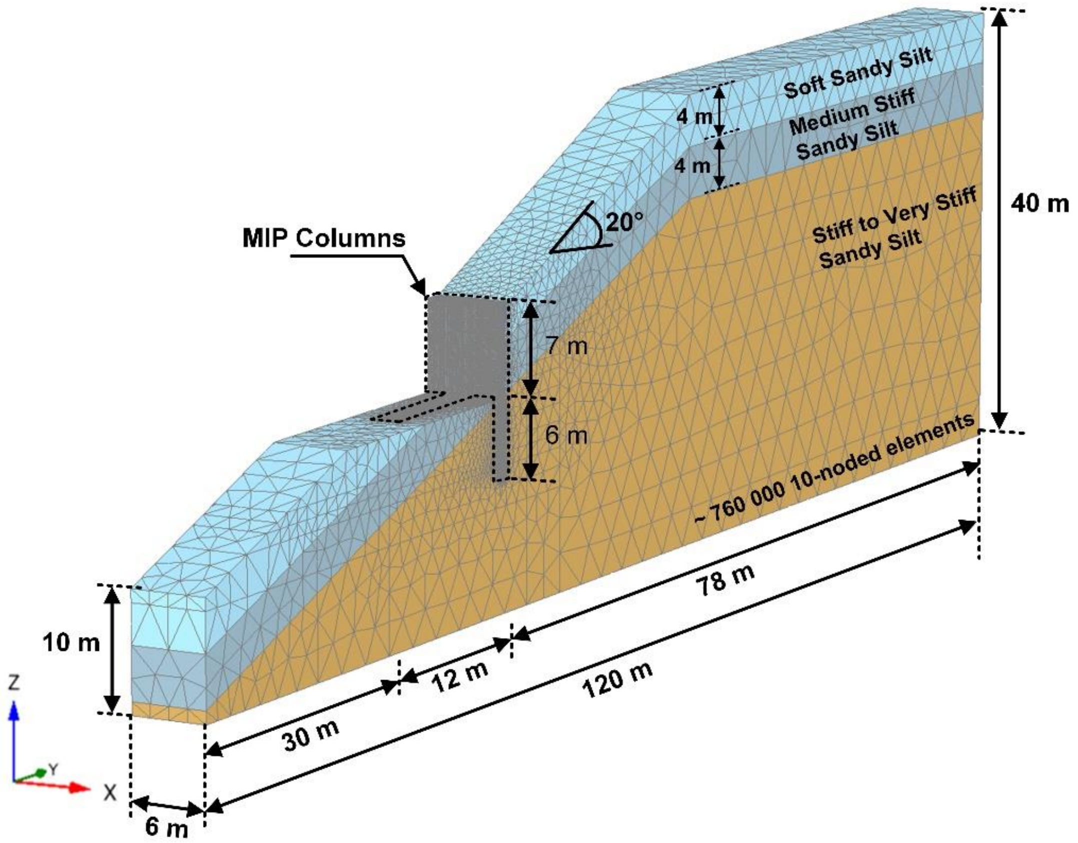

Fig. 51: Schematic view of the wall geometry

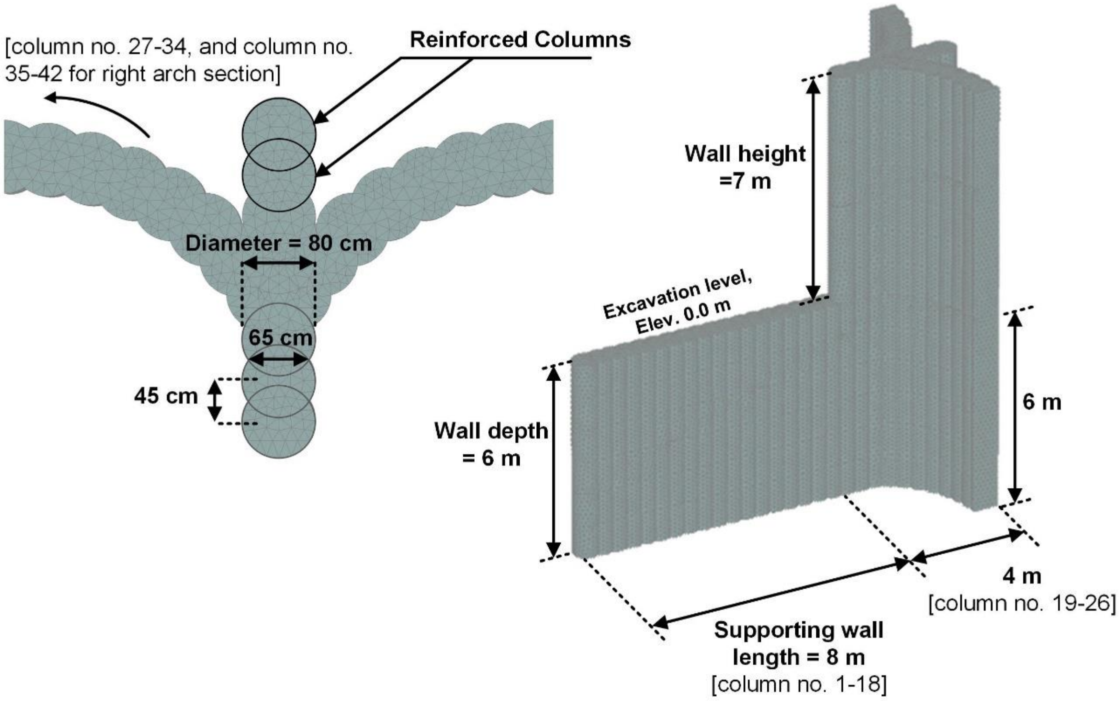

Fig. 52: Wall configuration with details

Tab. 4: Input parameters for soil layers

Parameter	Unit	Soft Sandy Silt (Upper)	Medium Stiff Sandy Silt (Middle)	Stiff to Very Stiff Sandy Silt (Lower)
γ_{unsat}	[kN/m³]	20	20.5	21
E_{50}^{ref}	[MN/m²]	10	25	45
σ_{ref}	[kN/m²]	100	100	100
E_{oed}^{ref}	[MN/m²]	10	25	45
E_{ur}^{ref}	[MN/m²]	30	75	135
m	[-]	0.5	1.0	1.0
c'	[kN/m²]	0	1	5
φ'	[°]	25	27.5	30
ψ'	[°]	0.0	0.0	0.0
ν_{ur}	[-]	0.2	0.2	0.2
K_0^{nc}	[-]	0.58	0.54	0.5
G_0^{ref}	[MN/m²]	62.5	156.25	281.25
$\gamma_{0.7}$	[-]	1.5E-04	1.5E-04	1.5E-04

5.3 Constitutive model used for MIP walls

The constitutive model employed for modelling the behaviour of the MIP-columns (referred to as the concrete model in the following), was originally developed to model shotcrete linings in tunnelling, as explained in detail in Schädlich & Schweiger (2014) and only a brief summary is given for continuity. The model is capable of incorporating the increase in stiffness and strength over time, strain hardening and softening in compression and tension, and creep and shrinkage. As the emphasis in this study is on the evaluation of the development of cracks in the MIP-columns with progressing excavation, the time dependent behaviour is switched off because the columns can be considered as cured when excavation was started.

The model is formulated in the framework of strain hardening/softening elastoplasticity. The total strain ε comprises of elastic strain ε^e, plastic strain ε^p, creep strain ε^{cr}, and shrinkage strain ε^{shr}, as illustrated in Equation 13.

$$\varepsilon = \varepsilon^e + \varepsilon^p + \varepsilon^{cr} + \varepsilon^{shr} \tag{13}$$

Plastic strains are calculated according to strain hardening/softening elastoplasticity. The model employs a Mohr-Coulomb yield surface F_c for deviatoric loading and a Rankine yield surface F_t in the tensile regime (Fig. 53). Constant values of φ_{max} = 30° and ψ_{max} = 0° are employed in this study.

Strain hardening in compression follows a quadratic function up to peak strength f_c, with subsequent bi-linear softening, governed by a normalised hardening/softening parameter $H_c = \varepsilon_3^p / \varepsilon_{cp}^p$, where ε_3^p = minor plastic strain, and ε_{cp}^p = minor plastic strain at peak in uniaxial compression Fig. 54a). Full mobilization of f_c coincides with H_c = 1, after which linear softening takes place corresponding to the fracture energy in compression G_c, failure strength is reached at H_{cf}. The softening rate is governed by the fracture energy G_c, which is used within a smeared approach to ensure mesh independent results.

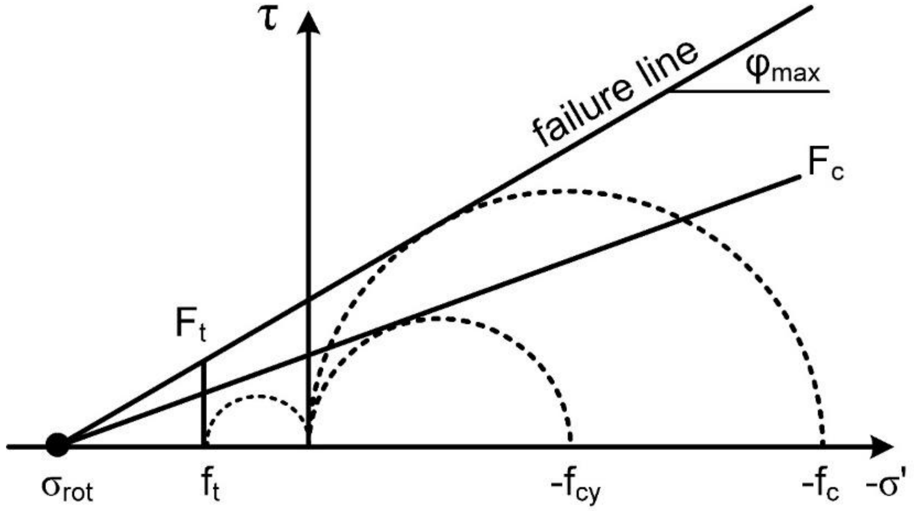

Fig. 53: Yield surfaces and failure envelope (Schädlich & Schweiger 2014)

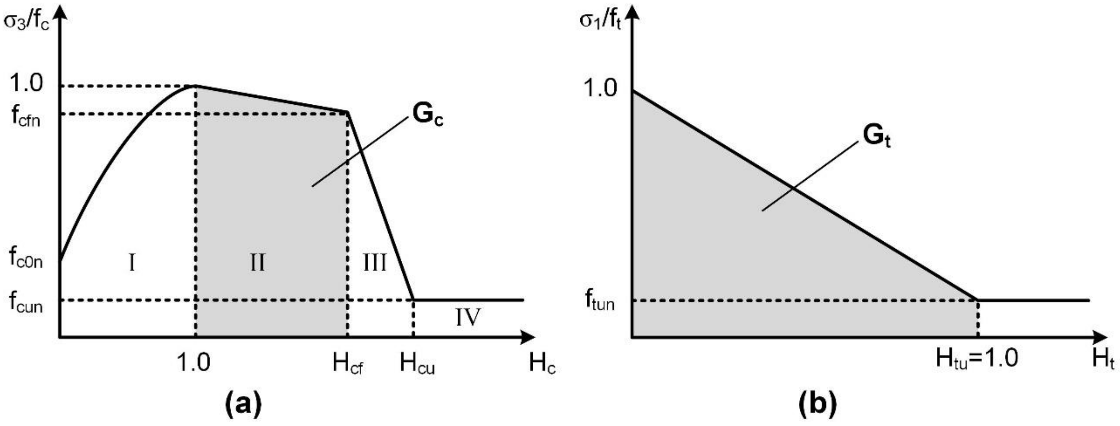

Fig. 54: Normalised stress-strain curve: (a) in compression and (b) in tension (modified from Schädlich & Schweiger 2014)

The model behaviour in tension is linear elastic until the tensile strength f_t is reached. Linear strain softening follows, governed by the normalised tension softening parameter $H_t = \varepsilon_1^p / \varepsilon_{tu}^p$, where ε_1^p = major principal plastic strain, and ε_{tu}^p = plastic ultimate strain in uniaxial tension (Fig. 54b).

$$f_{ty} = f_t \cdot (1 + (f_{tun} - 1) \cdot H_t) \tag{14}$$

ε_{tu}^p is derived from the fracture energy in tension, G_t and the characteristic length of the finite element, L_{eq}, which provides the necessary regularization to avoid mesh dependency in the numerical results. L_{eq} is calculated from the size of the finite element, A_{el}, and the number of stress points per element, n_{GP} (Pölling 2000).

$$\varepsilon_{tu}^p = \frac{2 \cdot G_t}{(1 + f_{tun}) \cdot f_t \cdot L_{eq}} \tag{15}$$

$$L_{eq} = 2\sqrt{\frac{A_{el}}{\sqrt{3} \cdot n_{GP}}} \tag{16}$$

Once the residual strength, $f_{tu} = f_{tun} \cdot f_t$, is reached, no further softening takes place. A state variable H_t is introduced indicating the state of tensile stresses and cracking. H_t is equal to 0, which means that value of the tensile stress is below or equal to F_t, $0 < H_t < 1$ describes the softening zone, and $H_t > 1$ indicates the residual level.

The material parameters used in this study are listed in Tab. 5. As for this project, no experimental data have been available for the MIP-columns and, therefore, reasonable strength and stiffness parameters based on experience have been assumed. However, Dik (2017) studied the behaviour of steel beam reinforced cement-treated soil by means of finite element investigations and compared the results with a real-scale three-point bending test, as reported by Denies et al. (2014) and Denies et al. (2015). The results showed that the variations of tensile fracture energy followed approximately linearly with tensile strength, as depicted in Fig. 55.

One of the most important parameters for this type of analysis involves the fracture energy in tension and compression, G_t and G_c respectively, whereas G_t is of major importance. The values of tensile fracture energy are small, even for high cement-soil ratios, because this value is affected by the maximum aggregate size and usually ranges from 7 to 45 N/m as summarized in Tab. 6 (Namikawa & Koseki 2006, Tariq & Maki 2014). For comparison, values with cement-treated Singapore marine clay are also listed in Tab. 6 (Lee 2014). The value chosen for the reference analysis in this study is 10 N/m, but it is varied to highlight the influence of this parameter.

As indicated in Fig. 52, some columns have been reinforced by a steel bar placed in the centre of the column along the entire length of individual column. In order to account for this in a simplified manner, the tensile strength of these columns has been increased (see Tab. 5) but the reinforcing bar is not explicitly modelled as a structural element. In addition, the value for fracture energy G_t is not increased because firstly it would have been difficult to choose a correct value and secondly it is argued that with increasing tensile strength, the post peak behaviour becomes less crucial. It should be emphasized again that the purpose of this study is to investigate the behaviour of MIP-columns when used as supporting elements in excavations in some detail and not to analyse the case history, which serves as a basis for these analyses. Therefore, it is not important that the properties of the MIP-columns are based on experience and do not strictly correspond to the properties of the columns constructed for the actual project. For comparison reasons, some analyses have been performed employing the elastic-perfectly plastic Mohr-Coulomb constitutive model for the MIP-columns.

Tab. 5: Input parameter for MIP wall

Parameter			Concrete model	
Description		Unit	Wall	Reinforced columns
Unit weight	γ	[kN/m^3]	22	22
Young's modulus of cured MIP	E_{28}	[kPa]	300 000	300 000
Poisson's ratio	ν	[-]	0.15	0.15
Uniaxial compressive strength	$f_{c,28}$	[kPa]	1 200	1 200
Uniaxial tensile strength	$f_{t,28}$	[kPa]	125	600
Dilatancy angle	ψ_{max}	[°]	0	0
Normalised initially mobilised strength	f_{c0n}	[-]	0.15	0.15
Normalised failure strength (compression)	f_{cfn}	[-]	0.95	0.95
Normalised residual strength (compression)	f_{cun}	[-]	0.1	0.1
Uniaxial plastic failure strain	ε_{cp}^{p}	[-]	-0.0035	-0.0035
Compressive fracture energy	$G_{c,28}$	[kN/m]	30	30
Normalised residual tensile strength	f_{tun}	[-]	0.05	0.05
Tensile fracture energy	$G_{t,28}$	[kN/m]	0.01	0.01
Maximum friction angle	φ_{max}	[°]	30	30

Note: Input parameter for MC model: γ = 22 kN/m^3, E = 300 000 kPa, ν = 0.15, c'= 350 kPa, φ'= 30°, tension cut-off = 125 and 600 kPa for general and reinforced columns, respectively.

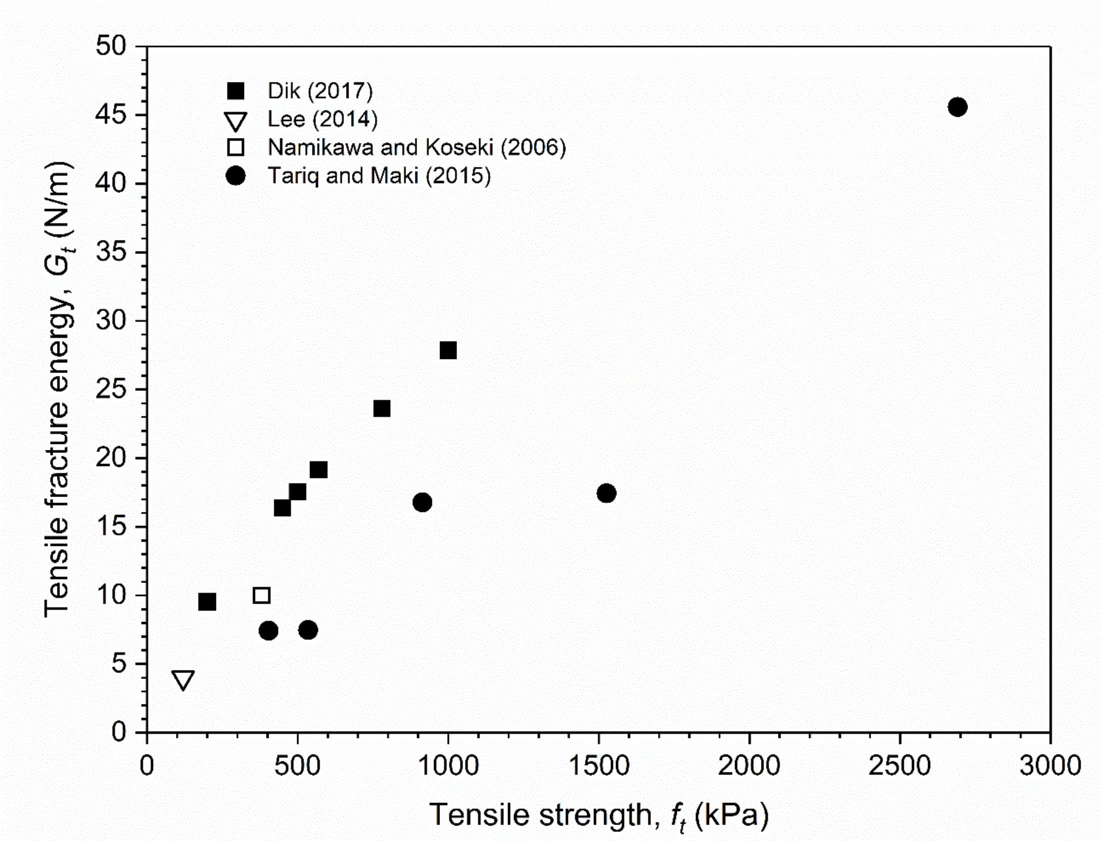

Fig. 55: Variations of tensile fracture energy with tensile strength

Tab. 6: Tensile fracture energy for cement-treated soil from a three-point bending notched beam test

Cement treated soil	G_t (N/m)	f_t (kPa)*	C_S	W_C	*w/d/l*	Reference
Sandy loam	9.5†-23.6†	200-1000	3-10	0.6-1.2	60/120/430	Dik (2017)
Singapore marine clay	2.6-4.4	120	25-35	0.6	5/5/20	Lee (2014)
Toyoura sand	9.3-12	380	15	1.9	4/4/16	Namikawa & Koseki (2006)
Uniformly graded sand	7.4-46	400-2600	30	1.0-1.9	10/10/40	Tariq & Maki (2014)

Note: C_S = cement-soil content (%), W_C = water-cement ratio; Size of specimen *w* = width; *d* = depth; and *l* = span length, unit in cm.
*Splitting tensile strength test.
†Back analysis of real-scale 3-point bending test on steel beam (HEA 240) reinforced cement-treated soil.

5.3.1 Constitutive model validation

The three-point bending test represents a typical method for determining the bending induced tensile stress and fracture of cement-treated soil as in concrete (see Tab. 6). A two-dimensional FE-analysis was conducted to investigate the influence of G_t on the strain-softening behaviour of cement-treated sand based on experiments by Namikawa & Koseki (2006). The finite element meshes, geometry, input parameters and results are shown in Fig. 56a. The analysis is performed displacement-controlled.

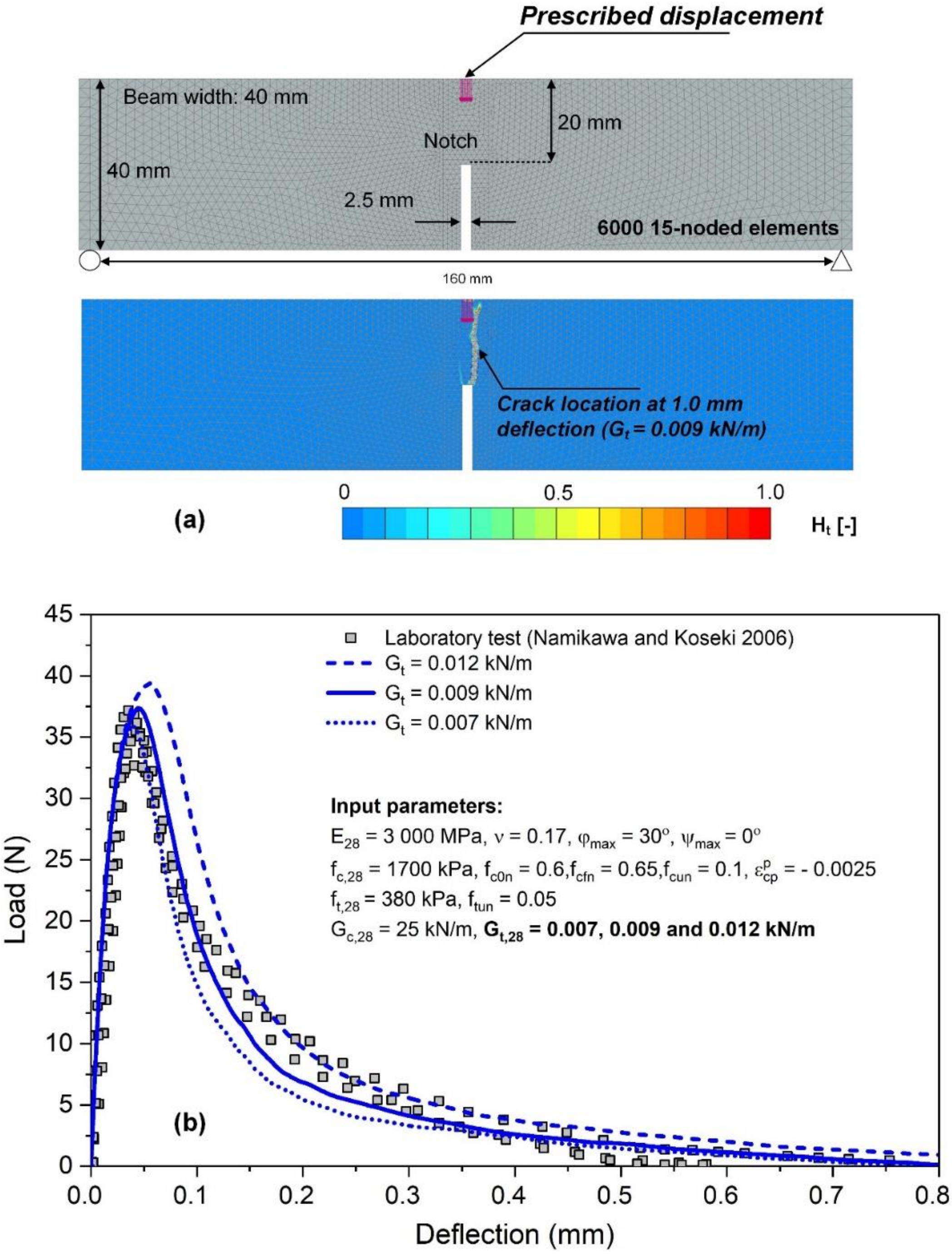

Fig. 56: Constitutive model validation: three-point bending test

The comparison of calculated load deflection curves with the experimental data is shown in Fig. 56b. The deflection was monitored at the bottom of the notched-beam using a laser type displacement transducer. It follows that the load-displacement behaviour agrees very well with the experiment. After reaching the peak load, the model is able to reflect the strain softening behaviour of cement-treated sand. Moreover, it is obvious that the softening regime is influenced by the value of G_t. Fig. 56a illustrates the contour plot of the tension softening parameter H_t which also indicates that cracks initiate correctly from the tip of the notch at 1.0 mm deflection.

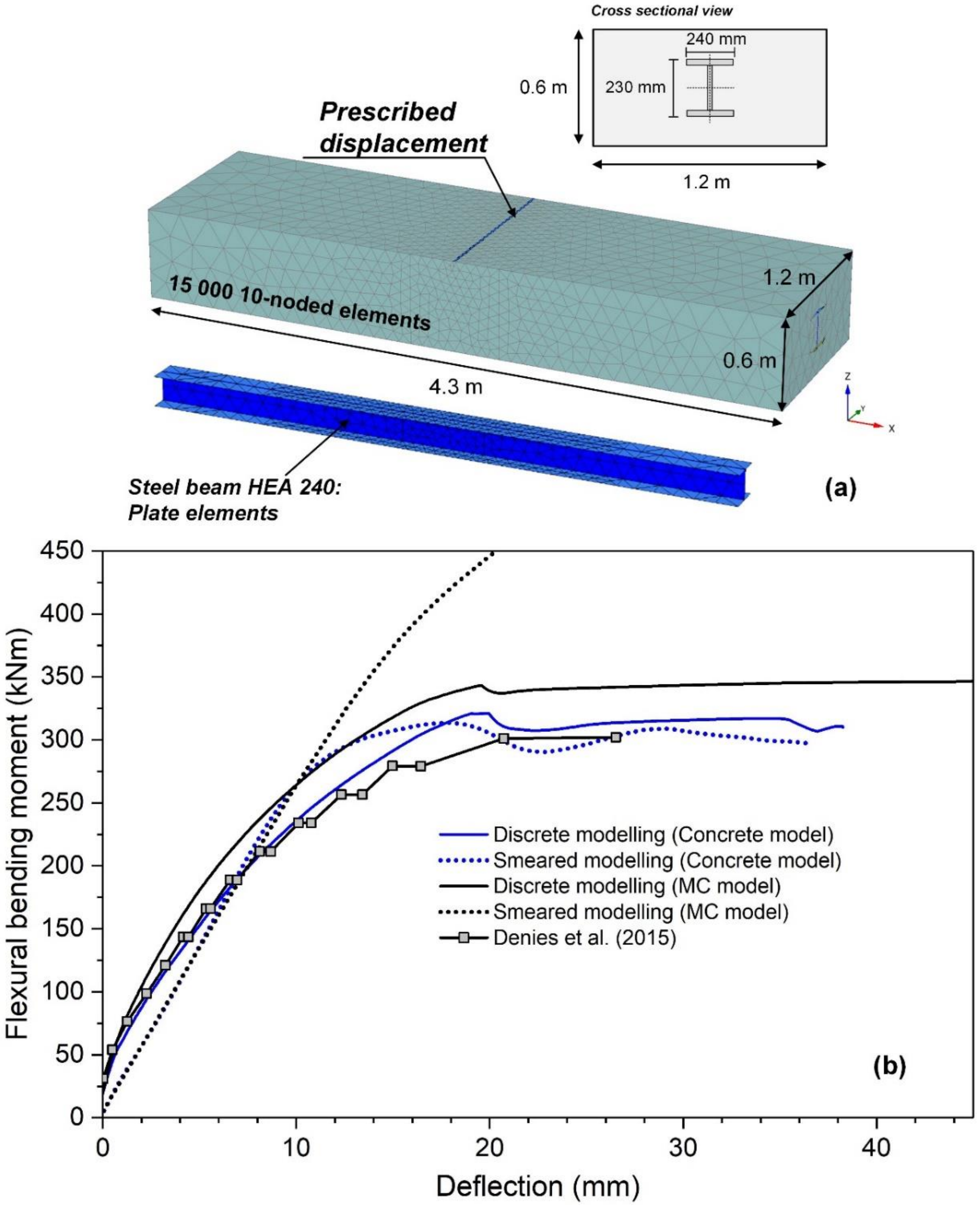

Fig. 57: Constitutive model validation: bending test of steel reinforced cement-treated soil

Tab. 7:Input parameters for investigation of reinforcement modelling

Parameter			Concrete model	
Description		Unit	Discrete model	Smeared model
Unit weight	γ	[kN/m^3]	20	20
Young's modulus of cured MIP	E_{28}	[MPa]	2 000*	2 000*
Poisson's ratio	ν	[-]	0.2	0.2
Uniaxial compressive strength	$f_{c,28}$	[kPa]	2 000*	1 2000
Uniaxial tensile strength	$f_{t,28}$	[kPa]	200*	4 200
Dilatancy angle	ψ_{max}	[°]	0	0
Normalised initially mobilised strength	f_{c0n}	[-]	0.15	0.15
Normalised failure strength (compression)	f_{cfn}	[-]	0.95	0.95
Normalised residual strength (compression)	f_{cun}	[-]	0.1	0.1
Uniaxial plastic failure strain	ε_{cp}^{p}	[-]	-0.002	-0.002
Compressive fracture energy	$G_{c,28}$	[kN/m]	30	30
Normalised residual tensile strength	f_{tun}	[-]	0.05	0.05
Tensile fracture energy	$G_{t,28}$	[kN/m]	0.016	0.01
Maximum friction angle	φ_{max}	[°]	30	30

Note: Input parameters for reinforced steel beam (HEA 240): E = 200 GPa, ν = 0.29, Yield stress = 235 MPa

*Selected parameter values are based on back-analysis of Dik (2017) and for steel reinforced cement-treated sand reported by Denies et al. (2014) and Denies et al. (2015)

As previously mentioned, there is no experimental data suitable for the properties of MIP-columns for the project and, therefore, reasonable strength and stiffness parameters based on experience have been assumed. In order to demonstrate the capability of the model with respect to modelling reinforced cement-treated soil, a 3D numerical simulation of a bending test was carried out and validated with a real-scale bending test conducted by Denies et al. (2014) and Denies et al. (2015).

Two different approaches for the modelling of reinforcement have been investigated, namely discrete modelling (i.e. modelled as a structural element) and the smeared approach. The input parameters are summarized in Tab. 7. A steel beam (HEA 240) was taken as reinforcement for the cement-sand mixture. Fig. 57a represents schematically the test setup, dimensions and finite element mesh. Again, prescribed displacements are used for simulating the bending test.

By modelling the reinforcement explicitly and adopting a fully bonded interface, the results show that using the concrete model accurately predicts the flexural bending moment capacity, whereas the MC model (φ' = 30° and c' = 550 kPa, tension cut-off = 250 kPa) overestimates the bending strength, approximately by 10% (Fig. 57b). If the smeared modelling approach is adopted the elastic-perfectly plastic MC model significantly overestimates the bending moment, whereas the concrete model still yields very reasonable results. It has to be mentioned that the compressive and tensile strengths of the beam in the smeared approach are calculated based on the condition that the steel is yielding and the ultimate compressive strain in the cement-treated soil is reached in the compression zone (i.e. strain compatibility condition, specified strain).

$$\sigma = \frac{M_{net}}{W_{smeared}} \leq f_{t,smeared} \tag{17}$$

where $M_{net} = 26.32\ kN/cm^2 \times 38\ cm^2 \times 0.3\ m\ \approx 300\ kNm$

$\mathrm{W}_{\mathrm{smeared}} = bh^2/6 = 0.072\ m^3$

$f_{t,smeared} \approx\ 4\,200\ kN/m^2$

Based on these results it seems justified to adopt the smeared approach for taking into account the reinforcement, present only in a limited number of columns, for this investigation.

5.4 Results and discussions

5.4.1 Reference geometry

The investigated parameter combinations are summarized in Tab. 8. The material sets include different values for the tensile strength (f_t) and different values for the tensile fracture energy (G_t). The analyses for set A account for a higher tensile strength in the reinforced columns and a variation in G_t. The analyses for set B represent cases when the columns are not reinforced. It should be noted that the smeared approached is used for reinforcement modelling in both cases.

Fig. 58 shows the variations of tensile stresses and the progressive development of crack patterns for the case of High f_t, Low G_t. The distributions of tensile stresses along the reinforced column (location indicated in Fig. 58a) are indicated in a stepwise drop to residual from stage 6 to 7 (i.e. excavation depth of 6 m from top of the wall elevation down to final excavation stage at 7 m). In the final excavation stage (Stage 7) as illustrated in Fig. 58b, the tension crack (i.e. H_t > 1.0) occurs at the reinforced columns at around excavation level (indicated by zero wall elevation).

Tab. 8: Tensile strength and tensile fracture energy parameters for the analysis of reference geometry

Set	Cases	General columns		Reinforced columns		Remarks
		f_t (kPa)	G_t (kN/m)	f_t (kPa)	G_t (kN/m)	
A	High f_t, Low G_t	125	0.01	600	0.01	
	High f_t, High G_t	125	0.01	600	1.0	Reference analysis
	MC model	125	-	600	-	MC model
B	Low f_t, Low G_t	125	0.01	125	0.01	Less reinforcement

Note: The input parameter for the MC model is described in Tab. 5

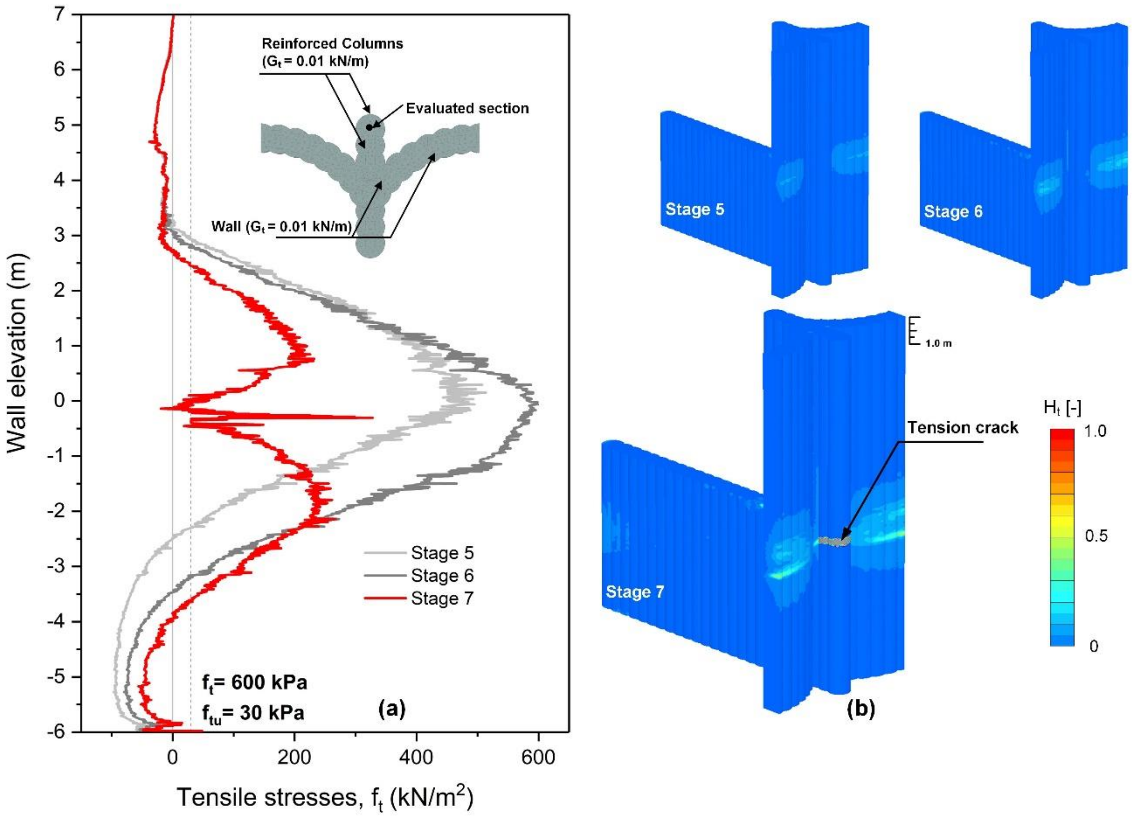

Fig. 58: Changes in tensile stresses and (b) the progressive development of crack patterns in the case of High f_t, Low G_t

Fig. 59a compares the lateral deflection of a column at the backside of the wall (location indicated in the figure) for three different analyses, namely employing the concrete model (for all columns), but with different values for the fracture energy G_t for the reinforced columns (High f_t, Low G_t and High f_t, High G_t) and the Mohr-Coulomb model. It follows that similar results are obtained with Mohr-Coulomb and the concrete model when G_t is large (behaviour is more ductile). This is to be expected because if the softening behaviour is not pronounced, the two models are similar when tension-cut off is activated in the Mohr-Coulomb model.

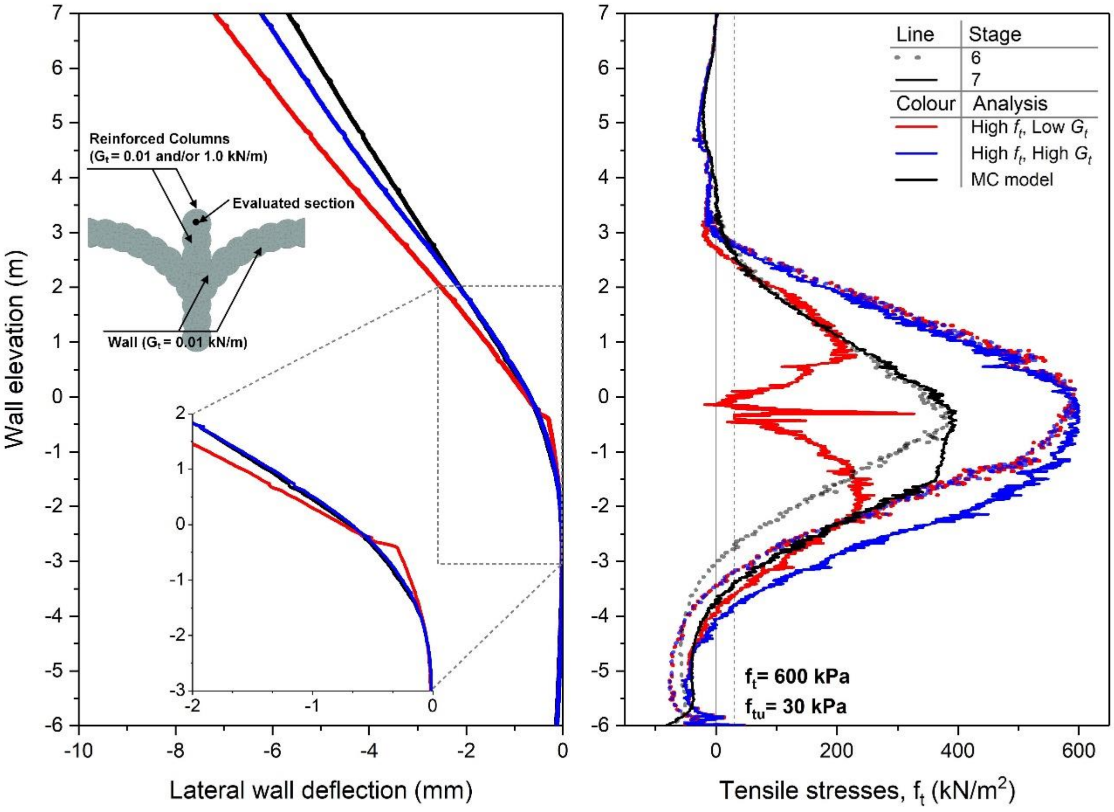

(a)

(b)

Fig. 59: Reference geometry: (a) lateral wall deflection and (b) calculated tensile stresses at the backside of the wall

The differences in lateral wall deflection become larger when the softening is more pronounced because the tensile stresses remain at the tension cut-off value and are not reduced to a residual value (f_{tu} = 30 kPa) in the MC model. In the case of small tensile fracture energy (i.e. G_t =0.01 kN/m, behaviour is more brittle), a kink in the deflection curve is obviously seen indicating that cracking has occurred in the column.

This is confirmed in Fig. 59b where a profile of tensile stresses along the column is plotted. The drop to zero in stress in the excavation stage from 6 to 7 for the analysis with G_t = 0.01 kN/m is obvious (High f_t, Low G_t). It could indicate that a significantly different stress distribution in the MIP wall is obtained, as compared to the situation when applying a simple Mohr-Coulomb failure criterion with tension cut-off for the wall, in particular when a brittle response is anticipated.

Additionally, it is apparent that these cracks increase the maximum displacement at the top of the wall, the overall stability, however, is still guaranteed. Although the mesh is very fine in this area, some stress oscillations are observed but it is argued that this does not affect the overall behaviour.

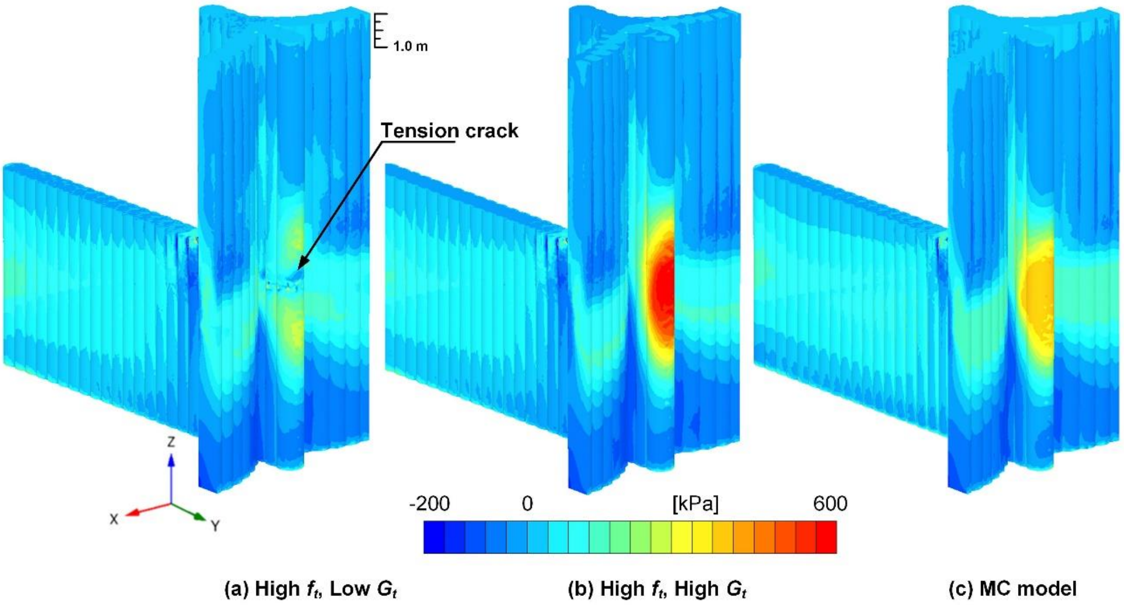

(a) High f_t, Low G_t (b) High f_t, High G_t (c) MC model

Fig. 60: Contour lines of principal tensile stresses (σ_3) of the MIP wall

This becomes more obvious if stresses in the MIP-columns are considered, which are subject to significant bending during excavation. Fig. 60 shows a contour plot of the principal stress σ_3, whereas only tensile stresses are shown after the final excavation stage. Again, it is clearly observed that the stress distribution is similar for Mohr-Coulomb and the concrete model with a high value for G_t. When applying the concrete model with a low G_t value tension cracking or hinge formation and subsequent strength reduction (i.e. zero tensile stresses) can be observed, approximately at the excavation level. Additionally, these cracks do not have a serious effect on the excavation side (Fig. 61) where compression softening does not occur (H_c < 1.0), although the contour plot of H_c indicates a strain concentration at the excavation level.

It should be mentioned that compression softening is governed by the value of the compressive fracture energy G_c, but this parameter has not been varied in this study. The failure in cement-treated soil could be influenced by the compressive strength. It is however argued that for the purposes of this study this aspect is less severe. The resulting tensile stresses along the column at the arch section of the wall are plotted in Fig. 62 and it follows that the different assumptions made for G_t for the reinforced columns do not have a significant influence on the stresses in these columns, at least not for the given geometrical configuration.

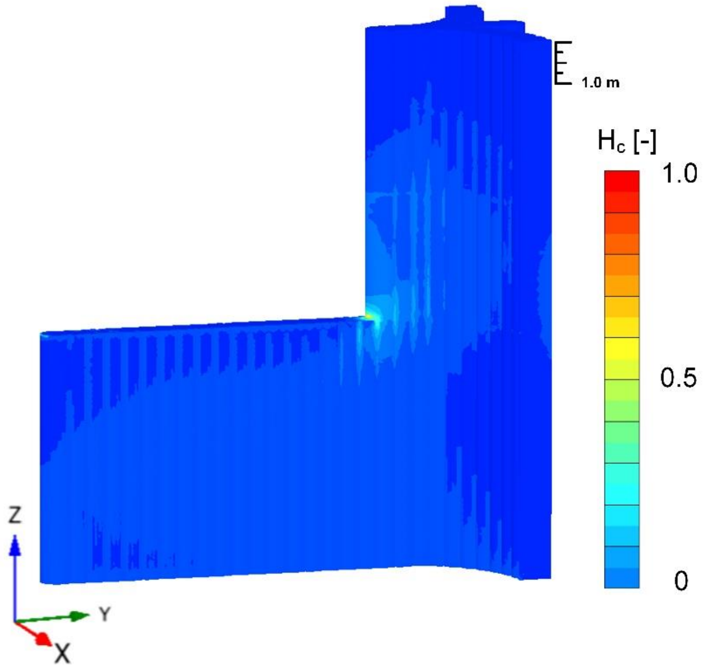

Fig. 61: Contour lines of H_c parameter in the case of High f_t, Low G_t ($H_c > 1.0$ indicates compression softening)

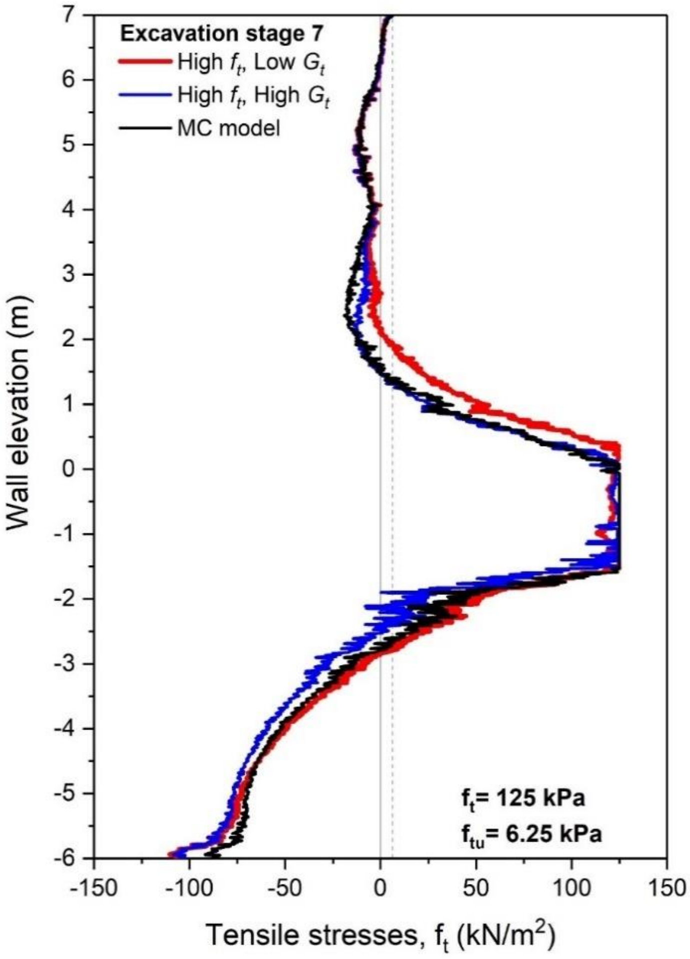

Fig. 62: Calculated tensile stresses at the arch section

Moreover, the reinforced columns with lower G_t appear to have cracks at the final excavation level. Hence, the stress redistributes to the arch section and, therefore, for the case with low G_t at reinforced columns, it shows slightly higher tensile stress (Fig. 62).

Fig. 63 and Fig. 64 show the effect of the reinforcement in the two columns on the backside of the wall. The analyses involve considering the softening and limiting tensile stresses to the tensile strength of 600 kPa and 125 kPa for the case of High f_t, Low G_t and Low f_t, Low G_t, respectively resulting in a significant tensile stress redistribution at the backside of the wall. The reduced tensile strength has only a minor influence on the increase in the lateral deflection of the column at the backside of the wall (Fig. 63).

A comparison of the calculated tensile stress between the cases of High f_t, Low G_t and Low f_t, Low G_t is made for excavation stages 5 to 7 and shown in Fig. 64. As expected, due to the lower tensile strength in reinforced columns they reach the limit strength at an early stage of the excavation (Stage 6, Fig. 64b) and this indicates that the missing reinforcement leads to a downward shift of the tensile stresses.

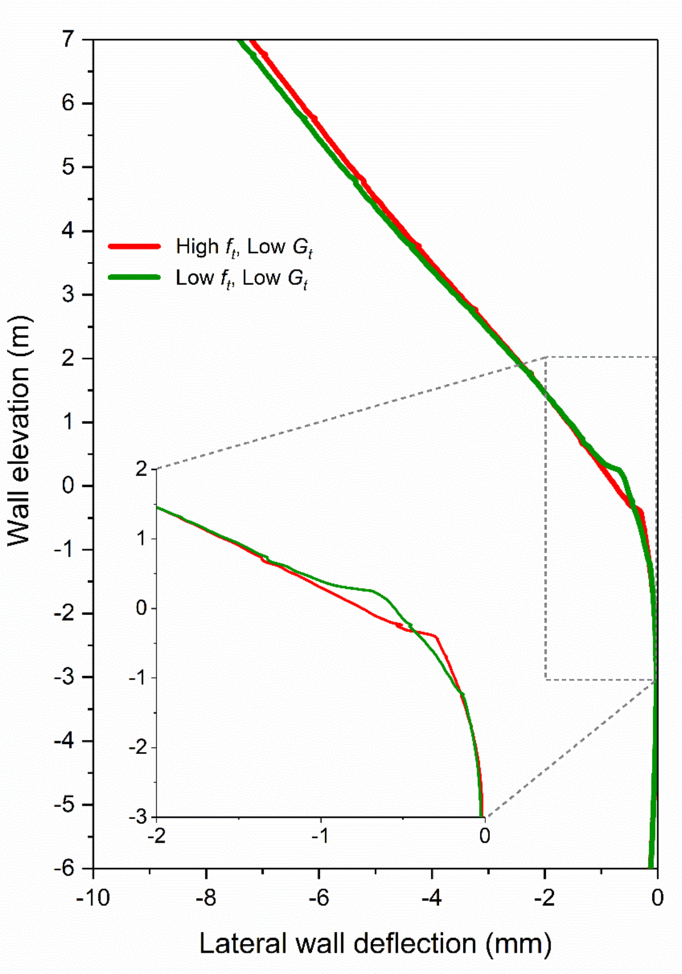

Fig. 63: Effect of the tensile strength of reinforced column on lateral wall deflection

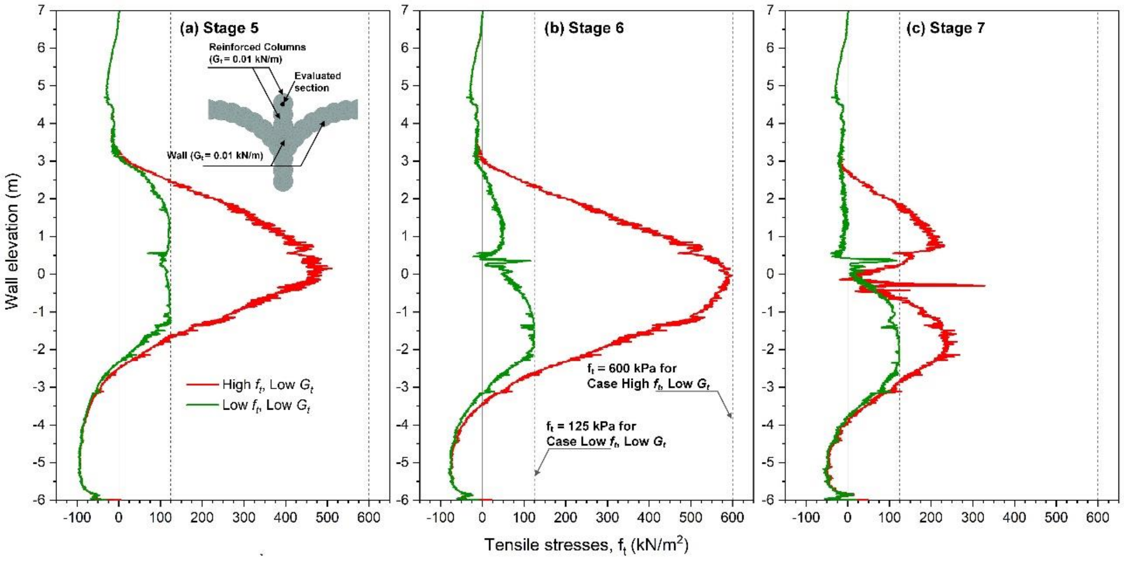

Fig. 64: Calculated tensile stresses for High f_t, Low G_t and Low f_t, Low G_t: (a) stage 5; (b) stage 6 and (c) stage 7

5.4.2 Influence of geometry

As mentioned in the previous section, the behaviour of MIP-columns is dominated by the tensile strength of the soil-cement mixed and by the bending resistance, in particular when the columns are not reinforced (i.e. brittle behaviour). In order to investigate the potential for the optimization of the layout of the MIP-columns, a study was performed varying the geometry of the support structure.

The reference geometry (wall type 1) is the one depicted in Fig. 52 and wall types 2 to 5 are shown in Fig. 65. It should be mentioned that wall type 1, adopted in the case history, is based on a conventional design without using numerical methods. It is the purpose of this study to explore by means of advanced numerical models whether a possible reduction in the volume of MIP-columns is possible without compromising the stability of the structure. Thus, the length of the columns at the arch has been reduced as a first step (wall type 2, Fig. 65a), then the columns of supporting walls have been removed (wall type 3, Fig. 65b). The combination of wall type 2 and 3 is shown in Fig. 65c and, finally, wall type 5 is presented in Fig. 65d which can be considered as extreme case.

Fig. 66 shows the lateral wall deflections with different types of wall. As expected, the horizontal wall deformations increase when reducing the dimensions of the support structure. Nevertheless, the analysis shows that it is possible to achieve equilibrium even with the worst-case scenario (wall type 5).

Fig. 67 illustrates the calculated tensile stresses at the reinforced column from excavation stages 5 to 7. At excavation stage 5 the maximum tensile strength is not reached for all geometries (Fig. 67a), but when excavation progresses, cracking starts to develop in some of the configurations (Fig. 67b) and for excavation stage 7 cracking is evident for all geometries (compare also Fig. 59 for the reference geometry). The resulting tensile stresses along the column at the arch section of the wall are not influenced by changes in the wall geometry, as illustrated in Fig. 68.

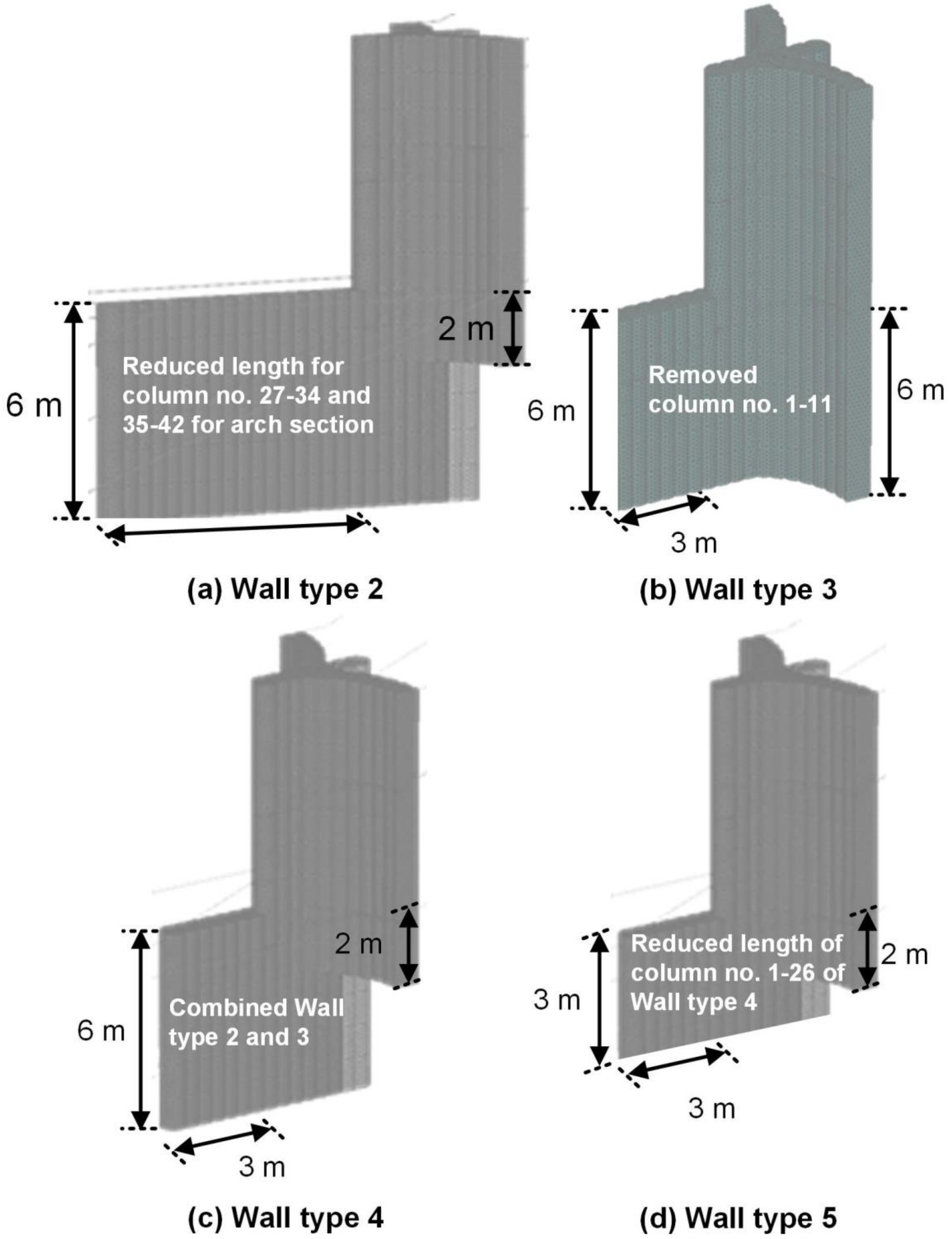

Fig. 65: Different wall type geometries

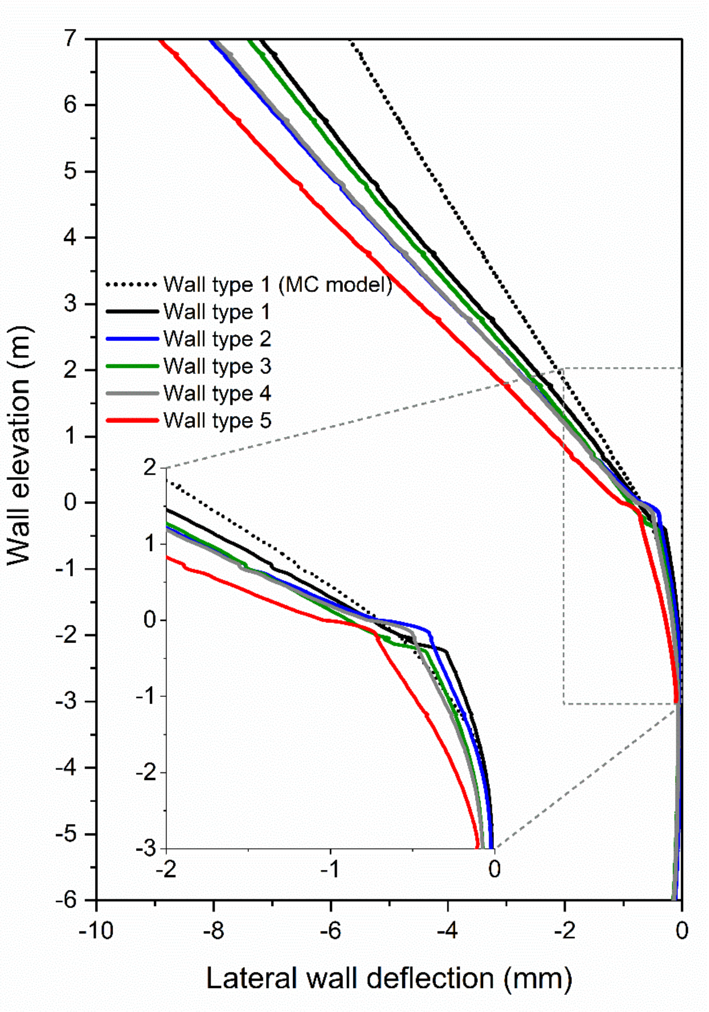

Fig. 66: Lateral wall deflection for different types of wall

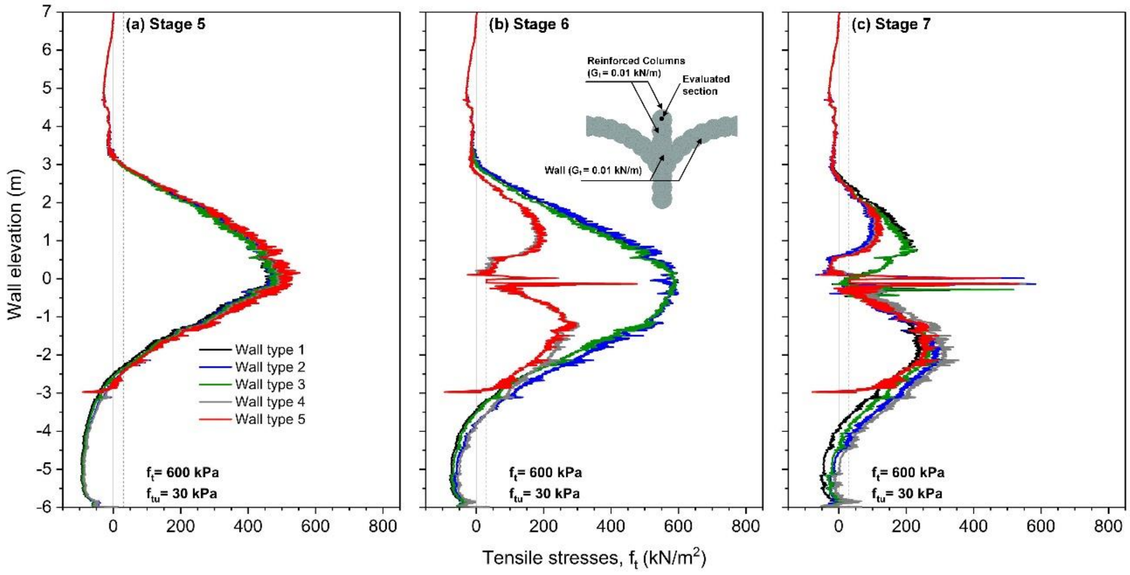

Fig. 67: Calculated tensile stresses for different types of walls at reinforced column: (a) stage 5; (b) stage 6 (c) stage 7

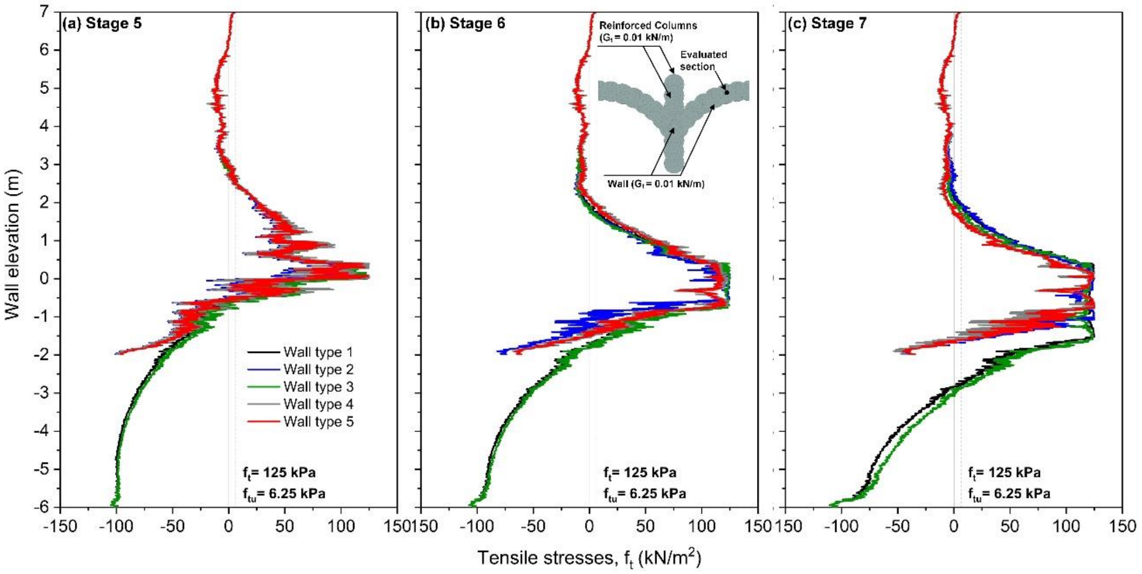

Fig. 68: Calculated tensile stresses for different types of walls at arch sections: (a) stage 5; (b) stage 6 and (c) stage 7

As mentioned above, even for wall type 5 equilibrium can be achieved in the finite element analysis. However, from a design point of view this is not sufficient because input parameters represent characteristic parameters and, therefore, no safety margin is introduced. With respect to EC7, a partial factor on material parameters has to be introduced when employing Design Approach 3 (DA3). Although “structural elements”, and in this context the MIP-columns can be considered as such, are not explicitly dealt with in EC7, in combination with DA3 it seems logical to introduce a partial factor not only to soil strength, but also to the strength parameters of the MIP-columns. If, with reduced strength parameters, equilibrium can be achieved in the finite element calculation, it can be argued that design requirements according to EC7 are fulfilled. A similar approach has been adopted by Schweiger et al. (2017) for the design of shallow tunnels supported by a shotcrete lining. In the following section it is shown that it is a feasible approach also for the problem discussed in this chapter.

5.4.3 Application of Eurocode 7

Only the reference geometry (wall type 1), and the extreme case (wall type 5, see Fig. 65) are considered for investigating the application of Eurocode 7. The calculations were carried out according to Eurocode 7 Design Approach 3 (DA3). Consequently, the characteristic strength parameters of soil layers ($tan\varphi'$ and c') and MIP-columns (f_c and f_t) are reduced by a partial factor of 1.25, whereas different combinations (see Tab. 9) have been investigated due to the fact that with EC7 it is not clear on how to deal with structural elements, in particular if they cannot be considered to behave as linear elastic material, as is the case with the MIP-columns.

Of particular note is that normalised residual strength in compression and tension were adopted to be the same as for the characteristic strength parameters (f_{cun} = 0.1 and f_{tun} = 0.05, see Tab. 5), i.e. only the peak strength has been factored, but because they are normalised factoring is implicitly assumed.

However, the input G_t-value has been adopted in the same as for the characteristic strength, because the fracture energy is generally quantified as the toughness (i.e. ductile or brittle behaviour), rather than the failure strength (i.e. f_c and f_t). It is acknowledged that this is an assumption which could be questioned, but it has been considered to be reasonable for the purposes of the study. However, this could be a topic for additional investigation. Furthermore, it is by no means clear what partial factor should be applied to G_t because there is no prior experience available to act as a guideline and EC7 in general only factors strength.

Tab. 9: Analyses performed according to EC7-DA3

Wall	Cases	Partial factors		General columns		Reinforced columns		Results
		Soil	*Wall*	f_t (kPa)	G_t (kN/m)	f_t (kPa)	G_t (kN/m)	Uy (mm)[a]
1	W1-S	1.25	-	125	0.01	600	0.01	15.8[b]
	W1-W	-	1.25	100	0.01	480	0.01	7.5[b]
	W1-SW	1.25	1.25	100	0.01	480	0.01	16.5[b]
	W1-SWGt	1.25	1.25	100	0.01	480	1.0	8.3[b]
5	W5-S	1.25	-	125	0.01	600	0.01	107[d]
	W5-W	-	1.25	100	0.01	480	0.01	57[e]
	W5-SW	1.25	1.25	100	0.01	480	0.01	36[c]
	W5-SWGt	1.25	1.25	100	0.01	480	1.0	32[e]

Note: The characteristic strength parameters of soil layers ($tan\varphi'$ and c') and MIP-columns (f_c and f_t) are reduced by a partial factor of 1.25.

[a] Lateral wall displacement at top of the reinforced column.

[b] Solution is converged.

[c,d,e] Failure occurs at stage 5, 6 and 7, respectively.

As mentioned previously, failure in the analysis is defined by means of the non-convergence of the iteration procedure, i.e. when a state of equilibrium could not be established with the factored strength parameters of soil and/or structural elements. The strength reduction, i.e. φ'-c' reduction (Brinkgreve et al. 2017) is not performed in this study, therefore no factor of safety is explicitly defined, but the partial factors on strength are applied at the beginning of the analysis. If equilibrium is achieved with the factored strength parameters, the requirements of EC7 are fulfilled and no explicit calculation of the safety factor is required. Please note that the concrete model considers softening and cracking and this cannot be taken into account in a standard strength reduction procedure. Additionally, being in line with Eurocode7 stiffness is not factored in, although it is acknowledged that this is an issue which could be discussed.

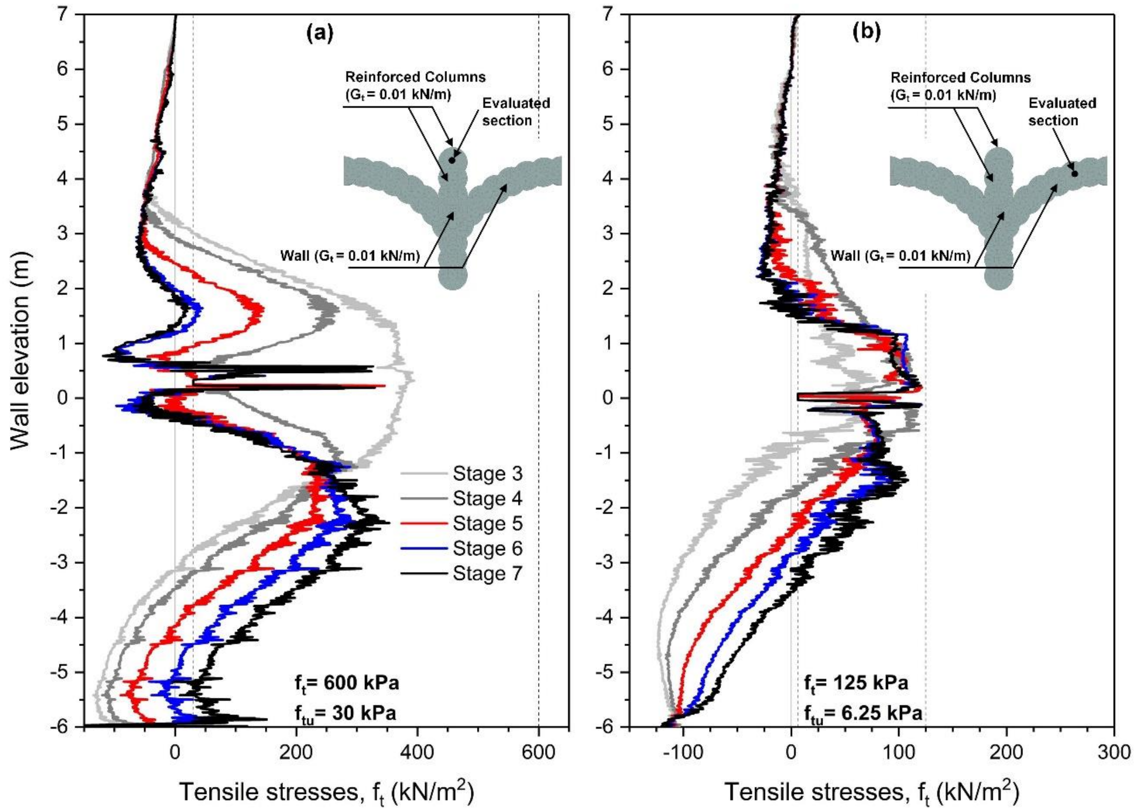

Fig. 69: Calculated tensile stresses for W1-S: (a) reinforced column and (b) arch section.

Fig. 69 and Fig. 70 show the development of tensile stresses in the reinforced column and a column in the centre of the arch (the location is indicated in the figures) for wall types 1 and 5 for the case when the partial factor is only applied to soil strength, but not to the MIP-columns (denoted as W1-S and W5-S). It can be observed from Fig. 69 that for wall type 1 the tensile stresses start to reduce indicating tension softening in excavation stage 4 for the reinforced column (Fig. 69a), and in subsequent excavation stages also for the arch section (Fig. 69b).

However, the decreasing trend of tensile stresses occurs simultaneously in both columns (i.e. in excavation stage 5) for wall type 5, which is illustrated in Fig. 70. This is consistent with the numerical investigation of Hashash & Whittle (1996) which states that the structural failure (i.e. ultimate bending moment has been reached) is likely to occur prior to the development of the failure mechanism in the soil. In addition, the analysis cannot be completed up to the final excavation stage and, therefore, the design would not be valid according to EC7. Equilibrium and stability are not obtained in the finite-element calculation at stage 6 for wall type 5 (Fig. 70).

Fig. 71 shows the crack development at the end of excavation for wall type 1 (Fig. 71a) and at the stage where failure occurs for wall type 5 (Fig. 71b). The failure also affects the behaviour on the excavation side where compression softening is indicated for the case of low G_t, indicated by the softening parameter H_c.

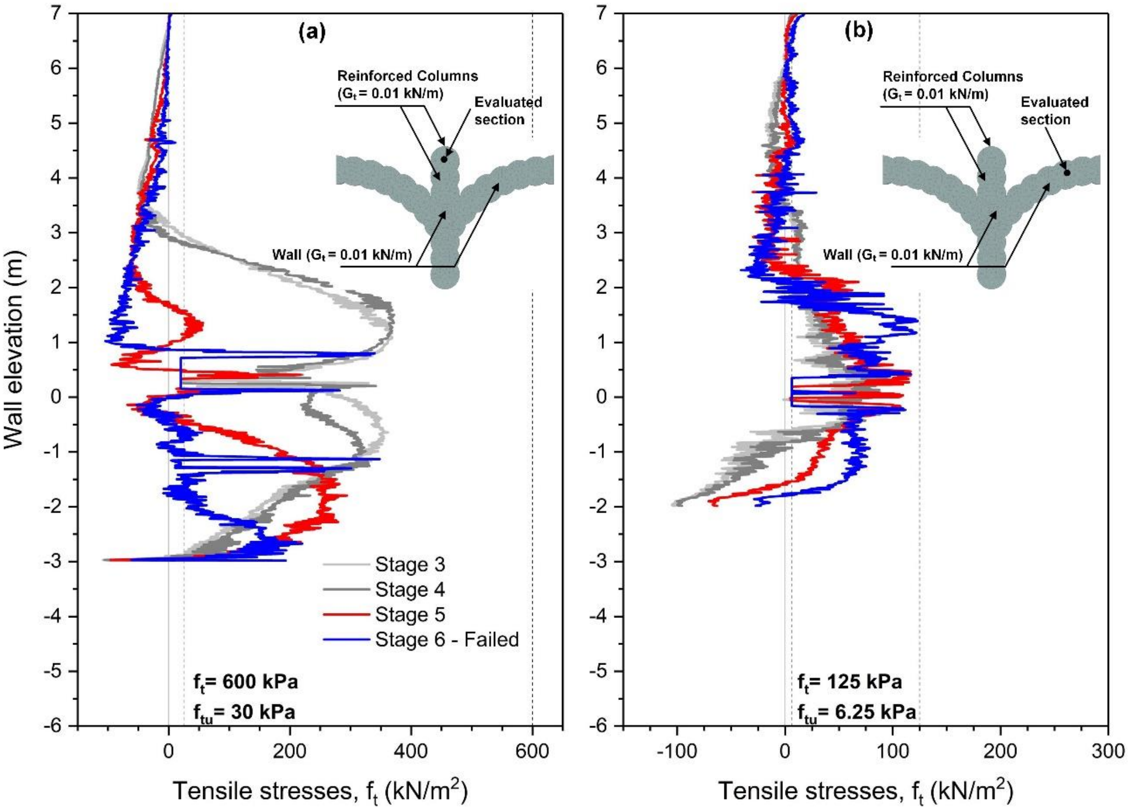

Fig. 70: Calculated tensile stresses for W5-S: (a) reinforced column and (b) arch section

Fig. 72 shows the calculated tensile stresses according to EC7-DA3 for wall type 1. The stepwise development of tensile stresses in the reinforced column is presented in Fig. 72a - Fig. 72c.

For the case when the partial factor is only applied to the MIP-columns (denoted as Wall1-W) the calculated tensile stresses are lower than for all cases where the soil strength is reduced for excavation stage 3 (where S denotes soil). This can be expected because the earth pressure acting on the wall is smaller in this case (Fig. 72a). However, at later stages of excavation cracking also occurs under these assumptions (Fig. 72c).

Tab. 9 summarizes at which excavation stage the analysis for wall type 5 fails, together with the calculated wall displacements which significantly increase, also indicating unstable behaviour. At the end of the excavation, it is evident that for the case when the partial factor is applied to the soil and the MIP-columns and G_t = 1.0 kN/m for reinforced columns (denoted as Wall1-SWGt), tensile stresses are redistributed along the reinforced column at the backside of the wall (Fig. 72c) leading to an acceptable tensile stress state along the column at the arch section (Fig. 72d).

The stress distribution for wall type 5 when the partial factor is applied to soil strength and the MIP-columns (W5-SW) is compared to wall type 1 as illustrated in Fig. 73. The difference in geometry, the reduced material strength and consequently the increased earth pressure result in unstable behaviour before reaching the final excavation level (Fig. 73b). Fig. 73d shows the drop of tensile stresses due to cracking at stage 5 for case W5-SW at which failure is indicated at the arch section (see Tab. 9).

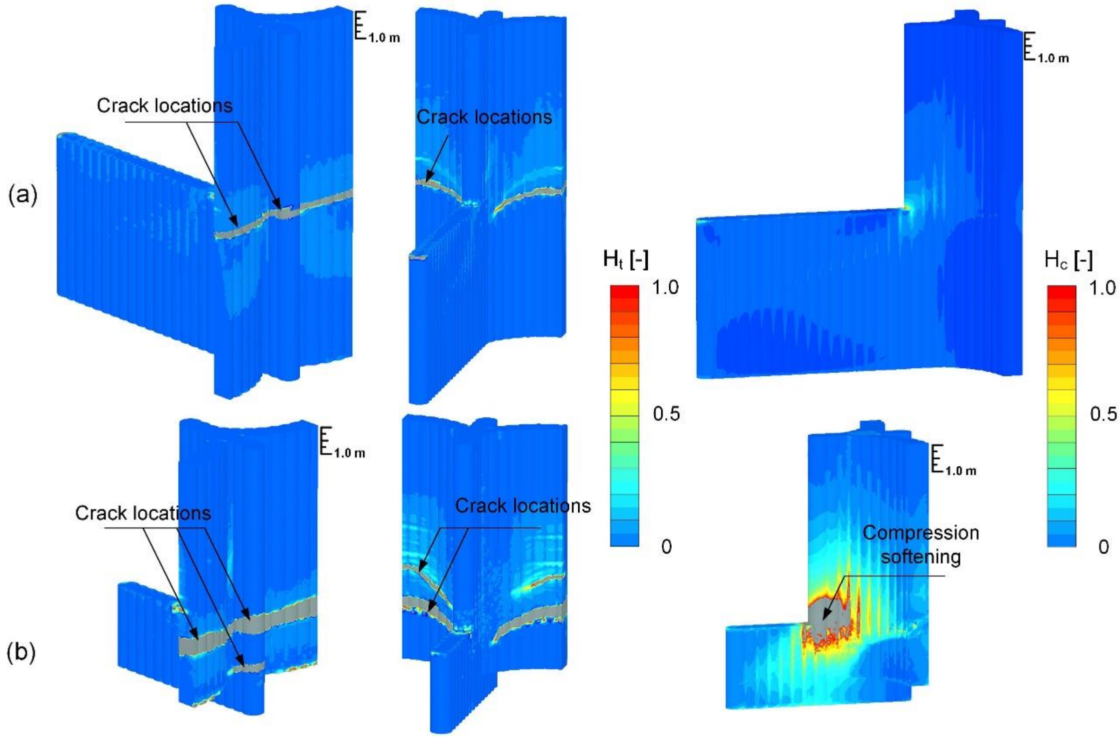

Fig. 71: Crack patterns and compression softening: (a) W1-S and (b) W5-S (failed at stage 6)

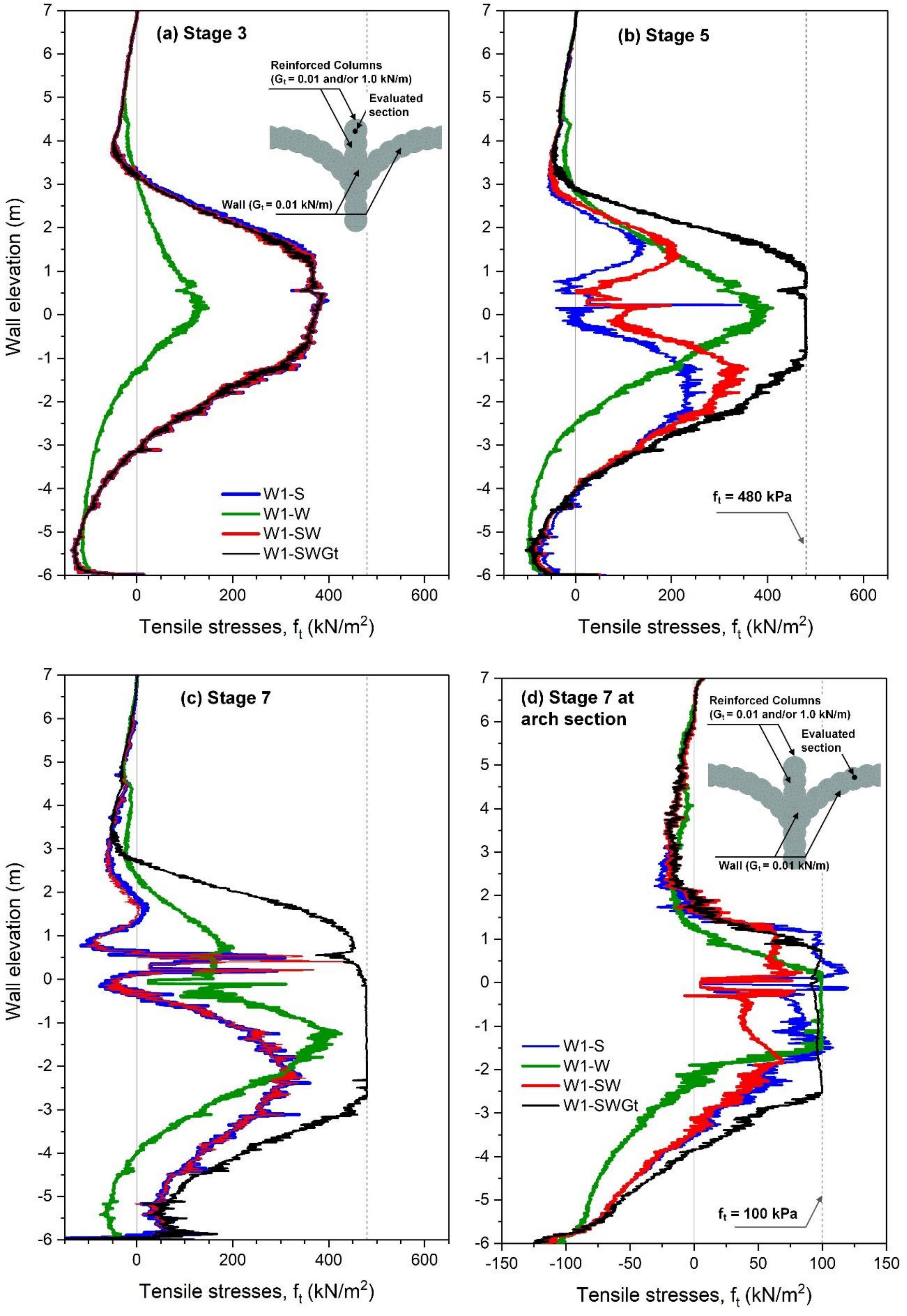

Fig. 72: Calculated tensile stresses of wall type 1 according to EC7-DA3: (a) stage 3; (b) stage 5; (c) stage 7 at arch section

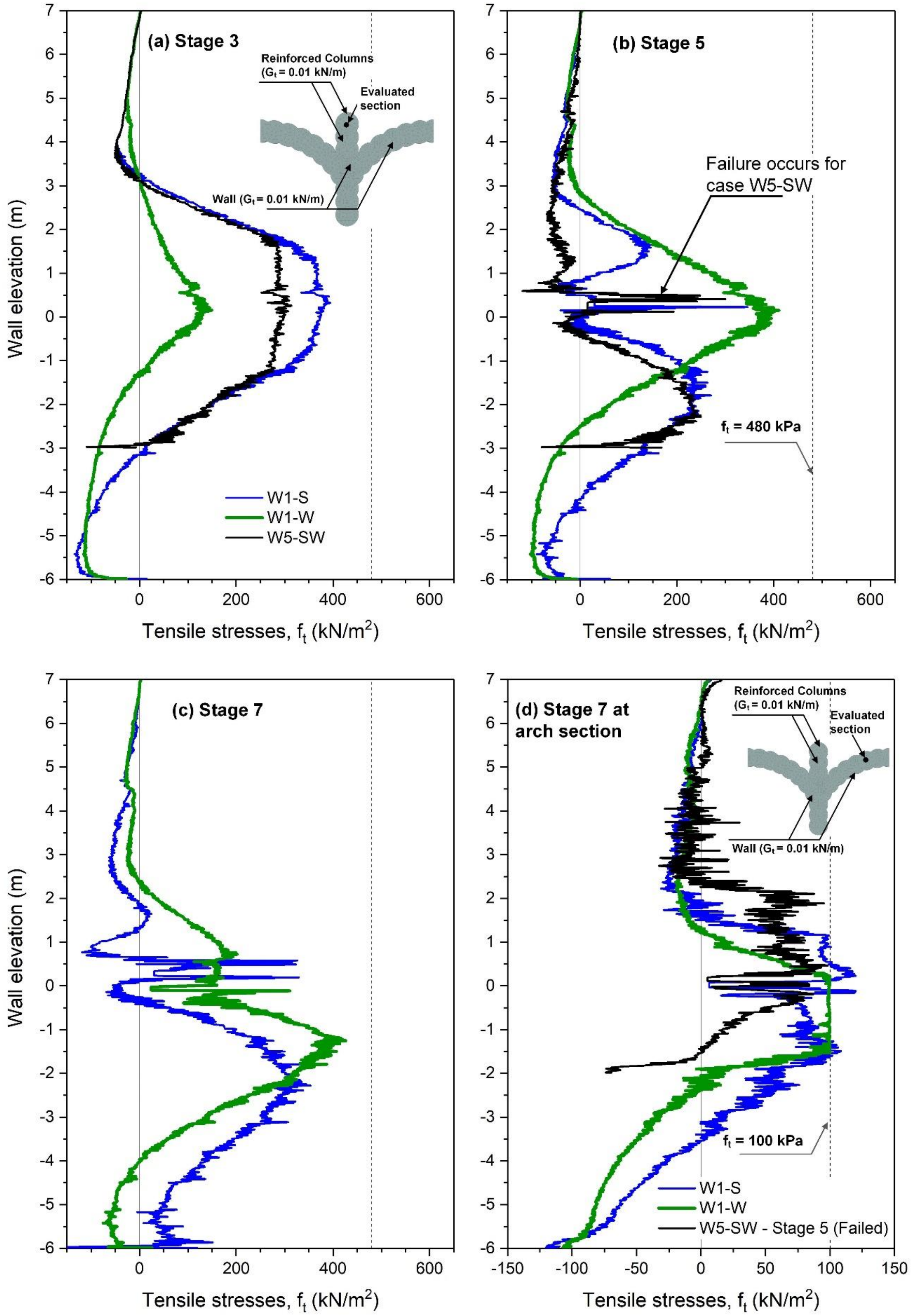

Fig. 73: Comparison of calculated tensile stresses for wall type 1 and 5: (a) stage 3; (b) stage 5; (c) stage 7 at the arch section

From the numerical studies performed the conclusion can be drawn that EC7-DA3 is applicable to assess the design of such structures in accordance with Eurocode 7. However, it should be kept in mind that the behaviour of soil-structure interaction problems such as deep excavations are also governed by stiffness and not only by strength, but EC7 does not consider factoring stiffness and, therefore, it has also not been investigated here. Furthermore, the non-linear material behaviour of support structures, in particular in the context of numerical analyses, is not covered in EC7. Based on the results of this study it is claimed that the proposed approach is a step forward towards a more rational design of complex geotechnical structures by exploiting the full capabilities of advanced numerical modelling, taking into account highly nonlinear material behaviour while still be in line with EC7. However, it is acknowledged that more sensitivity studies are required before consistent and robust recommendations for practical engineering could be formulated (e.g. Lees & Walter 2018).

5.5 Alternative solutions for slope stabilisation

5.5.1 Influence of buttress systems

The buttress system has been successfully adopted as an alternative auxiliary measure in addition to retaining structures. The performance of buttress systems could effectively reduce deformation and, thus, enhance the stability of excavation work. Depending on the type of support system, Lim & Ou (2018) presented the combined diaphragm wall, buttress and partial floor slabs as a strut-free retaining system, concluding that the main two factors controlling wall deflections are the combined stiffness between the diaphragm wall and the buttress and the frictional resistance between the buttress and the soil. Marte et al. (2017) introduced the buttress system as an additional part of arch structures constructed using the Deep Mixing Method (see Fig. 50) for supporting excavation in slopes. In this section, a parametric study on the influence of buttress systems will be discussed. Fig. 74 illustrates the investigated buttress systems. The buttress system was introduced to the previous investigated geometries (wall type 1 and 5).

Fig. 75 compares lateral wall deflection of wall type 1 and wall type 6 at the final stage of excavation. As expected, the wall deflections of wall type 6 are significantly reduced. Moreover, it can be observed that when the buttress is removed in a successive stage, the deformation can still be controlled and minimized. This indicates the important role of the buttress in the deformation control mechanism.

Differences in mobilized shear stresses are depicted in Fig. 76. It is evident that for wall type 1 the mobilised shear stress is concentrated between the arch section and the supporting part, and exceeds the limit of shear strength of 1440 kPa (Fig. 76a), whereas the shear stress of wall type 6 is more uniformly distributed across the buttress, and decreases across the panel length (Fig. 76b). It should be noted that shear strength is calculated based on the Mohr-Coulomb failure criterion (Uniaxial compressive strength = 5 MPa and $\varphi' = 30°$). The fully mobilisation of shear stress is influent when reducing the column and panel length as illustrated in Fig. 76c, and, consequently, results in different deformation mechanisms (i.e. overturning, see Fig. 79).

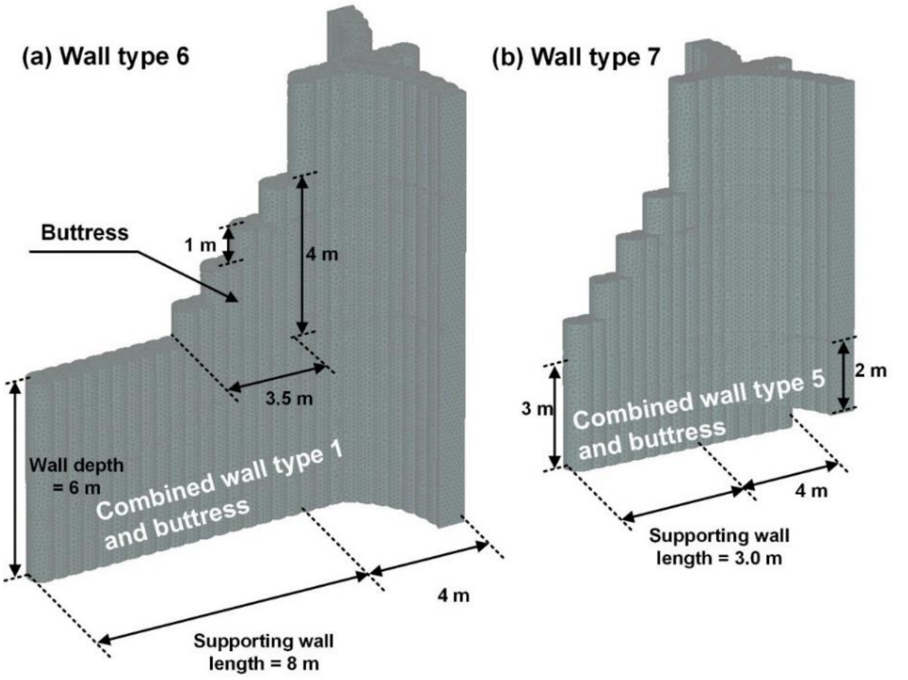

Fig. 74: Investigated geometries; (a) wall type 6 and (b) wall type 7

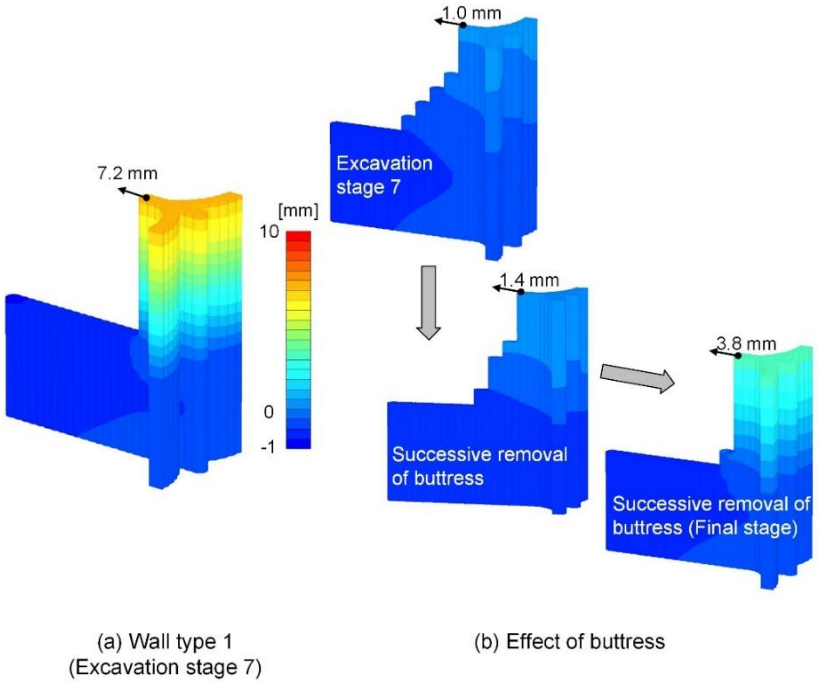

(a) Wall type 1 (Excavation stage 7)

(b) Effect of buttress

Fig. 75: Influence of buttresses on lateral wall deflection

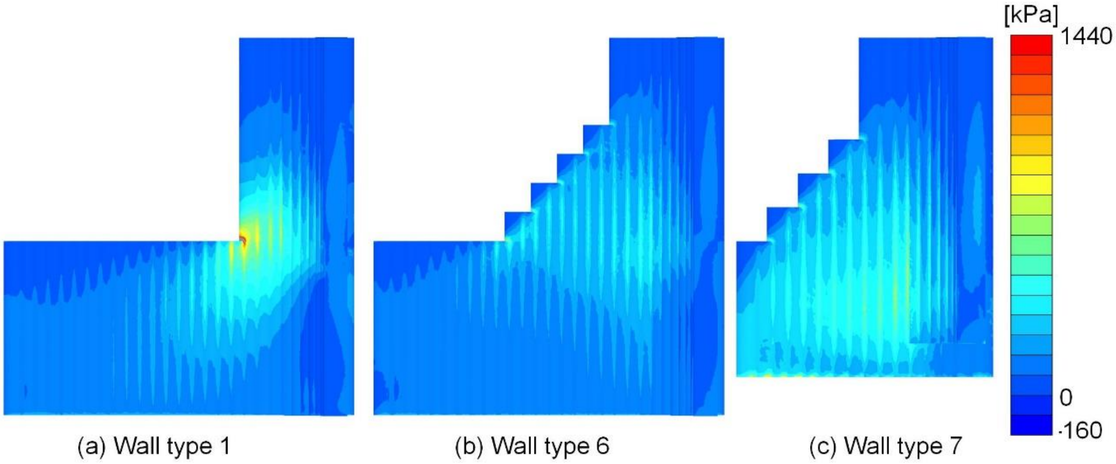

Fig. 76: Mobilised shear stress of MIP-structures after final excavation

The influence of buttresses on normal stresses concentration at the panel section is shown in Fig. 77. At a certain stage of buttress removal, it is seen that normal stresses are significantly reduced at the final stage of excavation and are more evenly distributed along the panel length (along the y-axis). Similar observations can be expected in mobilised shear stress (Fig. 78).

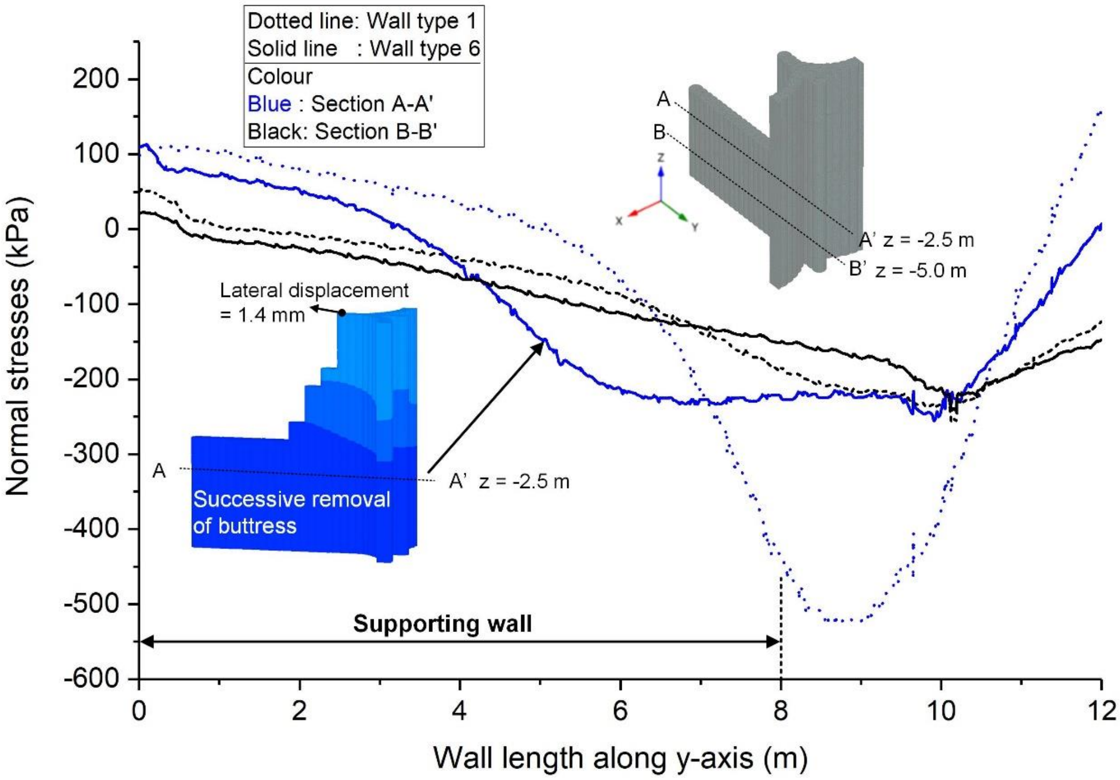

Fig. 77: Influence of buttresses on normal stresses concentration

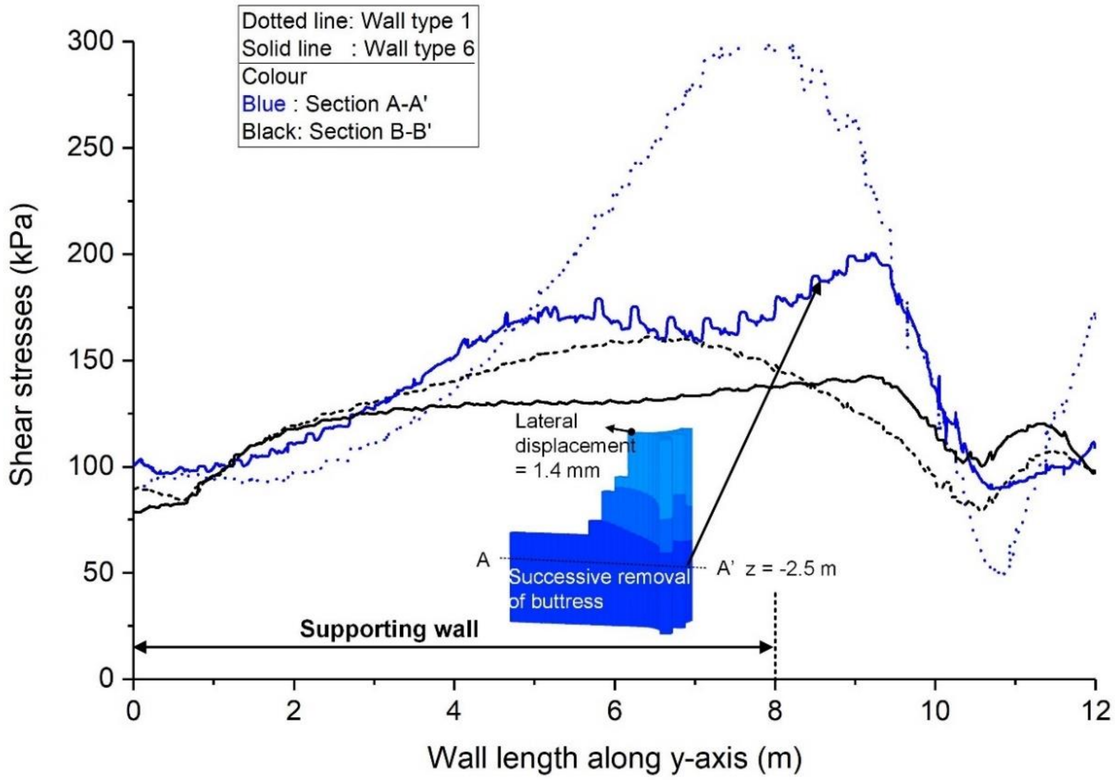

Fig. 78: Influence of buttresses on mobilised shear stresses

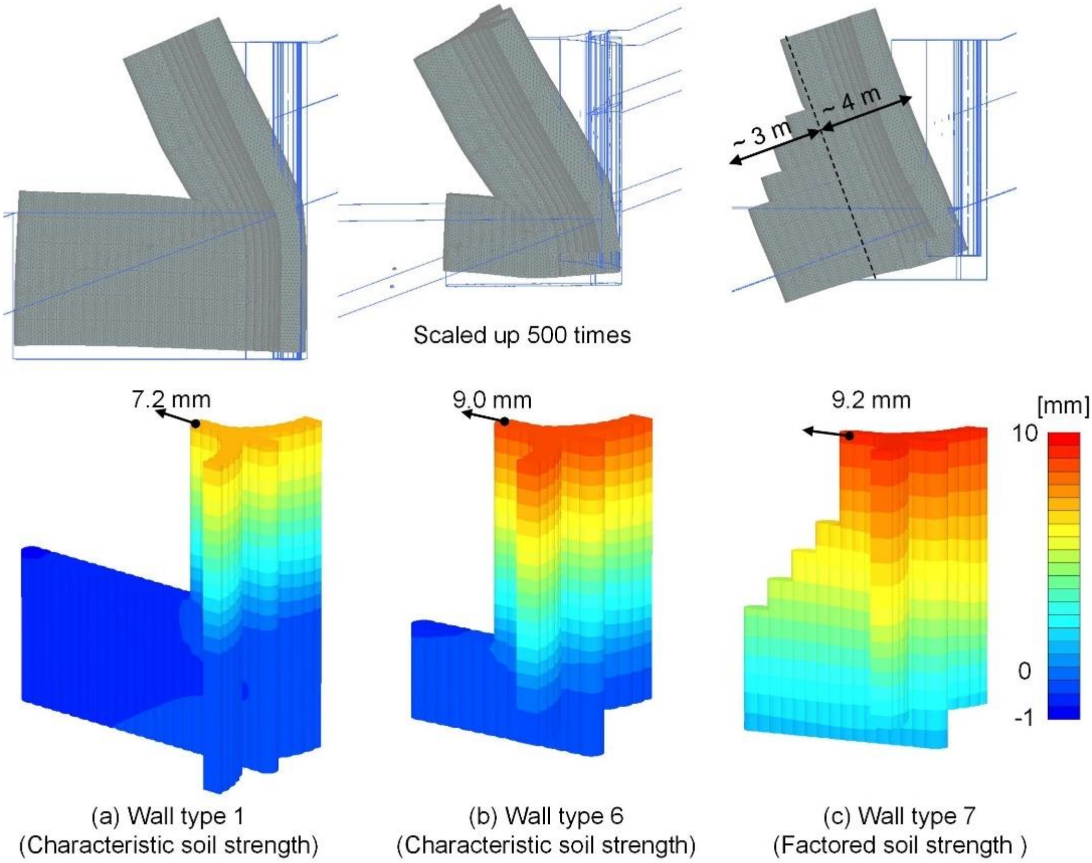

(a) Wall type 1
(Characteristic soil strength)

(b) Wall type 6
(Characteristic soil strength)

(c) Wall type 7
(Factored soil strength)

Fig. 79: Comparison of wall types for different design approaches

5.5.2 Influence of steel reinforcement

The influence of steel reinforcement has been investigated. The structural layout was changed and only the arch section was considered. However, due to very high slenderness ratios, material strength and stiffness were also adopted to concrete properties representing low reinforcement and high reinforcement at the arch section, as illustrated in Fig. 80.

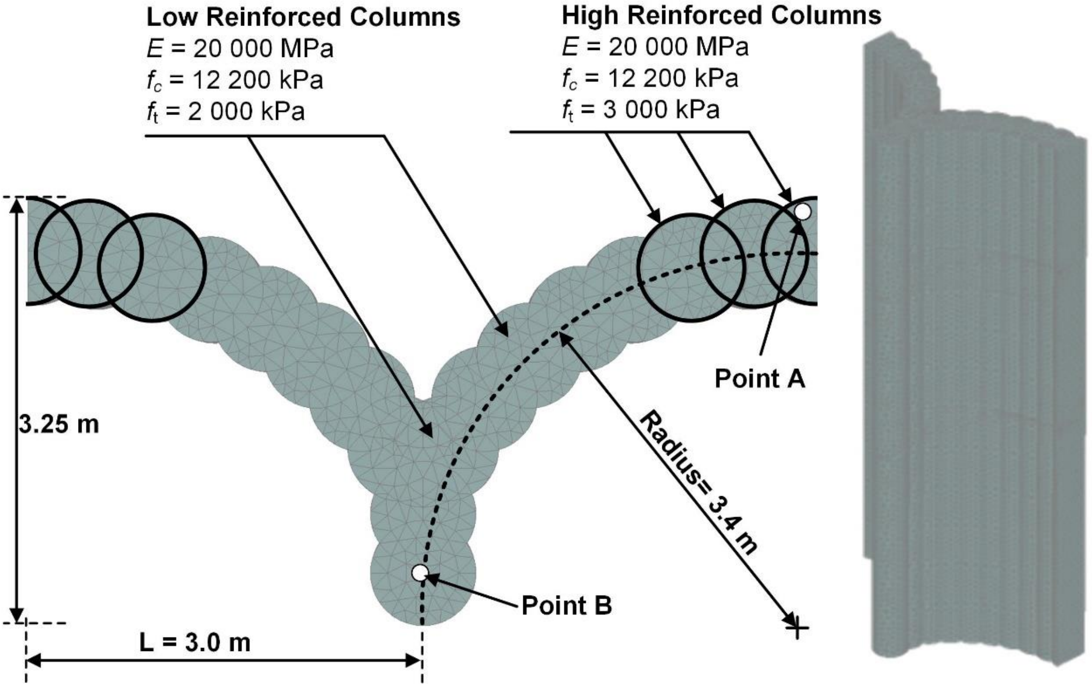

Fig. 80: Geometry and details of the arch structure

The tensile fracture energy of reinforced concrete is very low. However, it was reported by Rabaiotti & Malecki (2018) that by back calculation of an in-situ pullout load test of barrette piles, tensile strength f_t and tensile fracture energy G_t are 3000 kPa and 200 N/m, respectively. The chosen G_t and $f_t$values are shown in Fig. 81, and the remaining parameters are referred to in Tab. 5.

Fig. 82 shows the lateral wall deflection and total displacement contours at the final excavation level. The lateral wall deflection of the two locations (indicated in Fig. 80) indicates a rigid wall movement (i.e. cantilever movement) resulting from the higher strength and stiffness of the material adopted. As the cantilever movement dominates the overall behaviour, the resulting stress concentration occurs only at the embedded part (below the excavation level, Fig. 83a), and tensile stress at reinforced columns are well below its tensile strength (Fig. 83b).

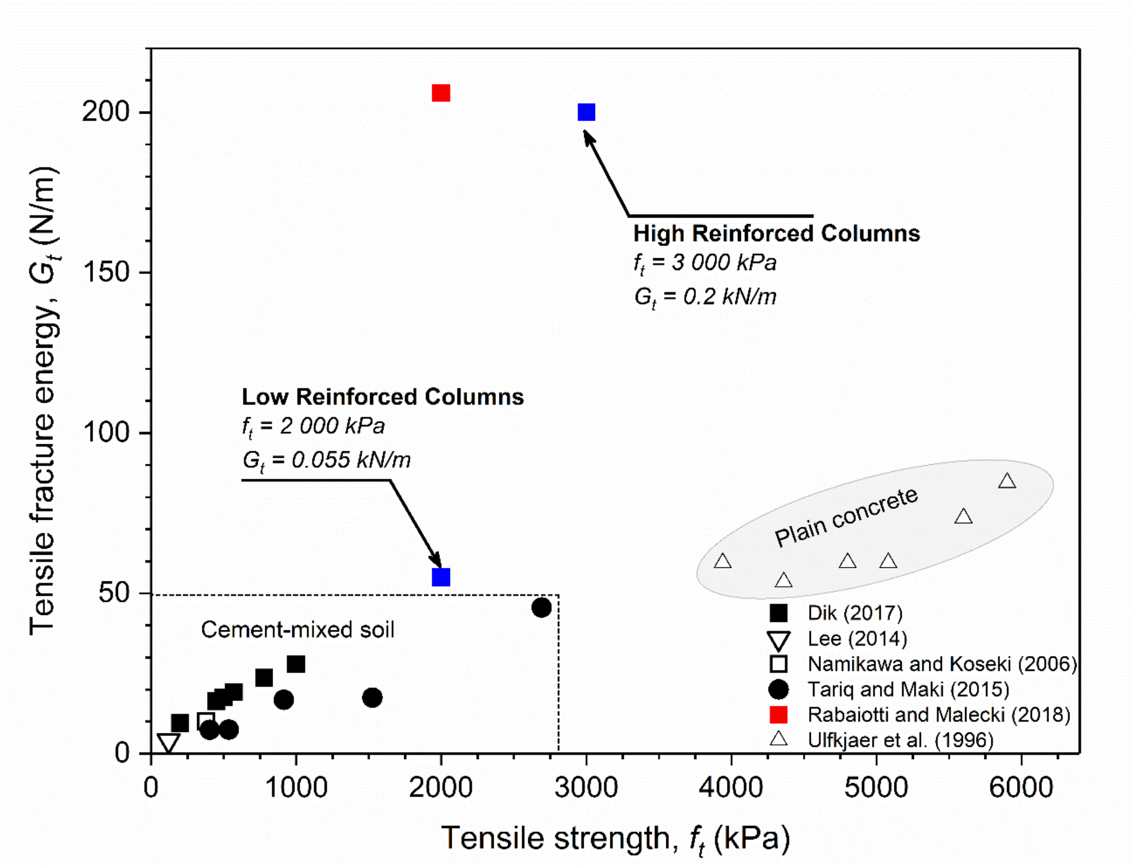

Fig. 81: Tensile strength (f_t) and fracture energy (G_t) due to steel reinforcement

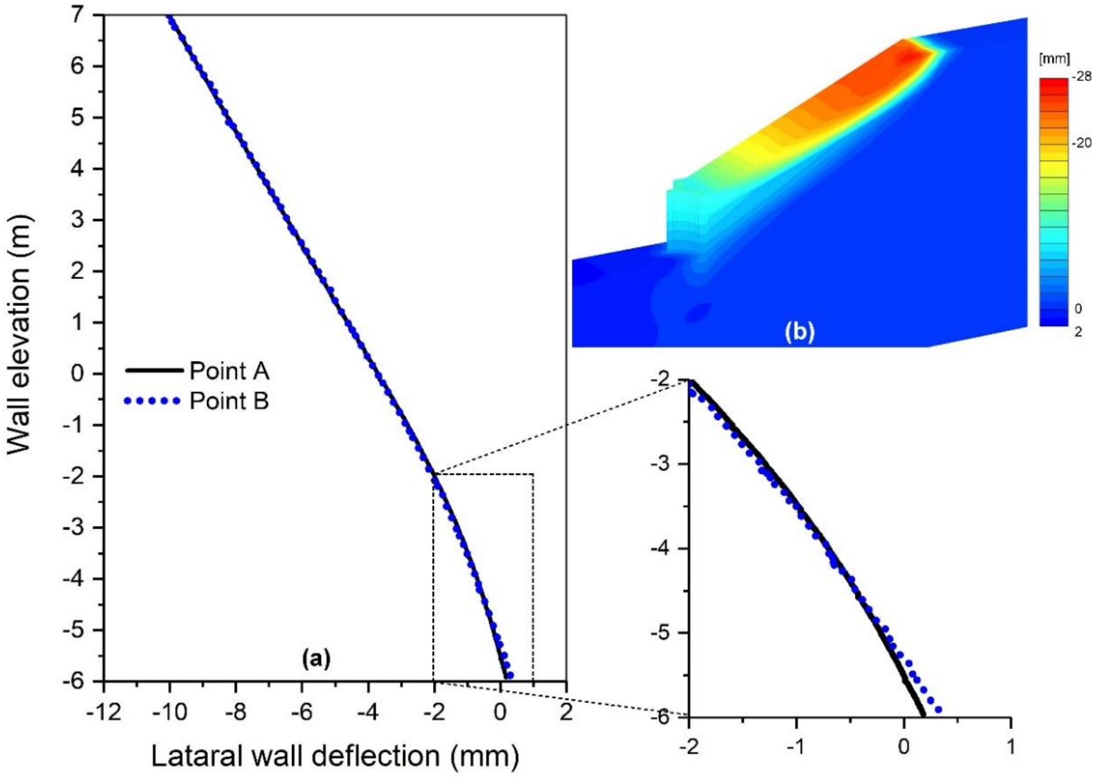

Fig. 82:(a) Lateral wall deflection; (b) total displacement contours

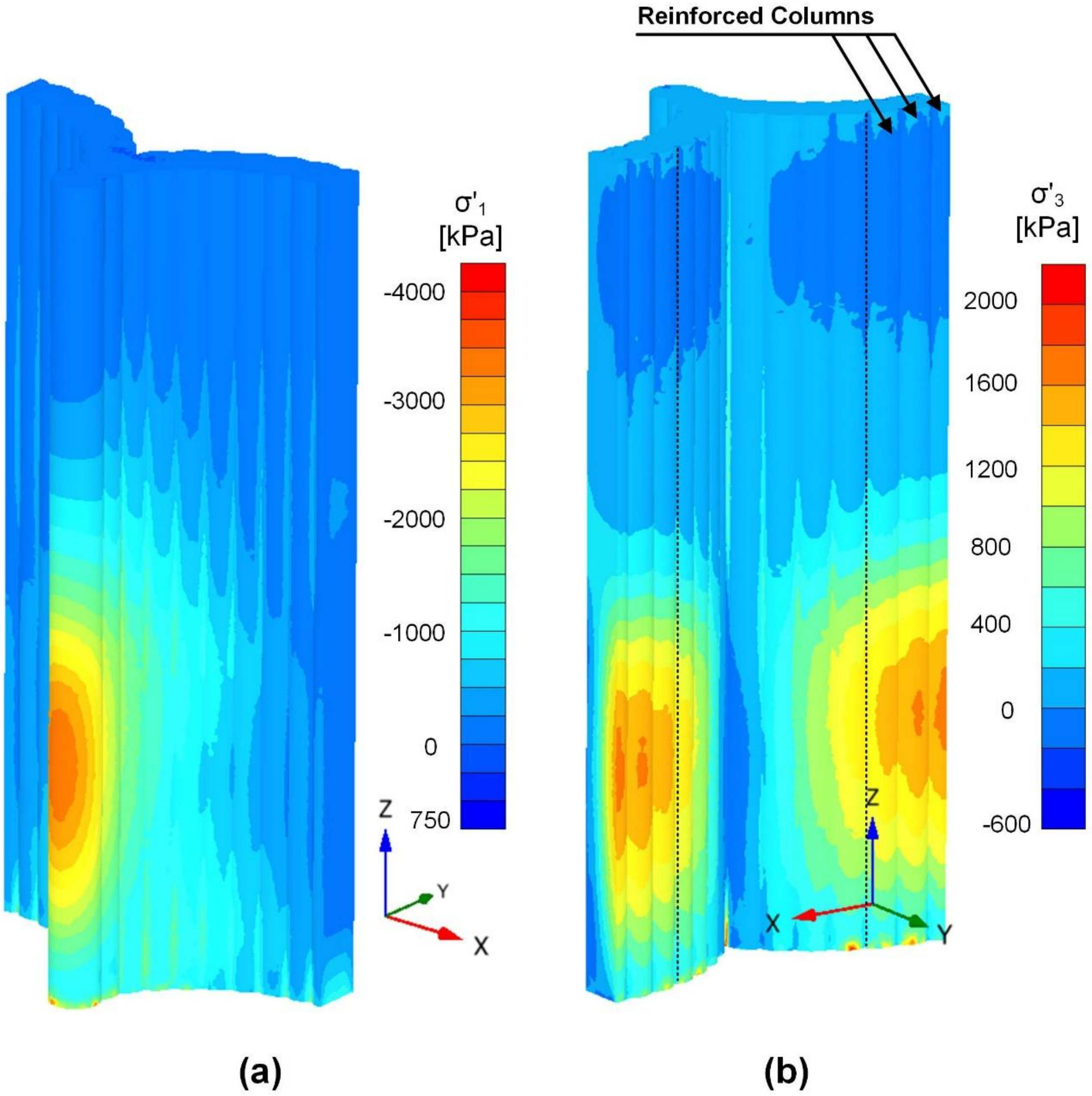

Fig. 83: Contour lines for (a) major principal stress, σ_1'; (b) tensile stress, σ_3'

5.6 Conclusion

An extensive parametric study was carried out to investigate the behaviour of mixed in place columns (MIP) for supporting an excavation in a slope by means of FE-analyses. Emphasis was put on the behaviour of the supporting structure after reaching the tensile strength of the column material. An advanced constitutive model for concrete was applied to allow modelling of the mechanical behaviour of the MIP structure, in order to capture the initiation of cracks and the crack development with progressive excavation. It can be shown that significantly different stress distributions in the MIP wall are obtained when compared to applying a simple Mohr-Coulomb failure criterion with a tension cut-off for the wall.

In order to investigate the potential for savings, a parametric study was performed changing the geometry of the supporting structure. Column length and supporting panel length were reduced and several combinations were investigated. It was found that a reduction of column and supporting panel lengths would still lead to equilibrium, but from a design point of view this would not be sufficient because no safety margin is introduced when performing the analysis using characteristic strength parameters. Therefore, additional analyses were performed according to EC7 utilizing Design Approach 3 where partial factors on soil strength and, in this particular case, also on the strength of the MIP-columns are applied. It was shown that for the reference geometry equilibrium could still be achieved, but for the extreme case investigated, this was no longer the case. Thus, it can be concluded that this type of analysis is suitable for designing this type of geotechnical structures in accordance with EC7.

6 Parametric study for shaft excavation

6.1 Introduction

Circular excavations are often carried out for the construction of underground storage tanks, hydraulic and power facilities, inspection or access chambers and service entrances. As such, circular vertical shafts are often employed as the retaining systems for these excavations and adopted as the starting and ending sections for underground tunnelling and pipe jacking projects. The significant benefits of using circular excavation are: (a) minimizing interior lateral bracings due to large structural stiffness providing space for construction activities; (b) potential to reduce wall embedment depth below the final excavation level under certain conditions; and (c) taking full advantage of the arching effect of the ground, minimizing and controlling ground movement.

As lateral soil stresses acting on circular walls are resisted by axial thrusts in the circular shaft linings, hoop compression of a circular shaft must be considered in the design. In addition, attention must also be paid the moments and shearing forces depending on the types of wall, i.e. sheet pile, mixed-in-place columns or diaphragm walls. Hence, the design analysis of circular vertical shaft involves the structural design of lining for stability, as well as to ensure soil movements induced by excavation one within acceptable limits.

However, as a consequence of geological features and construction imperfections may lead to localized failure (crack initiation) and a reduction in overall stiffness, although the overall structural failure does not occur (Poulos 2015). A critical aspect is the presence of defective piles, e.g. if secant piles serve as a retaining structure, which may result in increased lateral deflection and additional bending moments in such piles. This induced lateral response can become quite severe because defective piles will lead to a loss of symmetric in the retaining structure. In addition, the effect of construction processes on secant pile shafts (i.e. primary and secondary piles) and the strength of the unreinforced low strength piles (the primary piles) are critical to the design as they need to be sufficient to transmit hoop compression forces. Low strength piles must not be too stiff or strong (i.e. 2-4 MPa at seven days, Wharmby 2011) as this can result in poor overlapping and verticality (exceeding tolerances).

The effects of imperfections are frequently ignored or simplified. Random field finite element analysis can be carried out to represent the uncertainty of the system of the nominal radius and positioning errors (e.g. Liu et al. 2015, Liu, et al. 2018) but theses analyses are computationally very demanding. The preliminary study presented in the following attempts to identify some of the causes of crack initiation (i.e. overloading) and the effects of geometrical imperfections (i.e.

distorted shape configurations) for secant pile shaft excavations by means of FE-investigations.

6.2 Geometry and finite element model

The simplified soil profile, the geometric layout adapted from Boehler (2017) and Trunk et al. (2018), and the construction sequence are shown in Fig. 84 together with the locations of points of interest (i.e. points A to C) in order to compare the distribution of earth pressure around the periphery of the shaft. The geological condition adopted is simplified as medium dense gravel sand and the input parameters for the Hardening soil model are included in Fig. 84. The groundwater is 2.0 m below the ground surface. The shaft was subjected to asymmetric loading conditions (i.e. crane = 200 kPa and excavator = 30 kPa).

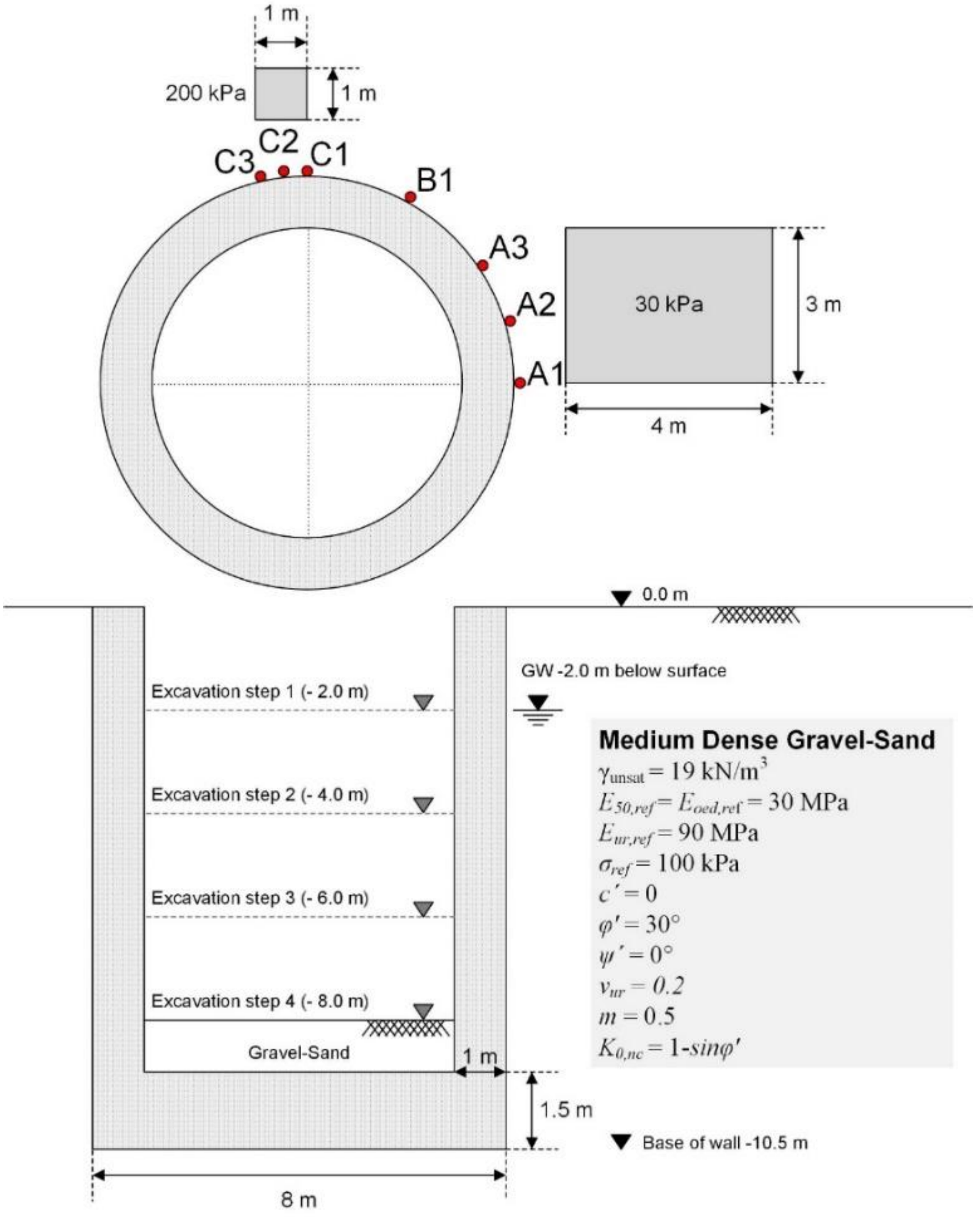

Fig. 84: Schematic view of the wall geometry and top view with locations of interest

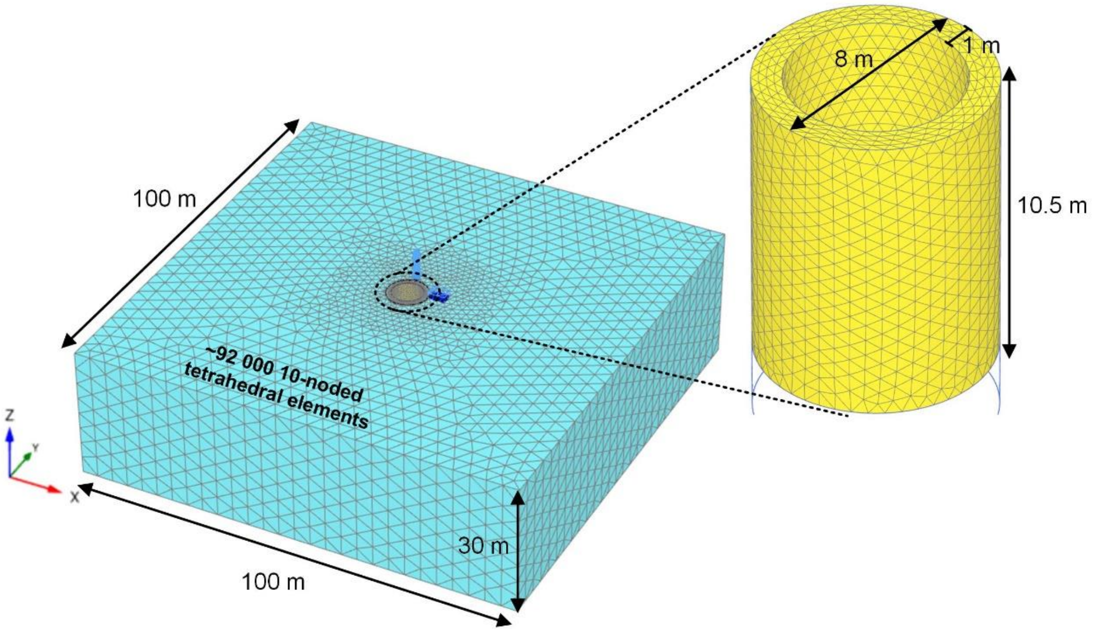

Fig. 85: FE-mesh with details

Tab. 10: Input parameters for shaft in reference analysis

Description		Unit	Value
Unit weight	γ	[kN/m^3]	22
Young's modulus of cured MIP	E_{28}	[kPa]	6.0E+06
Poisson's ratio	ν	[-]	0.15
Uniaxial compressive strength	$f_{c,28}$	[kPa]	6 000
Uniaxial tensile strength	$f_{t,28}$	[kPa]	300
Dilatancy angle	ψ_{max}	[°]	0
Normalised initially mobilised strength	f_{c0n}	[-]	0.15
Normalised failure strength (compression)	f_{cfn}	[-]	0.95
Normalised residual strength (compression)	f_{cun}	[-]	0.1
Uniaxial plastic failure strain	ε_{cp}^{p}	[-]	-0.0035
Compressive fracture energy	$G_{c,28}$	[kN/m]	30
Normalised residual tensile strength	f_{tun}	[-]	0.05
Tensile fracture energy	$G_{t,28}$	[kN/m]	0.01
Maximum friction angle	φ_{max}	[°]	30

6.3 Reference analysis

The finite element mesh (using 10-noded tetrahedrons) and the entire structural layout are shown in Fig. 85.

The reference analysis employed the geometry depicted in Fig. 84 and Fig. 85. The following calculation steps were performed, but only the results for the final stage are presented;

- initial stress state following by activated the shaft (wished-in-place),
- apply surcharge load conditions (crane = 200 kPa and excavator = 30 kPa),
- stepwise excavation with lowering of the groundwater table inside excavation.

The constitutive model described in section 5.3 is used to model the piles and the input parameters are tabulated in Tab. 10.

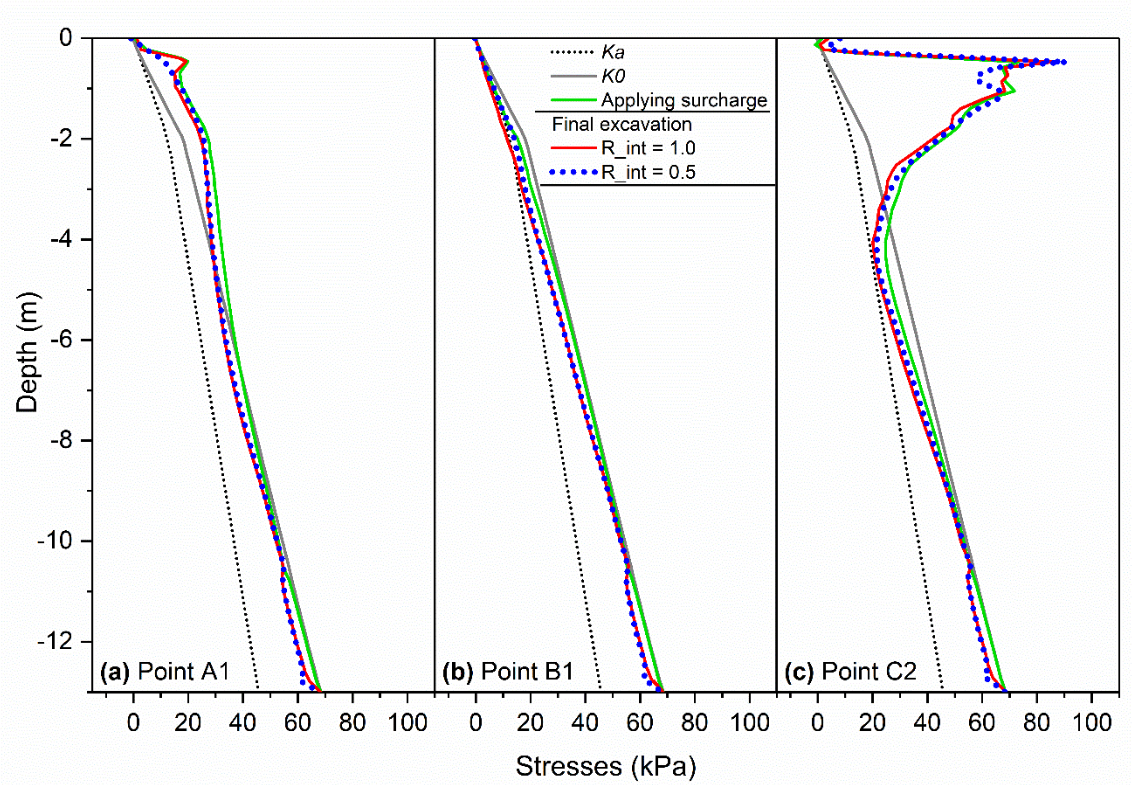

Fig. 86: Lateral stresses acting on the wall in various locations

Fig. 86 shows the lateral stresses at different locations along the shaft for the final excavation stage. The lateral pressures show a slight reduction from the in-situ condition (K_0) at the location B1 (see Fig. 84) where there is no influence of the surcharge and the wall behaves as a very rigid support element. Hence, very small wall deformations are expected (Fig. 87). The surcharge loads (at A1 and C2) affect the lateral stresses on the shaft lining to a depth of approximately 4.0 m below the ground surface. Interfaces properties (R_{int} = 1 and R_{int} = 0.5) have a negligible effect on the distribution of lateral pressure at the final excavation stage. Comparisons of active earth pressures were made using K_a (Rankine's theory), whereas an analytical solution, for example that used in Cheng et al. (2007), is not comparable due to the surcharge effect.

The radial displacement, bending moment, and hoop forces along the shaft are shown in Fig. 87. The changes in stresses and deformations are relatively small, indicating that the arching effects are significant. Comparative studies for determining of lateral earth pressure and relative displacement on cylindrical shafts can be found e.g. by Tobar & Meguid (2010).

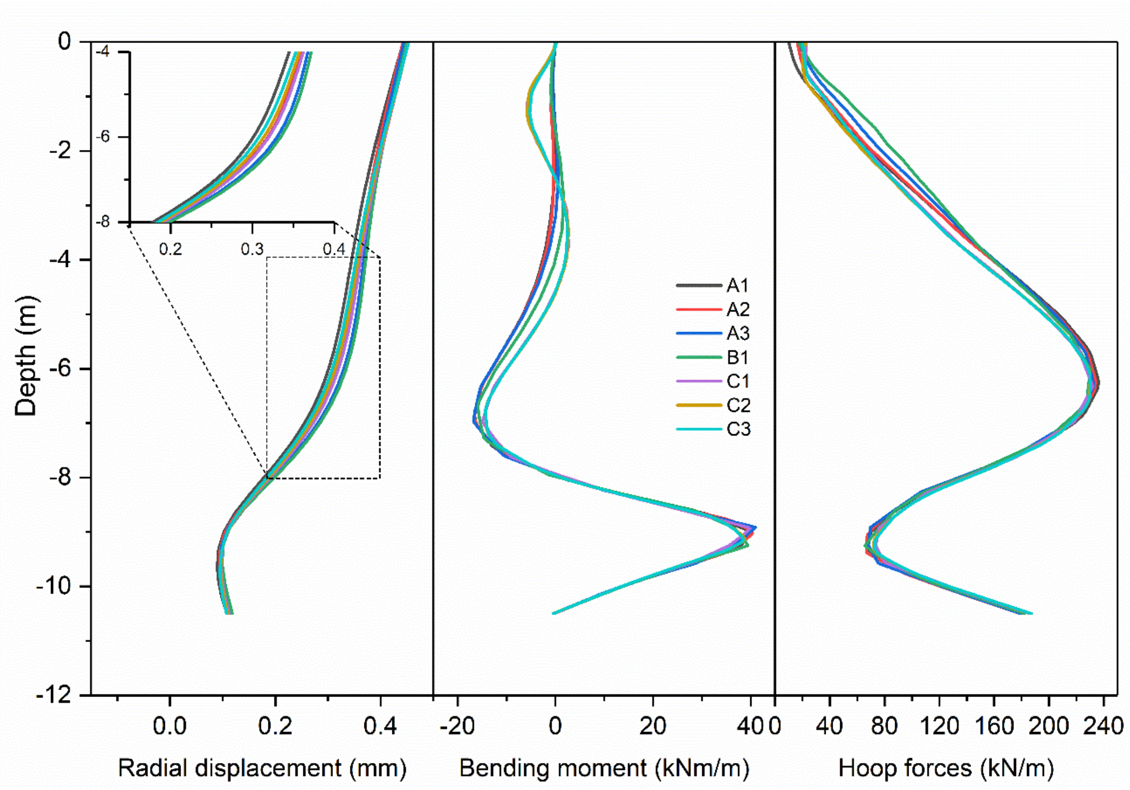

Fig. 87: Radial displacement, bending moments and hoop forces

The effects of surcharge loading on normal stresses(σ_n') and tensile stresses (σ_3') are shown in Fig. 88 and Fig. 89 respectively. It can be that a larger loading area results in larger zone which is influenced by the load (i.e. by Excavator, Fig. 88). Tensile stress concentration localises at the top of the shaft (Fig. 89).

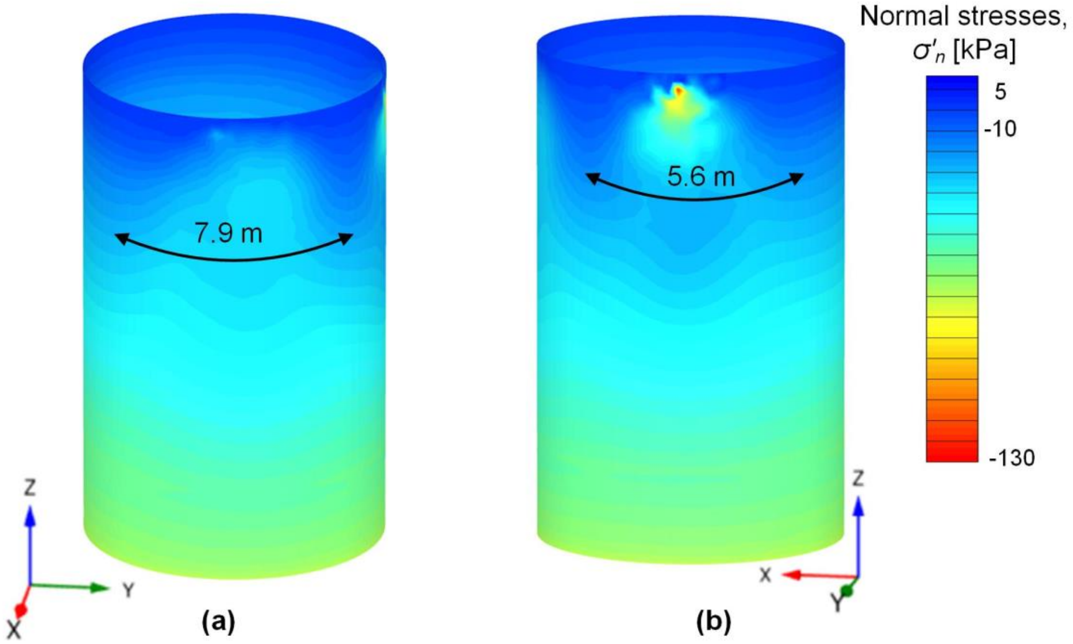

Fig. 88: Influence zone of surcharge loading; (a) by excavator and (b) by crane

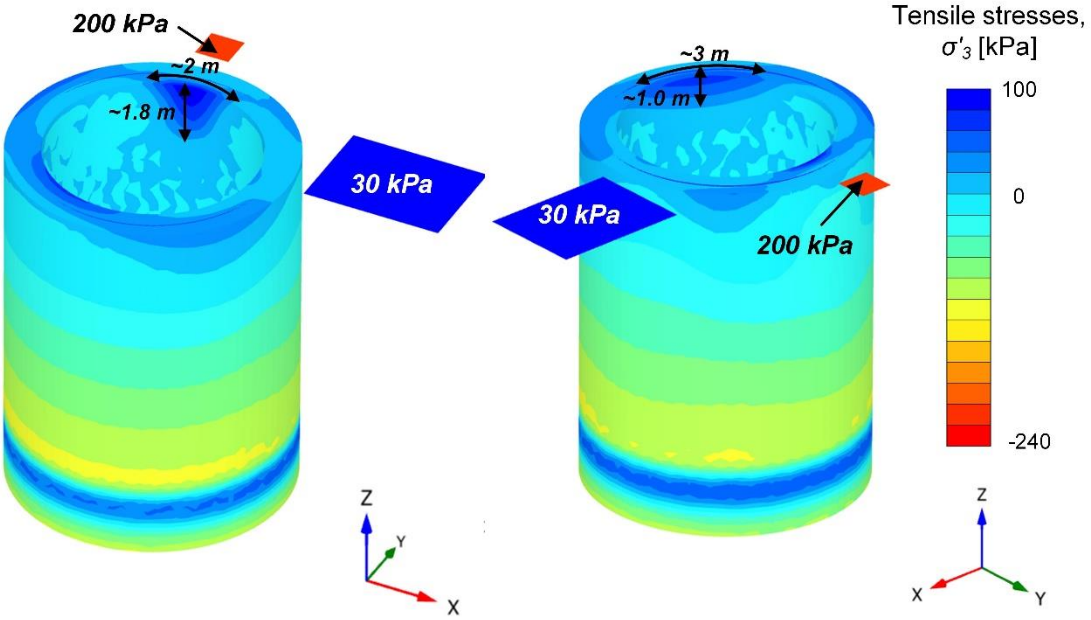

Fig. 89: Influence of surcharge on tensile stress concentration, σ_3'

6.4 Failure initiation for shafts

A parametric study was carried out to investigate the potential failure of the shaft and crack initiation. The calculations adopted the same geometry as discussed in the previous section (see Fig. 84 and Fig. 85). Surcharge loading was increased until failure has been reached at the final excavation level (excavation step 4 at 8.0 m below ground level). The cases analysed are shown in Fig. 90. The tensile fracture energy (G_t = 0.001, 0.005 and 0.01 kN/m) has been varied to elaborate the system response and crack patterns.

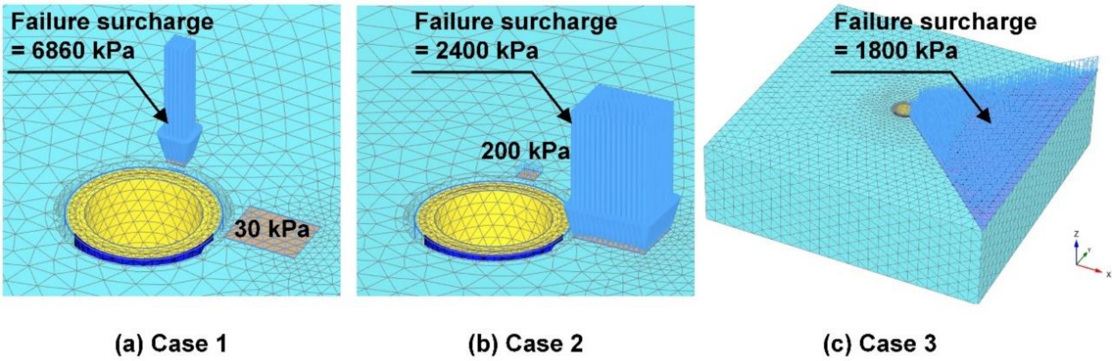

(a) Case 1 (b) Case 2 (c) Case 3

Fig. 90: Cases analysed investigating the potential failure of shaft and crack initiation

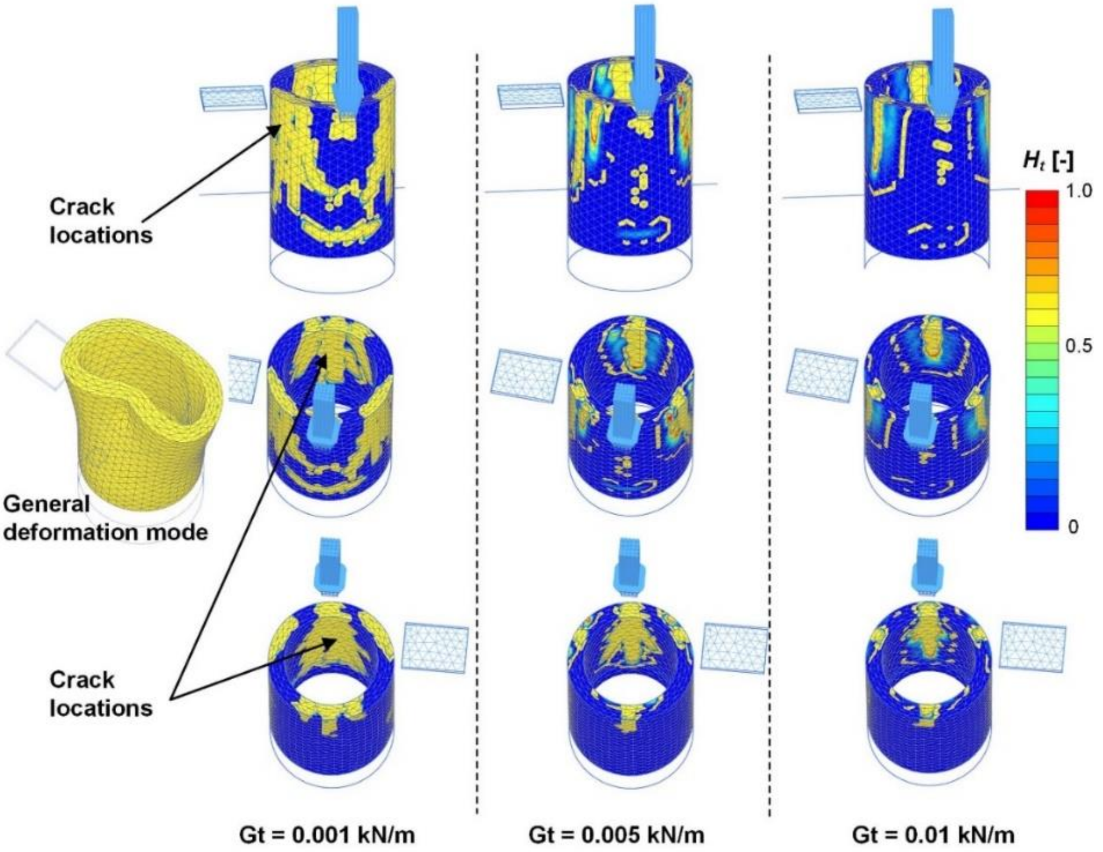

Fig. 91: Crack patterns for Case 1 with different tensile fracture energy, G_t

Fig. 91, Fig. 92 and Fig. 93 show the crack patterns for the cases analysed - 1, 2 and 3, respectively. The crack opening is indicated by the drop to zero tensile stresses at residual ($f_{tu} = f_{tun} \cdot f_t$), where the tensile softening parameter H_t is larger than 1.0. As expected, the smaller G_t (0.001 kN/m) reflects brittle behaviour and forms larger crack openings, whereas the larger value (i.e. 0.01 kN/m) leads to a more ductile response. The larger areas of loading (cases 2 and 3) lead to much larger cracks resulting in lower surcharge loads of failure (Fig. 90).

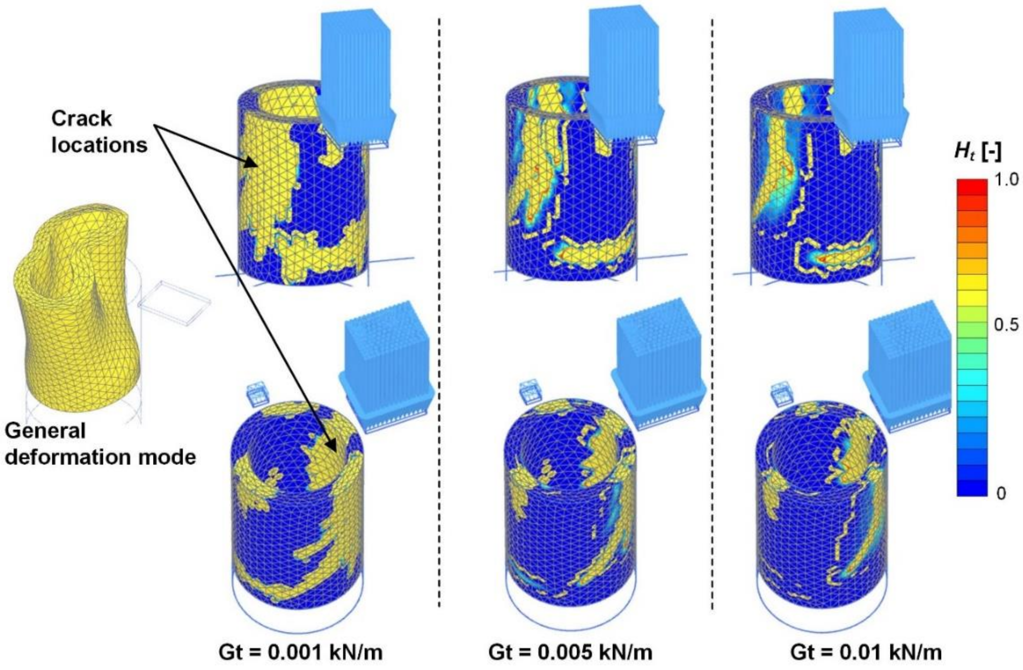

Fig. 92: Crack patterns for Case 2 with different tensile fracture energy, G_t

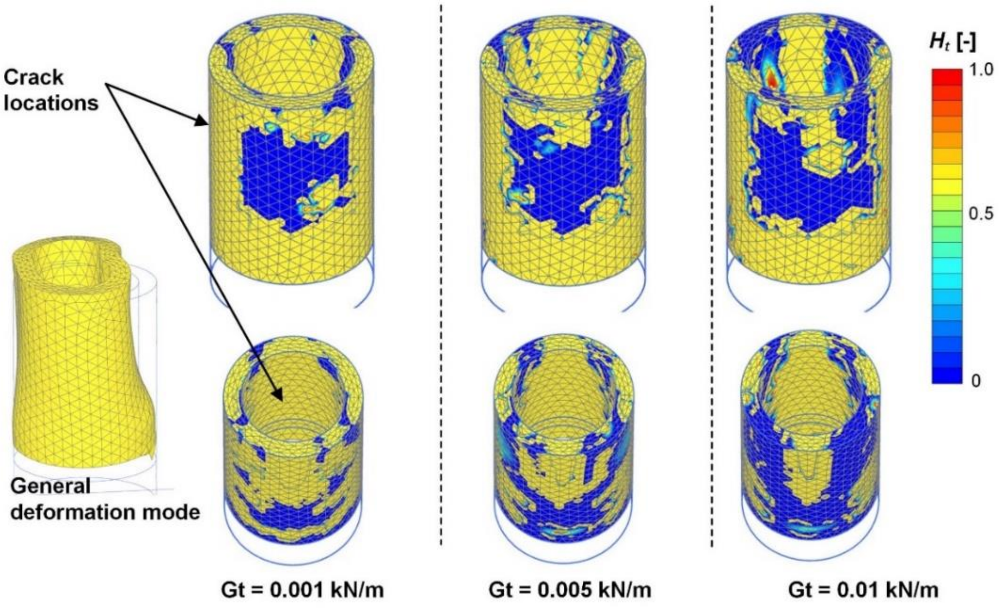

Fig. 93: Crack patterns for Case 3 with different tensile fracture energy, G_t

6.5 Simplified plane strain analysis of imperfections

A 2D plane strain analysis was performed to be able to model individual columns of secant pile shafts investigating imperfections. The representative section is of two-thirds of the wall's height, and the lateral pressure at rest (K_0) is approximately 40 kPa. The detail of the geometry is shown in Fig. 94. The calculation steps are as follows:

- applying the stress (40 kPa) along the boundary (fixed boundary),
- activate the shaft (wished-in-place),
- plastic nil-step,
- deactivate soil elements inside the excavation area.

In addition, different shaft configurations are considered in order to model possible imperfection, e.g. due to deviations in verticality, as shown in Fig. 95. The parameters adopted are the same as those used for the reference analysis in section 6.3. The tensile strength $f_{t,28}$ of the secant pile was reduced to 80 kPa to investigate the occurrence of potential failure

Fig. 96 shows the deformation patterns for each type of wall configuration. It follows that the deformation localizes when the arch is not formed, and the hoop stress cannot transfer across the section (Fig. 97).

Fig. 98 shows the distributions of tensile stresses across the secant pile shaft at failure. The tensile stresses drop from a peak strength ($f_{t,28}$ = 80 kPa) to residual indicating cracking. Values of $H_t > 1.0$ are observed indicating residual conditions as illustrated in Fig. 99.

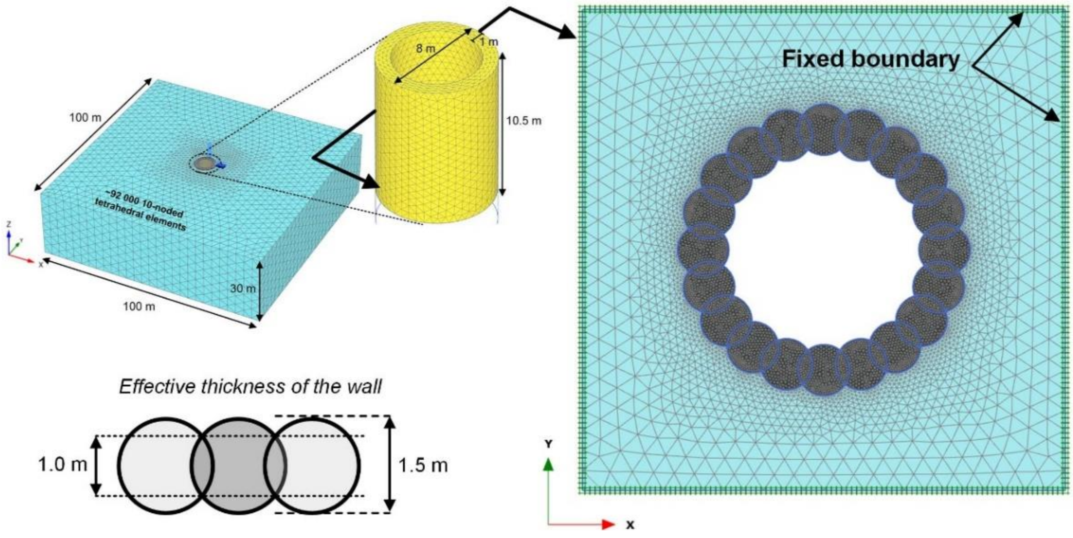

Fig. 94: Simplified plane strain problem

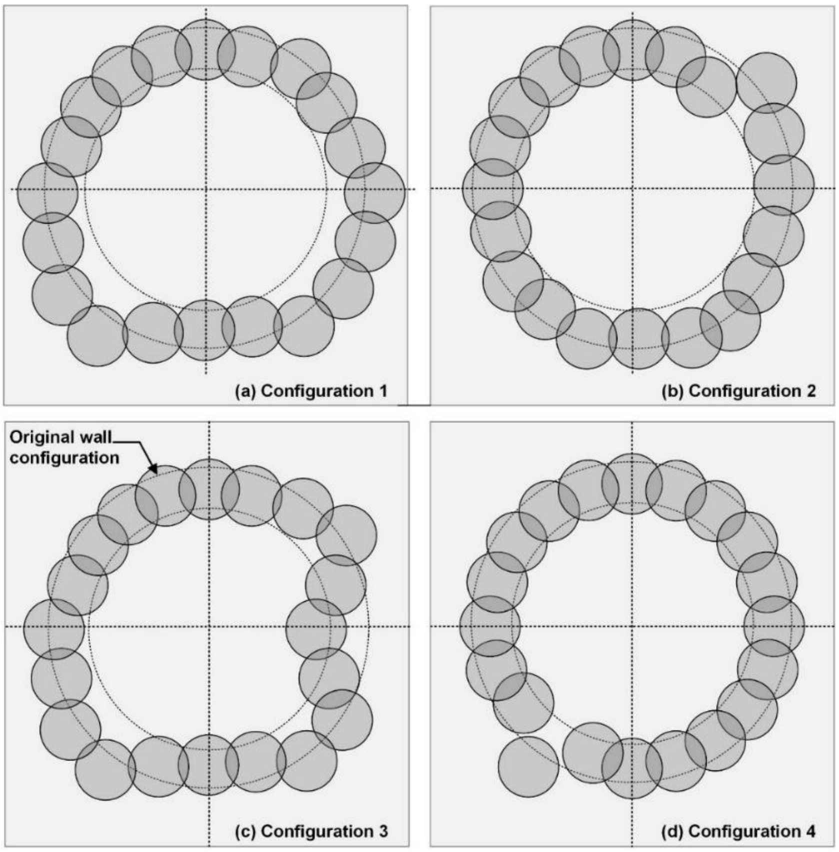

Fig. 95: Shaft configurations for failure investigation

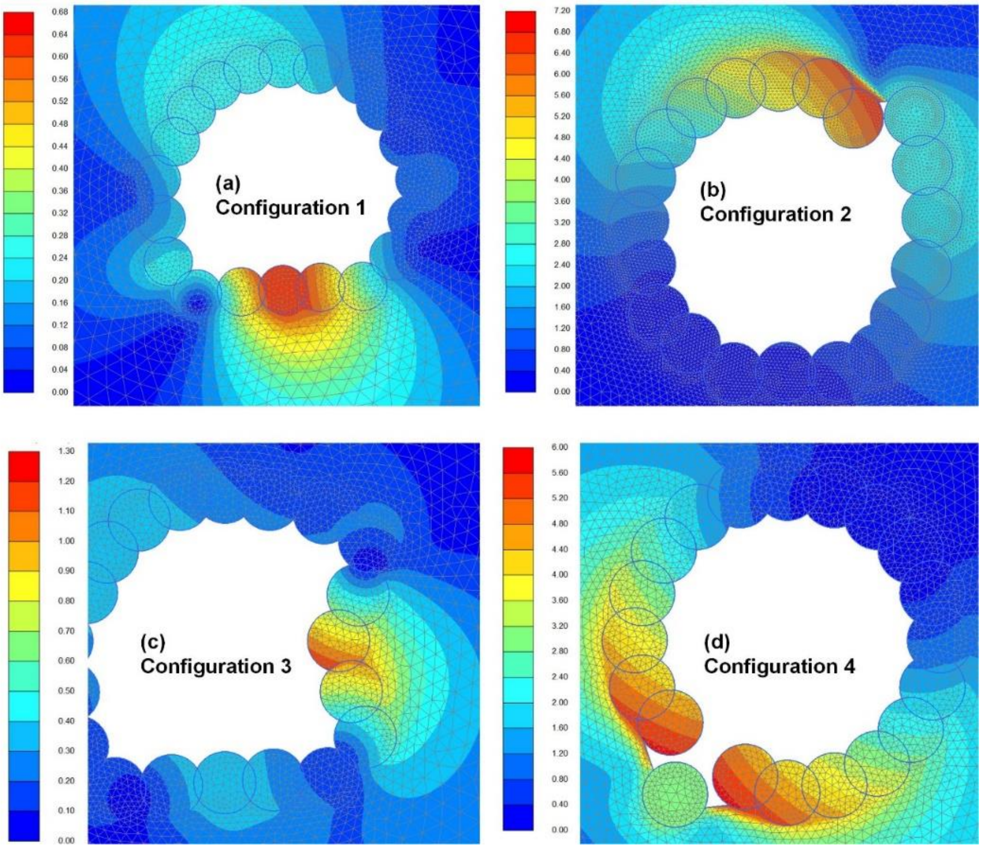

Fig. 96: Contour lines of total deformations at failure (units in mm)

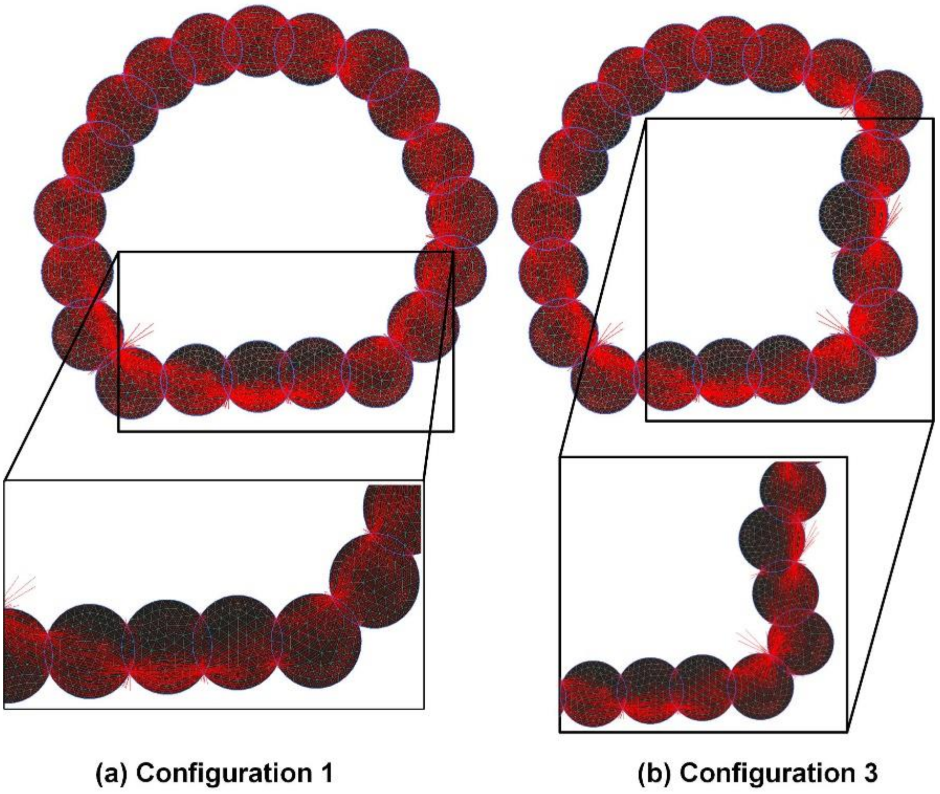

Fig. 97: Principal stresses direction for shaft configurations 1 and 3

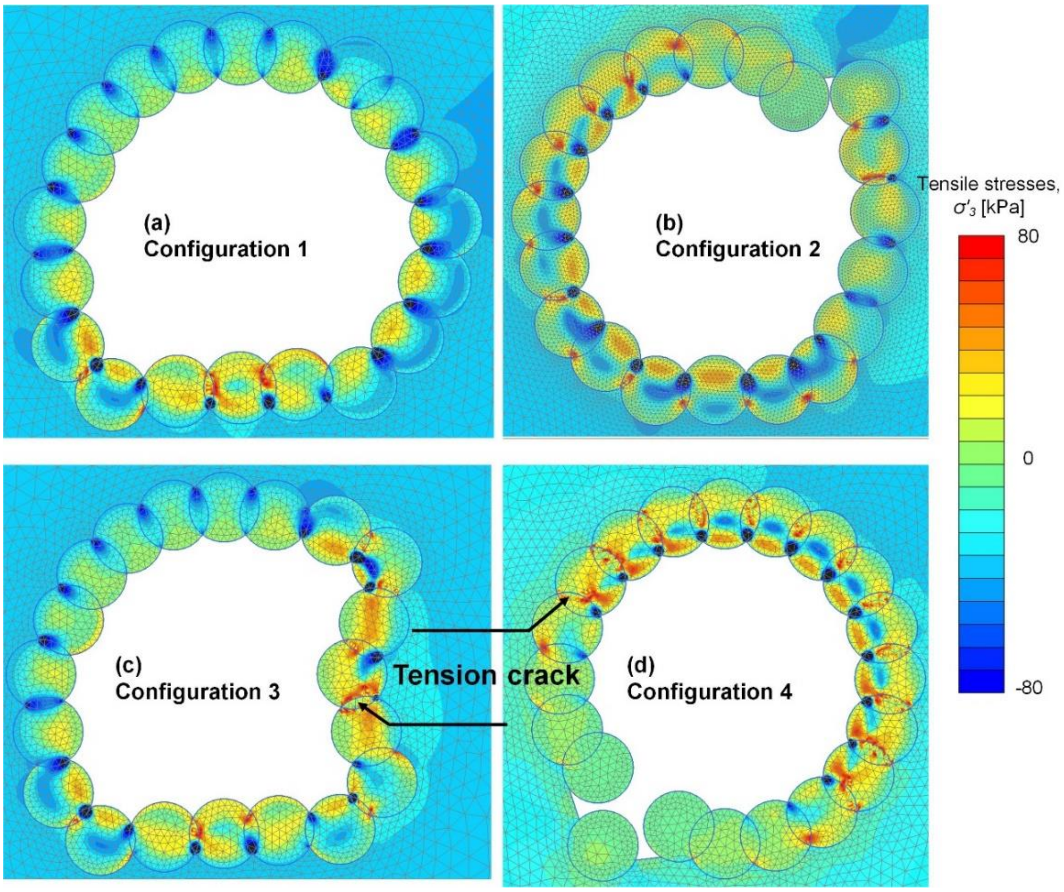

Fig. 98: Contour lines of principal tensile stresses, σ_3'

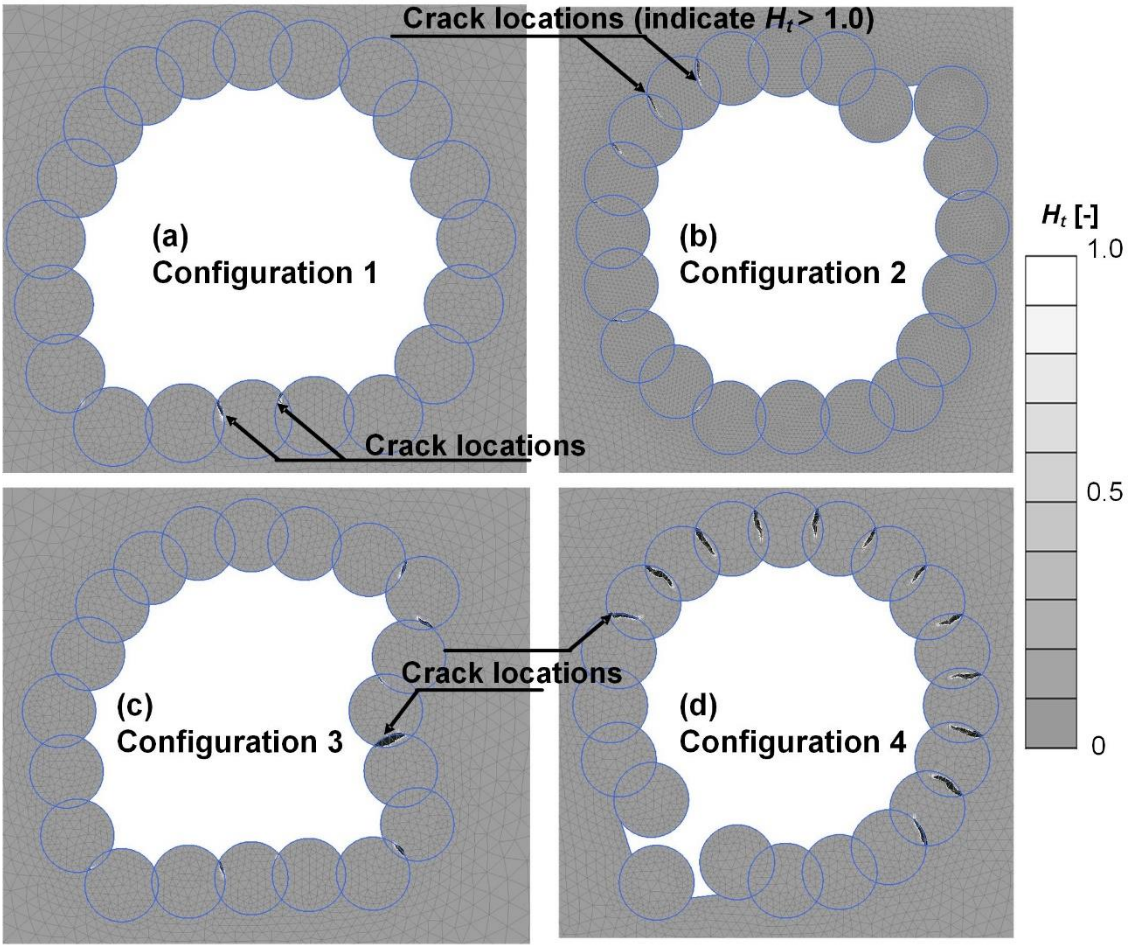

Fig. 99: Crack patterns and tension softening parameters (H_t > 1.0 indicates tension softening)

6.6 Summary

In principle, circular shafts structure display very stiff behaviour because of spatial arching effects and hoop compression force transfer within the system. However, imperfections, e.g. due to loss of verticality, will lead to unsymmetric systems and eventually to failure. The possible crack locations in the secant pile wall are between the interface of individual columns.

7 Case histories

7.1 Undrained analysis of deep excavation in soft soil

7.1.1 Project description

Silom Station is located in an environmentally sensitive location and in a highly congested urban area. The station involved the deepest excavation of the first Bangkok underground MRT project involving a 20 km long railway tunnel. The station adopted a stacked-platform type excavation which has five levels of floor slabs, as illustrated in Fig. 100. The excavation was deepened to a final level of 32.6 m and the toe penetrated into the second sand layer at 46.5 m depth. Hence, dewatering was required to reduce uplift pressure for the excavation. The details of the project are given by Hooi (2003).

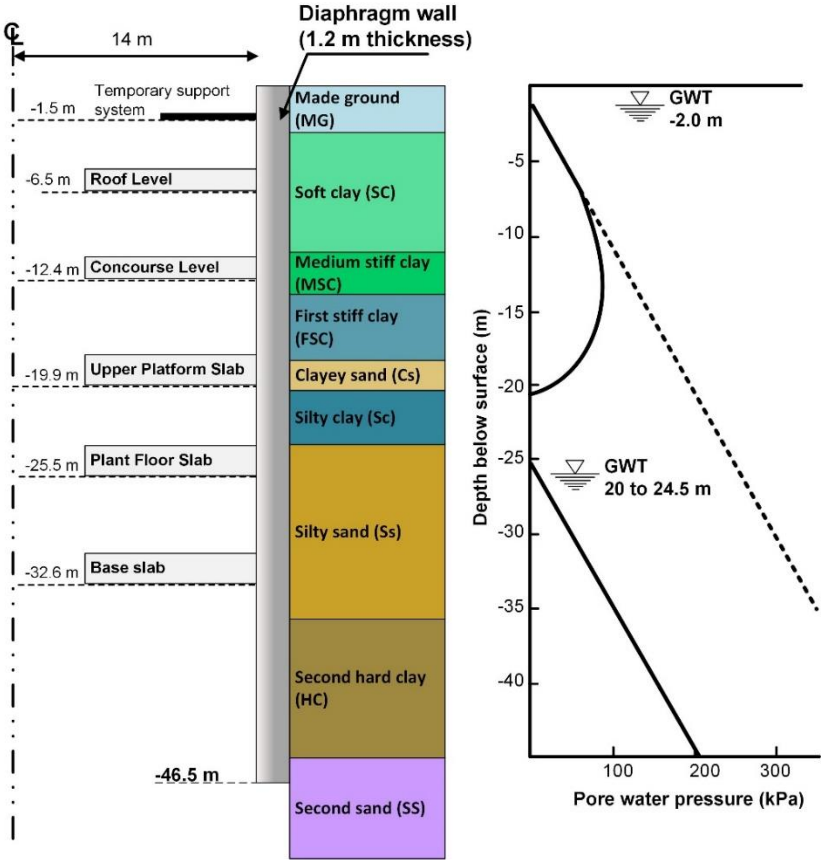

Fig. 100: Geometry and subsoil conditions

A summary of the subsoil conditions at this station is presented in Fig. 101. The ground conditions comprise of a thick marine soft silty clay layer of 12-15 m thickness. It is underlain by alternating layers of alluvial stiff to hard clay and dense to very dense sand to gravel. The well-known Bangkok soft clay has high plasticity, low strength and high compressibility. Values for undrained shear obtained from the undrained triaxial shear test (UIC) and field vane shear tests show a larger scatter and included some very low measurements in first stiff clay and the second hard clay layers. Fig. 101 shows the data obtained from the site investigation and laboratory (Oedometer and CRS test) tests at a nearby construction site (DMR 2011). It follows that the clay layers (soft to very stiff) can be considered as normally to slightly overconsolidated. The undrained shear strength ratio of the normally consolidated clay can be assumed to be $S_u = 0.265\sigma'_{v0}$ (for triaxial compression mode with $K_0 = 0.5$) (Seah & Lai 2003).

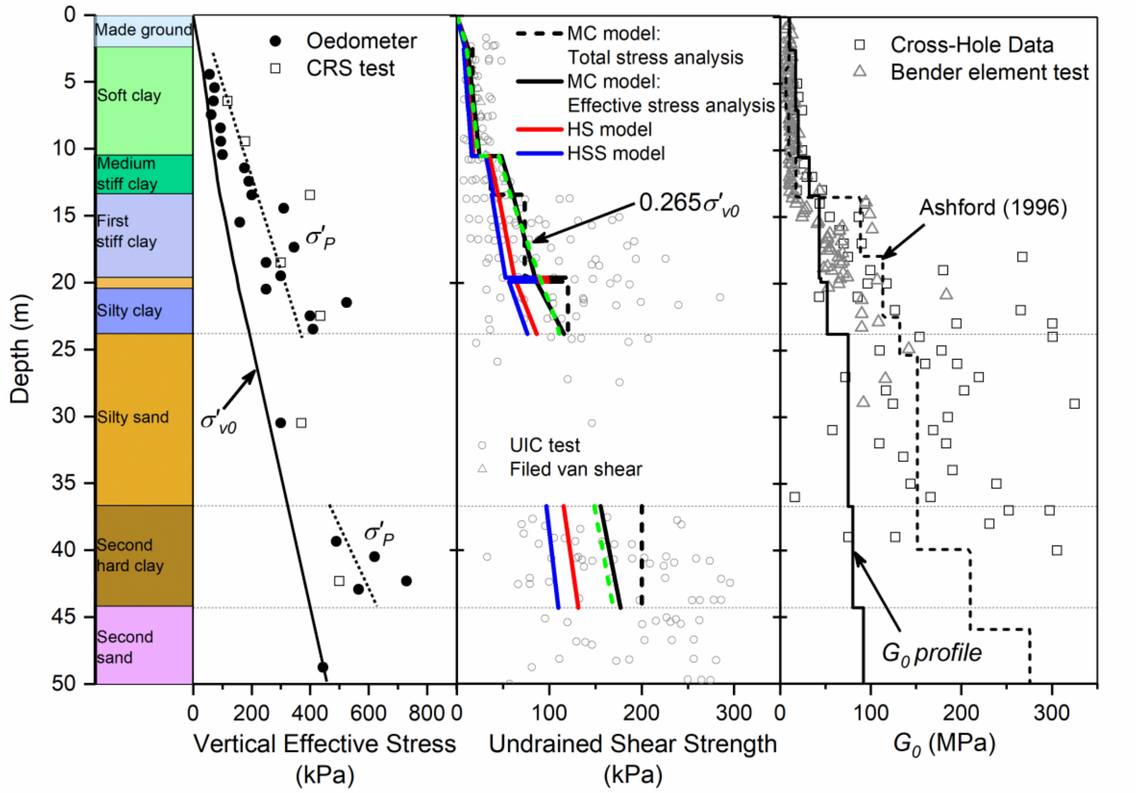

Fig. 101: Soil profile with measured data in Bangkok subsoil

7.1.2 FEM mesh and soil models

Finite element simulations were carried out representing one particular cross-section. Measurements of surface settlement and lateral wall deflections are obtained from inclinometer data obtained around the station periphery to validate plane strain assumptions. Fig. 102 depicts the finite element mesh with the properties of the structural support elements.

The Mohr-Coulomb (MC), Hardening Soil (HS) and Hardening Soil Small (HSS) models were used to represent the mechanical behaviour of the soils and parameters are summarised in Tab. 11 and Tab. 12. A small strain shear modulus G_0 was adopted according to the in-situ test and laboratory tests, as shown in Fig. 101. The suggested profile by Ashford et al. (1996) is plotted for comparison. The reference shear strain at 70%G_0 is taken from the stiffness reduction curve (Teachavorasinskun et al. 2002, see Fig. 21).

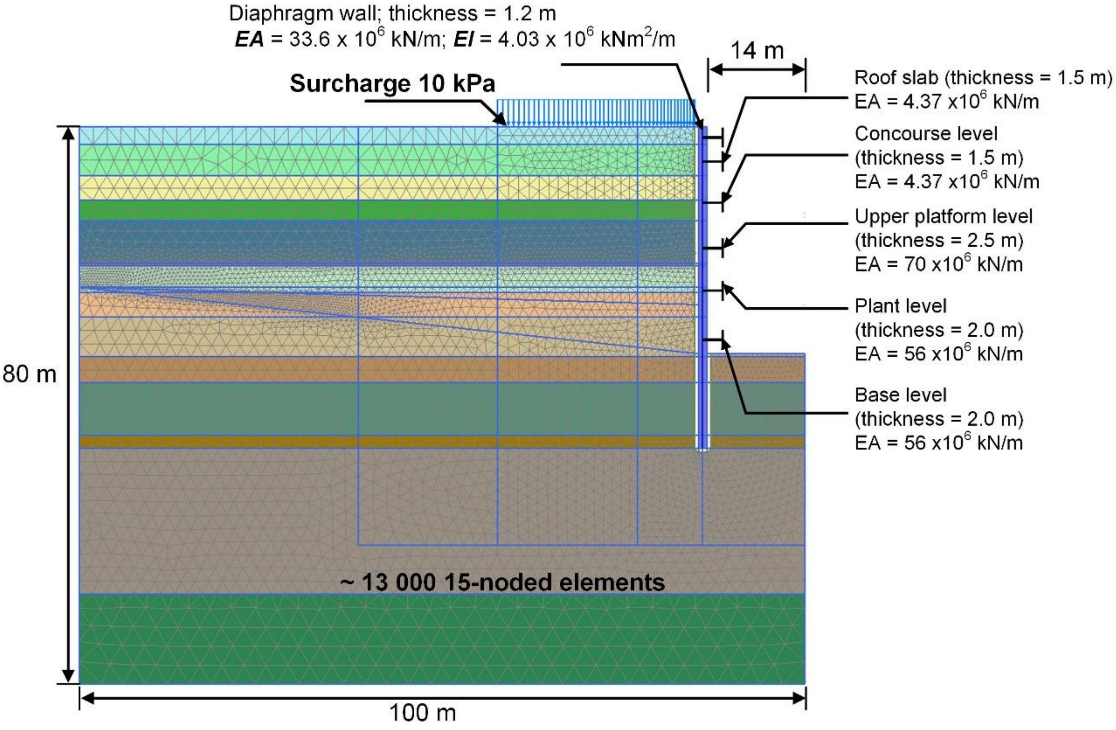

Fig. 102: FE-Mesh and structural properties

Tab. 11: Input parameters of MC model for Bangkok soft soil

	Unit	MG	SC	MSC	FSC	Cs	Sc	Ss	HC	SS
γ_{unsat}	[kN/m^3]	18	16	16.9	19.4	19.5	20.5	19.5	20	20
γ_{sat}	[kN/m^3]	18	16	16.97	19.45	20.7	21.3	21	20.2	21.4
E_u	[MN/m^2]	13.5	8.35[a]	18.4	76.7	65.8	113	135	204	263
E'	[MN/m^2]	10.8	8.35[a]	18.4	38.3	36.6	62	114	93	243
ν	[-]	0.35	0.35	0.35	0.35	0.35	0.35	0.29	0.35	0.29
c'	[kN/m^2]	0.1	0.1	0.1	0.1	0.1	0.1	0.1	0.1	0.1
φ'	[°]	25	23	23	23	27	23	36	23	36
ψ'	[°]	0.0	0.0	0	0	0	0	6	0	6
S_u	[kN/m^2]	0.2	16.7[b]	36.72	73.48	120	120	0	200	0
k_x, k_y	cm/day	8.6	0.04	0.09	0.09	0.86	0.09	8.6	0.02	8.6

[a] stiffness increases with depth = 1100z, where z is a reference depth

[b] undrained increases with depth 2.2z, where z is a reference depth

Tab. 12: Input parameters of HS and HSS models for Bangkok soft soil

	Unit	MG	SC	MSC	FSC	Cs	Sc	Ss	HC	SS
E_{50}^{ref}	[MN/m^2]	5.0	5.8	9.2	10.2	9.3	15.6	31	17.1	39
E_{oed}^{ref}	[MN/m^2]	5.0	5.8	9.2	10.2	9.3	15.6	31	17.1	39
E_{ur}^{ref}	[MN/m^2]	25.0	46.6	73.4	102.2	27.8	124.6	120	170	117
m	[-]	0.5	1	1	0.85	0.8	0.85	0.8	0.8	0.5
R_f	[-]	0.9	0.9	0.9	0.9	0.9	0.9	0.9	0.9	0.9
c'	[kN/m^2]	0.1	0.1	0.1	0.1	0.1	0.1	0.1	0.1	0.1
φ'	[°]	25	23	23	23	27	23	36	23	36
ψ'	[°]	0.0	0.0	0	0	0	0	6	0	6
ν_{ur}	[-]	0.2	0.2	0.2	0.2	0.2	0.2	0.2	0.2	0.2
K_0^{nc}	[-]	0.57	0.61	0.61	0.61	0.5	0.61	0.42	0.61	0.4
G_0^{ref}	[MN/m^2]	10.4	19.5	32	43	45	52	75	80	92
$\gamma_{0.7}$	[%]	0.04	0.06	0.02	0.002	0.02	0.02	0.02	0.01	0.02
R_{int}	[-]	0.65	0.7	0.65	0.6	0.7	0.7	0.7	0.6	0.8

Note: Cs, Sc, and Ss are assumed as drained.

The calculations are carried out as fully-coupled consolidation analyses. The stage excavations are presented as follows:

- Generation of initial stress (K_0-procedure)
- Activation of diaphragm wall (wished-in-place)
- Activation of surcharge (10 kPa)
- Excavation to 1.5 m
- Installation of a temporary support system
- Consolidation - 14 days
- Excavation and groundwater lowering to 6.5 m
- Installation of roof slab
- Consolidation - 25 days
- Excavation and groundwater lowering to 12.4 m
- Installation of concourse slab
- Consolidation - 62 days
- Excavation and groundwater lowering to 19.9 m

- Installation of upper platform slab
- Consolidation - 49 days
- Dewatering and groundwater lowering to 26.5 m
- Excavation to 25.5 m
- Installation of plant slab
- Consolidation - 46 days
- Dewatering and groundwater lowering to 33.5 m
- Excavation to 32.6 m
- Installation of base slab
- Consolidation - 133 days

7.1.3 Reference analysis

In Fig. 103 lateral deflections of the diaphragm wall are shown at various stages of the excavation. At the early stages of excavation (i.e. excavation to the roof level and the concourse level, Fig. 103a and Fig. 103b), the HS and HSS predict similar deflected shapes of cantilever wall movements and correspond satisfactorily with the field observations. However, large discrepancies in lateral wall movements are obtained by the MC model (total and effective stress analyses). This clearly demonstrates the influence of stress dependent and small strain stiffness and consequently more realistic wall deflections at intermediate stages can be obtained employing advanced constitutive model.

The computed lateral deflections in Fig. 103d show a bulge movement around the excavation level, which contrasts with the monitored data. This may attributable to the 3D effect of excavation, the influence of performing the dewatering, and the assumption of undrained modelling for silty sand layers.

Fig. 104a compares lateral wall movement and Fig. 104b compares surface settlement at the final excavation level and it is apparent that the HS and HSS models show quite different behaviour compared to the MC model.

In Fig. 104a the lateral wall movements predicted by the MC model with total stress analysis show the largest deflections, but of course this strongly depends on the chosen stiffnesses. The HSS model predicts a deeper settlement trough at the final excavation level than the HS model (see Fig. 105), which is also more in agreement with the monitored data. However, it should be mentioned that the choice of parameter $\gamma_{0.7}$ (shear strain at which the G_{max} is reduced to 70%) is a sensitive and parameter has an influence on the results of the HSS model.

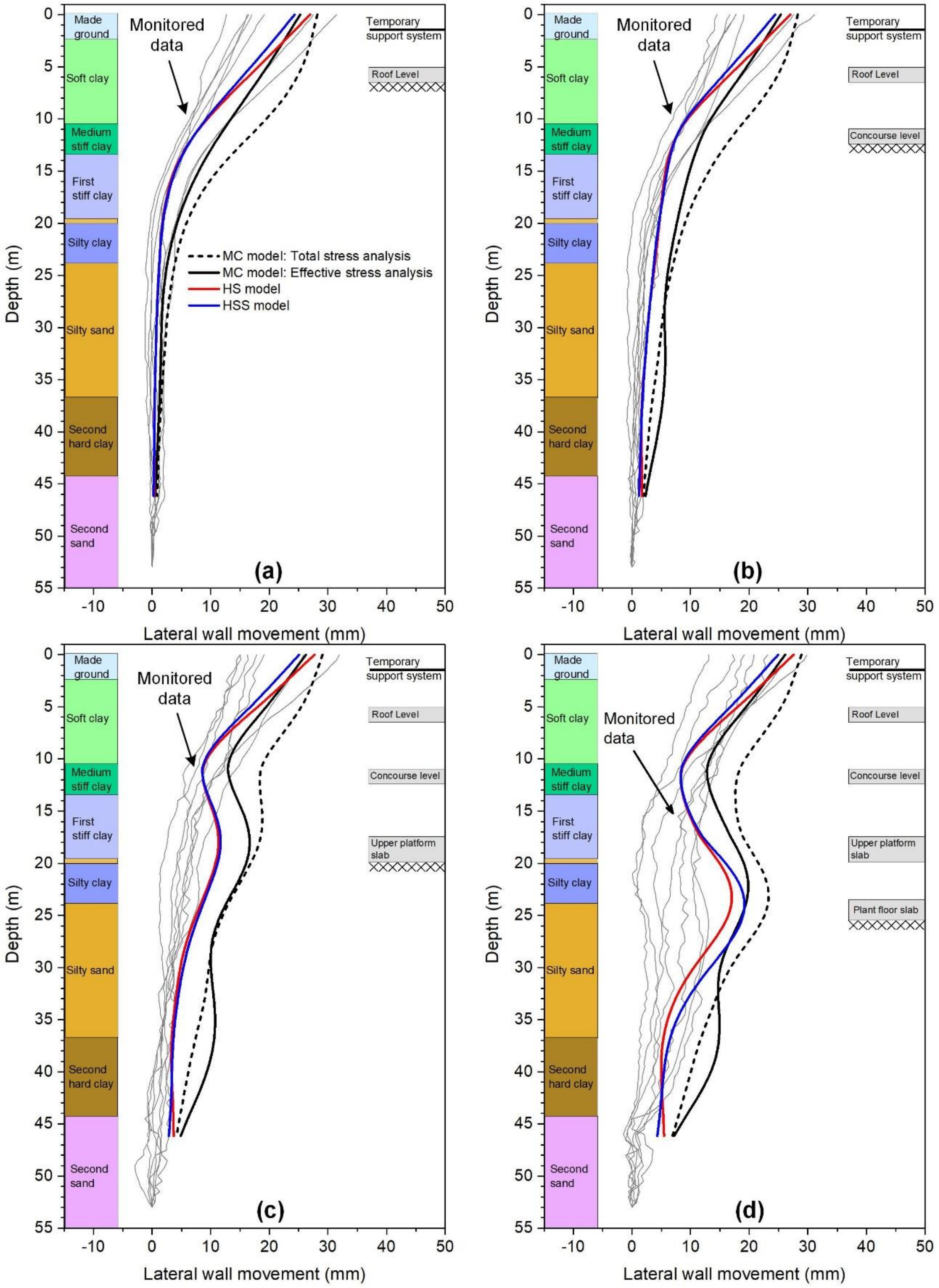

Fig. 103: Comparison of lateral deflection for different stages of excavation

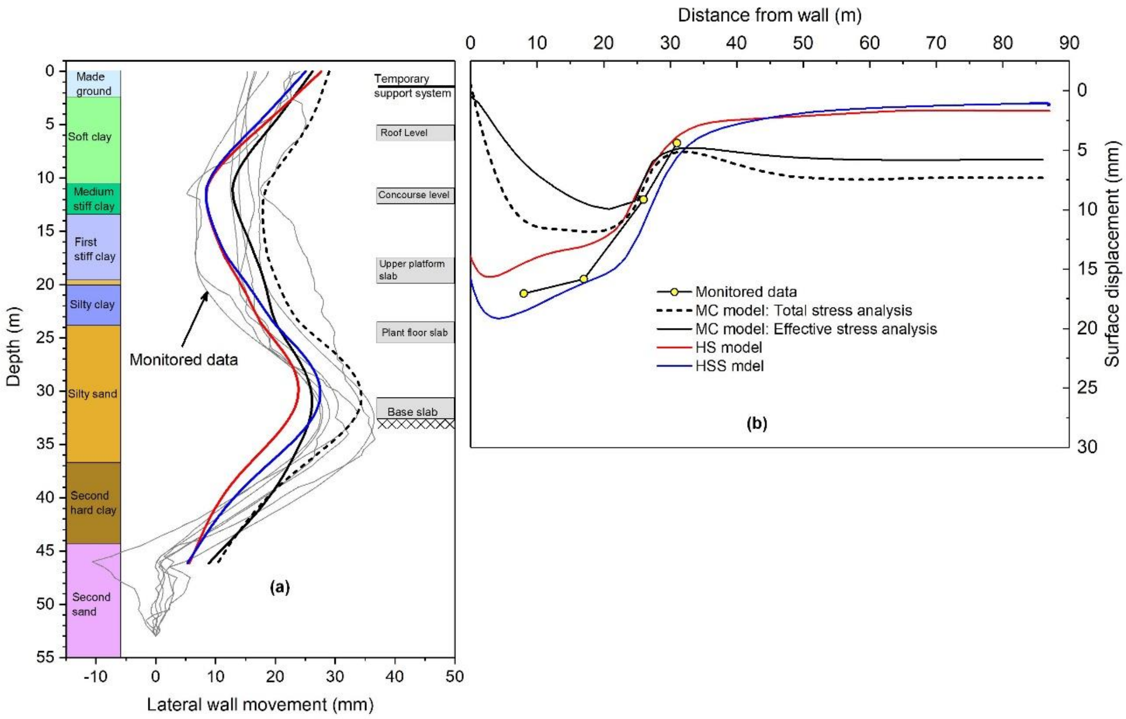

Fig. 104: (a) lateral deflection; (b) surface displacement of final stage of excavation

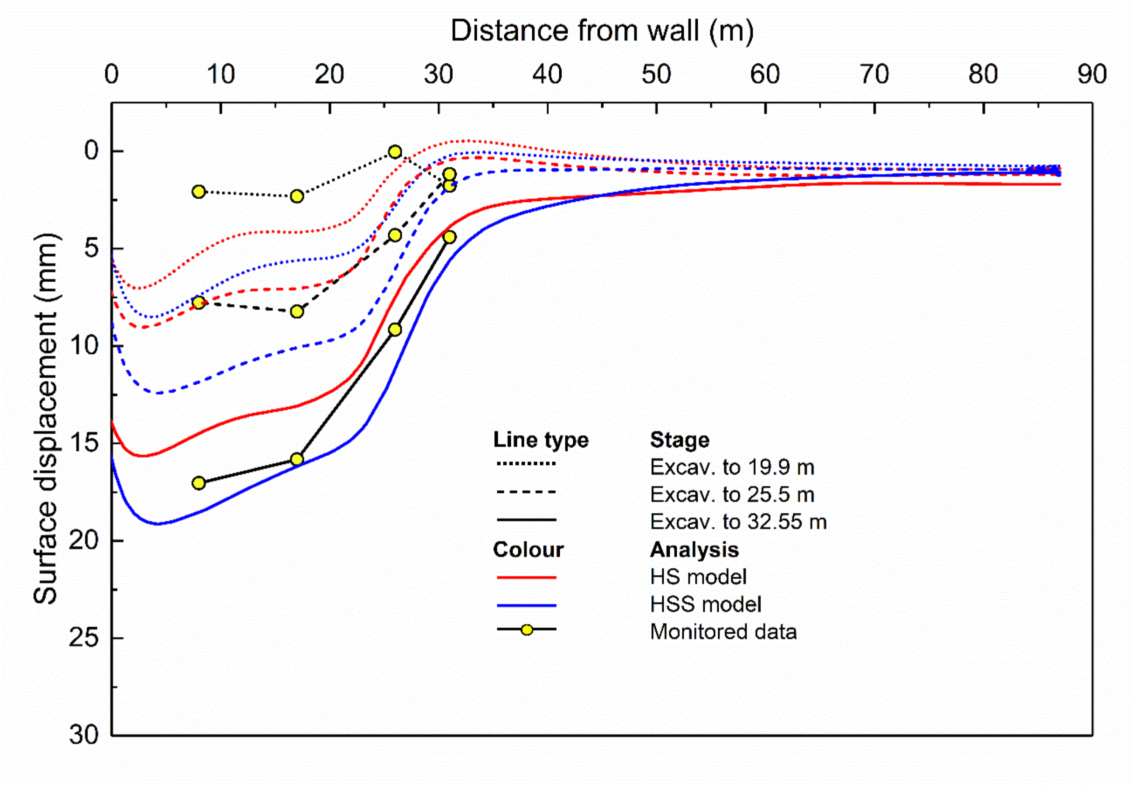

Fig. 105: Predicted surface displacement for HS and HSS models

7.1.4 Influence of stress dependent stiffness

In the standard HS and HSS model stiffness is dependent on σ_3 which may lead to unrealistic values when highly overconsolidation soils are unloaded as is the case at the base of an excavation. Therefore, an extensive parametric study has been carried out in order to investigate the influence of stress dependent stiffness using the Generalized Hardening Soil model (GHS) to describe the mechanical behaviour of the clay layers.

Only a short explanation of the GHS model is given herein. The GHS model is a user-defined soil model which allows the use of different configurations for the stress and strain dependency. It is a more modular version of the Hardening Soil model with small strain stiffness. These features are described as follows:

- *Stress Dependent Stiffness*, i.e. the soil stiffness $\boldsymbol{E_{ur}}$ is constant during the calculation based on the reference stiffness [0], or the $\boldsymbol{E_{ur}}$ is constant during the phase, but based on the stress at the beginning of the calculation phase [1], or it is updated for every calculation step based on the chosen stress dependency formula [2].
- *Strain Dependent Stiffness*, can be considered either as in the HS model [0], or the HSS model [1]
- *Stress Dependency Formula*, for which the stress dependency can be considered, namely:
    - stress dependency based on σ_3 and strength parameters as in the HSS model [0], as shown in Equation 10,
    - stress dependency based on σ_3 and preconsolidation pressure p_c [1],

$$E_{ur} = E_{ur}^{ref}\left(\frac{(\sigma_3 + p_c)/2}{p^{ref}}\right)^m \tag{18}$$

    - and stress dependency based on mean effective stress p' and preconsolidation pressure p_c [2].

$$E_{ur} = E_{ur}^{ref}\left(\frac{(p' + p_c)/2}{p^{ref}}\right)^m \tag{19}$$

In case of option [1] or [2], a minimum value of the numerator of $p^{ref}/100$ is used.

It should be noted that other stiffnesses E_{50}, E_{oed} and G_0 follow the same stress-dependency formula as E_{ur}.

The investigated cases for this analysis are shown in Tab. 13. The analyses adopted the GHS model for the clay layers whereas the HSS model was used for the other layers (see Fig. 101 and Tab. 12). It is acknowledged that the clay layers in Fig. 101 are lightly over-consolidated ($OCR = \sigma'_p/\sigma'_{v0} > 1$) due to deposition and stratigraphy. However, for the purposes of this study (GHS1 and GHS2), the current analyses have been carried out using $OCR = 1$, and, therefore, the preconsolidation pressure p_c in Equation 8 and/or 9 is equivalent to the initial in-situ stress.

Tab. 13: Investigated cases for stress dependent stiffness

Formulation	Case analyzed		Remark
	GHS1	GHS2	
Stress dependent stiffness	2	2	Stiffness updated within each calculation step
Strain dependent stiffness	1	1	HS small model
Stress dependent formula	1	2	Investigated scenarios

Note: OCR = 1 is assumed for both cases.

7.1.5 Influence of anisotropic small strain stiffness

In previous analyses, the soil is assumed to behave isotropically at very small strains (< 10^{-6}), even though the strongly cross anisotropic behaviour of natural soil stiffness has been identified through laboratory tests (e.g. Atkinson 1975, Gasparre 2005). Schädlich (2012) and Schädlich & Schweiger (2013) summarized the degrees of anisotropy on various soil types, i.e. E'_h/E'_v ≈ 0.8…1.2 for sands, E'_h/E'_v ≈ 0.4…0.7 for gravel, E'_h/E'_v ≈ 0.4…0.7 for gravel, and E'_h/E'_v ≈ 1.7…2.3 for over-consolidated clay.

A recent investigation of the cross-anisotropic elastic parameters of Bangkok clay Ratananikom et al. (2013) and Yimsiri et al. (2013) showed a significant degree of anisotropy under isotropic and general stress states, and a degree of anisotropy E'_h/E'_v of 1.3 was reported. Similar degrees of anisotropy have been published for natural sedimentary clay (E'_h/E'_v = 1.3-1.7, Nishimura 2014), and soft Taipei clay (E'_h/E'_v = 1.15-1.44, Teng, et al. 2014).

In this section, the influence of anisotropic small strain stiffness on ground movements during excavation is investigated. An enhanced Multilaminate constitutive model accounting for cross anisotropic elasticity in the small strain range was adopted for soft clay to first stiff clay layers, whereas the HSS model was used for the other layers. The details of this model are presented in Schädlich, (2012) and Schädlich & Schweiger (2013). The model description has been described briefly in section 3.3.6. The focus of this study is the small strain stiffness behaviour.

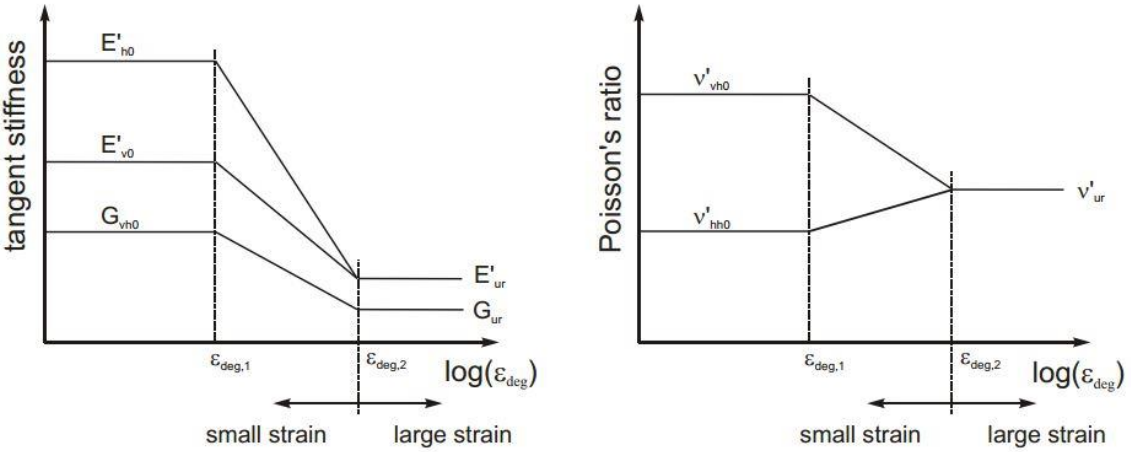

Fig. 106: Degradation of anisotropic small strain stiffness, Poisson's ratios and transition to large strain behaviour (after Schädlich 2012)

Multilaminate constitutive models are based on the concept that material behaviour can be formulated in terms of a number of integration planes with varying orientations. Each plane represents a sector of a virtual sphere of unit radius around the stress point and is assigned a weight factor according to the proportion of its sector with regard to the volume of the unit sphere. The local stress vector is obtained by projecting the global stress vector into the integration planes, using the transformation matrix. Local plastic strain increments are calculated according to plasticity theory on the integration plane level.

It is assumed that the initially anisotropic material approaches isotropy with increasing accumulated shear strain. The small strain stiffness degradation depends on the magnitude of the deviatoric strain (ε_{deg}). A tri-linear function describes the degradation with regard to logarithmic of ε_{deg}, as illustrated in Fig. 106. The parameters $\varepsilon_{deg,1}$ and $\varepsilon_{deg,2}$ represent input parameters and define the deviatoric strain at the onset of degradation and the transition to large strain. Fig. 107 shows an example of the adopted function of the small strain degradation of the model for Bangkok soft clay.

The stress dependence of anisotropic stiffness parameters is taken into account for the initial stress state, according to Equation 20. The same exponent m is assumed for all axial and shear moduli. The input values $E'_{h0,iso}$, $E'_{v0,iso}$ and $G_{vh0,iso}$ characterize the inherent anisotropy of the material and, hence, refer to isotropic stress states. Changes in elastic stiffness parameters after the initial stress state depend on changes in mean stress p' (Equation 21).

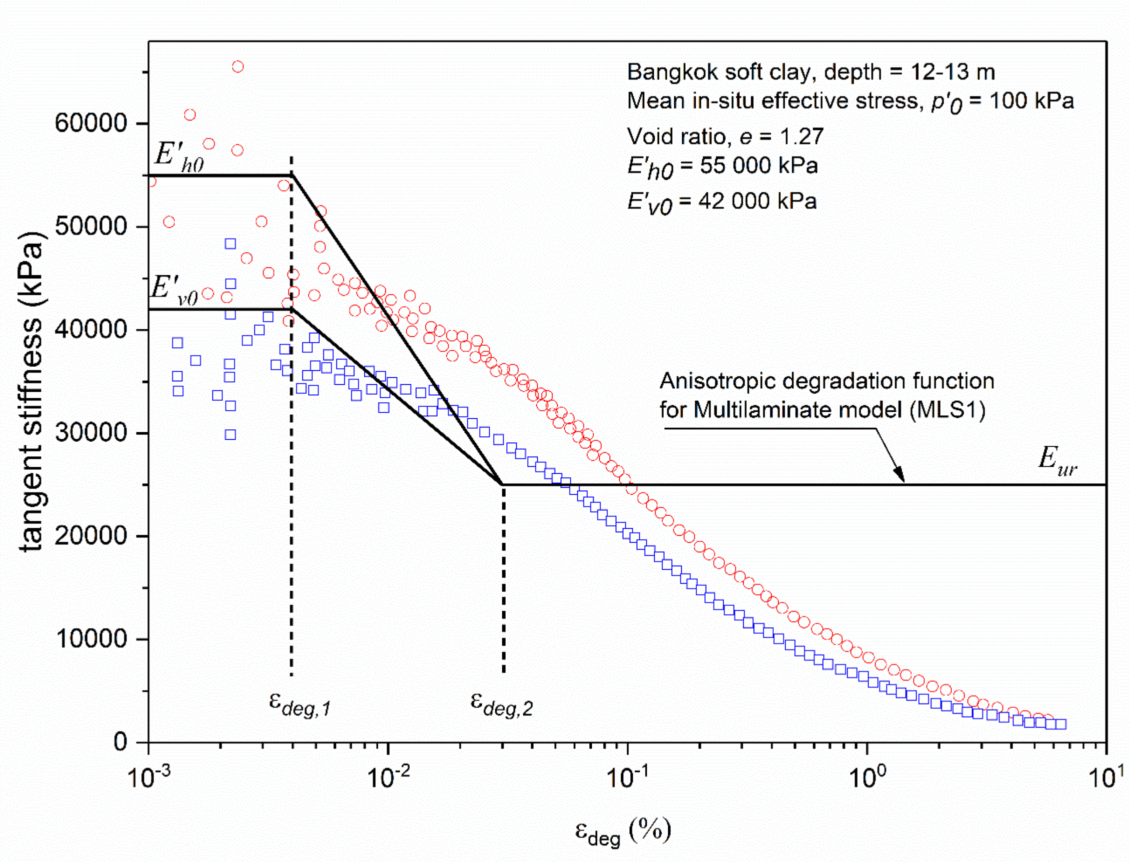

Fig. 107: Degradation of anisotropic small strain stiffness for Multilaminate model and laboratory test (Yimsiri et al. 2013)

$$E'_{h0,ref} = E'_{h0,iso} \cdot \left(\frac{\sigma'_{h0}}{p'_0}\right)^m \; ; \; E'_{h0,ref} = E'_{h0,iso} \cdot \left(\frac{\sigma'_{h0}}{p'_0}\right)^m \; ;$$

$$G_{vh0,ref} = G_{vh0,iso} \cdot \left(\frac{\sqrt{\sigma'_{v0} \cdot \sigma'_{h0}}}{p'_0}\right)^m \tag{20}$$

$$E'_{h0} = E'_{h0,ref} \cdot \left(\frac{p'}{p_{ref}}\right)^m \; ; \; E'_{v0} = E'_{v0,ref} \cdot \left(\frac{p'}{p_{ref}}\right)^m \; ;$$

$$G_{vh0} = G_{vh0,ref} \cdot \left(\frac{p'}{p_{ref}}\right)^m \tag{21}$$

The input parameters are given in Tab. A 2. The small strain stiffness moduli for conducting parametric studies are listed in Tab. 14. Two sets of parameters are investigated. MLS1 and MLS2 denote different ratios of horizontal to vertical small strain stiffness (E'_h/E'_v). In MLS1, the E'_h/E'_v is 1.3, as reported by Yimsiri, et al. (2013), and the small strain modulus is the same as with the HSS model (Tab. 12). In MLS2, only the E'_h/E'_v is decreased to 0.5. Anisotropic Poisson's ratios υ'_{vh}= 0.077 and υ'_{hh}= 0.1 have been utilized within all calculations, as well as the stiffness degradation parameters $\varepsilon_{deg,1}$ = 4×10^{-3} and $\varepsilon_{deg,2}$= 3×10^{-2}.

Tab. 14: Case analyses on the influence of anisotropic small strain stiffness

Case analyses	$E'_{h0,ref}$ (MPa)	$E'_{v0,ref}$ (MPa)	E'_{h0}/E'_{v0}	$G_{vh0,ref}$ (MPa)
MLS_1	55	42	1.3	see
MLS_2	30	60	0.5	Tab. 12

Fig. 108 compares the results of total displacement at the final excavation stage from the HS, HSS and GHS models (see Tab. 13). The influence of the stress dependency configurations of the GHS model is obvious and a reduction of uplift movement at the bottom of the excavation of about 25-28% compared to HS and HSS models is observed. However, it is observed that the difference between GHS1 and GHS2 is small because the analyses have been carried out using $OCR =$ 1, and, hence, the preconsolidation pressure p_c is equivalent to the initial in-situ stress.

Wall deflection at various stages for different investigated constitutive models is shown in Fig. 109. The influence of different assumptions of stress dependent stiffness has a negligible effect on lateral wall movement. Taking into account the anisotropic small strain stiffness for MLS1 reduces wall deformation by about 23%, particularly in soft clay layers, whereas with MLS2 wall deflection at the top increased by 25% with respect to the isotropic small strain stiffness case (HSS model). A similar trend can be observed for the final stage of excavation in Fig. 110.

The prediction of the settlement trough behind the diaphragm wall is shown in Fig. 111. The predicted ground surface settlement trough with monitored data shows a quantitative and qualitative improvement, especially the concave distribution of settlement at a distance of 40 m behind the diaphragm wall. The settlement for the case considering the influence of stress dependent stiffness delivers only marginal differences between cases GHS_1 and GHS_2, and indicates a wider as well as a deeper settlement trough, but not for the analyses with the multilaminate model. Taking anisotropic small strain stiffness into account reduces surface settlement at the stage before the final level has been reached (Fig. 111a and Fig. 111b).

Additionally, the MLS_1 with high stiffness in the horizontal direction ($E'_h/E'_v =$ 1.3) predicts the trend of increasing settlement with an acceptable agreement with the measured data for all stages. The influence of anisotropic elastic stiffness on excavation in soft soil is confirmed by Teng et al. (2014), who reported a difference of about 10-43% between anisotropic and isotropic models when predicting wall deflection, settlement and lateral soil movement behind walls. The model used in the study incorporated anisotropy (E'_h/E'_v = 1.38-1.54) and the degradation of shear stiffness G'_{hh}/G'_{vv} = 1.15-1.44 at the small strain region. The difference in vertical initial vertical stiffness in MLS_2 delivers deeper and narrower settlement troughs and this emphasizes again the influence of anisotropy in the small strain range.

It follows from Fig. 112 that the calculated bending moments are higher with the MC model with total stress analysis compared to more advanced models.

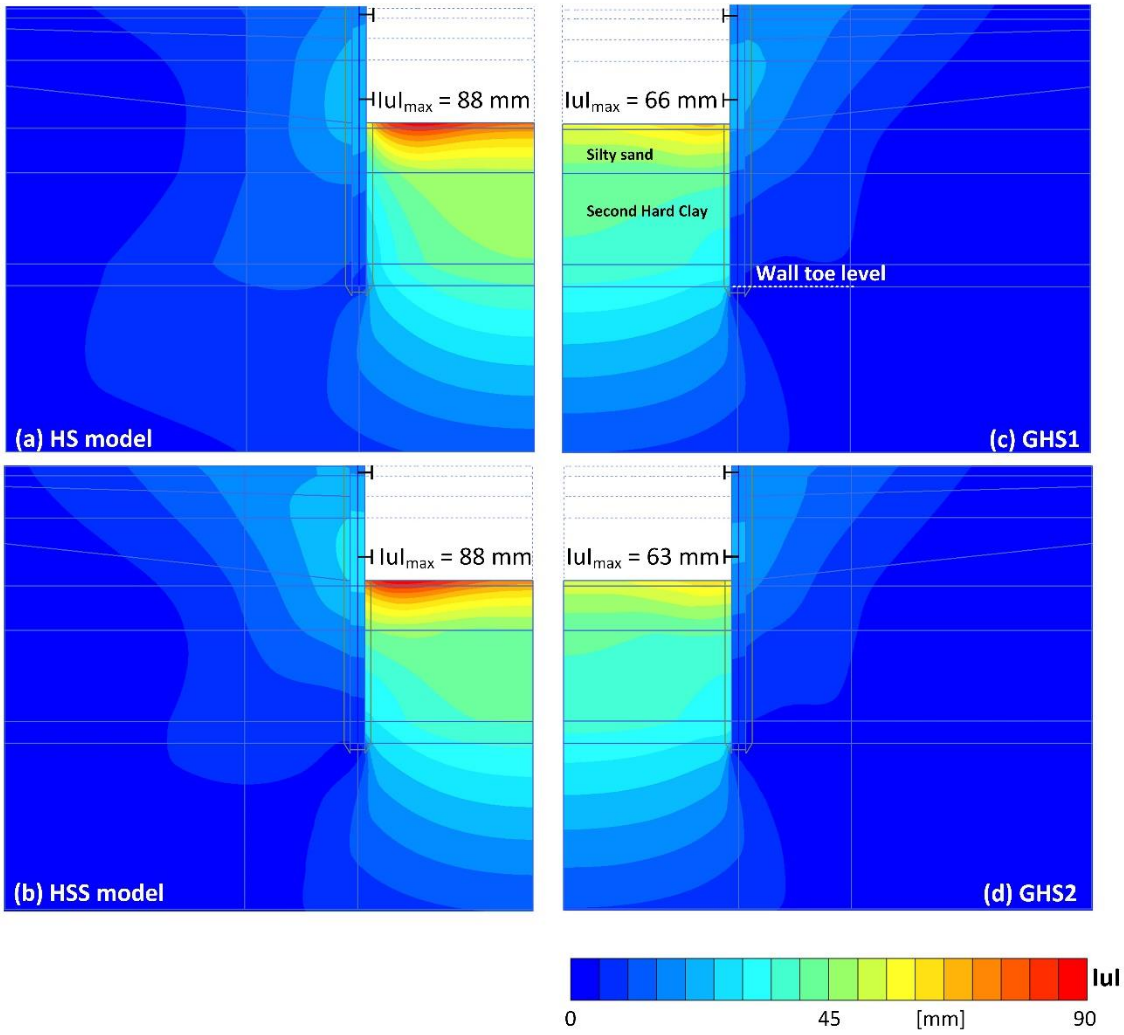

Fig. 108: Contours of total displacement at base level excavation

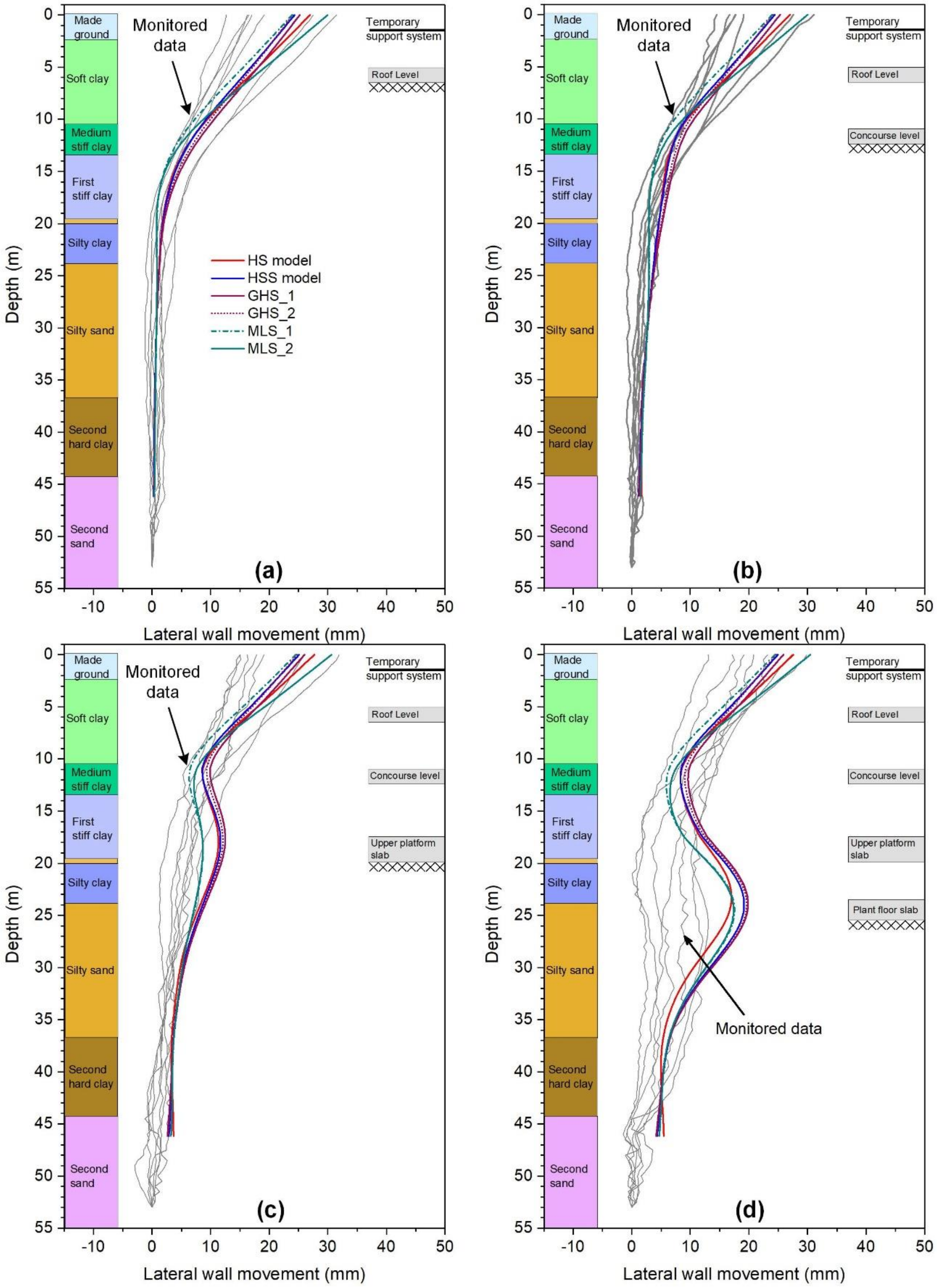

Fig. 109: Comparison of lateral deflection for different stages of excavation

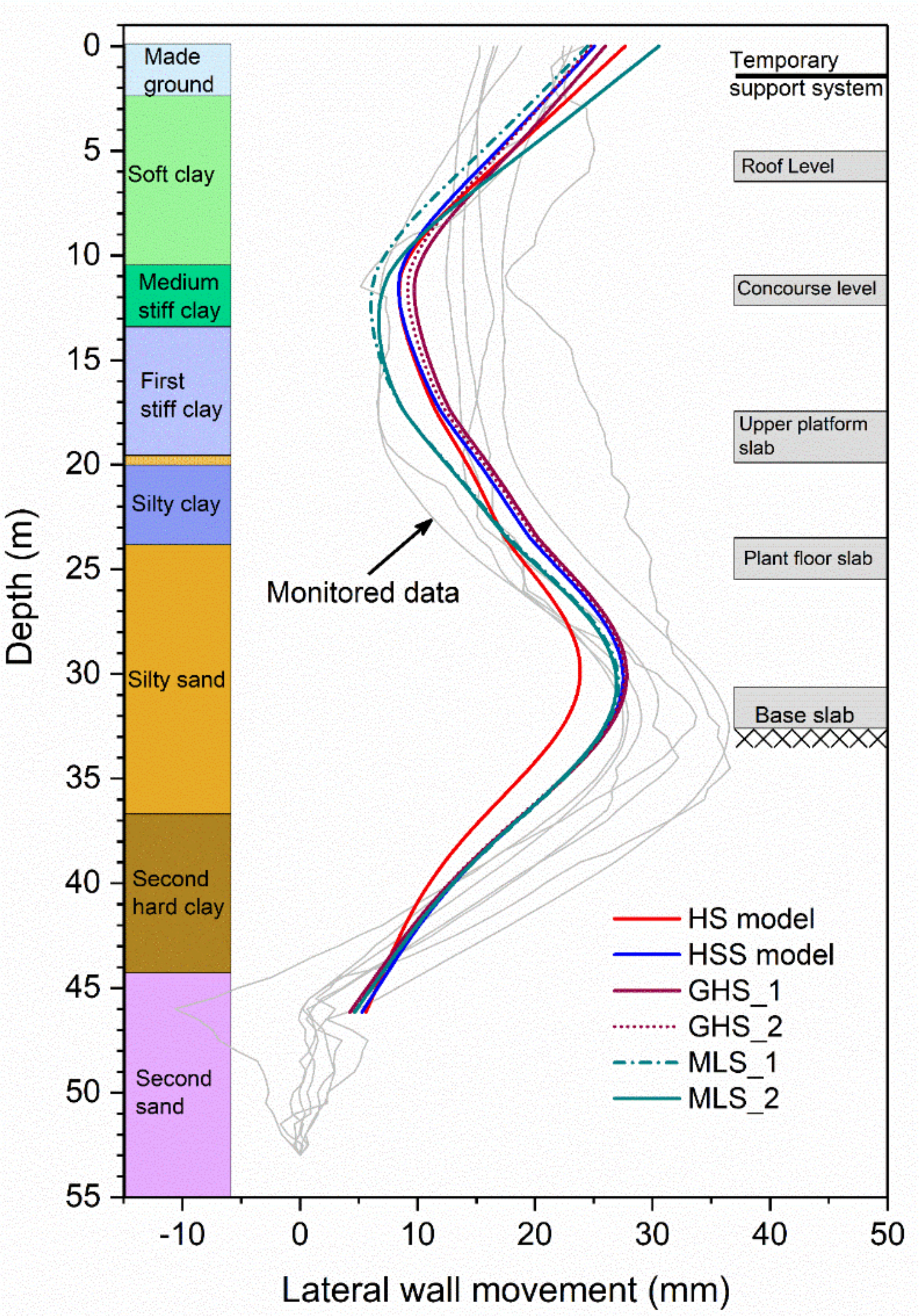

Fig. 110: Comparison of lateral deflection for different models at the final excavation

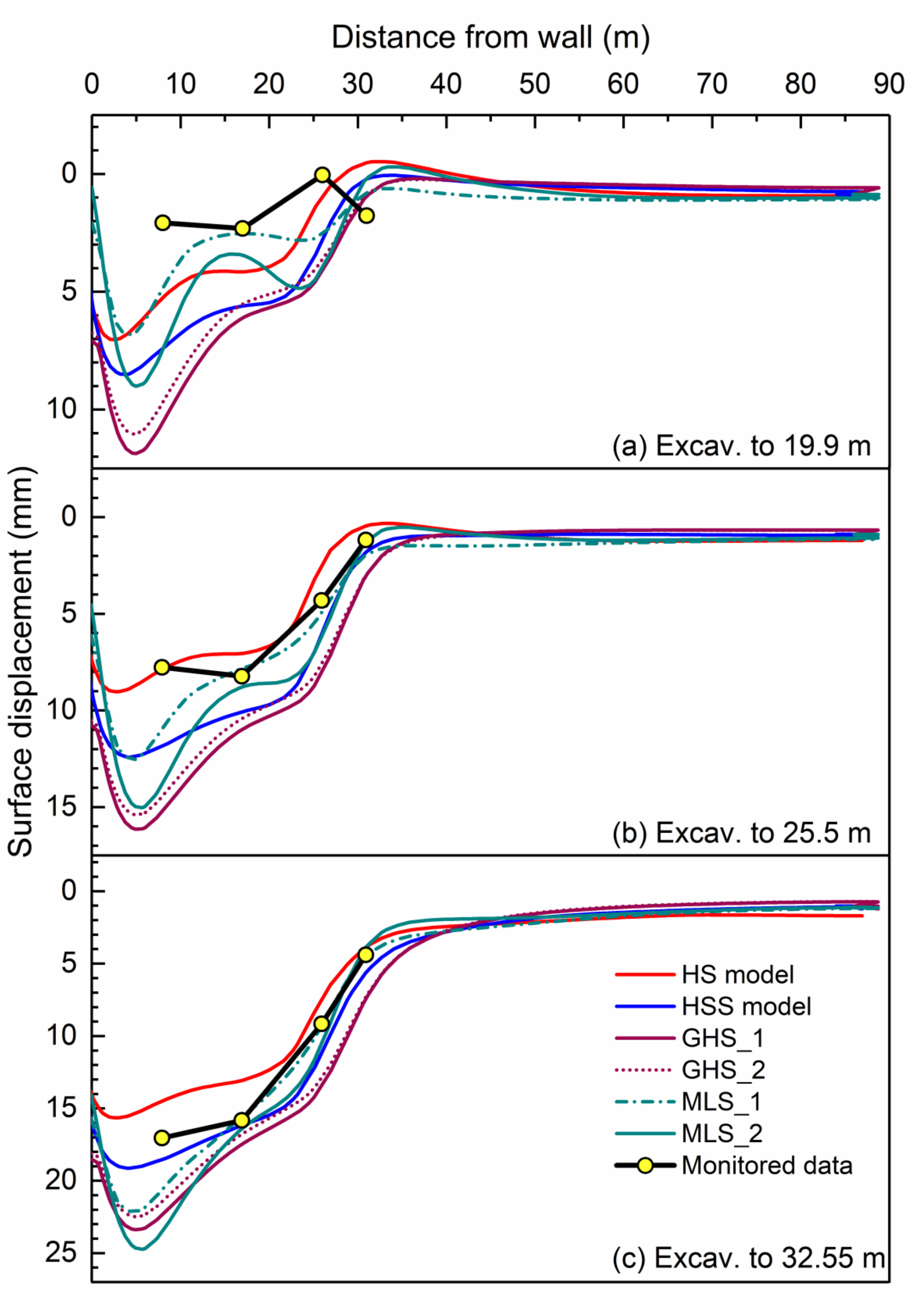

Fig. 111: Predicted surface displacement with different models

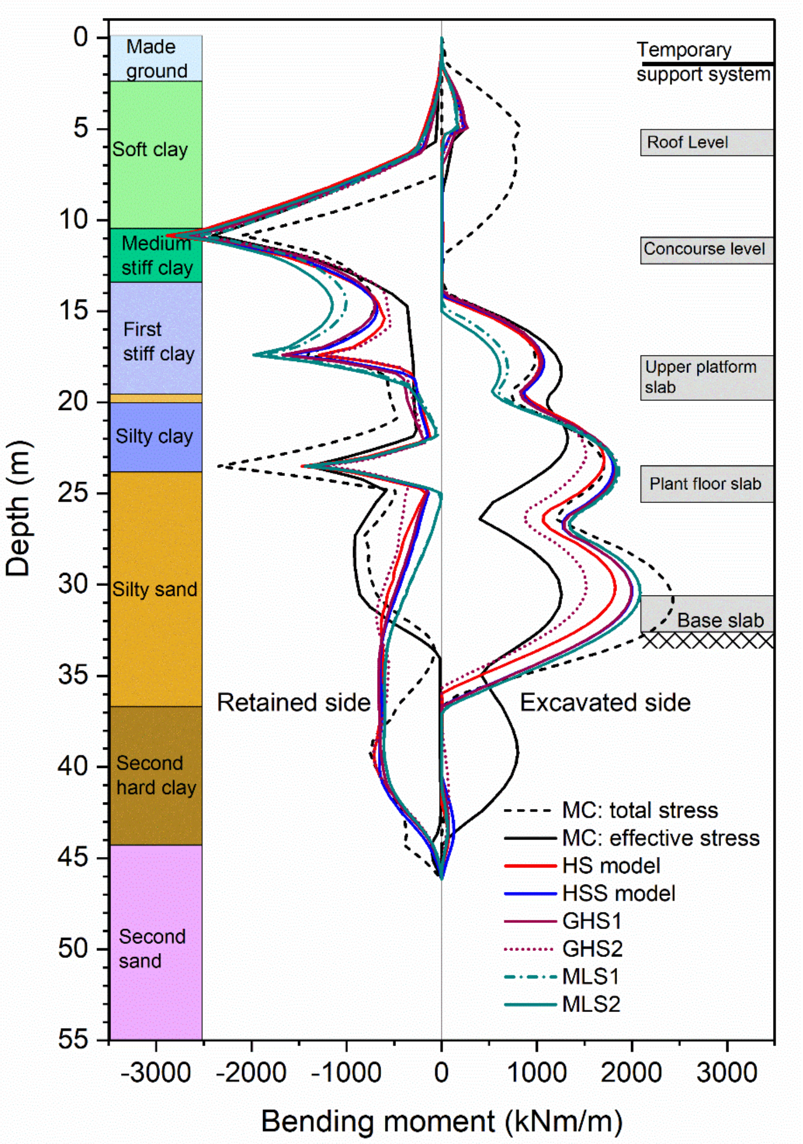

Fig. 112: Computed bending moment at the final stage of excavation

7.2 Time-dependent effects of support systems

7.2.1 Problem description

A 33.2 m diameter circular sheet pile wall (or cofferdam), supported by multiple levels of concrete ring beams (RB) was excavated mainly in soft to medium clays layers, namely Chicago glacial clay. The subsoil profile and measured data are summarized in Fig. 113 (Arboleda-Monsalve et al. 2018). The performance of the excavation indicates excessive ground movements exceeding allowable limits (Fig. 114). The concrete ring beams can resist the excavation-induced earth and water pressures only when the circular shape is closed, and concrete is fully cured and therefore sufficient time is elapsed before excavation starts.

In Fig. 114 the lateral wall movement readings are presented. It is observed that a significant lateral wall movement occurred when the excavation reached the soft clay layer (i.e. excavated to RB4 at 83 days and indicated by region (1) in Fig. 114). The rapid excavation from RB1 to RB6 was completed in less than 80 days, as indicated by region (2). Arboleda-Monsalve et al. (2018) reported that the performance of the excavation could be attributed to the combined effects of low curing time, concrete material time-dependent behaviour and water freezing temperature, thus resulting in additional lateral movements. Moreover, it was shown that the low-site-specific temperature during construction (Fig. 114, right), ranging from -5 to 10°C reduced the concrete 28-day compressive strength and nearly doubled the time necessary to reach 100% concrete maturity with respect to ideal curing conditions. The periods of (3) and (4) represent the delay in construction activities (i.e. construction of deep foundations) and monitoring of long term behaviour. A more detailed description of this project has been given by Arboleda-Monsalve et al. (2018).

An FE-analysis has been carried out in order to demonstrate the importance of the influence temperature and time dependency of structural support systems in predicting the ground movement of the circular excavation.

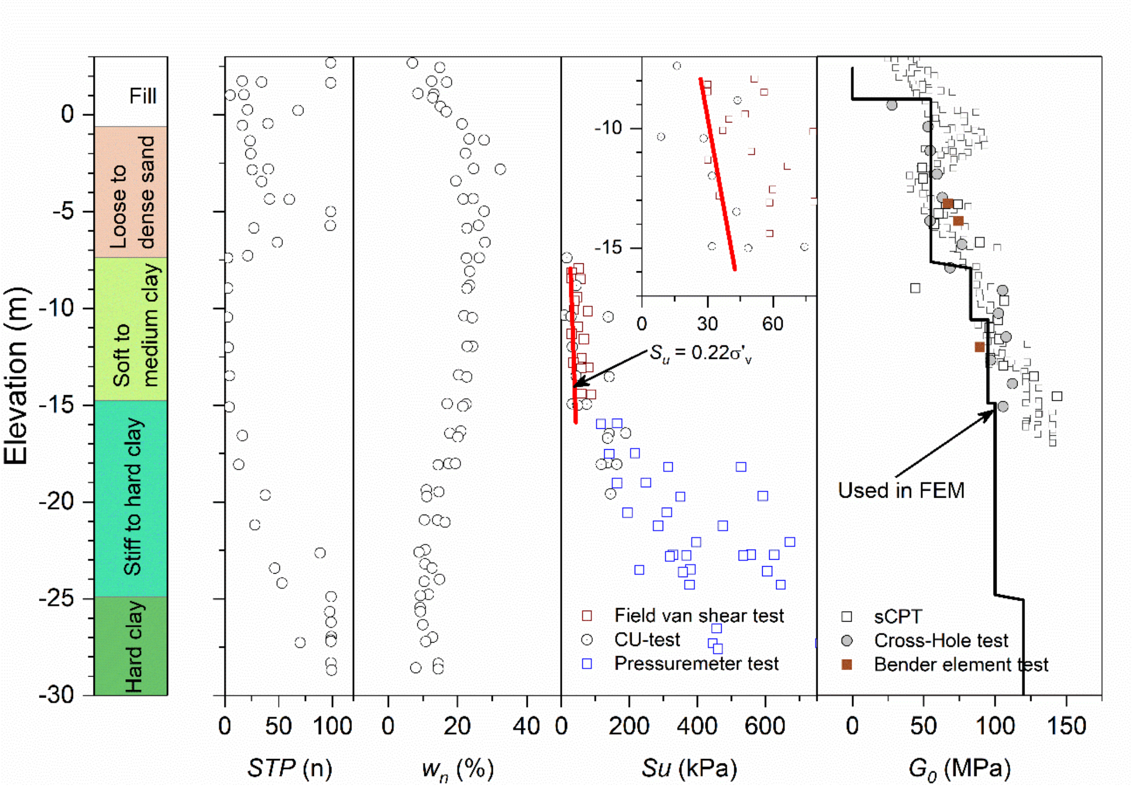

Fig. 113: Subsoil conditions and measured data (after Arboleda-Monsalve et al. 2018)

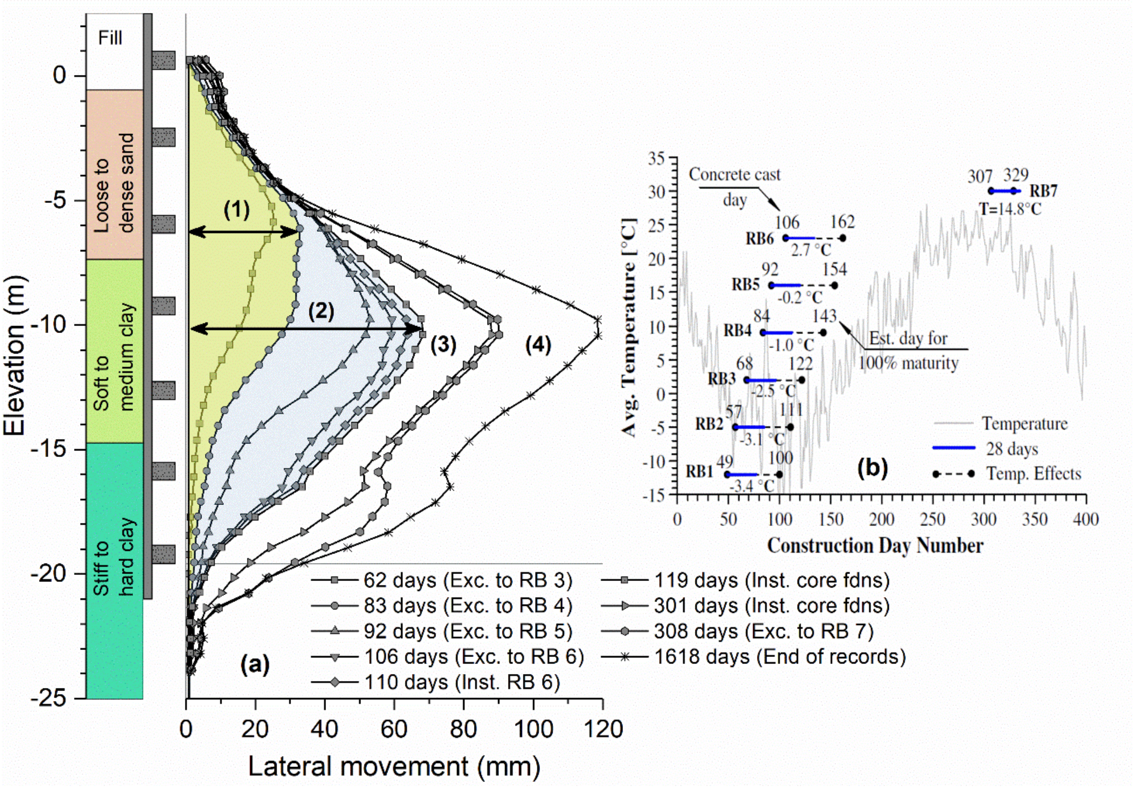

Fig. 114: Lateral ground movements and temperature during excavation (after Arboleda-Monsalve et al. 2018)

7.2.2 FEM mesh and constitutive models

A two-dimensional finite element analysis under axisymmetric conditions was carried out to investigate the time dependency effects of concrete ring beams in the circular excavation. The construction sequence followed in the numerical simulation is depicted in Fig. 115. The following calculation phases are performed: generation of in-situ stress state, activation of sheet pile wall and construction sequences as shown in Fig. 115. The main construction activities (i.e. ring beam installation and excavation) were simulated by plastic calculations, followed by consolidation calculation allowing for the dissipation of excess porewater pressures. The additional surcharge was activated just before the installation of RB3.

The steady-state pore pressures were calculated based on the definition of hydraulic boundary conditions and coefficients of permeability assigned to the different soil layers. Groundwater lowering inside the excavation area was considered as being below base level in each excavation stage.

Fig. 116 shows the details of the finite element mesh. The ring beam was modelled using a continuum element connected directly to the sheet pile wall. The sheet pile wall was modelled as linear elastic material accounting for axial and flexural stiffness of 144.7 mm of thickness.

The HSS soil model is employed for all soil layers. The input parameters have been calibrated against the test data on soft to medium stiff Chicago clay, as reported by Calvello & Finno (2004), Jung et al. (2007), and Finno & Cho (2011) and are listed in Tab. 15.

Fig. 117 compares the experimental and calculated oedometric compression tests for soft clay (SC) and medium stiff clay (MC). The ratio of $E_{50}^{ref}/E_{oed}^{ref}$ was taken as 1.4-1.6 for soft to medium stiff clay and as 2.9 for stiff to hard clay. The $E_{ur}^{ref}/E_{50}^{ref}$ for soft to hard soil ranges from 3-7 with a power of stress dependency stiffness, m of about 1. The stress path obtained with the HSS model predicts reasonably accurately the responses obtained from undrained triaxial compression tests (Fig. 117, right). It is mentioned that OCR > 1 is defined and the back analyses because the CK_0U test indicate that the clay layer is slightly over-consolidated.

Fig. 118 shows acceptable agreement of the calculated secant shear modulus degradation compared with the experiments. The adopted G_0^{ref} profile is indicated in Fig. 113.

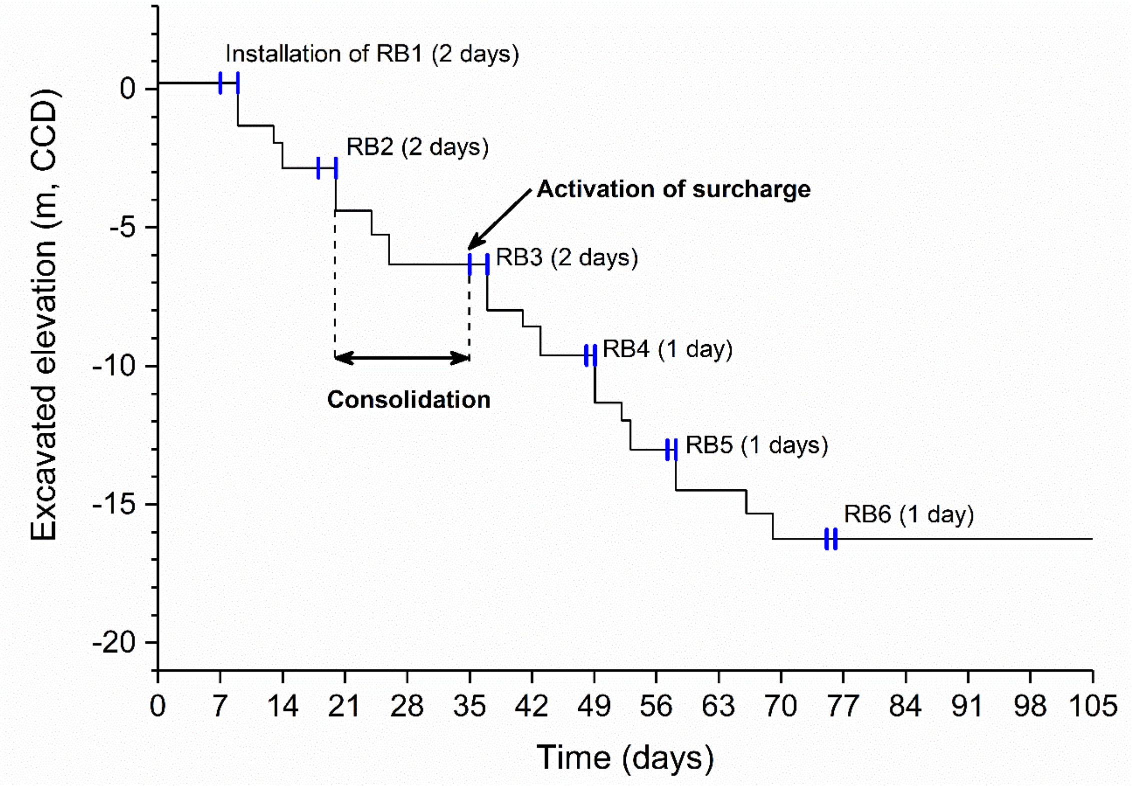

Fig. 115: Excavation sequence adopted in FE-analysis

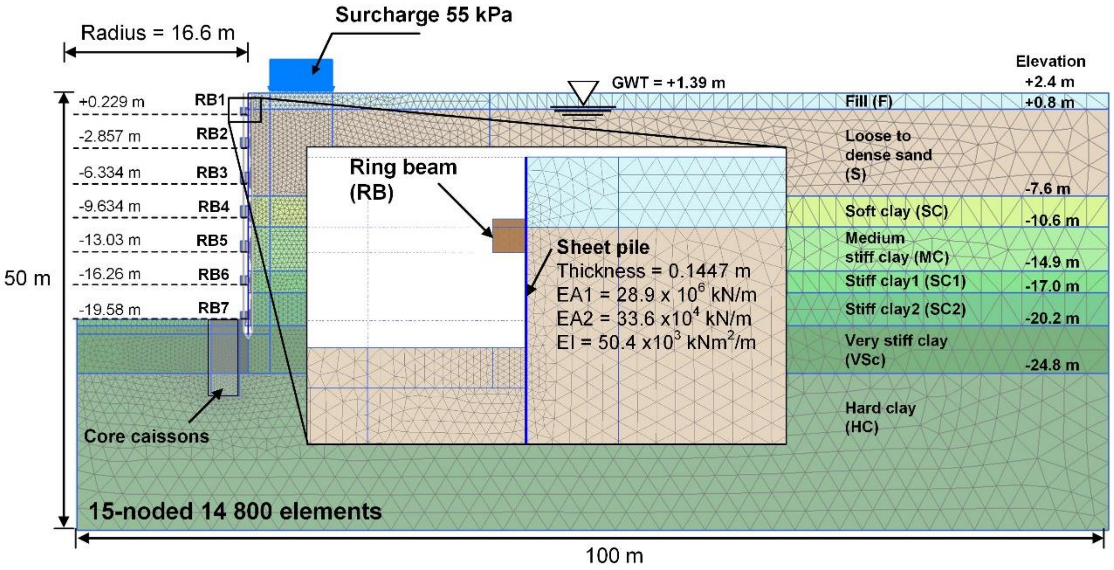

Fig. 116: FE-mesh with details

Tab. 15: HSS model parameters for circular excavation

	Unit	F	S	SC	MC	SC1	SC2	VSc	HC
γ_{unsat}	[kN/m^3]	18.9	18.9	18.9	18.9	18.9	18.9	19.6	19.6
γ_{sat}	[kN/m^3]	18.9	18.9	18.9	18.9	18.9	18.9	19.6	19.6
E_{50}^{ref}	[MN/m^2]	7.2	7.2	2.4	4.0	11.7	11.7	15.3	24.7
E_{oed}^{ref}	[MN/m^2]	7.2	7.2	1.6	2.4	4.1	4.1	2.4	17.3
E_{ur}^{ref}	[MN/m^2]	21.6	21.6	10	30.5	30.5	30.5	46.0	74.0
m	[-]	0.5	0.5	1	1	0.94	0.94	0.94	0.6
OCR	[-]	1.5	1.5	1.5	1.37	1.7	1.7	1.5	1.4
R_f	[-]	0.9	0.9	0.7	0.71	0.83	0.83	0.83	0.9
c'	[kN/m^2]	1	1	0	0	0	0	0	0
φ'	[°]	25	23	23	23	27	23	36	23
ψ'	[°]	0	0	0	0	0	0	0	0
ν_{ur}	[-]	0.2	0.2	0.2	0.2	0.2	0.2	0.2	0.2
K_0^{nc}	[-]	0.47	0.40	0.59	0.52	0.48	0.48	0.6	0.6
G_0^{ref}	[MN/m^2]	-	50	81	95	83.4	120	270	360
$\gamma_{0.7}$	[%]	-	0.01	0.007	0.008	0.012	0.012	0.01	0.01
k_x, k_z	[cm/day]	0.015	1524	0.015	0.015	0.015	0.015	0.015	0.015
k_y	[cm/day]	0.009	1524	0.009	0.009	0.009	0.009	0.009	0.009
R_{int}	[-]	0.5	0.67	1	1	0.5	0.5	0.5	0.5

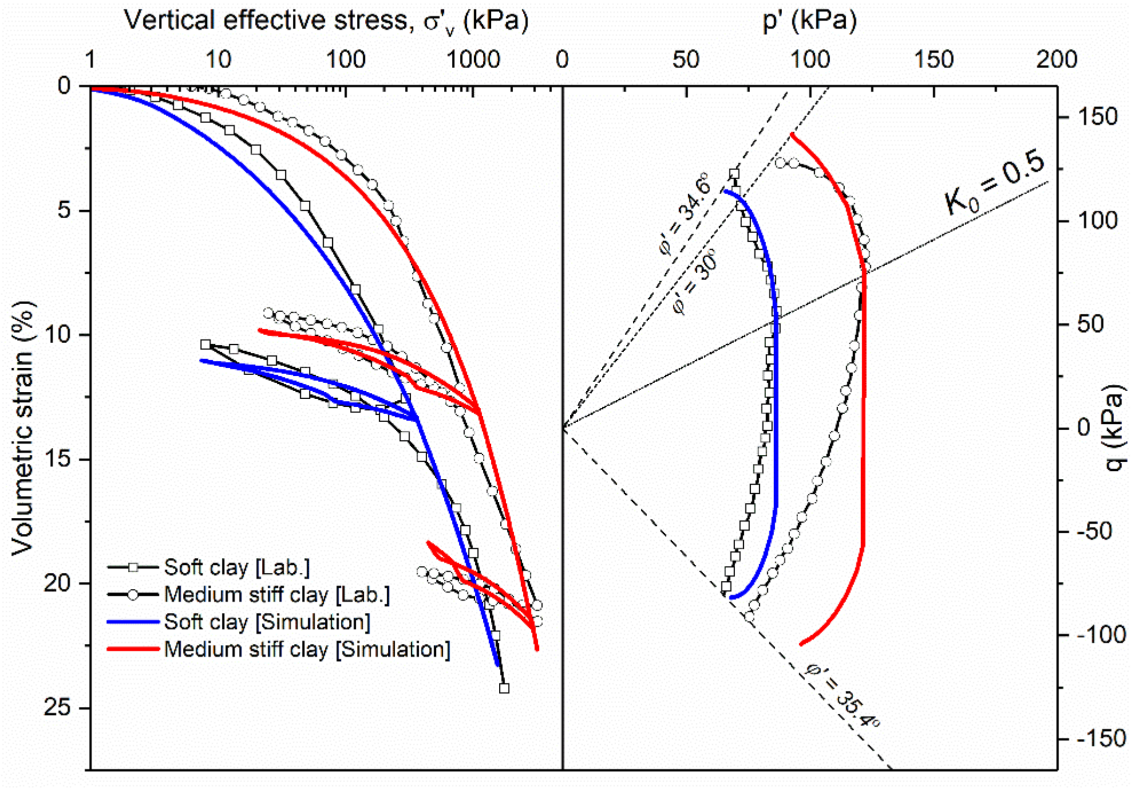

Fig. 117: Calibrated oedometer test and K_0-consolidated triaxial test

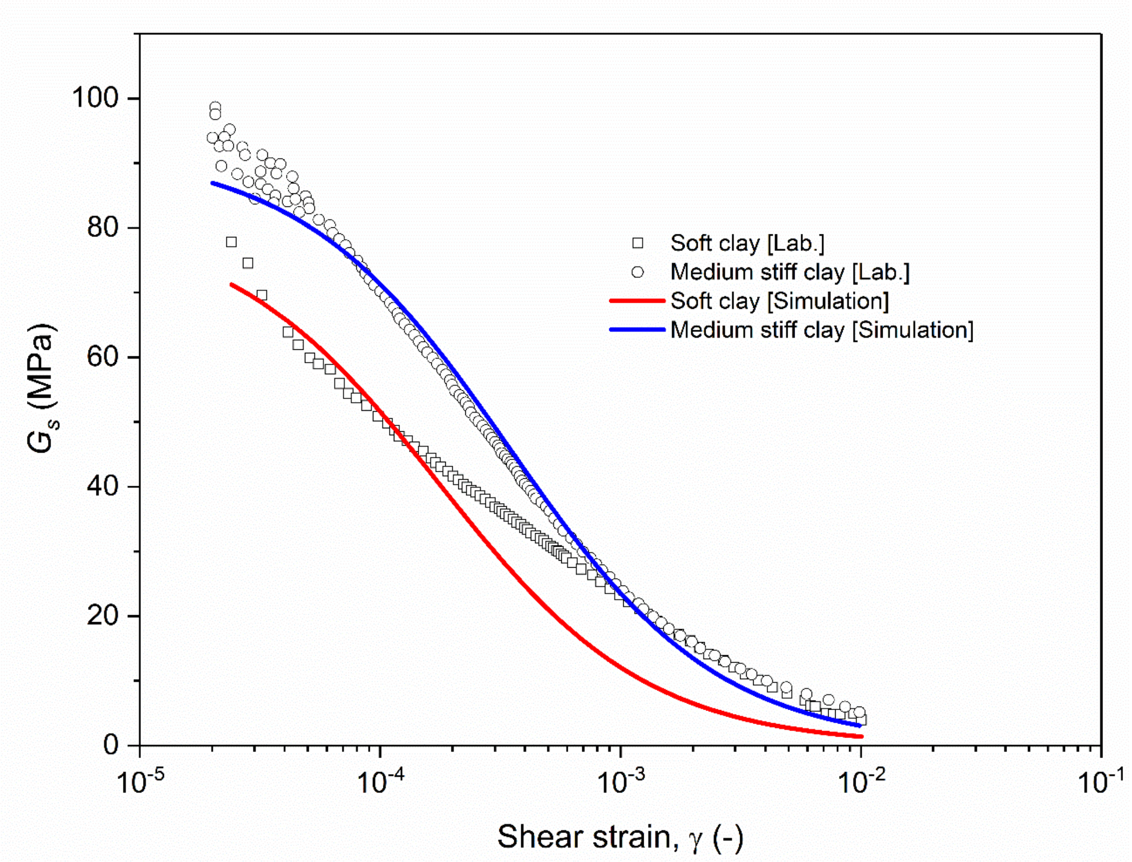

Fig. 118: Prediction shear stiffness degradation for soft clay and medium stiff clay

7.2.3 Time dependency for support systems

- Strength and stiffness

The concrete model (Schädlich & Schweiger 2014) was adopted to describe the time dependency behaviour of concrete ring beams. The description for the model is given in section 5.3 and only the time dependency part will be described in this section.

As illustrated in Equation 13, total strains can be decomposed into elastic strains ε^{e}, plastic strains ε^{p}, creep strains ε^{cr}, and shrinkage strains ε^{shr}. An increase in Young's modulus E with time t follows the recommendation of the CEB-FIP model code (CEB-FIP 1990):

$$E(t) = E_{28} \cdot e^{s_{stiff} \cdot \left(1 - \sqrt{t_{h_{ydr}}/t}\right)} \tag{22}$$

$$s_{stiff} = \frac{ln(E_1/E_{28})}{\sqrt{t_{h_{ydr}}/1d} - 1} \tag{23}$$

where E_{28} is Young's modulus of cured concrete and is assumed constant for $t <$ 1h and for $t > t_{hydr}$, t_{hydr} is the time until full curing, t is the time in days and s_{stiff} is the parameter governing stiffness development with time.

Similarly, the increase of compressive strength with time $f_c(t)$ follows the approach of E. At a very early stage a lower limit of $f_c = 0.005 \cdot f_{c,28}$ is adopted.

$$f_c(t) = f_{c,28} \cdot e^{s_{strength} \cdot \left(1 - \sqrt{t_{h_{ydr}}/t}\right)} \tag{24}$$

$$s_{strength} = \frac{ln\left(f_{c,1}/f_{c,28}\right)}{\sqrt{t_{h_{ydr}}/1d} - 1} \tag{25}$$

As already pointed out by Arboleda-Monsalve et al. (2018), the considerable wall movement was attributed to delays in the gain of the compressive strength and stiffness of the ring beams because they are influenced by rapid construction processes and low temperatures during concrete curing. The development of compressive strength for ring beams is shown in Fig. 119. The measured compressive strengths at 28 days were 59±8 MPa and are within the lower and upper bound of concrete strength following standards. It is noted that the prediction of compressive strength over time is theoretically based on a controlled temperature of 20°C in typical laboratory conditions.

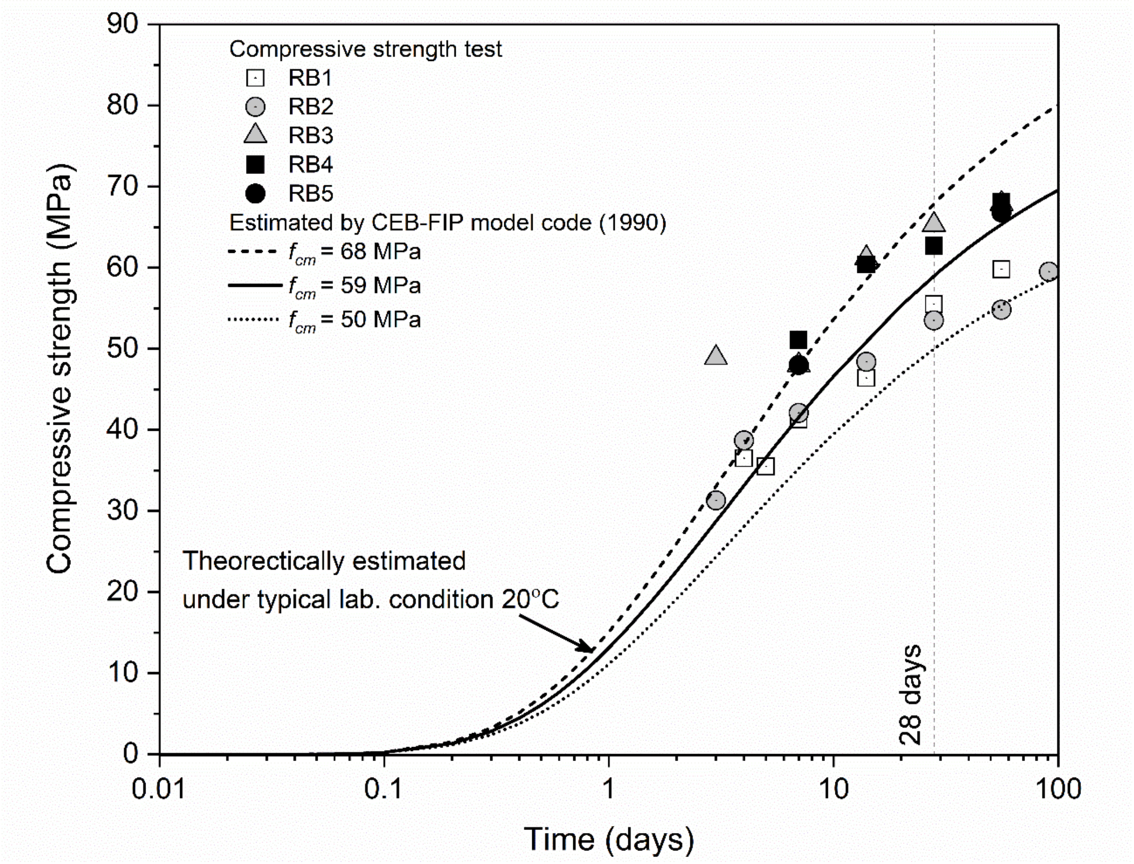

Fig. 119: Development of compressive strength with time

However, it is clear from the construction records that variations in temperature during the ring beam installation remained below 20°C which slowed down the curing process and affected the hydration process of concrete and aggregates (Fig. 114, right). Temperature adjustment values in terms of compressive strength were outlined by (CEB-FIP 1990) when estimating the full maturity of concrete.

$$t_T = \sum_{i=1}^{b} \Delta t_i \cdot exp\left[13.65 - \frac{4000}{273 + T(\Delta t_i)}\right] \tag{26}$$

$$f_c'(t,T) = (1.06 - 0.003T) f_c'(t) \tag{27}$$

where Δt_i is the number of days, where temperature T prevails, and $T(\Delta t_i)$ is the mean temperature (°C) during the period Δt_i. Therefore, increasing compressive strength with time as influenced by the temperature effects is calculated by replacing the concrete age t and compressive strength $f_c(t)$ in Equation 24 by t_T and $f_c'(t,T)$ from Equation 26 and 27, respectively.

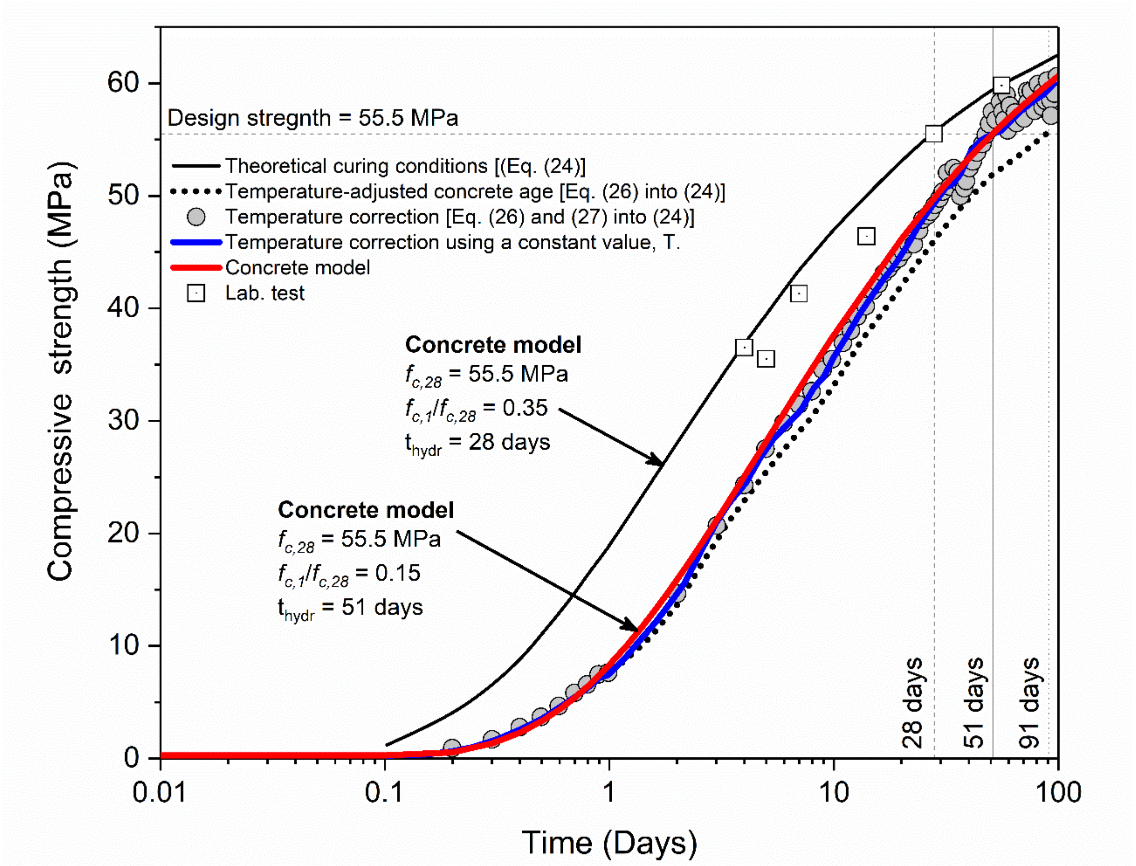

Fig. 120: Temperature adjusted compressive strength of RB1

For example, Fig. 120 shows the calculations of temperature adjusted concrete age with RB1. According to a design compressive strength of about 55.5 MPa at 28 days, the effect of temperature on concrete age (i.e. substituting Equation 26 into 24) indicates a delay in compressive strength gain to 91 days. The concrete maturity, which indicates how the compressive strength of the concrete has increased with time as affected by temperature effects, is estimated by replacing the concrete age of Equation 26 and additionally the temperature correction on compressive strength is calculated using Equation 27 and results in the delay to 51 days.

Moreover, the temperature correction using a constant value during the installation of ring beams (see Fig. 114, right) suggested by Arboleda-Monsalve, et al. (2018) shows a negligible effect on the concrete maturity compared with the temperature correction variable. The prediction using the concrete model indicates a clear distinction between the theoretical and temperature correction of the compressive strength development over time.

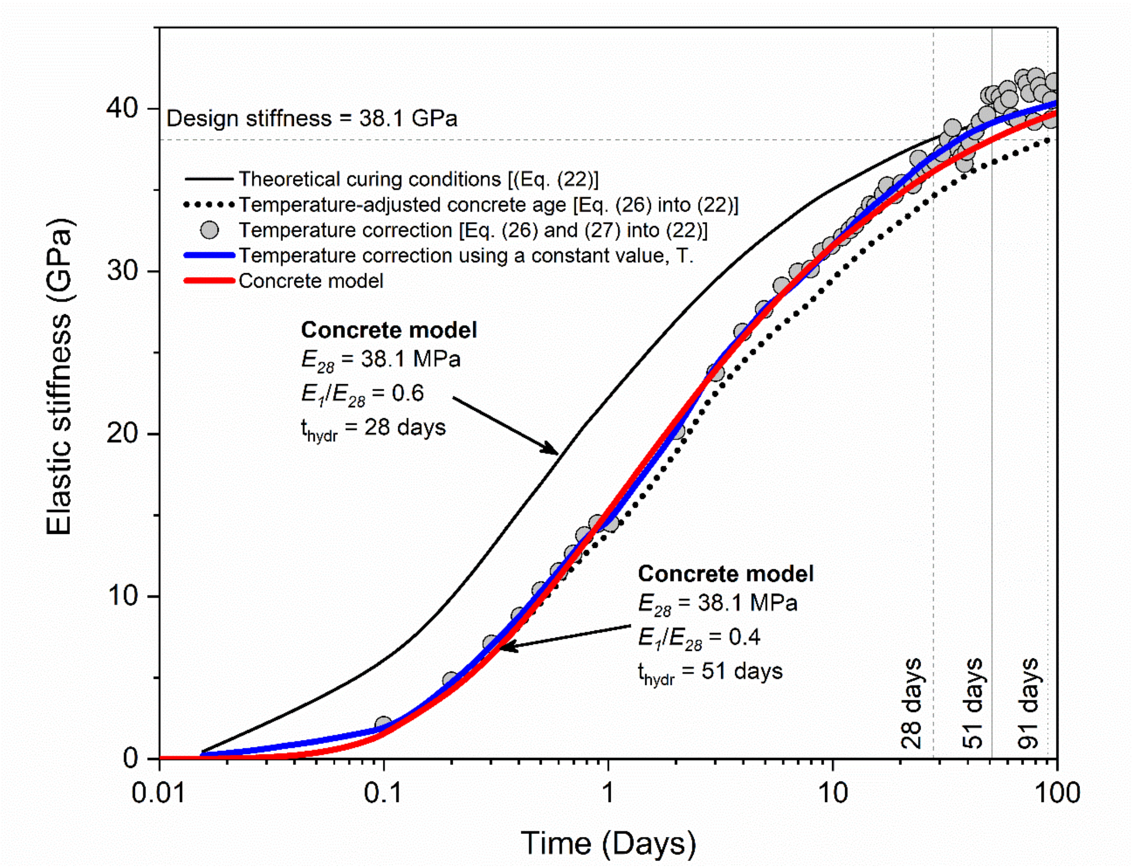

Fig. 121: Temperature adjusted elastic stiffness of RB1

The concrete elastic stiffness is calculated using the following equation:

$$E_c(t) = E_c(t) \cdot \sqrt{\frac{f_c'(t)}{f_c'(28)}} \tag{28}$$

Temperature effects are included in the increase in the modulus of elasticity by including the concrete age and compressive strength as influenced by temperature using Equation 26 and 27. Similar trends are observed for concrete stiffness, as depicted in Fig. 121.

- Creep and shrinkage

A viscoelastic approach is adopted to model creep behaviour. Creep strains ε^{cr} increase linearly with stress $\boldsymbol{\sigma}$ and are related to elastic strains via the creep factor ϕ^{cr}.

$$\varepsilon^{\infty}(t) = \frac{\phi^{cr} \cdot \boldsymbol{\sigma}}{\boldsymbol{D}} \cdot \frac{t - t_0}{t + t_{50}^{cr}} \tag{29}$$

where $\boldsymbol{D}$ represents the linear elastic stiffness matrix. The evolution of creep with time t is governed by the start of loading at time t_0 and the parameter t_{50}^{cr}. For instantaneous loading ($t_0 = 0$), t_{50}^{cr} equals the time until 50% of creep strains have evolved. For concrete utilizations higher than 45% of f_c, non-linear creep effects are accounted for according to EC 2 (2004).

Shrinkage is modelled in the context of isotropic loss of volume with time, which is independent of any stress state. Shrinkage strains ε^{shr} are calculated as:

$$\varepsilon^{shr}(t) = \varepsilon_{\infty}^{shr} \cdot \frac{t}{t + t_{50}^{shr}} \tag{30}$$

where $\varepsilon_{\infty}^{shr}$ is the final axial shrinkage strain, and t_{50}^{shr} is the time when 50% of shrinkage has already occurred.

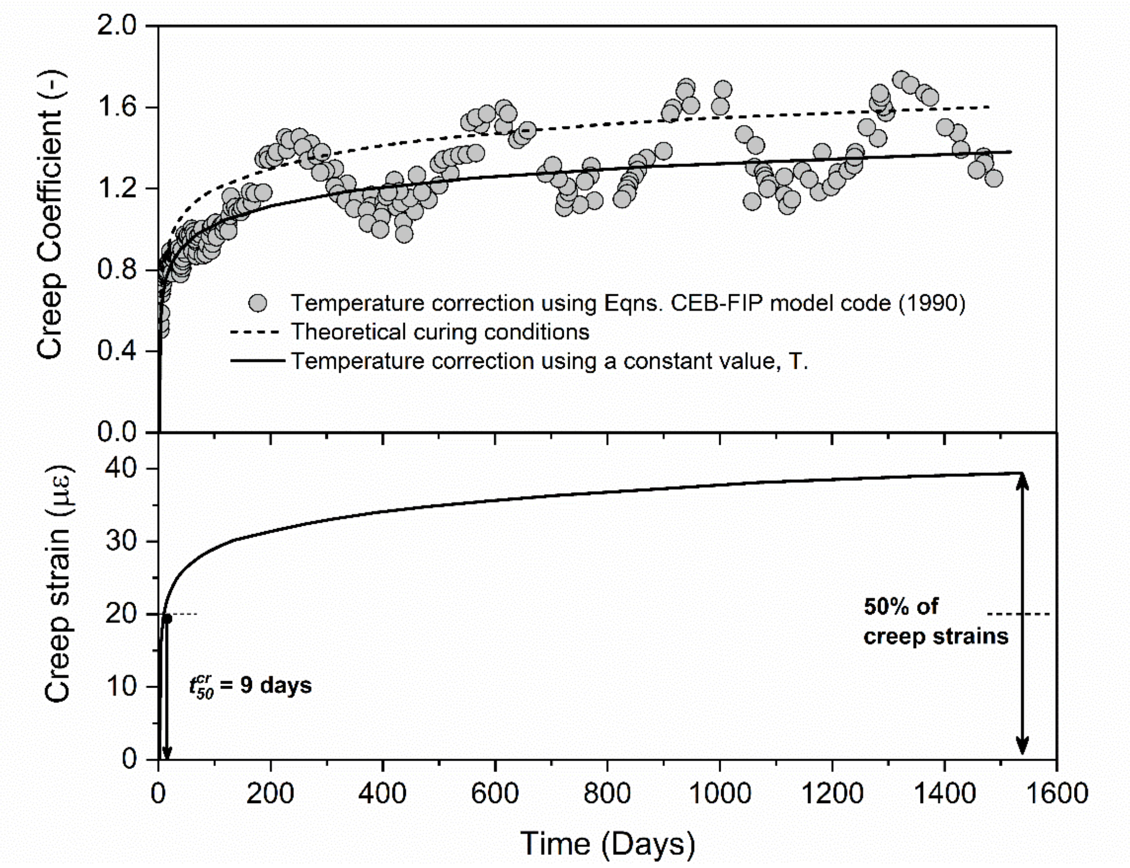

Fig. 122: Temperature adjusted creep coefficients of RB1

The estimated creep coefficient and shrinkage strain by Arboleda-Monsalve et al. (2018) are presented in Fig. 122 and Fig. 123, respectively. The creep coefficient is defined by the ratio of elastic strains at the initial time of loading to the additional strain developed with time by the summation of the drying and basic creep (i.e. creep in the absence of moisture exchange) factors in terms of the compressive strength, relative humidity, cross-sectional shape and type of cement. The shrinkage strain represents a decrease in volume of the concrete due to the moisture loss caused by exposure to the environment.

The calculations including time-dependent effects follow the model code (CEB-FIP 1990). A constant temperature of 10℃ was assumed for RB1. The computed creep coefficient was estimated under theoretical curing conditions in a controlled laboratory environment and modified to include temperature effects. Shrinkage strain follows a similar trend. The differences are obviously seen after 100 days of curing. Hence, low temperature appears to be beneficial to the development of creep and shrinkage strains.

According to the concrete model, taking RB 1 for instance, the input parameters for creep (ϕ^{cr}= 1.38, t_{50}^{cr} = 9 days) and shrinkage ($\varepsilon_{\infty}^{shr}$ = 200 $\mu\varepsilon$, t_{50}^{shr} = 50 days) can be estimated from Fig. 122 and Fig. 123, respectively. The concrete model input parameters for ring beams are summarized in Tab. 16.

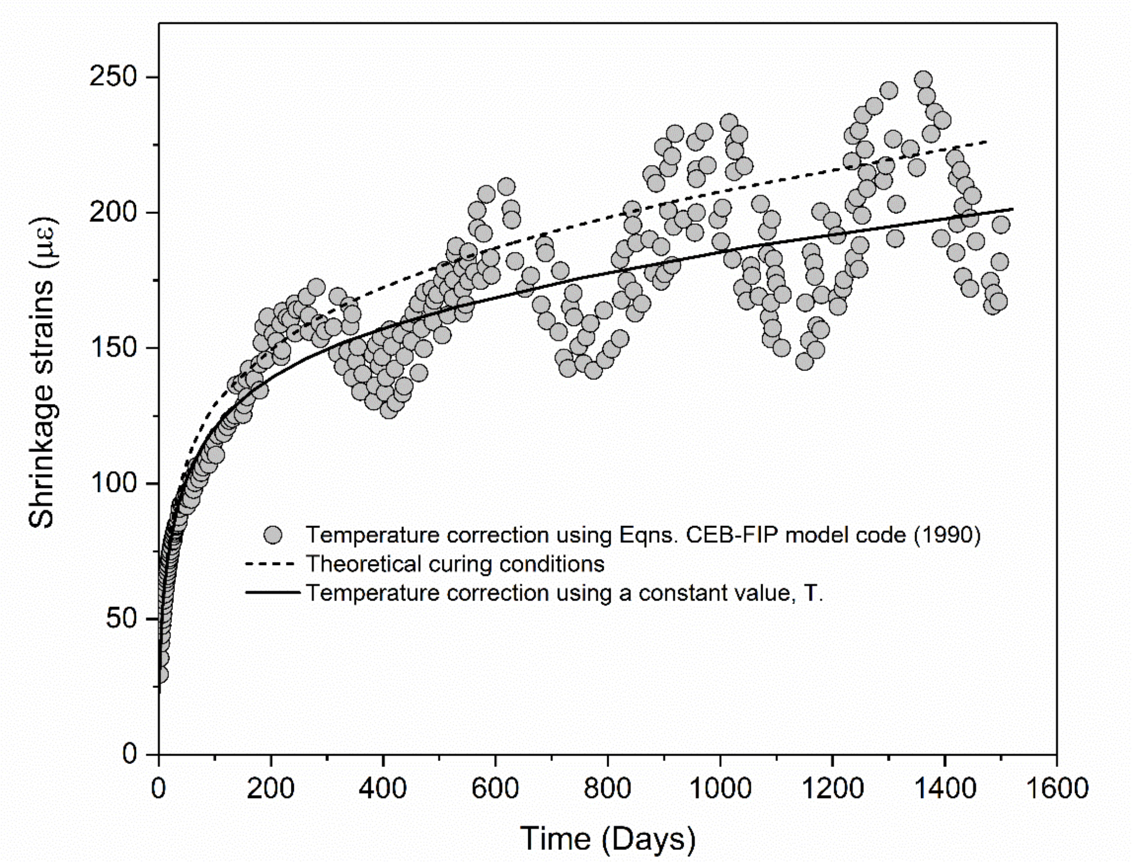

Fig. 123: Temperature adjusted shrinkage strains of RB1

Tab. 16: Input parameters for ring beams

	Unit	RB1	RB2	RB3	RB4	RB5	RB6	RB7
$E(t)$	[GPa]	38.1	37.6	40.2	38.3	39.1	37.6	38.1
ν	[-]	0.2	0.2	0.2	0.2	0.2	0.2	0.2
f_{ct}	[MPa]	55.5	53.5	65.3	56.4	60.1	53.5	55.5
f_{c0n}	[-]	0	0	0	0	0	0	0
f_{cfn}	[-]	0.26	0.27	0.2	0.22	0.2	0.27	0.26
f_{cun}	[-]	0	0	0	0	0	0	0
G_c	[kN/m]	70	70	70	70	70	70	70
φ_{max}	[°]	37	37	37	37	37	37	37
ψ	[°]	0	0	0	0	0	0	0
f_t	[MPa]	5.55	5.35	6.53	5.64	6.0	5.4	5.5
f_{tun}	[-]	0	0	0	0	0	0	0
G_t	[kN/m]	0.25	0.25	0.25	0.25	0.25	0.25	0.25
t_{hydr}	[days]	51	54	54	59	62	56	22
E_1/E_{28}	[-]	0.38	0.38	0.38	0.45	0.33	0.40	0.62
f_{c1}/f_{c28}	[-]	0.14	0.14	0.14	0.19	0.10	0.15	0.38
ε_{cp}^{p} at 1h/8h/24h	[‰]	-10/-1/-0.95	-10/-1/-0.96	-12/-1.1/-1.0	-12/-1.1/-0.98	-10/-1.1/-0.97	-10/-1/-0.95	-12/-1/-0.95
a	[-]	16	16	16	16	16	16	16
$\varepsilon_{\infty}^{shr}$	[‰]	-0.203	-0.192	-0.205	-0.193	-0.198	-0.195	-0.210
t_{50}^{shr}	[days]	50	50	50	50	50	50	50
ϕ^{cr}	[-]	1.38	1.42	1.22	1.39	1.32	1.46	1.49
t_{50}^{cr}	[days]	9	9	9	9	9	9	9

7.2.4 Results

The parametric study was conducted in order to investigate the influence of time dependent factors on concrete ring beam installation and the impact on the performance of the circular excavation. Tab. 17 summarizes the cases analysed in the parametric study.

Tab. 17: Cases analysed with circular excavation

No.	Description	Denoted	Strength	Stiffness	Shrinkage	Creep
1	All relevant factors	ALL	✓	✓	✓	✓
2	Shrinkage	SHR	✓	✓	✓	
3	Creep	CRP	✓	✓		✓
4	Constant strength/stiffness	CON	f_{c1}/f_{c28} = 1.0	E_{c1}/E_{c28} = 1.0		
5	Time dependent, t_{hydr} = 28 without Temp. effect	Thydr28	✓	✓		

Fully coupled flow consolidation was carried out adopting the construction sequence depicted in Fig. 115. It is noted that the time in the numerical simulation denoted in Fig. 115 is subtracted from the actual monitoring time during installation of the ring beams (see Fig. 114). Thus, the results from the numerical simulation presented here are compared with the actual times from the construction project.

Fig. 124 to Fig. 126 compare the predicted lateral wall deflections with the monitored data at different stages of excavation. The time dependency behaviour is of less importance at excavation to RB3 (Fig. 124a) because from the initial records of the inclinometer (inclinometer records start at day 56), the analyzed time period was only 6 days, and, hence, the increase in the strength and stiffness of ring beams does not play an important role in lateral wall movement.

After excavation to RB4 is reached, the predicted lateral wall movement is dominated by time-dependency, creep and shrinkage. In Fig. 125b (i.e. excavation to RB6) it is evident that using constant strength and stiffness (denoted as CON) underestimates wall movements by 25% compared to the monitored data and all relevant factors (denoted as ALL, see Tab. 17). Besides the constant strength and stiffness, the other factors have negligible effects on ground movement predictions.

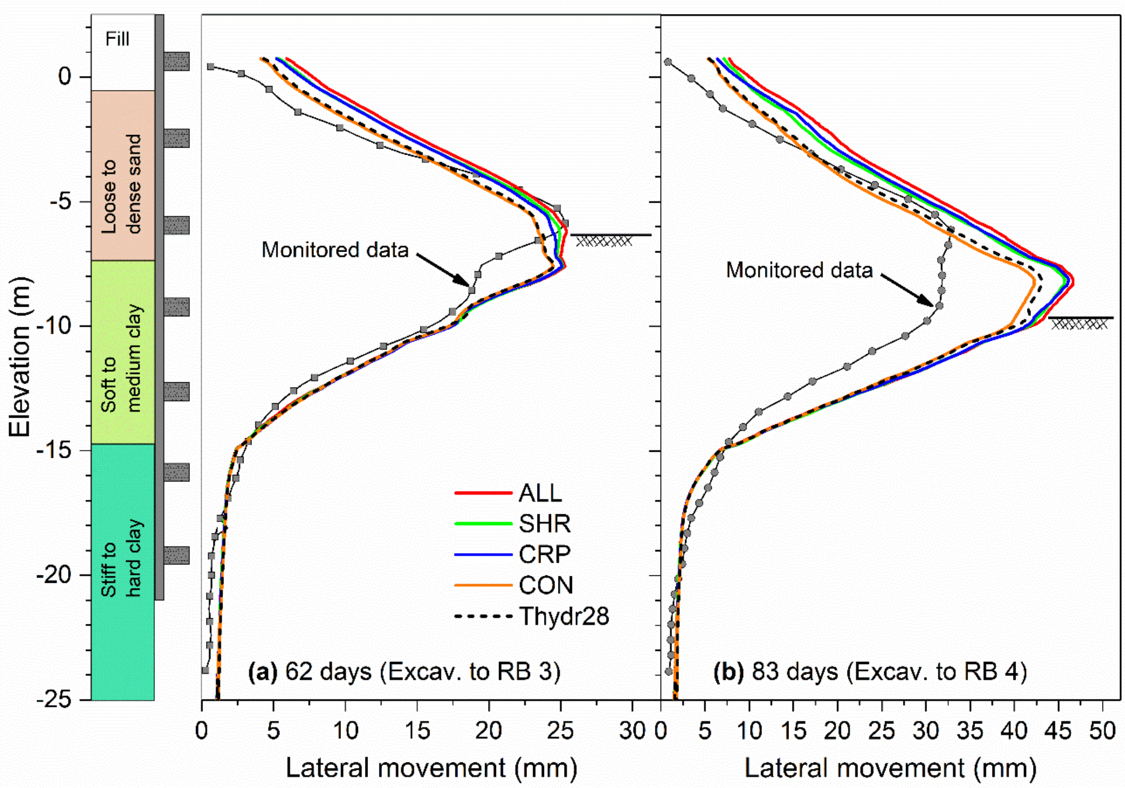

Fig. 124: Predicted lateral soil movements of excavation to; (a) RB3 and (b) RB4

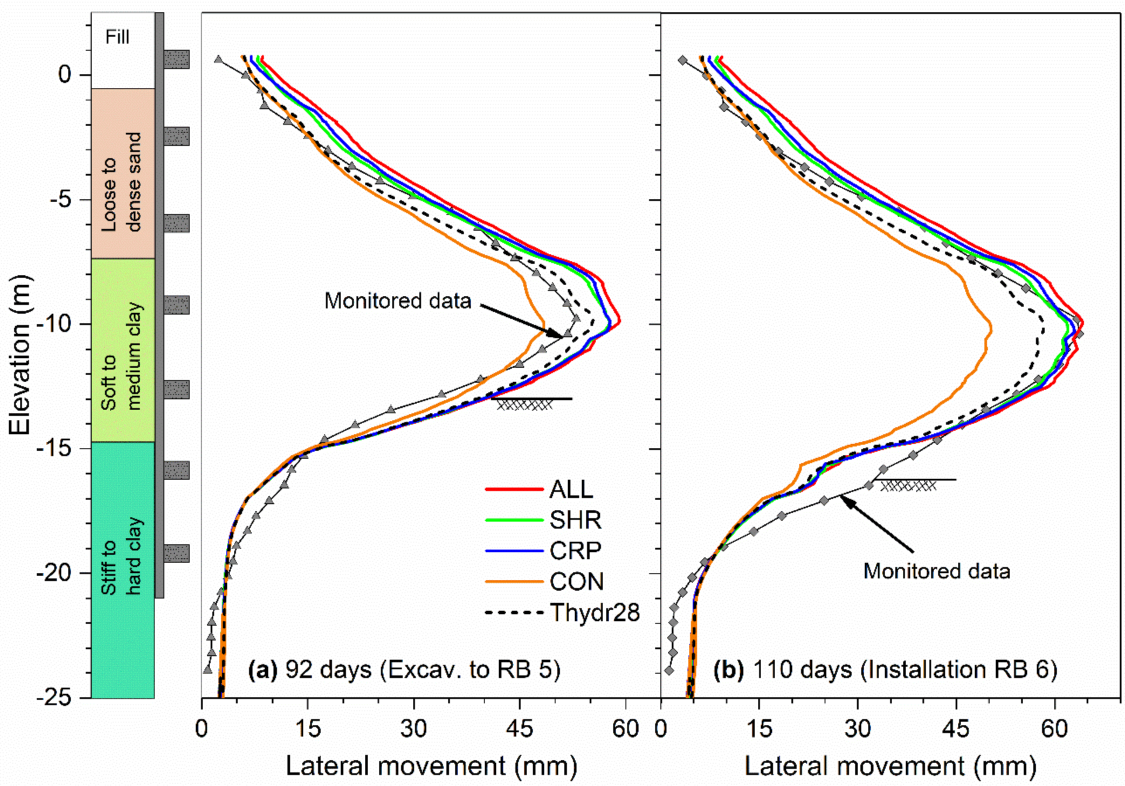

Fig. 125: Predicted lateral soil movements of excavation to; (a) RB5 and (b) RB6

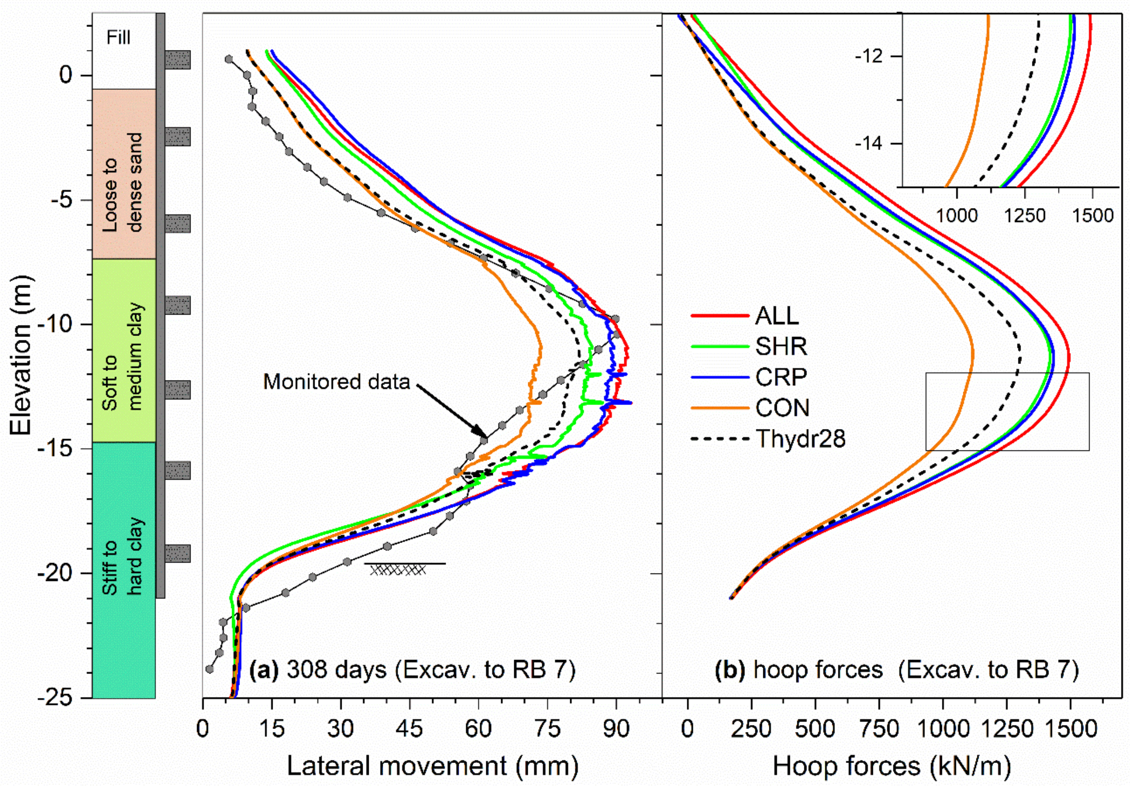

Fig. 126: (a) Predicted lateral soil movements of excavation to RB 7 (b) hoop forces

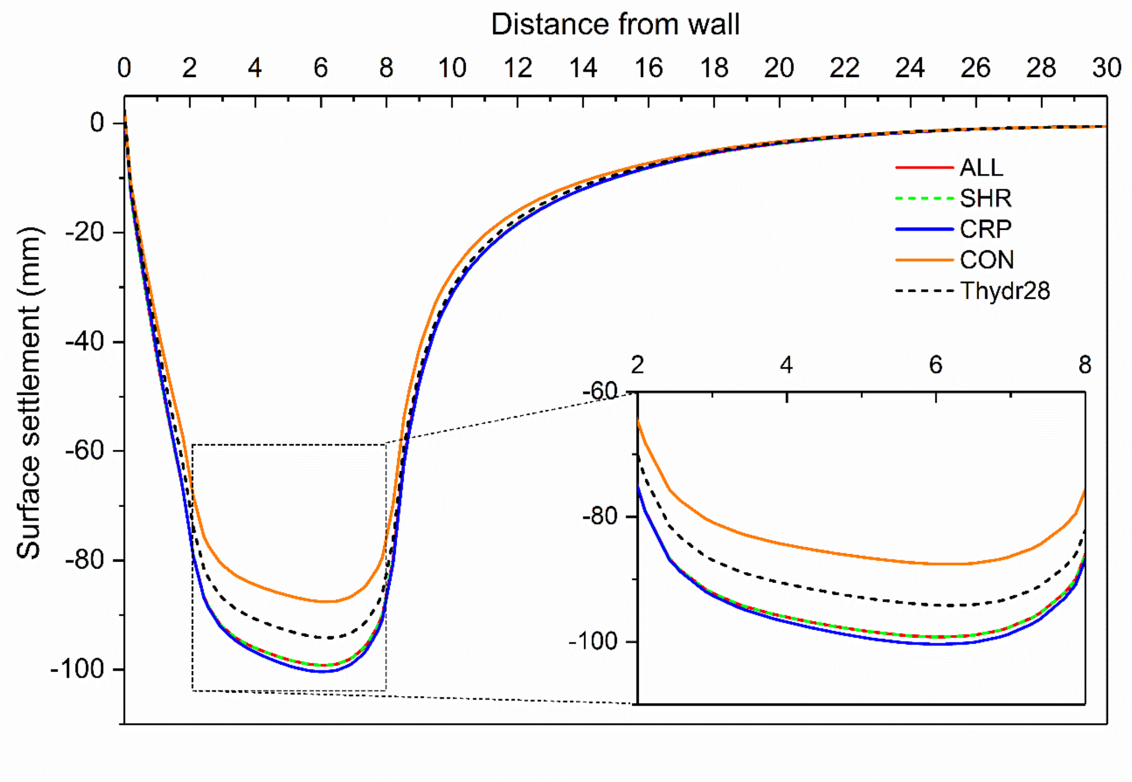

Fig. 127: Predicted surface displacement at excavation to RB7

Comparison for the final stage of excavation is shown in Fig. 126 and at this stage the maturity of ring beams (RB1 to RB6) has been reached. The combined effect of creep (CRP) and time dependency is only slightly larger than that of shrinkage (SHR). Neglecting the temperature affected concrete maturity (Thydr28) resulting in an underestimation of maximum wall displacement as well as the deflected shape of the wall. Although the construction of the caissons was explicitly included in the numerical analysis accounting for a consolidation stage, it is argued that this is really a 3D problem and, hence, the wall deflected shapes do not match acceptably with the monitored data. A similar trend can be observed with hoop forces (Fig. 126b). From all analyses, similar settlement troughs are obtained, but maximum values of surface displacement differ (Fig. 127).

7.3 Summary of case histories

This chapter indicates the importance of appropriate constitutive models for analysing deep excavations problems. Reasonable agreement with the monitored data is obtained by comparing results from the excavations in Bangkok and Chicago subsoil conditions.

An improvement of lateral wall deflections and surface settlement predictions is achieved with advanced constitutive models adopted for analysing a deep excavation in Bangkok subsoils conditions. The predicted undrained shear strength as a consequence of the constitutive model used has been addressed by employing a comparison of the simple elastic-perfectly plastic model with a double hardening plasticity model. It is observed in the numerical simulations using the HS and HSS models that soil below the excavation level behaves less stiff than in reality. Different assumptions for the stress dependency of stiffness (i.e. pre-consolidation stress, mean and minor principal stresses) lead to a significant reduction in the uplift movement of the soil below the bottom of the excavation.

Moreover, the influence of anisotropic small strain stiffness was discussed, and analyses were carried out by means of multilaminate soil models. The predictions of lateral wall displacement do not seem to be influenced by the initial anisotropic stiffness. However, improvements in settlement predictions during and at the final excavation stages are achieved.

In the second case history, time-dependent properties of concrete affected by temperature are identified as a primary source of excessive ground movement during the early stages of excavation. Ignoring these effects can lead to inaccurate predictions of ground movement.

8 Conclusions and further research

8.1 Conclusions

In this work, excavation induced deformations and structural forces in support systems have been analysed using the Finite Element Method. The research presented in this thesis contributes towards: 1) the use of more realistic constitutive models in the analysis of complex geotechnical boundary value problems, 2) the understanding of some of the fundamental mechanisms controlling the stability and performance of deep excavations and 3) the feasibility and applicability of advanced constitutive models for designing geotechnical structures in accordance with standard design approaches.

The detailed behaviour of retaining structures is studied extensively with the main focus being related to interactions between the soil and structural support system and their influence on stability during construction. Depending on the soil stratigraphy, the corresponding soil properties and different types of retaining system, inadequate strutting or passive soil failure due to inadequate penetration depth represent a considerable factor influencing failure. The significant influence of wall embedment was investigated in chapter 4 by analysing a 30-m deep excavation in marine clay in conjunction with the failure of individual struts. It is shown that significant stress redistribution capacity is available which is however strongly dependent on the embedment depth of the wall. It was shown that a number of struts may fail without causing the entire excavation to collapse. The results of shorter wall embedment clearly indicate an increase in vertical and horizontal load redistribution in struts, as well as a reduction in the number of individual struts which may fail without causing the collapse of the system. In a two-dimensional plane strain analysis, only entire layers of struts can fail and only redistribution in the vertical direction is possible, which is not realistic and results in an overestimation from a practical point of view. As the predicted undrained shear strength is a consequence of the constitutive model adopted, the importance of the constitutive model when performing an undrained analysis in terms of effective stress has been emphasized.

Additionally, two different scenarios, namely involving ductile and brittle support systems, to account for strut failure in the analyses were considered. In the reference case, individual struts were removed one by one based on a predefined sequence, even if neighbouring struts had already reached their limiting capacity - representing a “ductile” behaviour. In the second case, neighbouring struts which had reached their capacity were removed from the system immediately, simulating a “brittle” behaviour. It clearly follows that these modelling assumptions lead to different results, the latter being more critical.

The application of an advanced constitutive model to the cement-mixed soil in order to support an excavation in a slope in chapter 5 demonstrated that significantly different stress distributions in structures are obtained as compared to applying a simple Mohr-Coulomb failure criterion with a tension cut-off for the wall. It can be anticipated that initiation of cracks and crack development with both progressing excavation and the geometrical imperfections will have a significant influence on excavation performance but not for overall stability (chapters 5 and 6). An extensive parametric study was carried out changing the geometry of the supporting structure and additional analyses were performed according to EC7 utilizing Design Approach 3, where partial factors on soil strength and, in this particular case, also on the strength of the MIP-columns are applied. It could be shown that this type of analysis is well suited for designing such types of geotechnical structures in accordance with EC7.

Serviceability limit state represents one of the key issues in the field of deep excavation design. Hence, consideration regarding deformations plays a very dominant role in planning. To improve predictions for deep excavations, advanced constitutive models should be taken into consideration for soil layers and structural elements (chapter 7). The series of analyses presented in this research explored in a detailed way the use of double hardening plasticity models to predict ground movements due to excavation, comparing results obtained with the measurements from the Bangkok case study. Accurate results are obtained by considering small strain stiffness. While the influence of different formulations stress dependent stiffness (i.e. pre-consolidation stress, mean and minor principal stresses) has a negligible effect on wall deflection, it contributes to a decrease in the uplift movement of the soil below the bottom of the excavation level concerned. Modelling anisotropic small strain stiffness revealed that improvements in settlement predictions during and at the final stage of excavation are achieved. Predictions of ground movements seem to be controlled by the rate of stiffness degradation in both vertical and horizontal directions, implying that shearing behaviour controls predictions during excavations.

Furthermore, in the second case history the influences time-dependent of concrete properties, creep and shrinkage affected by temperature were investigated. It was shown that ignoring these effects can lead to inaccurate predictions of ground movements.

8.2 Further research

A number of issues have been addressed within this thesis and various general conclusions are drawn. However, there remain some limitations in the analysis, together with unsolved problems. Recommendations for further research in the field of numerical analysis for deep excavations concern the following aspects:

- The failure of structural support systems is modelled as comprising elastic-perfectly plastic materials (no softening), i.e. a maximum normal force is specified meaning that a further load increase in the strut is not possible but there is no procedure to “fail” the strut and therefore the struts reaching the maximum load had to be removed from the system manually for the next calculation phase, resulting in a new stress redistribution caused by the removal of a particular strut. The development of scripting language (i.e. Python scripting) should be introduced in order to facilitate this procedure.

- Besides the simple wall-support connection (i.e. failure under compression), most connections behave either as pin-jointed or as full-moment to reflect the plastic-hinge properties in a wall. Struts can be considered as acting under compressive force, followed by strain softening, or modelled with additional bending moment rotation generated by the lateral deflection and buckling of the strut. The different types of wall and support connections should be investigated in more detail.

- FE-investigation on the influence of wall embedment depth on stability should be carried out in accordance with the design approach employed in particular projects.

- Design charts in order to indicate the potential failure of soil and structural support system should be developed.

- The application of the advanced constitutive model for soil and structure should be investigated in accordance with the EC7.

9 Bibliography

Addenbrooke, T. I., Potts, D. M. & Puzrin, A. M., 1997. The influence of pre-failure soil stiffness on the numerical analysis of tunnel construction. *Géotechnique,* 47(3), pp. 693-712.

Arboleda-Monsalve, L. G. & Finno, R., 2015. Influence of Concrete Time-Dependent Effects on the Performance of Top-Down Construction. *Journal of Geotechnical and Geoenvironmental Engineering,* 141(4), pp. 1-13.

Arboleda-Monsalve, L. G. et al., 2018. Performance of Urban Cofferdams Braced with Segmental Steel and Reinforced Concrete Ring Beams. *Journal of Geotechnical and Geoenvironmental Engineering,* 144(4), pp. 1-12.

Arroyo, M. et al., 2012. Simulation of cement-improved clay structures with a bonded elasto-plastic model: A practical approach. *Computers and Geotechnics,* 45(9), pp. 140-150.

Ashford, S., Jakrapiyanum, W. & Lukkanaprasit, P., 1996. *Amplification of Earthquake Ground Motions in Bangkok,* Thailand: AIT research report submitted to the Public Works Department.

Atkinson, J. H., 1975. Anisotropic elastic deformations in laboratory tests on undisturbed London Clay. *Géotechnique,* 25(2), pp. 357-374.

Atkinson, J. H., 1993. *The Mechanics of Soils and Foundations.* 1st ed. London: McGraw-Hill College.

Atkinson, J. H., Richardson, D. & Stallebrass, S. E., 1990. Effect of recent stress history on the stiffness of overconsolidated soil. *Géotechnique,* 40(4), pp. 531-540.

Atkinson, J. H. & Sallfors, G., 1991. Experimental determination of stress-strain-time characteristics in laboratory and in situ tests. *Proc. 10th European Conference on Soil Mechanics and Foundation Engineering, Associazione Geotechnica Italiana(ed.), Florence, Italy, Vol. 3,* pp. 915-956.

Bahrami, M., Khodakarami, M. I. & Haddad, A., 2018. 3D numerical investigation of the effect of wall penetration depth on excavations behavior in sand. *Computers and Geotechnics,* 98(6), pp. 82-92.

Benz, T., 2007. *Small-Strain Stiffness of Soils and its Numerical Consequences.* Stuttgart: Ph.D. thesis, Universität Stuttgart.

Benz, T., Vermeer, P. A. & Schwab, R., 2009. A small-strain overlay model. *International Journal for Numerical and Analytical Methods in Geomechanics,* 33(1), pp. 25-44.

Bjerrum, L. & Eide, O., 1956. Stability of strutted excavations in clay. *Géotechnique,* 6(1), pp. 32-47.

Blackburn, J. T. & Finno, R. J., 2007. Three-dimensional responses observed in an internally braced excavation in soft clay. *Journal of Geotechnical and Geoenvironmental Engineering,* 133(11), p. 1364–1373.

Boehler, C., 2017. *Vergleich von Berechnungsansätzen für im Düsenstrahlverfahren hergestellte Schächte.* Basel: Bachelor thesis, Fachhochschule Nordwestschweiz (in German).

Bolton, M. D., Lam, S. Y. & Osman, A. S., 2009. *Geotechnical aspects of underground construction in soft ground.* London, CRC Press.

Bolton, M. D. & Powrie, W., 1987. The collapse of diaphragm walls retaining clay. *Géotechnique,* 37(3), pp. 335-353.

Boone, S. J. & Crawford, A. M., 2000. Braced excavations: Temperature, elastic modulus, and strut loads. *Journal of Geotechnical and Geoenvironmental Engineering,* 126(10), pp. 870-881.

Briaud, J. L., Nicholson, P. & Lee, J., 2000. Behavior of full-scale VERT wall in sand. *Journal of Geotechnical and Geoenvironmental Engineering,* 126(9), pp. 808-818.

Brinkgreve, R., Kumarswamy, S. & Swolfs, W., 2017. *PLAXIS 2D 2017 - User Manual.* Delft: Plaxis bv.

Bryson, L. S. & Zapata-Medina, D. G., 2012. Method for estimating system stiffness for excavation support walls. *Journal of Geotechnical and Geo-Environmental Engineering,* 138(9), p. 1104–1115.

Burland, J. B., 1990. On the compressibility and shear strength of natural clays. *Géotechnique,* 40(3), pp. 329-378.

Burland, J. B. & Hancock, R. J. R., 1977. Underground car park at the house of commons. *The Structural Engineer,* 55(2), pp. 87-100.

Cabarkapa, Z. et al., 2003. Design and performance of a large diameter shaft in Dublin Boulder Clay. *BGA International Conference on Foundations: Innovations, observations, design and practice,* p. 176–185.

Calvello, M. & Finno, R. J., 2004. Selecting parameters to optimize in model calibration by inverse analysis. *Computers and Geotechnics,* 31(5), p. 411–425.

CEB-FIP, 1990. *Design code – comite Eurointernational du Beton.* London: Thomas Telford.

Cheng, X. S. et al., 2017. Experimental study of the progressive collapse mechanism of excavations retained by cantilever piles. *Canadian Geotechnical Journal,* 54(4), p. 574–587.

Cheng, X. S. et al., 2017. Study of the progressive collapse mechanism of excavations retained by cantilever contiguous piles. *Engineering Failure Analysis,* 71(1), p. 72–89.

Cheng, Y. M., Hu, Y. Y. & Wei, W. B., 2007. General Axisymmetric Active Earth Pressure by Method of Characteristics—Theory and Numerical Formulation. *International Journal of Geomechanics,* 7(1), pp. 1-15.

Chen, R. P. et al., 2015. Failure Investigation at a Collapsed Deep Excavation n Very Sensitive Organic Soft Clay. *Journal of Performance of Constructed Facilities*, 23(3), pp. 1-14.

Choosrithong, K. & Schweiger, H. F., 2018. Influence of Individual Strut Failure on Performance of Deep Excavation in Soft Soil. *Proceedings of China-Europe Conference on Geotechnical Engineering, In: Wu W., Yu HS. (eds),* pp. 316-319.

Choosrithong, K. & Schweiger, H. F., 2019. Numerical Investigation of Sequential Strut Failure on Performance of Deep Excavations in Soft Soil. *International Journal of Geomechanics, Accepted.*

Choosrithong, K., Schweiger, H. F. & Marte, R., 2019. Finite Element Analysis of Mixed-in-Place Columns (MIP) Supporting Excavations in Slopes Considering Tension Softening. *Canadian Geotechnical Journal, Accepted.*

Chowdhury, S. S., Deb, K. & Sengupta, A., 2013. Estimation of Design Parameters for Braced Excavation: Numerical Study. *International Journal of Geomechanics,* 13(3), pp. 234-247.

Cho, W. & Finno, R. J., 2010. Stress-strain responses of block samples of compressible Chicago glacial clays. *Journal of Geotechnical and Geoenvironmental Engineering,* 136(1), pp. 178-188.

Clayton, C. R. I. & Heymann, G., 2001. Stiffness of geomaterials at very small strains. *Géotechnique,* 51(3), pp. 245-255.

Clayton, C. R. I., Milititsky, J. & Woods, R. I., 1993. *Earth pressure and earth retaining structures.* 2nd ed. London: Chapman & Hall.

Clough, G. W. & Duncan, J. M., 1971. Finite element analyses of retaining wall behavior. *Journal of the Soil Mechanics and Foundations Division, ASCE,* 97(12), p. 1657–1674.

Clough, G. W. & Hansen, L. A., 1981. Clay Anisotropy and Braced Wall Behavior. *Journal of the Geotechnical Engineering,* 107(7), pp. 893-913.

Clough, G. W. & O'Rourke, T., 1990. Construction induced movements of in-situ walls. *ASCE Geotechnical special publication No.25 - Design and Performance of Earth Retaining,* p. 439–470.

Clough, G. W., Smith, E. M. & Sweeney, B. P., 1989. Movement Control of Excavation Support Systems by Iterative Design, Current Principles and Practices. *Foundation Engineering Congress, ASCE,* Volume 2, pp. 869-884.

COI, 2005. *Report of the Committee of Inquiry into the incident at the MRT circle line worksite that led to collapse of Nicoll Highway on 20 April 2004,* Singapore: Ministry of Manpower.

Corral, G. & Whittle, A. J., 2010. Re-Analysis of Deep Excavation Collapse Using a Generalized Effective Stress Soil Model. *Earth Retention Conference 3, American Society of Civil Engineers,* p. 720–731.

De Moor, E. K., 1994. An analysis of bored pile/diaphragm wall installation effects. *Géotechnique,* 44(2), pp. 341-347.

Denies, N. et al., 2015. Large-scale bending tests on soil mix elements. *In Proceedings of the International Foundations Congress and Equipment Expo of San Antonio IFCEE,* pp. 2394-2409.

Denies, N. et al., 2014. Real-scale tests on soil mix elements. *In Proceedings of the DFI-EFFC 11th International Conference on Piling and Deep Foundations,* p. 647–656.

Dik, I., 2017. *Analysis of the capacity of a reinforcement detail in a soil-mix wall: An experimental and numerical approach.* Delft: M.Sc. Thesis, Delft University of Technology.

DMR, 2011. *Impact assessment of underground structure due to groundwater rebound in Bangkok and surrounding area,* Thailand: Department of Mineral Resources.

Do, T. N., Ou, C. & Lim, A., 2013. Evaluation of Factors of Safety against Basal Heave for Deep Excavations in Soft Clay Using the Finite-Element Method. *Journal of Geotechnical and Geoenvironmental Engineering,* 139(12), pp. 2125-2135.

Do, T. N., Ou, C. Y. & Chen, R. P., 2016. A study of failure mechanisms of deep excavations in soft clay using the finite element method. *Computers and Geotechnics,* 73(3), pp. 153-163.

Eide, O., Aas, G. & Josang, T., 1972. Special application of cast-in place walls for tunnels in soft clay in Oslo. *Proc. 5th European Conf. on Soil Mechanics and Foundation Engineering*, p. 485–498.

Fabris, C., Schweiger, H. F. & Tschuchnigg, F., 2018. FE-analysis of anchor pull out tests using advanced constitutive models. *In Proceedings of The 9th European Conference on Numerical Methods In Geotechnical Engineering (NUMGE)*, pp. 125-132.

Finno, R. J., 2009. Analysis and numerical modeling of deep excavations. *Geotechnical Aspects of Underground Construction in Soft Ground – Ng, Huang & Liu (eds)*, pp. 87-97.

Finno, R. J., 2018. Field Performance Data and Support of Excavation Design. *Ralph B. Peck Medal Lecture*.

Finno, R. J., Atmatzidis, D. K. & Perkins, S. B., 1989. Observed Performance of a Deep Excavation in Clay. *Journal of Geotechnical Engineering*, 115(8), pp. 1045-1064.

Finno, R. J., Blackburn, J. T. & Roboski, J. F., 2007. Three-Dimensional Effects for upported Excavations in Clay. *Journal of Geotechnical and Geoenvironmental Engineering*, 113(1), pp. 30-36.

Finno, R. J. & Cho, W., 2011. Recent Stress-History Effects on Compressible Chicago Glacial Clays. *Journal of Geotechnical and Geoenvironmental Engineering*, 137(3), pp. 197-207.

Finno, R. J. & Roboski, J. F., 2005. Three-dimensional responses of a tied-back excavation through clay. *Journal of Geotechnical and Geoenvironmental Engineering* , 128(8), pp. 273-282.

Frangopol, D. M. & Curley, J. P., 1987. Effects of Damage and Redundancy on Structural Reliability. *Journal of Structural Engineering*, 113(7), pp. 1533-1549.

Freiseder, G. M., 1998. *Ein Beitrag zur numerischen Berechnungen von tiefen Baugruben in weichen Böden.* Graz: Ph.D. Thesis, Technische Universität Graz.

Fuentes, R., Pillai, A. & Ferreira, P., 2018. Lessons learnt from a deep excavation for future application of the observational method. *Journal of Rock Mechanics and Geotechnical Engineering*, 10(3), pp. 468-485.

Fujita, K., 1994. Soft ground tunnelling and buried structures. *13th International Conference on Soil Mechanics and Foundation Engineering, New Delhi*, pp. 89-107.

Gaba, A., Simpson, B., Powrie, W. & Beadman, D., 2003. *CIRIA C580 Embedded retaining walls - guidance for economic design.* London: CIRIA.

Galavi, V., 2007. *A multilaminate model for structured clay incorporating inherent anisotropy and strain softening.* Graz: Dissertation Technische Universität Graz.

Gasparre, A., 2005. *Advanced laboratory characterisation of London Clay.* London: Ph.D. thesis, Imperial College.

Gasparre, A. et al., 2007. The stiffness of natural London clay. *Géotechnique,* 57(1), pp. 33-47.

Goh, A., Fan, Z., Hanlong, L. & Wengang, Z., 2018. Numerical Analysis on Strut Responses Due to One-Strut Failure for Braced Excavation in Clays. *Proceedings of the 2nd International Symposium on Asia Urban GeoEngineering, Springer Series in Geomechanics and Geoengineering*, pp. 1-15.

Gourvenec, S. M. & Powrie, W., 1999. Three-dimensional finite-element analysis of diaphragm wall installation. *Géotechnique,* 49(6), pp. 801-823.

Gunn, M. J. & Clayton, C. R. I., 1992. Installation effects and their importance in the design of earth-retaining structures. *Géotechnique,* 42(1), pp. 137-141.

Haghayeghi, A. R. & Mirzakashani, M., 1994. Case Study - Performance of Diaphragm Walls During Construction; Predictions vs. Field Measurements. *Structures Congress XII,* pp. 264-270.

Hashash, Y. M. A. et al., 2003. Temperature correction and strut loads in Central Artery excavations. *Journal of Geotechnical and Geoenvironmental Engineering,* 129(6), pp. 495-505.

Hashash, Y. M. A. & Whittle, A. J., 1996. Ground Movement Prediction for Deep Excavations in Soft Clay. *Journal of Geotechnical Engineering,* 122(6), pp. 474-486.

Hight, D. & Higgins, K., 1994. An approach to the prediction of ground movements in engineering practice: background and application. *Prefailure Deformation of Geomaterials,* pp. 909-945.

Hong, Y. & Ng, C. W., 2013. Base stability of multi-propped excavations in soft clay subjected to hydraulic uplift. *Canadian Geotechnical Journal,* 50(2), pp. 153-164.

Hooi, K., 2003. *Ground Movements Associated with Station Excavations of the First Bangkok MRT Subway.* Bangkok: M. Eng. Thesis, Asian Institute of Technology.

Hsieh, P. G. & Ou, C. Y., 1998. Shape of ground surface settlement profiles caused by excavation. *Canadian Geotechnical Journal,* 35(6), pp. 1001-1017.

Hsieh, P. G., Ou, C. Y. & Liu, H. T., 2008. Basal heave analysis of excavations with consideration of anisotropic undrained strength of clay. *Canadian Geotechnical Journal 45(6):788-799,* 45(6), pp. 788-799.

Hsieh, Y. M., Dang, P. H. & Lin, H. D., 2017. How Small Strain Stiffness and Yield Surface Affect Undrained Excavation Predictions. *ASCE International Journal of Geomechanics,* 17(3), pp. 1-13.

Husain, M. & Tsopelas, P., 2004. Measures of Structural Redundancy in Reinforced Concrete Buildings. I: Redundancy Indices. *ASCE Journal of Structural Engineering,* 130(11), pp. 1651-1658.

Ignat, R., Baker, S., Liedberg, S. & Larsson, S., 2016. Behavior of braced excavation supported by panels of deep mixing columns. *Canadian Geotechnical Journal,* 53(10), pp. 1671-1687.

Janbu, N., 1997. State-of-the-art report on Slopes and Excavations in Normally and Lightly Overconsolidated Clays. *Proceedings of the 9th International Conference on Soil Mechanics and Foundation Engineering, Tokyo,* pp. 549-566.

Jardine, R. J., Potts, D. M., Fourie, A. B. & Burland, J. B., 1986. Studies of the influence of non-linear stress-strain characteristics in soil structure interaction. *Géotechnique,* 36(3), pp. 377-396.

Jardine, R. J., Symes, M. J. & Burland, J. B., 1984. The measurement of soil stiffness in the triaxial apparatus. *Géotechnique,* 34(3), pp. 323-340.

Jen, L. C., 1998. *The design and performance of deep excavations in clay.* Cambridge, MA: Ph.D. thesis, Massachusetts Institute of Technology.

Jiahui, H., 2003. *Cyclic and post-cyclic behaviour of soft clays.* Singapore: Ph.D thesis, National University of Singapore.

Jung, Y. H., Cho, W. & Finno, R. J., 2007. Defining Yield from Bender Element Measurements in Triaxial Stress Probe Experiments. *Journal of Geotechnical and Geoenvironmental Engineering,* 133(7), pp. 841-849.

Karlsrud, K. & Andresen, L., 2005. Loads on Braced Excavations in Soft Clay. *International Journal of Geomechanics* , 5(2), pp. 107-113.

Kempfert, H. G. & Stadel, M., 1997. Berechnungsgrundlagen für Baugruben in normalkonsolidierten weichen bindigen Böden. *Bauingenieur 72, Springer-VDI*, pp. 207-214.

Kung, G. T. C., 2009. Comparison of excavation-induced wall deflection using top-down and bottom-up construction methods in Taipei silty clay. *Computers and Geotechnics,* 36(3), pp. 373-385.

Kuwano, R. & Jardine, R., 2002. On the applicability of cross-anisotropic elasticity to granular materials at very small strains. *Géotechnique,* 52(10), pp. 727-749.

Lafleur, J., Silvestri, V., Asselin, R. & Soulie, M., 1988. Behaviour of test excavation in soft champlain sea clay. *Canadian Geotechnical Journal* , 26(4), pp. 705-715.

Lam, S., Haigh, S. & Bolton, M. D., 2014. Understanding ground deformation mechanisms for multi-propped excavation in soft clay. *Soils and Foundations,* 54(3), p. 296–312.

Lam, S. Y., 2010. *Ground movements due to excavation in clay: physical and analytical models.* Cambridge: Ph.D. thesis, University of Cambridge.

Lam, S. Y. & Bolton, M. D., 2011. Energy Conservation as a Principle Underlying Mobilizable Strength Design for Deep Excavations. *Journal of Geotechnical and Geoenvironmental Engineering,* 137(11), pp. 1062-1074.

Larsson, S., Malm, R., Charbit, B. & Ansell, A., 2012. Finite element modelling of laterally loaded lime-cement columns using a damage plasticity model. *Computers and Geotechnics,* 44(6), pp. 48-57.

Lee, F. H., Hong, S. H., Gu, Q. & Zhao, P., 2011. Application of Large Three-Dimensional Finite Element Analyses to Practical Problems. *International Journal of Geomechanics,* 11(6), pp. 529-539.

Lee, F. H., Lee, Y., Chew, S. & Yong, K., 2005. Strength and modulus of marine clay-cement mixes. *Journal of Geotechnical and Geoenvironmental Engineering,* 131(2), pp. 178-186.

Lee, F. H., Yong, K. Y., Quan, K. C. N. & Chee, K. T., 1998. Effect of Corners in Strutted Excavations: Field Monitoring and Case Histories. *Journal of Geotechnical and Geoenvironmental Engineering,* 124(4), pp. 339-349.

Lee, S. A., 2014. *Characterization and modeling of cement treated soil column used as cantilever earth retaining structure.* Singapore: Ph.D. thesis, National University of Singapore.

Lees, A. S. & Walter, H., 2018. Consideration of numerical methods in next generation Eurocode 7 (EN 1997)—current state of the amendment. *In Proceedings of*

The 9th European Conference on Numerical Methods In Geotechnical Engineering (NUMGE), pp. 927-933.

Leung, E., Pappin, J. & Koo, R., 2010. Determination of Small Strain Modulus and Degradation for in- Situ Weathered Rock and Old Alluvium Deposits. *International Conferences on Recent Advances in Geotechnical Earthquake Engineering and Soil Dynamics, San Diego, California*, pp. 1-7.

Lim, A. & Ou, C., 2018. Performance and Three-Dimensional Analyses of a Wide Excavation in Soft Soil with Strut-Free Retaining System. *International Journal of Geomechanics*, 18(9), pp. 1-18.

Lin, D. G., Chung, T. C. & Phien-Wej, N., 2003. Quantitative evaluation of corner effect on deformation behavior of multi-strutted deep excavation in Bangkok subsoil. *Geotechnical Engineering 34(1): 41-57,* 34(1), pp. 41-57.

Liu, Y. et al., 2015. Effect of spatial variation of strength and modulus on the lateral compression response of cement-admixed clay slab. *Géotechnique*, 65(10), pp. 851-865.

Liu, Y. et al., 2018. Lateral compression response of overlapping jet-grout columns with geometric imperfections in radius and position. *Canadian Geotechnical Journal*, 55(9), pp. 1282-1294.

Long, M., 2001. Database for retaining wall and ground movements due to deep excavations. *Journal of Geotechnical and Geoenvironmental Engineering*, 127(3), pp. 203-224.

Low, S., Ng, D., Chin, Y. & Ting, E., 2012. A Singapore case history of temporary removable ground anchor design to TR26. *The IES Journal Part A: Civil & Structural Engineering*, 5(3), pp. 181-194.

Lüftenegger, R., Schweiger, H. & Marte, R., 2013. Innovative solutions for supporting excavations in slopes. *In Proceedings of the 18th International Conference on Soil Mechanics and Geotechnical Engineering*, p. 2047–2050.

Marr, W. A. & Hawkes, M., 2010. Displacement-Based Design for Deep Excavations. *Earth Retention Conference (ER2010)*, pp. 82-100.

Marte, R., Scharinger, F. & Lüftenegger, R., 2017. Panels made by the deep mixing method for a building pit support in a slope. *In Grouting 2017*, pp. 385-394.

Marte, R., Schweiger, H. F., Choosrithong, K. & Lüftenegger, R., 2019. Sicherung von Baugrubenwänden und Geländesprüngen mittels scheibenartiger Stützelemente. *In the 12 Österreichische Geotechniktagung (In German)*, pp. 117-128.

Mašín, D., 2009. 3D modeling of a NATM tunnel in high K0 clay using two different constitutive models. *Journal of Geotechnical and Geoenvironmental Engineering,* 135(9), pp. 1326-1335.

Mašin, D. & Herle, I., 2005. Numerical analysis of a tunnel in London Clay using different constitutive models. *Proceedings of the 5th international symposium TC28 on geotechnical aspects of underground construction in soft ground*, p. 595–600.

Milligan, V. & Lo, K., 1970. Observations on some basal failures in sheeted excavations. *Canadian Geotechnical Journal,* 7(2), pp. 136-144.

Moore, J. & Longworth, T., 1979. Hydraulic uplift of the base of a deep excavation in Oxford Clay. *Géotechnique,* 29(1), pp. 35-46.

Moorman, C., 2004. Analysis of wall and ground movements due to deep excavations in soft soil based on a new worldwide database. *Soils and Foundations,* 44(1), pp. 87-98.

Moormann, C. & Klein, L., 2013. Deep Excavations with special ground shape. *Fifth Biot Conference on Poromechanics,* 10-12 July , pp. 1372-1381.

Muramatsu, M. & Abe, Y., 1996. Considerations in shaft excavation and peripheral ground deformation. *In: Mair, R. J. and Taylor, R. N. (eds.), Geotechnical Aspects of Underground Construction in Soft Ground*, pp. 173-179.

Namikawa, T. & Koseki, J., 2006. Experimental determination of softening relations for cement-treated sand. *Soils and Foundations,* 46(4), pp. 491-504.

Ng, C. W. W., Leung, E. H. Y. & Lau, C. K., 2004. Inherent anisotropic stiffness of weathered geomaterial and its influence on ground deformations around deep excavations. *Canadian Geotechnical Journal,* 41(1), pp. 12-24.

Ng, C. W. W. & Lings, M. L., 1995. Effects of Modeling Soil Nonlinearity and Wall Installation on Back Analysis of Deep Excavation in Stiff Clay. *Journal of Geotechnical Engineering,* 121(10), pp. 687-695.

Ng, C. W. W. & Yan, R. W. M., 1999. Three-dimensional modelling of a diaphragm wall construction sequence. *Géotechnique,* 49(6), pp. 825-834.

Nishimura, S., 2014. Cross-anisotropic deformation characteristics of natural sedimentary clays. *Géotechnique,* 64(12), pp. 981-996.

Nishimura, S., Nishiyama, T. & Murakami, A., 2005. Inverse analysis of soft grounds considering nonlinearity and anisotropy. *Soils and Foundations,* 45(2), pp. 87-95.

Nova, R., Castellanza, R. & Tamagnini, C., 2003. A constitutive model for bonded geomaterials subject to mechanical and/or chemical degradation. *International Journal for Numerical and Analytical Methods in Geomechanics,* 27(9), pp. 705-732.

O’Rourke, T. D., 1993. Base stability and ground movement prediction for excavations in soft clay. *Retaining structures, Thomas Telford,* p. 131–139.

O’Rourke, T. D. & McGinn, A. J., 2006. Lessons learned for ground movements and soil stabilization from the Boston Central Artery. *Journal of Geotechnical and Geoenvironmental Engineering,* 132(8), pp. 966-989.

Osman, A. S. & Bolton, M. D., 2006. Ground movement predictions for braced excavations in undrained clay. *Journal of Geotechnical and Geoenvironmental Engineering* , 132(4), pp. 465-477.

Osterberg, J. O., 1989. Necessary Redundancy in Geotechnical Engineering. *Journal of Geotechnical Engineering,* 115(11), pp. 1513-1531.

Ou, C. Y., Chiou, D. C. & Wu, T. S., 1996. Three-dimensional finite element analysis of deep excavations. *Journal of Geotechnical and Geoenvironmental Engineering,* 112(5), pp. 337-345.

Ou, C. Y., Hsieh, P. G. & Chiou, D. C., 1993. Characteristics of ground surface settlement during excavation. *Canadian Geotechnical Journal,* 30(5), pp. 758-767.

Ou, C. Y., Shiau, B. Y. & Wang, I. W., 2000. Three-dimensional deformation behavior of the Taipei National Enterprise Center (TNEC) excavation case history. *Canadian Geotechnical Journal,* 37(2), pp. 438-448.

Peck, R. B., 1969. Deep Excavation and Tunneling in Soft Ground. State-of-the-Art Report.. *Proceedings of the 7th International Conference on Soil Mechanics and Foundation Engineering, Mexico,* , pp. 225-290.

Pennington, D. S., Nash, D. F. T. & Lings, M. L., 1997. Anisotropy of G0 shear stiffness in Gault clay. *Géotechnique,* 47(3), pp. 391-398.

Phien-Wej, N., Humza, M. & Aye, Z. Z., 2012. Numerical modeling of diaphragm wall behavior in Bangkok soil using hardening soil model. *eotechnical Aspects of Underground Construction in Soft Ground - 7th International Symposium (IS-Rome),* p. 715–722.

Poh, T. & Wong, I., 1998. Effects of construction of diaphragm wall panels on adjacent ground field trial. *Journal of Geotechnical and Geoenvironmental Engineering,* 124(8), pp. 749-156.

Poh, T. & Wong, I., 2001. A field trial of jet-grouting in marine clay. *Canadian Geotechnical Journal,* 38(2), pp. 338-348.

Pölling, R., 2000. *Eine praxisnahe, schädigungsorientierte Materialbeschreibung von Stahlbeton für Strukturanalysen.* Bochum: Ph.D. thesis, Ruhr-Universität, Bochum (In German).

Pong, K. et al., 2012. Design considerations for one-strut failure according to TR26 – a practical approach for practising engineers. *The IES Journal Part A: Civil & Structural Engineering,* 5(3), pp. 166-180.

Potts, D. M., 2003. Numerical analysis: a virtual dream or practical reality?. *Géotechnique,* 53(6), p. 535–573.

Potts, D. M., Axelsson, K., Grande, L. & Schweiger, H. F., 2002. *Guidelines for the use of advanced numerical analysis.* London: Thomas Telford Publishing.

Potts, D. M. & Day, R. A., 1990. The use of sheet pile retaining walls for deep excavations in stiff clay. *Proceedings of the Institution of Civil Engineers, Part 1 Volme 88,* December, pp. 899-927.

Potts, D. M. & Fourie, A. B., 1986. A numerical study of the effects of wall deformation on earth pressures. *International Journal for Numerical and Analytical Methods in Geomechanics,* 10(4), pp. 383-405.

Potts, D. M. & Zdravkovic, L., 2001. *Finite Element Analysis in Geotechnical Engineering: Volume two - Application.* 1st ed. London: ICE Publishing.

Poulos, H. G., 2015. Pile Behavior—Consequences of Geological and Construction Imperfections. *Journal of Geotechnical and Geoenvironmental Engineering,* 131(5), pp. 538-563.

Powrie, W., Pantelidou, H. & Stallebrass, S. E., 1998. Soil stiffness in stress paths relevant to diaphragm walls in clay. *Géotechnique,* 48(4), pp. 483-494.

Puller, M., 2003. *Deep excavations: a practical manual.* London: Thomas Telford Publishing.

Rabaiotti, C. & Malecki, C., 2018. In situ testing of barrette foundations for a high retaining wall in molasse rock. *Géotechnique,* 68(12), pp. 1056-1070.

Ratananikom, W., Likitlersuang, S. & Yimsiri, S., 2013. An investigation of anisotropic elastic parameters of Bangkok Clay from vertical and horizontal cut specimens. *Geomechanics and Geoengineering: An International Journal ,* 8(1), pp. 15-27.

Richards, D. J., Clark, J. & Powrie, W., 2006. Installation effects of a bored pile wall in overconsolidated clay. *Géotechnique,* 56(6), pp. 411-425.

Rowe, P. W., 1962. The stress–dilatancy relation for static equilibrium of an assembly of particles in contact. *Proceedings of the Royal Society Series A,* Volume 269, pp. 500-557.

Schädlich, B., 2012. *A Multilaminate Constitutive Model for Stiff Soils.* Graz: Ph.D. thesis, Technische Universität Graz.

Schädlich, B. & Schweiger, H. F., 2013. Influence of anisotropic small strain stiffness on the deformation behavior of geotechnical structures. *International Journal of Geomechanics,* 13(6), pp. 861-868.

Schädlich, B. & Schweiger, H. F., 2014. A new constitutive model for shotcrete. *In Proceedings of The 8th European Conference on Numerical Methods In Geotechnical Engineering (NUMGE),* pp. 103-108.

Scharinger, F., 2007. *A multilaminate model for soil incorporating small strain stiffness.* Graz: Ph.D. Thesis, Technische Universität Graz.

Scharinger, F. & Schweiger, H. F., 2005. Undrained response of a double hardening multilaminate model for soils. *Proc. 11th Int. Conf. Computer Methods and Advances in Geomechanics, Turin,* p. 505–512.

Schütz, R., Potts, D. & Zdravkovic, L., 2011. Advanced constitutive modelling of shotcrete: Model formulation and calibration. *Computers and Geotechnics,* 38(6), pp. 834-845.

Schwamb, T., 2014. *Performance Monitoring and Numerical Modelling of a Deep Circular Excavation.* Cambridge: Ph.D. thesis, University of Cambridge.

Schweiger, H. F., 2001. Comparison of finite element results obtained for a geotechnical benchmark problem. *International Conference on Computer Methods and Advances in Geomechanics*, pp. 697-702.

Schweiger, H. F., 2002. Some remarks on pore pressure parameters A and B in undrained analyses with the hardening soil model. *PLAXIS Bulletin 12,* pp. 6-9.

Schweiger, H. F., 2008. The Role of Advanced Constitutive Models in Geotechnical Engineering. *Geomechanik und Tunnelbau* , 1(5), pp. 336-344.

Schweiger, H. F., Fabris, C., Ausweger, G. & Hauser, L., 2019. Examples of successful numerical modelling of complex geotechnical. *Innovative Infrastructure Solutions,* 4(2), pp. 1-10.

Schweiger, H. F., Paternesi, A. & Tschuchnigg, F., 2017. Eurocode 7-based design of SCL tunnels by means of numerical analyses. *Géotechnique,* 67(9), pp. 837-844.

Schweiger, H. F. et al., 2015. Finite element analysis of tunnel excavation and ground improvement techniques employing a new constitutive model for shotcrete. *In Proceedings 14th International Conference Computer Methods and Recent Advances in Geomechanics,* pp. 71-80.

Schweiger, H. F., Scharinger, F. & Lüftenegger, R., 2009. 3D finite element analysis of a deep excavation and comparison with in situ measurements. *in Geotechnical Aspects of Underground Construction in Soft Ground*, pp. 193-199.

Schweiger, H. F., Sedighi, P., Henke, S. & Borchert, K. M., 2014. Numerical modelling of ground improvement techniques considering tension softening. *In Proceedings of the 8th Int. Symposium on Geotechnical Aspects of Underground Construction in Soft Ground,* pp. 209-214.

Schweiger, H. F., Vermeer, P. A. & Wehnert, M., 2009. On the design of deep excavations based on finite element analysis. *Geomechanik und Tunnelbau,* 2(4), pp. 333-344.

Schweiger, H. F., Wiltafsky, C., Scharinger, F. & Galavi, V., 2009. A multilaminate framework for modelling induced and inherent anisotropy of soils. *Géotechnique*, 59(2), pp. 87-101.

Seah, T. H. & Lai, K. C., 2003. Strength and Deformation Behavior of Soft Bangkok Clay. *Geotechnical Testing Journal,* 26(4), pp. 1-11.

Sedighi, P., Schweiger, H. F. & Wehr, W. J., 2017. Effect of Jet-Grout Columns on the Seismic Response of Layered Soil Deposits. *International Journal of Geomechanics,* 17(3), pp. 1-13.

Shao, Y., Macari, E. & Cai, W., 2005. Compound deep soil mixing columns for retaining structures in excavations. *Journal of Geotechnical and Geoenvironmental Engineering,* 131(11), pp. 1370-1377.

Søreide, O. K., 2003. *Mixed hardening models for frictional soils.* Trondheim: Ph.D. thesis, Norwegian University of Science and Technology.

Symons, I. & Carder, D., 1993. Stress changes in stiff clay caused by the installation of embedded retaining walls. *In: Clayton, C. (ed.), Retaining structures,* pp. 227-236.

Tan, T. S. et al., 2003. A characterisation study of Singapore lower marine clay. *Characterisation and Engineering Properties of Natural Soils,* 2-4 December, p. 429–454.

Tariq, K. & Maki, T., 2014. Mechanical behaviour of cement-treated sand. *Construction nd Building Materials,* 58(5), pp. 54-63.

Teachavorasinskun, S., Thongchim, P. & Lukkunaprasit, P., 2002. Shear modulus and damping of soft Bangkok clays. *Canadian Geotechnical Journal,* 39(5), pp. 1201-1208.

Teng, F. C., Ou, C. Y. & Hsieh, P. G., 2014. Measurements and Numerical Simulations of Inherent Stiffness Anisotropy in Soft Taipei Clay. *Journal of Geotechnical and Geoenvironmental Engineering,* 140(1), pp. 237-250.

Terzaghi, K., 1943. *Theoretical soil mechanics.* New York: Wiley.

Tobar, T. & Meguid, M. A., 2010. Comparative evaluation of methods to determine the earth pressure distribution on cylindrical shafts: A review. *Tunnelling and Underground Space Technology,* 25(2), pp. 188-197.

TR26, 2010. *Technical reference for deep excavation.* Singapore: Spring Singapore.

Trunk, U., Zöhrer, A., Ackermann, T. & Chalmovsky, J., 2018. Entwurf, Bemessung und Nachweise von unbewehrten Düsenstrahlschächten. *Christian-Veder-Kolloquium, TU Graz*, pp. 183-201.

Tyagi, A. et al., 2017. Failure Modes of Tunnels with Improved Soil Surrounds. *Journal of Geotechnical and Geoenvironmental Engineering,* 143(11), pp. 1-13.

Ukritchon, B., Whittle, A. J. & Sloan, S. W., 2003. Undrained Stability of Braced Excavations in Clay. *Journal of Geotechnical and Geoenvironmental Engineering,* 129(8), pp. 738-755.

Vardanega, P. J. & Bolton, M. D., 2013. Stiffness of Clays and Silts: Normalizing Shear Modulus and Shear Strain. *Journal of Geotechnical and Geoenvironmental Engineering,* 139(9), p. 1575–1589.

Vermeer, P. A., 1978. A double hardening model for sand. *Géotechnique,* 28(4), pp. 413-433.

von Wolffersdorff, P. A. & Schweiger, H. F., 2008. Numerische Verfahren in der Geotechnik. In: K. J. Witt, ed. *GRUNDBAU -TASCHENBUCH Teil 1: Geotechnische Grundlagen.* Berlin: Ernst & Sohn, pp. 501-555.

Wang, A., Zhang, D. & Deng, Y., 2018. Lateral response of single piles in cement-improved soil: numerical and theoretical investigation. *Computers and Geotechnics*, 102(1), pp. 164-178.

Wehnert, M., 2006. *Ein Beitrag zur drainierten und undrainierten Analyse in der Geotechnik.* Stuttgart: Ph.D. Thesis, Universität Stuttgart.

Weißenbach, A., 1997. Kapitel „Baugrubensicherung“. Grundbau-Taschenbuch. In: 5th ed. Berlin: Ernst & Sohn, pp. 397-511.

Wharmby, N., 2011. Construction of Access Shafts for Tunnels and Deep Pipelines in Urban New Zealand. *14th Australasian tunnelling conference,* 8-10 March, pp. 161-166.

Whittle, A. J., Corral, G., Jen, L. C. & Rawnsley, R. P., 2015. Prediction and Performance of Deep Excavations for Courthouse Station, Boston. *Journal of Geotechnical and Geoenvironmental Engineering,* 141(4), pp. 1-13.

Whittle, A. J. & Davies, R. V., 2006. Nicoll Highway collapse: evaluation of geotechnical factors affecting design of excavation support system. *International Conference on Deep Excavations*, 28-30 June.

Whittle, A. J., Hashash, Y. M. A. & Whitman, R. V., 1993. Analysis of Deep Excavations in Boston. *Journal of Geotechnical Engineering,* 119(1), pp. 69-90.

Wiltafsky, C., 2003. *A multilaminate model for normally consolidated clay.* Graz: Ph.D. Thesis, Technische Universität Graz.

Xiao, H., Lee, F. H. & Liu, Y., 2017. Bounding Surface Cam-Clay Model with Cohesion for Cement-Admixed Clay. *International Journal of Geomechanics* , 17(1), pp. 1-22.

Xiao, H. W., Lee, F. H. & Chin, K. G., 2014. Yielding of cement-treated marine clay. *Soils and Foundations,* 54(3), pp. 488-501.

Yimsiri, S., Ratananikom, W., Fukuda, F. & Likitlersuang, S., 2013. Undrained strength-deformation characteristics of Bangkok Clay under general stress condition. *Geomechanics and Engineering,* 5(5), pp. 419-445.

Zdravkovic, L., Potts, D. M. & St John, H. D., 2005. Modelling of a 3D excavation in finite element analysis. *Géotechnique,* 55(7), pp. 497-513.

Zheng, G., Cheng, X. S., Diao, Y. & Wang, H. X., 2011. Concept and design methodology of redundancy in braced excavations. *Geotechnical Engineering Journal of the SEAGS & AGSSEA,* 42(3), pp. 13-21.

Appendix A

Material data for multilaminate model

Tab. A 1: Influence of individual strut failure - Multilaminate soil model parameters

Parameter	Unit	UM	F2	LM	OA1	OA2	OA3
E_{oed}^{ref}	[MN/m^2]	0.54	2.0	0.63	5.7	12.6	14.1
E_{ur}^{ref}	[MN/m^2]	4.03	9.0	4.72	54	120	141.6
m	[-]	1.0	1.0	1.0	0.6	0.6	0.6
ν_{ur}	[-]	0.2	0.2	0.2	0.2	0.2	0.2
A_{mat}	10^{-3}	7	7	7	2.5	2.5	2.5
K_0^{nc}	[-]	0.52	0.59	0.52	0.47	0.46	0.43
n_{cp}	[-]	21	21	21	21	21	21
ϕ_m	[°]	5	5	5	5	5	5
ψ_{min}	[°]	-3	-3	-3	-3	-3	-3
$m_{soft,\varphi}$	[-]	0.03	0.03	0.03	0.03	0.03	0.03
$m_{soft,c}$	[-]	1	1	1	1	1	1

Tab. A 2: Influence of anisotropic small strain stiffness - Multilaminate soil model parameters

Parameter	Unit	SC	MSC	FSC
E_{oed}^{ref}	[MN/m^2]	5.8	9.2	10.2
E_{ur}^{ref}	[MN/m^2]	46.6	73.4	102.2
m	[-]	1	1	0.85
ν_{ur}	[-]	0.2	0.2	0.2
A_{mat}	10^{-3}	7	7	2.5
K_0^{nc}	[-]	0.61	0.61	0.61
n_{cp}	[-]	21	21	21
ϕ_m	[°]	5	5	5
ψ_{min}	[°]	-3	-3	-3
$m_{soft,\varphi}$	[-]	0.03	0.03	0.03
$m_{soft,c}$	[-]	1	1	1
E_{v0}	[MN/m^2]	42	42	42
E_{h0}	[MN/m^2]	55	55	55
G_{vh0}	[MN/m^2]	19.5	32	43
ν_{hh0}	[-]	0.077	0.077	0.077
ν_{vh0}	[-]	0.1	0.1	0.1
$\varepsilon_{deg,1}$	[%]	0.004	0.004	0.004
$\varepsilon_{deg,2}$	[%]	0.03	0.03	0.03